

Scattering HCl Molecules from Au(111) and Ag(111) Surfaces

Thèse N° 9742

Présentée le 18 octobre 2019

à la Faculté des sciences de base
Unité de rattachement pour scientifiques ISIC
Programme doctoral en chimie et génie chimique

pour l'obtention du grade de Docteur ès Sciences

par

Jan Daniel GEWEKE

Acceptée sur proposition du jury

Prof. H. Girault, président du jury
Prof. A. Wodtke, Prof. R. Beck, directeurs de thèse
Prof. D. Nesbitt, rapporteur
Prof. D. Auerbach, rapporteur
Dr M. Lingenfelder, rapporteuse

2019

And when I die, and when I'm gone
There'll be [children] born
In this world to carry on, to carry on
— Blood, Sweat & Tears

Dedicated to the loving memory of Angelika Maak-Geweke
1955 – 2012

Acknowledgements

First of all, I would like to thank Alec Wodtke for giving me the opportunity to conduct the experiments in his group. Over the past years, I have really learned to appreciate your mixture of sometimes critical or even skeptical and *laissez-faire* guidance. Thank you for your inspiration.

Next, my thanks go to Kai Golibrzuch, Pranav R. Shirhatti, and Christof Bartels who introduced me to Beamer I and the rest of the lab equipment. You showed a lot of patience aligning lasers with me or explaining MATHEMATICA's vast functionality. I learned a lot from all of you!

I also acknowledge our group's frequent visitors Dan Auerbach and Igor Rahinov. Dan, you truly are a font of surface science wisdom (and beyond!). Igor, it was great to have someone around from time to time who worked with the same system. I've appreciated all the discussions, be it related to my work or more general, with both of you.

Further, I want to thank my Beamer I fellows Christoph Steinsiek, Sven Meyer, and Artur Mehling who lend a helping hand whenever needed for the experiments or simply made endless days of measurements more bearable.

That said, I would like to thank the whole group for providing me with a very nice working atmosphere (and the regular cake). Somebody was always there for simple chattering, sharing the joy and pain of experimental work, or discussing unexpected results.

I also need to acknowledge the mechanical and electronics workshops. Without their help it would have been impossible to conduct all of my experiments.

Finally, I want to thank my friends and my family. Without your support I would not be where I am today.

Last but not least, I cannot express enough gratitude to the most important people in my life. Anna, thank you for all your support, your help and your love throughout the years. Elea & Ava, it is pure joy to see you grow. I love you so much!

Göttingen, August 2019

J. G.

Abstract

In this thesis, I present an experimental molecular beam surface scattering study of dynamical processes involved when HCl molecules are scattered from Au(111) and Ag(111) surfaces. I investigated vibrational excitation, translational inelasticity and dissociative adsorption in combination with associative desorption. The experiments were conducted in an ultra-high vacuum (UHV) molecular beam/surface scattering apparatus equipped with a pulsed nanosecond infrared (IR) laser source for vibrational state manipulation and pulsed nanosecond ultraviolet (UV) lasers for quantum-state-resolved detection of molecules *via* resonance enhanced multi-photon ionization (REMPI) before and after the collisions.

For HCl/Au(111), I found surface temperature dependent vibrational excitation probabilities (VEPs) from vibrational state $\nu = 0 \rightarrow 1$ to be in the range of $10^{-5} - 10^{-3}$ for incidence energies of $\langle E_i \rangle = 0.67 - 0.99$ eV, which is low compared to other molecule-surface systems. On the other hand, VEPs for the $\nu = 1 \rightarrow 2$ transition were substantially higher at $10^{-3} - 10^{-2}$ for comparable incidence energies. In both cases, excitation probabilities could be divided into electronically adiabatic and nonadiabatic contributions where the latter exponentially depended on the surface temperature T_s . This combination of adiabatic and nonadiabatic vibrational excitation has so far been uniquely observed for HCl scattered from Au(111) and Ag(111) surfaces. Extracting $\langle E_i \rangle$ and T_s independent interaction coefficients, I found the nonadiabatic excitation to be stronger than the adiabatic one by a factor of 67 for the $\nu = 0 \rightarrow 1$ and 24 for the $\nu = 1 \rightarrow 2$ channel.

In comparison, on Ag(111) only the excitation from the vibrational ground state could be observed. With VEPs in the range of $10^{-4} - 10^{-3}$ being slightly higher than on gold, this difference was interpreted as enhanced nonadiabatic interactions on silver. Relatively low barriers to dissociation on both metal surfaces (e. g., compared to NO/Au(111)) might have led to the higher $\nu = 1 \rightarrow 2$ VEPs on Au(111). Further, the absence of higher excitation channels ($\nu = 2 \rightarrow 3$ on gold, $\nu = 1 \rightarrow 2$ on silver) might also be explained by the enhanced dissociation of HCl molecules incident in excited vibrational states.

Dissociation probabilities of HCl on metal surfaces were measured by AUGER electron spectroscopy after controlled molecular beam dosage monitored by a quadrupole mass spectrometer. Even though the dissociation probabilities on Ag(111) were predicted to be higher than on Au(111), I could not determine them within the current technical limitations. Additionally, the actual dissociation probabilities I determined on Au(111) employing AES

Abstract

remained below 0.06 – 0.17, which is lower than those predicted by a series of computational studies by a factor of 2 – 6. On the other hand, translational energy losses calculated in the latest AIMDEF study match the experimental results for $\nu = 1 \rightarrow 1$ and $\nu = 1 \rightarrow 2$ quite accurately. In sum, the results of this thesis, which all indicate that HCl exhibits both electronically adiabatic and nonadiabatic interactions with metal surfaces during scattering events, can serve as benchmark data to test and improve theoretical descriptions of gas-surface interactions, especially in those cases where nonadiabaticity plays an important role.

Keywords: HCl, Au(111), Ag(111), molecular beam, surface scattering, REMPI, vibrational excitation, translational inelasticity, dissociative adsorption

Zusammenfassung

In dieser Dissertation präsentiere ich die Ergebnisse einer Oberflächenmolekularstrahlstudie über dynamische Prozesse, die auftreten, wenn HCl Moleküle von Au(111)- und Ag(111)-Oberflächen gestreut werden. Ich habe die Vibrationsanregung, Translationsinelastizität und dissoziative Adsorption sowie assoziative Desorption untersucht. Die Experimente wurden in einer Ultrahochvakuumapparatur für Molekularstrahl-/Oberflächenstreuexperimente durchgeführt, welche mit gepulsten Nanosekundenlasern im IR-Bereich (für die Manipulation von Vibrationszuständen) und solchen im UV-Bereich (für die quantenzustandsselektive Detektion mittels resonanzverstärkter Mehrphotonenionisation vor und nach der Streuung) ausgestattet ist.

Auf Au(111) habe ich im Vergleich zu anderen Molekül/Oberflächen-Systemen eher geringe Vibrationsanregungswahrscheinlichkeiten (VAW) für den $\nu = 0 \rightarrow 1$ Übergang im Bereich von $10^{-5} - 10^{-3}$ für Einfallenergien von $\langle E_i \rangle = 0.67 - 0.99$ eV ermittelt. Im Vergleich dazu waren die VAW für die $\nu = 1 \rightarrow 2$ Anregung bei vergleichbaren $\langle E_i \rangle$ mit Werten im Bereich von $10^{-3} - 10^{-2}$ erheblich höher. In beiden Fällen konnten die VAW in elektronisch adiabatische und nichtadiabatische Beiträge aufgeteilt werden, wobei letztere exponentiell von der Oberflächentemperatur abhängig waren. Diese Kombination von adiabatischer und nichtadiabatischer Vibrationsanregung ist so bisher nur bei von Au(111) und Ag(111) gestreutem HCl beobachtet worden. Durch die Bestimmung von $\langle E_i \rangle$ - und T_s -unabhängigen Wechselwirkungskoeffizienten stellte sich heraus, dass die nichtadiabatische Anregung für den $\nu = 0 \rightarrow 1$ und den $\nu = 1 \rightarrow 2$ Übergang um den Faktor 67 bzw. 24 stärker war als die adiabatische.

Auf Ag(111) konnte hingegen nur der $\nu = 0 \rightarrow 1$ Übergang beobachtet werden. Die im Vergleich zu Gold leicht erhöhten VAW im Bereich von $10^{-4} - 10^{-3}$ wurden als stärkere nichtadiabatische Wechselwirkung mit Silber interpretiert. Relativ niedrige Dissoziationsbarrieren auf beiden Oberflächen (bspw. im Vergleich zu NO/Au(111)) könnten zu den höheren $\nu = 1 \rightarrow 2$ VAW auf Au(111) geführt haben. Darüber hinaus könnte auch die Abwesenheit der Anregungen von $\nu = 2 \rightarrow 3$ auf Au(111) und $\nu = 1 \rightarrow 2$ auf Ag(111) durch eine verstärkte Dissoziation der einfallenden HCl Moleküle in angeregten Vibrationszuständen zu erklären sein.

Die Dissoziationswahrscheinlichkeiten S_0 von HCl auf den Metalloberflächen wurden mit Augerelektronenspektroskopie ermittelt, nachdem die Oberflächen durch den Molekularstrahl einer bestimmten, durch Quadrupolmassenspektrometrie überwachten Dosis HCl

Abstract

ausgesetzt worden war. Obwohl die Dissoziation auf Ag(111) stärker als auf Au(111) sein sollte, konnte ich erstere vermutlich auf Grund der technischen Beschränkungen der Apparatur nicht bestimmen. Außerdem lagen die mittels AES auf Au(111) bestimmten $S_0 < 0.06 - 0.17$ um den Faktor 2 – 6 unter den Werten mehrerer theoretischer Berechnungen. Im Gegensatz dazu gab es eine gute Übereinstimmung der experimentellen Translationsenergieverluste für $v = 1 \rightarrow 1$ und $v = 1 \rightarrow 2$ mit der neuesten AIMDEF-Studie. In ihrer Gesamtheit können die Ergebnisse dieser Arbeit, die alle auf elektronisch adiabatische und nichtadiabatische Wechselwirkungen bei der Streuung von Metalloberflächen hindeuten, als Vergleichsdaten dienen, mit denen sich theoretische Modelle von Gas-Oberflächen-Interaktionen testen und verbessern lassen - insbesondere in den Fällen, in denen Nichtadiabatizität eine wichtige Rolle spielt.

Stichwörter: HCl, Au(111), Ag(111), Molekularstrahl, Oberflächenstreuexperimente, REM-PI, Vibrationsanregung, Translationsinelastizität, dissoziative Adsorption

Contents

Acknowledgements	v
Abstract (English/Deutsch)	vii
List of figures	xiii
List of tables	xvii
Acronyms	xix
I Introduction	1
1 Introduction	3
1.1 Motivation	3
1.2 Previous Experimental Work	5
1.3 Previous Theoretical Work	11
1.3.1 Density Functional Theory	11
1.3.2 Including Electronical Nonadiabaticity	12
1.3.3 Predictions on HCl/Au(111) Scattering	12
2 Experimental Details and Methods	15
2.1 General Setup	15
2.1.1 Pumping System	16
2.1.2 Generation of Molecular Beams	18
2.1.3 Detection of Molecules	18
2.1.4 Surface Mounting	19
2.2 Laser Systems	20
2.2.1 IR Laser Source	20
2.2.2 UV Laser Source	22
2.3 Methods	23
2.3.1 Surface Preparation	23
2.3.2 REMPI	23
2.3.3 TOF Techniques	25

Contents

2.3.4	AUGER Electron Spectroscopy	27
II	Results	31
3	Scattering HCl from Au(111)	33
3.1	Vibrational Excitation	33
3.1.1	Excitation from $\nu = 0 \rightarrow 1$	37
3.1.2	Excitation from $\nu = 1 \rightarrow 2$	49
3.1.3	Excitation from $\nu = 2 \rightarrow 3$	59
3.2	Translational Inelasticity	62
3.3	Dissociation	67
3.3.1	Initial Experiments	68
3.3.2	Increasing the Incidence Energy	69
3.3.3	Determination of Surface Coverage	73
3.3.4	Initial Sticking Probabilities	80
3.3.5	Potential Problems	88
3.3.6	Associative Desorption	91
4	Scattering HCl from Ag(111)	105
4.1	Vibrational Excitation	105
4.1.1	Excitation from $\nu = 0 \rightarrow 1$	105
4.1.2	Excitation from $\nu = 1 \rightarrow 2$	119
4.2	Translational Inelasticity	120
4.3	Dissociation	126
4.3.1	Cl ₂ Recombination	127
III	Discussion	129
5	Discussion	131
5.1	Vibrational Excitation	133
5.1.1	Comparison of Different Systems	133
5.1.2	Comparison with Theoretical Predictions	137
5.1.3	Kinetic Approach	138
5.2	Translational Inelasticity	142
5.2.1	HCl/Au(111)	142
5.2.2	HCl/Ag(111)	147
5.3	Dissociation	151
5.3.1	Comparison with Initial Theory	151
5.3.2	Further Theoretical Work	155
5.3.3	Associative Desorption	161

6	Conclusions	163
IV	Appendix	167
A	Appendix	169
A.1	Theoretical Methods	169
A.1.1	Density Functional Theory	169
A.2	Velocity and Kinetic Energy Distributions	171
A.2.1	Density-to-Flux and Domain Conversion	171
A.2.2	Detection Geometry	173
A.3	Angular Distributions	177
A.3.1	Incident Beam Width and Density	177
A.3.2	Line Detection	181
A.3.3	Ion Collection Efficiency	183
	Bibliography	185
	Curriculum Vitae	199

List of Figures

1.1	DFT literature analysis	4
1.2	Comparison NO-NH ₃	6
1.3	Comparison NO/Au - NO/LiF	7
1.4	Electron affinity as a proxy	9
1.5	Previous work: VEP of HCl($v = 0 \rightarrow 1$)	10
1.6	Previous work: Theoretical predictions on the dissociation	13
2.1	Beamer I sketch	17
2.2	Heated nozzle	19
2.3	Molecular beam line	20
2.4	IR system	21
2.5	UV system	22
2.6	General REMPI scheme	24
2.7	Energy diagram HCl	25
2.8	REMPI spectrum of HCl	26
2.9	Laser geometries for TOF experiments	27
2.10	TOF spectra example	28
2.11	Au(111) AUGER example	29
3.1	Sensitivity factors: REMPI spectra	36
3.2	Sensitivity factors: J dependence	36
3.3	T_s dependent REMPI spectra $v = 0 \rightarrow 1$ on Au(111)	38
3.4	Angular distributions $v = 0$ and $v = 1$ on Au(111)	39
3.5	Temporal distributions $v = 0$ and $v = 1$ on Au(111)	42
3.6	Temporal correction $v = 0$ and $v = 1$ on Au(111)	42
3.7	Detector gain scattering from Au(111)	43
3.8	Laser power dependence scattering from Au(111)	44
3.9	$v = 0 \rightarrow 1$ VEP on Au(111)	45
3.10	Erroneous line assignment in previous work	47
3.11	$A^{\text{ad.}}$ and $A^{\text{nonad.}}$ vs. E_i for $v = 0 \rightarrow 1$ on Au(111)	48
3.12	$v = 0 \rightarrow 1$ VEP on Au(111) incl. old data	49
3.13	T_s dependent REMPI spectra $v = 1 \rightarrow 2$	50

List of Figures

3.14 Velocity distributions for $v = 1 \rightarrow 2$ on Au(111)	51
3.15 Angular distributions $v = 1$ and $v = 2$ on Au(111)	53
3.16 Temporal distributions $v = 1$ and $v = 2$ on Au(111)	54
3.17 Temporal correction $v = 1$ and $v = 2$ on Au(111)	54
3.18 Laser power dependence scattering from Au(111)	55
3.19 $v = 1 \rightarrow 2$ VEP on Au(111)	57
3.20 $A^{\text{ad.}}$ and $A^{\text{nonad.}}$ vs. $\langle E_i \rangle$ for $v = 1 \rightarrow 2$ on Au(111)	58
3.21 REMPI spectra $v = 2 \rightarrow 3$ on Au(111)	61
3.22 TOF distributions $v = 1 \rightarrow 2$ on Au(111)	62
3.23 Velocity distributions $v = 1 \rightarrow 2$ on Au(111)	63
3.24 Kinetic energy distributions $v = 1 \rightarrow 2$ on Au(111)	65
3.25 T-R coupling $v = 1 \rightarrow 2$ on Au(111)	66
3.26 AUGER spectra examples on Au(111)	68
3.27 Vibrational population from the hot nozzle	70
3.28 Calibration of the Nozzle Temperature	71
3.29 Incident beam from the hot nozzle	72
3.30 AUGER spectra examples 2 on Au(111)	73
3.31 H_2 partial pressure rise	74
3.32 Incident beam width	75
3.33 Heavy species enrichment: pressure differences	76
3.34 Heavy species enrichment: pressure ratios	77
3.35 Representative AUGER line scans	78
3.36 Coverage vs. dose	82
3.37 T_s dependent coverage	84
3.38 S_0 vs. $\langle E_i \rangle$	85
3.39 S_0 fit vs. $\langle E_i \rangle$	87
3.40 ESD kinetics	88
3.41 REMPI-TPD of HCl, H_2 , and Cl	92
3.42 REMPI-TPD of HCl	93
3.43 REMPI-TPD analysis 1	95
3.44 REMPI-TPD analysis 2	98
3.45 REMPI-TPD analysis 3	100
3.46 Cl_2 REMPI	103
3.47 Cl_2 desorption from Au(111)	104
4.1 T_s dependent REMPI spectra $v = 0 \rightarrow 1$ on Ag(111)	107
4.2 Angular distributions $v = 0$ and $v = 1$ on Ag(111)	109
4.3 Angular distributions $v = 0$ and $v = 1$ on Ag(111) 2	110
4.4 Temporal distributions $v = 0$ and $v = 1$ for $\langle E_i \rangle = 0.66$ eV on Ag(111)	111
4.5 Temporal distributions $v = 0$ and $v = 1$ for $\langle E_i \rangle = 0.86$ eV on Ag(111)	112
4.6 Temporal distributions $v = 0$ and $v = 1$ for $\langle E_i \rangle = 1.00$ eV & 1.15 eV on Ag(111)	113

4.7	Temporal corrections $\nu = 0$ and $\nu = 1$ on Ag(111)	114
4.8	Detector gain scattering from Ag(111)	115
4.9	Laser power dependence scattering from Ag(111)	116
4.10	$\nu = 0 \rightarrow 1$ VEP on Ag(111)	117
4.11	$A^{\text{ad.}}$ and $A^{\text{nonad.}}$ vs. E_i for $\nu = 0 \rightarrow 1$ on Ag(111)	118
4.12	REMPI spectra $\nu = 1 \rightarrow 2$ on Ag(111)	119
4.13	TOF distributions $\nu = 0 \rightarrow 0$ and $\nu = 1 \rightarrow 1$ on Ag(111)	120
4.14	Velocity distributions $\nu = 0 \rightarrow 0$ and $\nu = 1 \rightarrow 1$ on Ag(111)	121
4.15	Kinetic energy distributions $\nu = 0 \rightarrow 0$ and $\nu = 1 \rightarrow 1$ on Ag(111)	123
4.16	T-R coupling $\nu = 0 \rightarrow 0$ and $\nu = 1 \rightarrow 1$ on Ag(111)	124
4.17	AUGER spectra examples on Ag(111)	126
4.18	Cl_2 desorption from Ag(111)	128
5.1	NO $\nu = 2 \rightarrow 3$ VEP on Au(111)	134
5.2	Electron Affinity as a proxy 2	135
5.3	Electron Affinity as a proxy 3	136
5.4	Nonadiabatic interaction strength from kinetic model	140
5.5	Kinetic model fit	141
5.6	Baule limit on Au(111)	143
5.7	Baule limit on Au(111) 2	147
5.8	Baule limit Au(111) vs. Ag(111)	148
5.9	TD component scattering from Ag(111)	149
5.10	Comparison of $S_0^{\nu=i}$ with theory	151
5.11	Comparison of S_0 with theory	153
5.12	Comparison of S_0 with theory fit	153
5.13	Comparison of S_0 with gathered theory	160
A.1	Geometrical issues of TOF measurements	174
A.2	TOF simulation results	175
A.3	Geometry for measuring angular distributions	177
A.4	Influence of the incident beam	180
A.5	Diluted density due to beam divergence	182
A.6	Diluted density due to velocity distribution	183
A.7	Ion collection efficiency	184

List of Tables

1.1	Summary of vibrational excitation	8
3.1	Scattering conditions for $\nu = 0 \rightarrow 1$ excitation on Au(111)	37
3.2	Detector gain scattering from Au(111)	41
3.3	$A^{\text{ad.}}$ and $A^{\text{nonad.}}$ for $\nu = 0 \rightarrow 1$ on Au(111)	45
3.4	Scattering conditions for $\nu = 1 \rightarrow 2$ excitation on Au(111)	50
3.5	Mean velocities for $\nu = 1 \rightarrow 2$ on Au(111)	52
3.6	$A^{\text{ad.}}$ and $A^{\text{nonad.}}$ for $\nu = 1 \rightarrow 2$ on Au(111)	58
3.7	$\frac{dA^{\text{ad.}}}{dE_i}$ and $\frac{dA^{\text{nonad.}}}{dE_i}$ on Au(111)	58
3.8	Experimental conditions for $\nu = 2 \rightarrow 3$ on Au(111)	60
3.9	Fitting parameters of velocity distributions $\nu = 1$ and $\nu = 2$ on Au(111).	64
3.10	T-R coupling $\nu = 0 \rightarrow 0$ and $\nu = 1 \rightarrow 1$ on Au(111)	66
3.11	Dissociation: incident beam conditions.	81
3.12	S_0 fit parameters	86
3.13	TPD resulty summary	99
4.1	Scattering conditions for $\nu = 0 \rightarrow 1$ excitation on Ag(111)	106
4.2	Parameters of angular distributions for $\nu = 0 \rightarrow 1$ excitation on Ag(111)	108
4.3	Detector gain scattering from Ag(111)	115
4.4	$A^{\text{ad.}}$ and $A^{\text{nonad.}}$ for $\nu = 0 \rightarrow 1$ on Ag(111)	118
4.5	$\frac{dA^{\text{ad.}}}{dE_i}$ and $\frac{dA^{\text{nonad.}}}{dE_i}$ on Au(111)	118
4.6	Fitting parameters of velocity distributions $\nu = 0 \rightarrow 0$ & $\nu = 1 \rightarrow 1$ on Ag(111).	122
4.7	T-R coupling $\nu = 0 \rightarrow 0$ and $\nu = 1 \rightarrow 1$ on Ag(111)	125
5.1	S_0 theory fit parameters	154

Acronyms

AES	AUGER electron spectroscopy
AIMD	<i>ab initio</i> molecular dynamics
APPH	AUGER peak-to-peak height
BBO	beta barium borate
BOA	BORN-OPPENHEIMER approximation
cw	continuous wave
DABCO	1,4-diazabicyclo[2.2.2]octane
DFT	density functional theory
DOF	degrees of freedom
DS	direct scattering
EF	electronic friction
EHP	electron-hole pair
ESD	electron stimulated desorption
FWHM	full width at half maximum
GGA	generalized gradient approximation
IAA	independent atom approximation
IESH	independent electron surface hopping
IR	infrared
LUMO	lowest unoccupied molecular orbital
MBD	MAXWELL-BOLTZMANN distribution
MCP	multi-channel plate

List of Tables

MD	molecular dynamics
ML	monolayer
PES	potential energy surface
REMPI	resonance enhanced multi-photon ionization
RGA	residual gas analyzer
S/N	signal-to-noise ratio
SFG	sum-frequency generation
SHG	second-harmonic generation
TD	trapping/desorption
TMP	turbo molecular pump
TPD	temperature programmed desorption
TOF	time-of-flight
TS	transition state
UHV	ultra-high vacuum
UV	ultraviolet
VEP	vibrational excitation probability

INTRODUCTION

1 Introduction

1.1 Motivation

Academic research on dynamics at surfaces is typically of fundamental nature due to experimental and theoretical limitations on modeling the complex processes in chemical reactors. Nevertheless, studies on the elemental steps in heterogeneous catalysis and the underlying physical and chemical processes are of utmost importance for practical application. Probably the most famous example is the HABER-BOSCH process for the production of NH_3 . Developed at the beginning of the 20th century, three scientists working on this system have been awarded with a NOBEL Prize in Chemistry since then: Fritz Haber in 1918¹, Carl Bosch in 1931², and Gerhard Ertl in 2007³. Nowadays, about 140 Mt of NH_3 are produced worldwide [4], 90 % thereof *via* the HABER-BOSCH process. In total, this single chemical production process accounts for about 1.4 % of the worldwide consumption of fossil fuels [5].

Although this might be an extreme case due to the enormous demand for NH_3 , which is mainly used for fertilizer production, improving existing and developing new catalysts in general will most probably continue to be one of the technical key issues in the 21st century. To a greater or lesser extent, it might prove crucial for tackling global problems like an ever-growing world population on the one hand and still-existing famine on the other hand, as well as energy storage and conversion, or environmental pollution (which are themselves all connected to each other).

In order to develop new catalysts or to improve existing ones in a reasonable manner, the elementary steps in catalytic reactions and the underlying physical principles need to be understood. That is, processes like physisorption, chemisorption, dissociation or simply collisions of atoms and molecules with a variety of surfaces have to be examined. Further,

¹ "for the synthesis of ammonia from its elements" [1]

² "in recognition of their contributions to the invention and development of chemical high pressure methods" [2]

³ "for his studies of chemical processes on solid surfaces" [3]

to overcome a purely descriptive picture and to develop comprehensive theories, the driving forces behind these processes need to be identified. Thus, many studies including my own are concerned with the energy exchange between molecules and surfaces during their encounter. Over the last few decades, a second possibility to do so apart from tedious experimental work has emerged. With the increasing computing capacity that is readily accessible from every place with an internet connection, computational chemistry has evolved from a niche to the forefront of research. Nowadays, with all its variations density functional theory (DFT) is probably the most widely-used method for computing electronic structures and related energies of molecules or, generally speaking, ensembles of atoms. Its growing importance can be seen in Fig. 1.1 which shows the steep increase in the number of publications on DFT per year from the 1990s onwards.⁴

These calculations are extremely useful, e. g., for the determination of transition states and

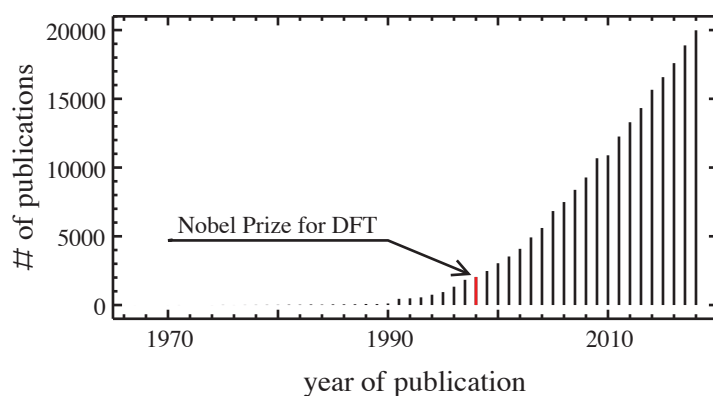


Figure 1.1 Results of a DFT literature analysis on WEB OF SCIENCE™. Shown are the absolute numbers of publications with the topic on DFT per year which exhibit a steep increase from the 1990s onwards. Depicted in red is the year 1998 when Walter Kohn was awarded the NOBEL prize in chemistry for his development of DFT.

corresponding energy levels, and in some cases have reached what is often referred to as *chemical accuracy* [6] (i. e., the errors in calculating energetic states are below $\sim 1 \text{ kcal mol}^{-1}$).⁵ With further increasing computing capacity and innovative approaches like the implementation of machine learning algorithms (e. g., neural network potentials [8]) theoretical chemists are closer than ever to what my supervisor Prof. Alec Wodtke likes to call the "*world's greatest microscope*" [9]. That is, chemical processes can be modeled and visualized on an atomistic level. Moreover, unknown reactions can be predicted and catalysts, for example, can be invented on the computer.

However, DFT calculations generally rely on the BORN-OPPENHEIMER approximation (BOA). In 1927, Max Born and Robert Oppenheimer published their seminal paper on separating the motion of light and fast electrons from that of the much heavier and slower

⁴ Literature search and analysis on <http://www.webofscience.com>. A search for the topics "DFT" OR "density functional theory" delivered slightly more than 200 000 entries for years 1965 - 2018.

⁵ It must be noted, though, that DFT functionals frequently used in modeling dynamics at surfaces such as PBE, PW91 or RPBE tend to underestimate reaction barriers [7].

atomic nuclei [10]. Within this approximation, the positions of the nuclei are frozen for the calculation of the electronic wavefunction. That is, an *electronic* SCHRÖDINGER equation is solved omitting the kinetic energy operator for the nuclei. Parametrically depending on nuclear coordinates, the resulting potential energy surface (PES) can then serve as a basis for electronically *adiabatic* dynamical calculations. Thus, although DFT is a powerful and important tool for surface scientists in general, accurate and sophisticated experimental work is required to determine the extent to which electronically *nonadiabatic* behavior, that cannot be captured by traditional DFT, plays a role in surface chemistry. The term "*nonadiabatic*" here refers to situations where the motion of electrons and nuclei should not be separated because electronic and vibrational or translational degrees of freedom are observed to interact.

1.2 Previous Experimental Work

To date, fingerprints of electronically nonadiabatic behavior have been found in different processes for several molecule/surface systems. In one of the first works, in 1985 Retner *et al.* examined NO($v = 0$) scattering from Ag(111) and found vibrationally excited molecules in $v = 1$ after the collision [11, 12]. In stark contrast to the work on vibrational excitation of NH₃ on Au(111) that was published around the same time by Kay *et al.* [13], NO excitation probabilities exhibited a linear, threshold-less dependence on the incidence translational energy E_i and an ARRHENIUS-like dependence on the surface temperature T_S (see Fig. 1.2). These findings lead to the conclusion that the vibrational energy must have come from the surface immediately provoking theoretical works by News [14] and by Gadzuk and Holloway [15]. Although different in detail, both suggested a charge transfer from the surface to the NO molecule at some distance from the surface. Here, among the most important system parameters were the work function of the surface and the electron affinity of the molecule. Transferring the electron back to the surface subsequently left the molecule vibrationally excited. This coupling of electronic to vibrational degrees of freedom (DOF) marks the breakdown of the BOA.

In the following years, electronic nonadiabaticity on the experimental side was mainly studied in the form of either vibrational relaxation or vibrational excitation of small, diatomic molecules being scattered from a single crystal surface.⁶ Experimental evidence for the importance of an accessible electron bath was delivered in a famous study by Huang *et al.* who compared the relaxation probabilities of NO molecules initially in highly excited vibrational states scattering from Au(111) and LiF [19]. While relaxation by several vibrational quanta was highly efficient on the metal surface, the insulator barely affected the vibrational state

⁶ Further studies include electronic excitations in metal surfaces upon H and D atom adsorption, e. g. on Schottky diodes [16] and metal-insulator-metal junctions [17]. Recently, Bünermann *et al.* found that the high translational energy loss in scattering H atoms from Au(111) can only be explained by electron-hole pair excitation [18].

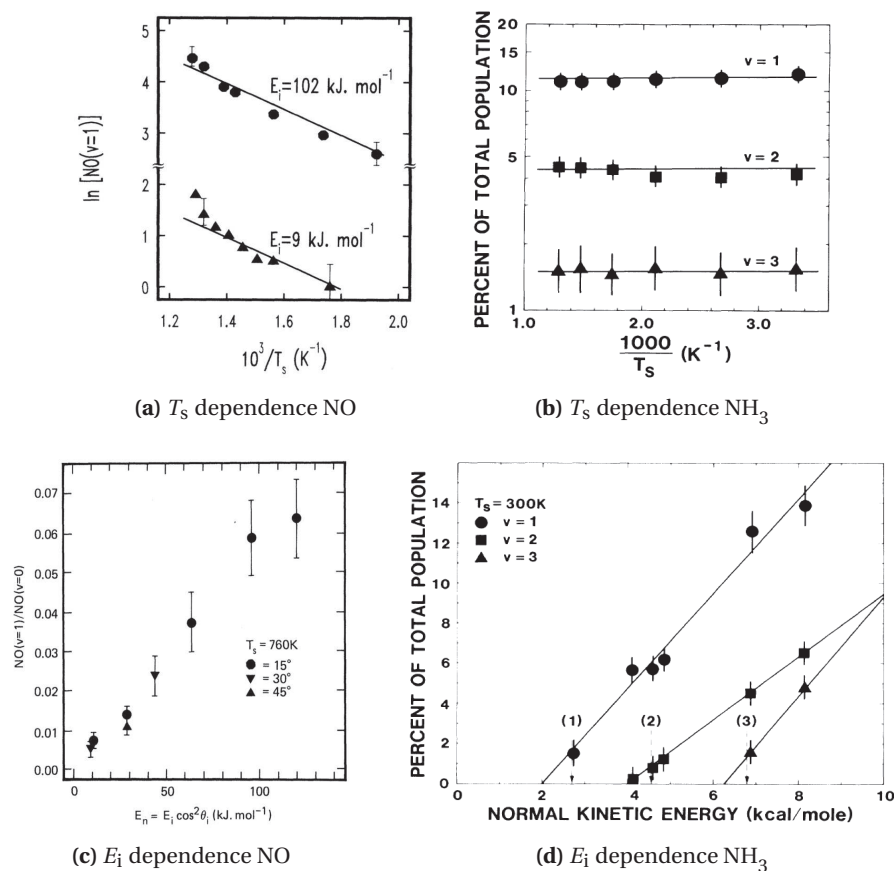


Figure 1.2 Surface temperature and incidence translational energy dependence of the vibrational excitation of NO and NH_3 . While NO showed an ARRHENIUS-like dependence on the surface temperature (a), the vibrational excitation of NH_3 seemed to be independent of T_s (b). For both molecules, the vibrational excitation dependence on E_i appeared to be approximately linear (c & d), but only for NH_3 there are energetic thresholds depending on the excited vibrational quanta (d). Taken from Refs. [12, 13].

of the molecules (see Fig. 1.3). In further experiments, electron emission from the surface was observed if the vibrational energy of the incident NO molecules surpassed the work function of a Cs-covered Au(111) surface [20]. Here, the coupling of vibrational to electronic degrees of freedom could directly be observed in the dependence of the electrons' kinetic energy on the vibrational state of the incident molecule [21]. Moreover, also the spatial orientation of a NO molecule during the collision was shown to influence the degree of vibrational energy transfer. Because the electron accepting lowest unoccupied molecular orbital (LUMO) has a higher probability density at the N atom, the likelihood of vibrational relaxation is increased when this side of the molecule points towards the surface during a collision [22, 23]. Several following studies shed light on vibrational excitation and relaxation in the NO/Au(111) system and the coupling of translational and vibrational degrees of freedom. Cooper, Golibrzuch *et al.* determined surface temperature and incidence

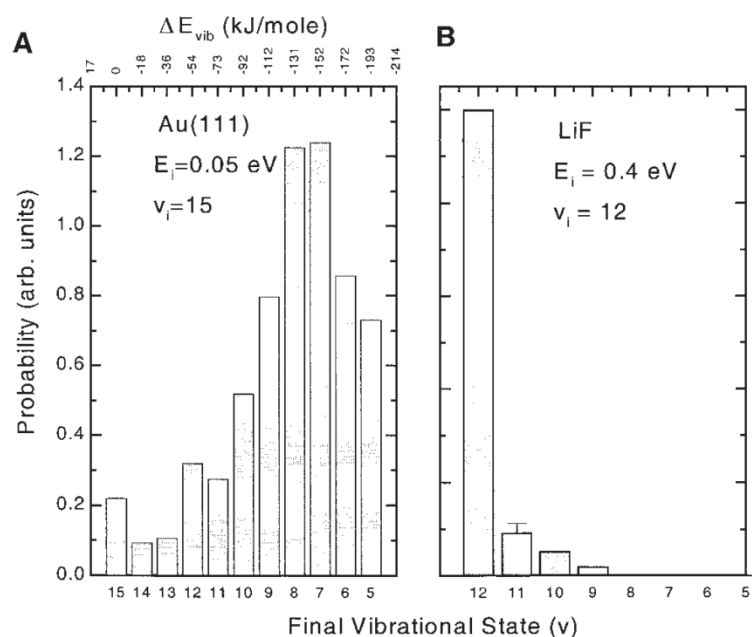


Figure 1.3 Vibrational state distributions of NO molecules after scattering from (A) Au(111) and (B) LiF. The initial vibrational states were $v = 15$ and $v = 12$, respectively. While molecules having encountered the metal surface exhibited a large probability of vibrational relaxation, those having encountered the insulator surface almost completely remained in the initial state. Taken from Ref. [19].

translational energy dependent excitation probabilities for $\text{NO}(v = 0 \rightarrow 1)$, $\text{NO}(v = 0 \rightarrow 2)$, and $\text{NO}(v = 0 \rightarrow 3)$ excitation to be in the range of $10^{-3} - 10^{-2}$, $10^{-4} - 10^{-3}$, and $10^{-5} - 10^{-4}$, respectively [24, 25]. In general, higher incidence translational energy lead to increased vibrational excitation as well as relaxation which was explained by stronger nonadiabatic interactions [26, 27]. In contrast, increasing surface temperature did enhance the excitation only while the relaxation was hardly influenced [26].

Beneath NO/Au(111) several other molecule-surface systems have been found to exhibit vibrational excitation that so far can only be explained by electronically nonadiabatic interactions (a summary of which can be found in Tab. 1.1). For NO/Cu(110) Watts *et al.* found $v = 0 \rightarrow 1$ excitation probabilities in the range of up to a few percent, similar to what was found on Au(111) [25] and Ag(111) [12]. On the other hand, for CO the $v = 0 \rightarrow 1$ excitation on Au(111) was approximately one order of magnitude less probable than for NO [28] while N_2 excitation could not be observed at all, even though relatively high incidence translational energies and surface temperatures were used [29]. Scattered from Pt(111) however, $\text{N}_2(v = 0 \rightarrow 1)$ excitation probabilities showed a similar trend and were on the same order as CO excitation on Au(111), with an upper limit of 6×10^{-3} (cf. Tab. 1.1).

Table 1.1 Summary of previously published experimental work concerned with vibrational excitation (nonadiabatic effects) in molecular beam scattering experiments.

SYSTEM	$\nu =$	E_i/eV^*	T_S/K^*	VEP [*]	REF.	
Au(111) + N ₂	0 → 1	1.16	1123	< 10 ⁻⁴ †	[29]	
	HCl	0 → 1	1.37	1073	9 × 10 ⁻⁵	[30]
	CO	0 → 1	0.84	973	7 × 10 ⁻³	[28]
	NO	0 → 1	1.05	973	5 × 10 ⁻²	[25]
		0 → 2	1.05	973	3 × 10 ⁻³	[25]
		0 → 3	0.40	1100	1 × 10 ⁻⁴	[31]
		2 → 3	0.62	573	3 × 10 ⁻²	[32]
Ag(111) + NO	0 → 1	1.24	760	6 × 10 ⁻²	[12]	
Cu(110) + NO	0 → 1	0.50	743	3 × 10 ⁻²	[33]	
Pt(111) + N ₂	0 → 1	1.16	1123	6 × 10 ⁻³	[29]	

* For a better comparability only upper limits are shown here.

† No signal could be detected.

As mentioned before, in order to explain the ranking of excitation probabilities in different systems, the difference of the metal's work function and the molecule's electron affinity can be used as one proxy [9].⁷ At least qualitatively this works relatively well for N₂, CO and NO scattered from various surfaces (see Fig. 1.4). H₂/Cu(111), one extensively studied system in terms of scattering and dissociation [36–38], also is in accordance with the ranking in Fig. 1.4. All of the experimental and theoretical studies so far have revealed at best negligible nonadiabatic influences, probably due to the highly negative electron affinity of the hydrogen molecule. On the other hand, one noteworthy exception from the ranking is the excitation of NO scattered from Pt(111) which according to Fig. 1.4 should be even less probable than on Au(111). This disagreement was explained by a greater density of states at the FERMI level that is supposed to compensate for platinum's higher work function [29]. The second system that seems to be out of place in a comparison of Tab. 1.1 and Fig. 1.4 is HCl/Au(111) which is the main research subject of this thesis. It was first studied by Lykke and Kay who investigated rotational state, translational energy and angular distributions

⁷ For vibrational relaxation processes, i. e. when incident molecules already are in excited vibrational states, the vertical electron binding energy has turned out to be an even more appropriate indicator of nonadiabatic interaction strength because it takes the stretching of the molecule's bond into consideration [34, 35].

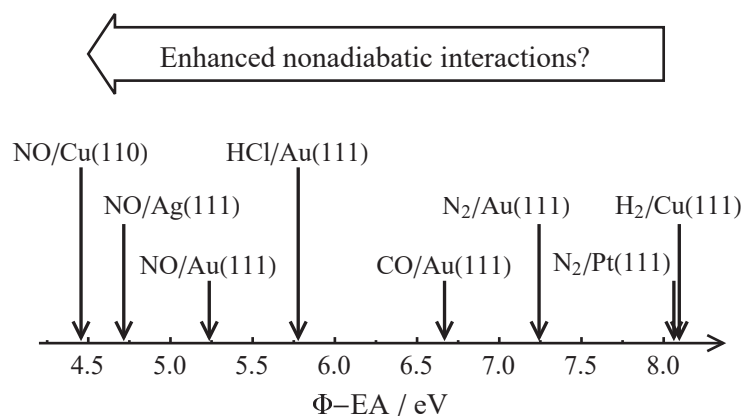


Figure 1.4 The difference of a metal's work function Φ and the molecule's electron affinity EA can be used as a proxy to at least qualitatively explain the ordering of nonadiabatic interaction strength. Values for work functions were gathered from Refs. [39–41], electron affinities were taken from Ref. [42].

after scattering ground state $\text{HCl}(v=0)$ [43]. Being unable to detect vibrationally excited molecules the authors estimated "the probability for vibrational excitation to be less than 0.01" [43]. Several years later, in experiments that partially laid the basis for this thesis, Ran *et al.* investigated the $\text{HCl}(v=0 \rightarrow 1)$ excitation [30, 44, 45]. Using an apparatus with a higher detection sensitivity, the authors identified HCl molecules in $(v=1)$ and determined the surface temperature and incidence translational energy dependence of the $v=0 \rightarrow 1$ excitation probabilities (see Fig. 1.5). In two ways, this system notably differed from the others mentioned above. First, the excitation probabilities were two to three orders of magnitude lower than in the case of CO and NO . This problem will be addressed and partly solved later in Sec. 3.1.1. Second, the temperature dependence of the VEPs hinted at a partly different mechanism of vibrational excitation. In general, temperature dependent VEPs have been successfully fitted by a function that resembles the classic ARRHENIUS equation in appearance:

$$P_{v,v'}(E_i, T_s) = A(E_i) \times \exp\left[\frac{-E_{v,v'}}{k_B T_s}\right] \quad (1.1)$$

where

$P_{v,v'}(E_i, T_s)$	probability for excitation from v to v'
E_i	mean incidence translational energy
T_s	surface temperature
$A(E_i)$	incidence energy dependent prefactor
$E_{v,v'}$	energetic spacing between v and v'
k_B	BOLTZMANN constant

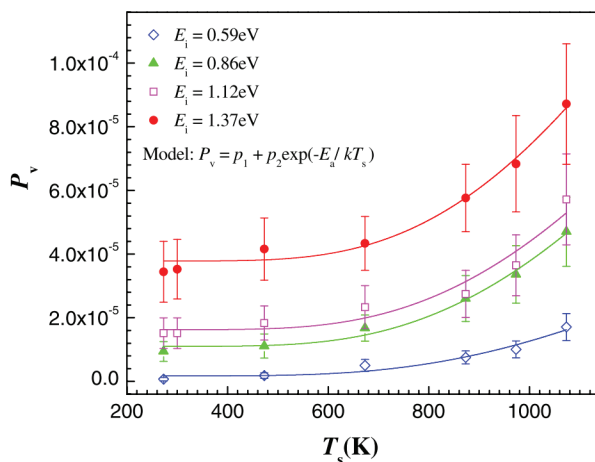


Figure 1.5 Surface temperature and incidence energy dependent vibrational excitation probability (VEP)s for $\nu = 0 \rightarrow 1$ excitation of HCl($\nu = 0$) scattered from a Au(111) surface. With increasing surface temperature as well as incidence energy, the excitation probability increased. The solid lines depict a fit to the data according to the model given in the legend that will be explained later in the text. Taken from Ref. [30].

Supported by the predictions of Gadzuk [46] that charge transfer between surface and molecule, which results in the formation of a transient anion, would lead to vibrational excitation, the exponential dependence on surface temperature was deduced without any further assumptions on the actual excitation mechanism by Rettner *et al.* for NO excitation on Ag(111) [11, 12]. In short, it results from the temperature dependent availability of electron-hole pairs (EHPs) at the surface with sufficient energy to excite the vibration.⁸ The incidence energy dependence, also described by Newns [14] and by Gadzuk [15, 46], basically stems from a stronger interaction for higher energy molecules. While behavior of this kind has been observed for all the systems mentioned above, the VEPs for HCl($\nu = 0 \rightarrow 1$) could only be fitted when a second coupling constant independent of T_s was added to Eq. 1.1 (see the model legend in Fig. 1.5). In opposite to the prefactor $A(E_i)$ (" p_2 " in Fig. 1.5) this second term exhibited a threshold in its E_i dependence leading the authors to assign it to adiabatic vibrational excitation. That is, part of the energy necessary to cross the vibrational gap does not stem from EHPs but from the incidence translational energy.

⁸ For a comprehensible derivation of Eq. 1.1 on the basis of a kinetic model including the conditions for which it should be valid, the reader is referred to Ref. [47].

1.3 Previous Theoretical Work

Experimental work on vibrational excitation in molecule-surface scattering has been accompanied by theoretical calculations from the very beginning. Although an all-encompassing discussion of theoretical techniques is beyond the scope of this thesis, a short introduction will be given. Most importantly, theoretical simulations directly connected to my experimental work will be presented.

1.3.1 Density Functional Theory

For a long time, theoretical treatment of surface processes was mostly limited to kinetic or thermodynamic, i. e. statistical approaches. As mentioned in the preceding section, that also included models for vibrational excitation which needed to be fit to experimental data or required reasonable guesses of coupling strength, charge transfer etc. This slowly started to change in the second half of the past century when Hohenberg, Kohn, and Sham introduced their *density functional theory* (DFT) in 1964 and 1965 [48, 49] (see Sec. A.1.1 in the appendix for a slightly more elaborate introduction). In short, within this theory potential energies depending on the relative nuclei positions in atomic ensembles can be calculated based on the BOA. However, depending on the choice of the exchange-correlation functional E_{XC} , which was introduced to correct for errors in the theory resulting from approximating many-electron interactions, for example calculated binding or transition state energies can vary considerably.⁹ Nevertheless, based on the multidimensional grid of potential energies, forces can be derived that act on the involved nuclei. For example, by fitting analytical potentials to the DFT points, continuous PESs can be obtained upon which dynamical computations like molecular dynamics (MD) or quantum chemical simulations can be carried out. In comparison, *ab initio* molecular dynamics (AIMD) simulations do not rely on analytical potentials but calculate forces *on the fly*. This in return limits the practical amount of calculable molecular trajectories to maybe a few hundreds instead of several thousands due to its higher computational costs.

In its basic form DFT can only be used to describe adiabatic interactions on a single PES since the dynamics of nuclei and electrons are assumed to be decoupled. However, as has been shown in the preceding paragraphs, nonadiabaticity does play an important role in various scattering dynamics from metal surfaces. Therefore, further DFT-based theories have been developed that are capable of including or at least approximating nonadiabatic interactions.

⁹ I will discuss examples in the comparison of my experimental work to theoretical predictions in Sec. 5.

1.3.2 Including Electronical Nonadiabaticity

Independent Electron Surface Hopping

Developed by Tully and co-workers [50, 51] the independent electron surface hopping (IESH) approach basically consists of three parts: First, ground state energies and charge densities are obtained by DFT calculations which are then used to fit a parametrized NEWNS-ANDERSON model [52]. On this basis, MD trajectories are simulated where molecules can statistically "hop" between different electronic adiabats. An advantage of IESH compared to other methods is the possibility to include a large number of moving surface atoms and an enormous number of electronic states so that nonadiabatic excitations can be modeled more reliably. To my best knowledge, the only system that has been extensively studied by means of IESH to date is NO/Au(111). While it was called "*the gold standard for electronically nonadiabatic dynamical treatment*" [27] that does predict a certain degree of vibrational relaxation, it has struggled to predict the correct amount of relaxation, its incidence translational energy dependence and the number of multibounces on the surface [27, 53].

Electronic Friction

In short, electronic friction (EF) is a damping force that acts on nuclei moving in the proximity of a metal surface's electron bath. Assuming that the electronic system of the surface quickly adopts to the changed nuclei potential (MARKOVIAN friction), the LANGEVIN equation for the motion of atoms can be described by:

$$m_i \ddot{R}_i = -\frac{\partial V(R)}{\partial R_i} - \sum_j \Lambda_{ij} \dot{R}_j + \zeta_i(t)$$

where V is the adiabatic PES and $\zeta_i(t)$ is a statistical random force. The middle term is the nonadiabatic friction depending on the particle's velocity and the electronic friction coefficients Λ_{ij} (cf. Refs. [54–56]). The latter are supposed to be positive at equilibrium so that EF can only dampen but not enhance nuclear motion [54, 56]. Further, for theoretical descriptions of scattering experiments *via* molecular dynamics with electronic friction (MDEF), it is important to note that EF relies on weak coupling and cannot describe charge transfer mechanisms as those presumed in the case of vibrational inelasticity [57].

1.3.3 Predictions on HCl/Au(111) Scattering

Prior to the start of my experimental work on HCl/Au(111), Liu *et al.* presented their computation of a PES for the dissociative adsorption of HCl and DCl molecules on the Au(111) surface and the subsequent quantum dynamics studies in three publications [58–60]. Using

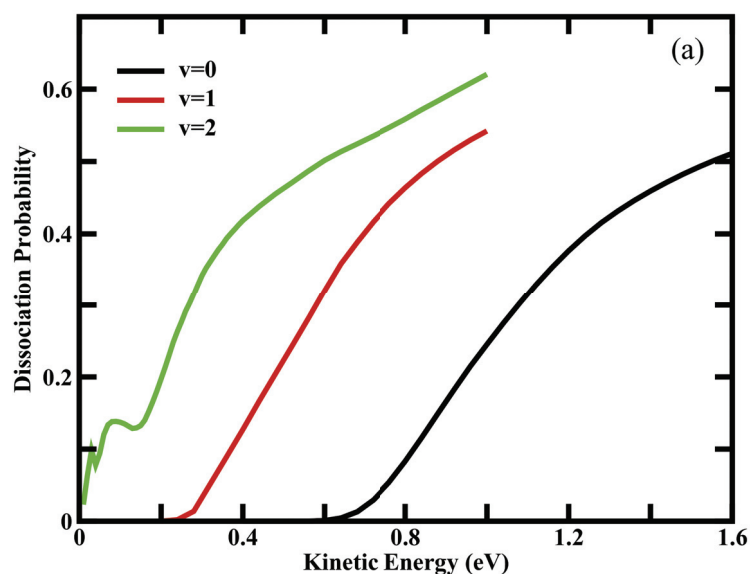


Figure 1.6 Theoretical predictions on the incidence translational energy dependent dissociation probability S_0 of HCl molecules on Au(111). Shown are the values for the three lowest vibrational states calculated with six-dimensional quantum dynamics calculations (time-dependent wave-packet approach). In a range that is easily accessible with seeded molecular beams of HCl in H_2 ($\langle E_i \rangle \approx 0.6 - 1.1$ eV), S_0 increases from 0 to ~ 0.3 for $v = 0$. Taken from Ref. [58].

the PW91 functional, the authors obtained a bridge site barrier to dissociation of 0.64 eV on a four layer, (2×2) unit cell surface. Carrying out six-dimensional quantum dynamics calculations using the time-dependent wave-packet approach lead to the dissociation probabilities S_0 shown in Fig. 1.6. In a range of incidence translational energies that is easily accessible with seeded molecular beams of HCl in H_2 ($E_i \approx 0.6 - 1.1$ eV), S_0 increased from 0 to ~ 0.3 for $v = 0$. For $v = 1$ and 2, the dissociation probabilities were predicted to be even higher (up to $S_0 = 0.6$ at $E_i = 1.0$ eV) which matched the predicted "late" transition state according to the POLANYI rules [61, 62].

Assuming these predicted values to be true, it should be feasible to experimentally confirm them. However, in none of the preceding experimental works on HCl/Au(111) scattering, fingerprints for the dissociation have been mentioned. Given that electronically nonadiabatic effects were observed in the vibrational excitation experiments and that they were not considered in the calculations, a comparison of experimental and theoretical values for S_0 promised to be interesting.

2 Experimental Details and Methods

Examining dynamics at surfaces in the form of energy exchange between several DOF when molecules collide with a surface requires the generation, manipulation and detection of the molecules' internal states at various stages of the collisional process. Only when the incidence conditions of the encounters are precisely determined, the dynamics of scattering processes can be deduced from the final state of the system. In the following sections I will thus present the instrumentation and experimental methods I used in my studies.

2.1 General Setup

For all experiments presented in this work the technical basis was an UHV chamber equipped with different instruments for preparation and characterization of the molecular beam and the surface. Fig. 2.1 visualizes the setup of the molecular beam surface scattering apparatus including several individual components. It has been described in detail several times [45, 63]; nevertheless the important parts will be explained in the following paragraphs.

As a whole, the apparatus consists of four connected, differentially pumped chambers:

1. the **source chamber**,
2. **differential stage I**,
3. **differential stage II**,
4. and the **scattering chamber**.

Connected to the scattering chamber, but not differentially pumped, is the preparation chamber (5). It houses an Ar⁺ ion gun (LKTech NGI-3000) for cleaning the surface from

adsorbates, an AUGER electron spectrometer (AES, Physical Electronics $\Phi 15 - 255G^1$) for elemental analysis of the surface and thus detection of impurities, and a residual gas analyzer (RGA, SRS RGA 200) for tracking the composition and concentration of gases inside the scattering chamber.

Conducting experiments on molecular beam scattering from surfaces under UHV is crucial for mainly two reasons. Under standard atmospheric conditions, i. e. air at a temperature of 20°C and under a pressure of 1 bar, a clean surface would be covered by a monolayer of adsorbates within a few nanoseconds under the assumption of a unit sticking coefficient and a molecular diameter of 3×10^{-10} m [64]. This would render studies of the bare surface impossible. However, lowering the pressure to 1×10^{-10} Torr increases this time span to 7 h which allows consecutive measurements over the day without the need of cleaning the surface in between.

At the same time, the mean free path λ , i. e. the average distance a molecule can travel between two collisions with other gas molecules, is also inversely proportional to the pressure. Over the same pressure range mentioned above it increases from 7×10^{-8} m to 5×10^5 m which ensures a collision-free molecular flow towards the surface.

$$\lambda \approx \frac{5 \times 10^{-3}}{p(\text{Torr})} \text{ cm}$$

[64]

2.1.1 Pumping System

Sufficient vacuum with a base pressure of $\sim 2 \times 10^{-10}$ Torr in the scattering chamber was maintained by a series of mainly turbo molecular pumps (TMPs) connected to the individual sub-chambers. Initially (i. e., for the experiments on vibrational excitation of HCl on Au(111)), the source chamber was pumped by a cryogenic pump (ASC, Cryo Plex-10 + M450 helium compressor) which had the advantage of large pumping speeds especially for H_2 (3000 L s^{-1}). Ongoing technical problems and the option to use He as carrier gas lead to the replacement of the pump by a large TMP with a nominal pumping speed of 1700 L s^{-1} for H_2 (Edwards, STPA2203C) for the experiments on dissociation of HCl on Au(111). Downstream, differential stages I and II are pumped by smaller TMPs with pumping speeds of 400 L s^{-1} (Osaka Vacuum, TG403) and 120 L s^{-1} (Osaka Vacuum, TF160CA) for N_2 , respectively. Between both stages there is a slide valve preventing the molecular beam to pass if closed and enabling the source chamber to be opened without venting the scattering chamber. The latter is pumped by a 350 L s^{-1} TMP (Leybold, NT360) backed by a second, smaller TMP (Pfeiffer, TPU062, 60 L s^{-1}).

¹ For the experiments on Au(111), later replaced by STAIB ESA 100 for experiments on Ag(111).

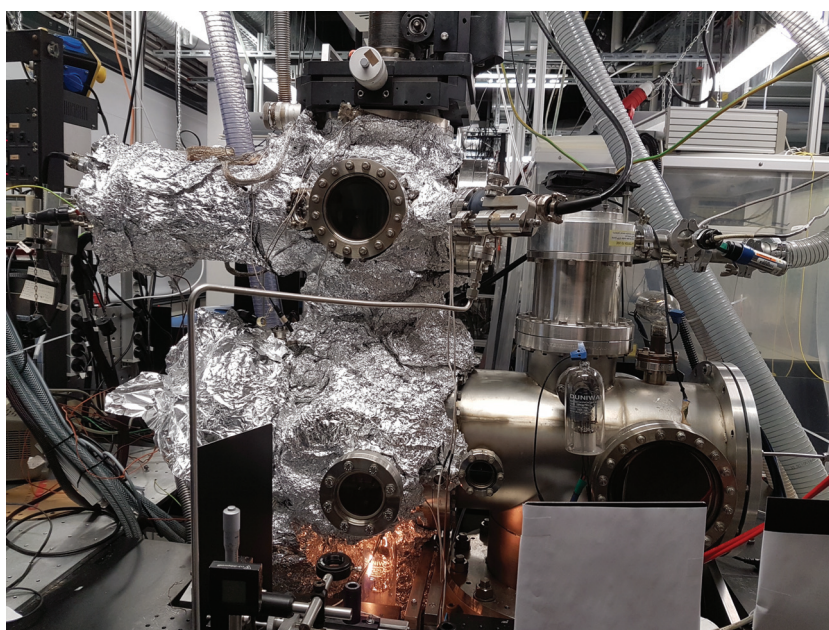
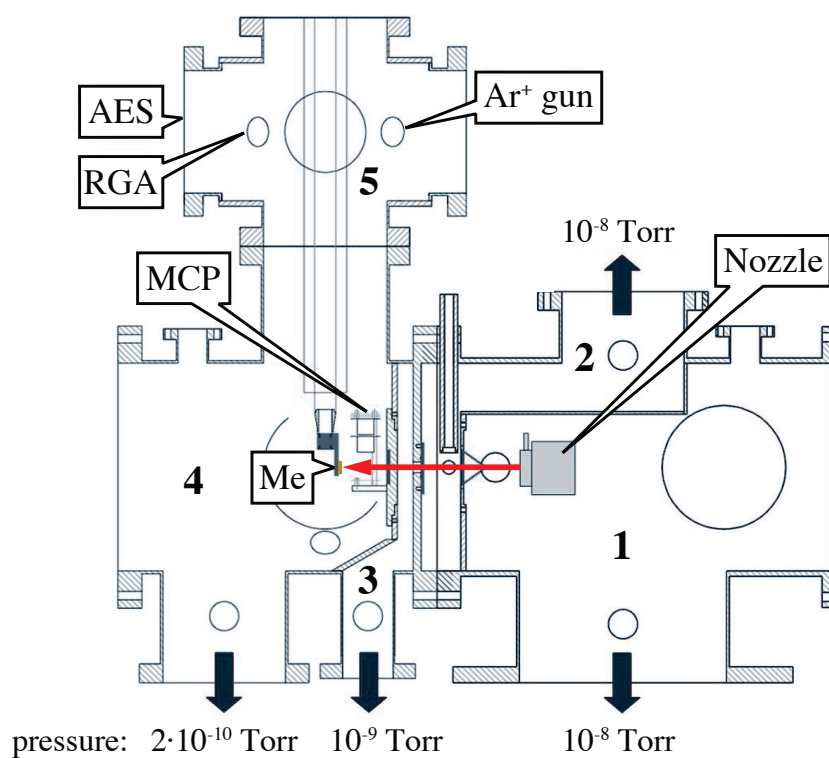


Figure 2.1 Sketch and image of the UHV molecular beam surface scattering apparatus. In the sketch, the individual components mentioned in the text as well as the base pressures (nozzle not operating) in the differentially pumped chambers are annotated. The image shows the apparatus from the same side as the sketch.

2.1.2 Generation of Molecular Beams

A collimated, practically collision-free flow of molecules in vacuum is called a *molecular beam*. In general, these beams are generated by expanding gas from a high-pressure reservoir through an orifice into the vacuum chamber. For the experiments described in this thesis pulsed nozzles were used. Here, a plunger that seals the valve in its resting position is lifted for a period of a few microseconds and closed again. This way, a temporal resolution in the range of several microseconds is possible opposed to continuous beam sources. Additionally, the background concentration of the investigated gas can be kept low by a pulsed operation mode. More precisely, the source chamber was equipped with a home-built, solenoid-driven valve operated with a backing pressure of ~ 8 bar at room temperature for scattering experiments. For dissociation experiments a modification in the form of a resistively heated silicon carbide tube [65] was attached to its front plate (see Figure 2.2). Passing a current of up to 2 A and 12 V through the SiC tube, an additionally attached *K*-type thermocouple read out a temperature of 700 °C.²

Assuming an ideal gas, the velocity v of the molecules in an isentropic expansion can be calculated from the nozzle temperature T_N and the specific heat capacity \hat{C}_p as

$$v = \sqrt{2 \int_T^{T_N} \hat{C}_p dt} \quad (2.1)$$

Further assuming that \hat{C}_p is constant within the temperature range and $T \ll T_N$ (i. e., cooling is very efficient), we obtain a simplified equation for the final velocity v_∞ ³:

$$v_\infty = \sqrt{2\hat{C}_p T_N} \quad (2.2)$$

With $\hat{C}_p(\text{HCl}) = 0.8 \text{ kJ kg}^{-1} \text{ K}^{-1}$ [68] and $T_N = 298 \text{ K}$ this would lead to $v_\infty \approx 690 \text{ m s}^{-1}$ in the case of pure HCl. However, *seeding* techniques can be employed to increase the molecules' velocity by addition of lighter carrier gases (here: H_2 or Ne) which transfer part of their kinetic energy to the heavier gas [66]. As a practical example, for a gas mixture of 3 % HCl in H_2 a mean velocity of $\langle v_i \rangle \approx 2300 \text{ m s}^{-1}$ was obtained which corresponded to a mean translational energy of $\langle E_i \rangle \approx 1.0 \text{ eV}$ (96 kJ mol^{-1}).

2.1.3 Detection of Molecules

Leaving the nozzle, the molecular beam passed through a 1.5 mm diameter skimmer and the two differential pumping chambers with 3 mm and 2 mm diameter apertures, respectively, before entering the UHV scattering chamber (see Fig. 2.3).

² Detailed information about the heating can be found in Sec. 3.3.

³ For a detailed introduction into molecular beam characteristics the reader is referred to Refs. [66, p. 14 ff.] and [67, p. 77 ff.]

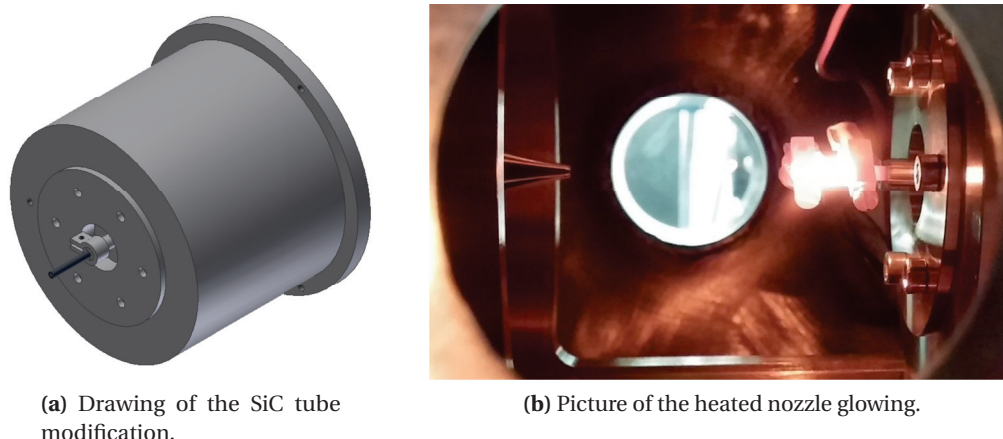


Figure 2.2 CAD drawing (a) and picture (b) of the running nozzle including the SiC tube modification for resistive heating.

For detection of molecules before and after scattering, they were ionized by laser radiation intersecting the molecular beam perpendicularly (see Methods, Section 2.3). A repeller accelerated the resulting ions through a collimating electrostatic lens onto a pulsed multi-channel plate (MCP) detector with two plates in Chevron configuration. Electrons generated in the MCPs were collected on an anode plate, the resulting signal was displayed on a digital oscilloscope (LeCroy, Wavesurfer 104 WXs-B) and read out by a computer with home-built LABVIEW programs.

2.1.4 Surface Mounting

The single crystals containing the surfaces of interest were mounted on a home-built sample holder attached to a 4-axis (x, y, z, θ) translation stage (Vacuum Generators, Omniax 800). Clamped between two tungsten wires, the sample was connected to two copper legs which were electrically isolated from the sample holder by sapphire plates. By passing a current through the sample, it could be resistively heated up to the materials melting point. Since the sapphire plates also ensured good thermal conductivity, the sample could be cooled down to approximately $-195\text{ }^{\circ}\text{C}$ by filling the cold finger inside the sample holder with liquid nitrogen. Monitoring the temperature of the surface was accomplished by a K -type thermocouple fixed in a small hole on the side of the crystal.

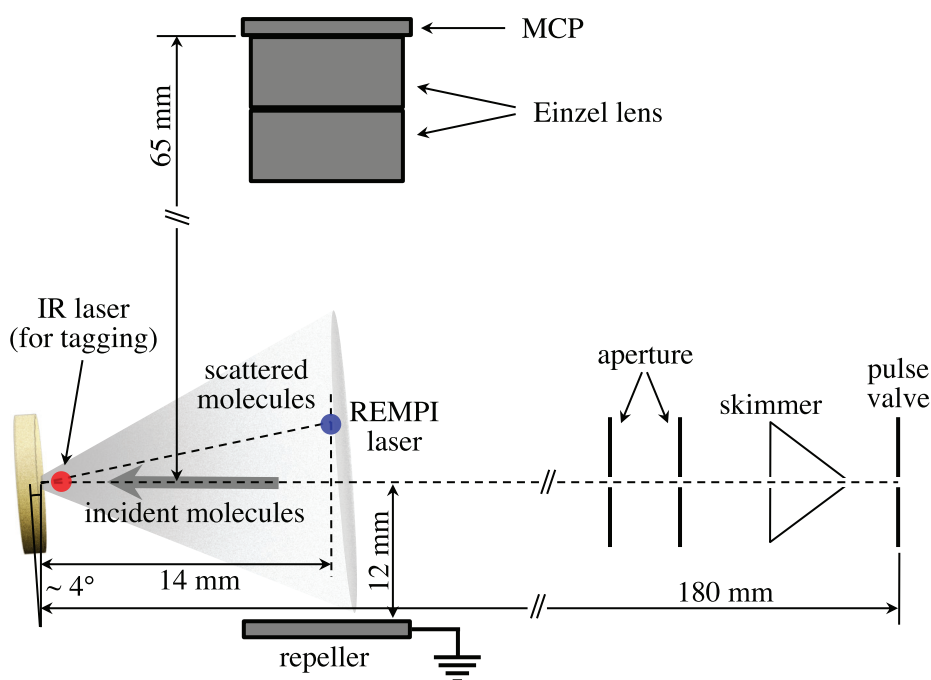


Figure 2.3 Drawing of the molecular beam line following the nozzle exit. Leaving the nozzle, the molecular beam passed through a 1.5 mm diameter skimmer and the two differential pumping chambers with 3 mm and 2 mm diameter apertures, respectively, before entering the UHV scattering chamber (cf. Fig. 2.1). For detection of molecules before and after scattering, they were ionized by laser radiation intersecting the molecular beam perpendicularly. A repeller accelerated the resulting ions through a collimating electrostatic lens onto a pulsed MCP detector with two plates in Chevron configuration.

2.2 Laser Systems

During my experiments I used two different laser systems: An IR source for manipulation (i. e., excitation into higher vibrational states) and an UV source for ionization and thus detection of molecules.

2.2.1 IR Laser Source

Several experiments like determining the vibrational excitation probabilities from higher vibrational states or measuring the velocity distribution in a double resonance setup required the excitation of molecules into higher vibrational states. For this purpose, the lab was equipped with a high-power, nanosecond-pulsed IR laser system. Fig. 2.4 shows the individual parts of this system: A continuous wave (cw) Nd:YLF laser (Coherent, Verdi V10, typical output ~ 5.5 W) pumped a cw dye ring laser (Sirah, Matisse DR, linewidth < 20 MHz, typical output ~ 400 mW). Its output ($\sim 625 - 665$ nm, depending on the IR transition) passed a FARADAY isolator (Qioptic, FI-630-5SV 30dB) and was pulse-amplified

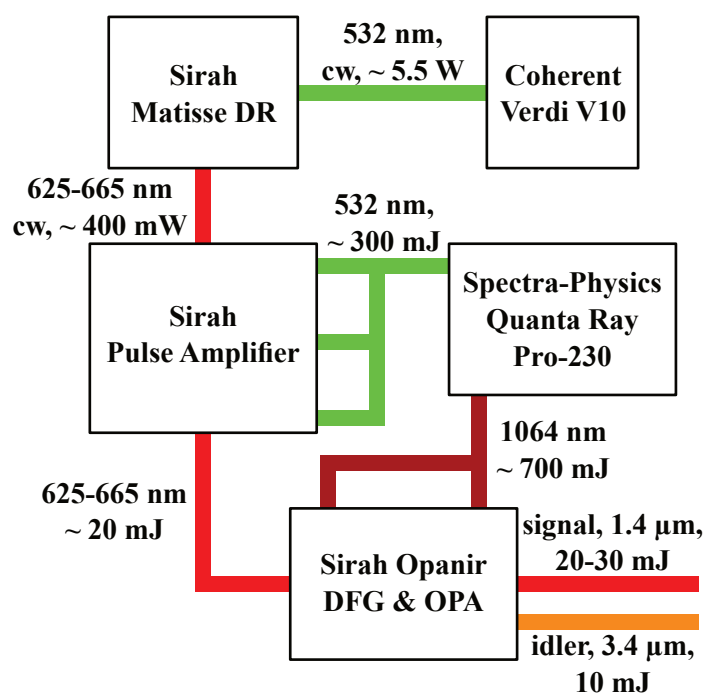


Figure 2.4 A simplified sketch illustrating the layout of the IR system. Following the flow chart from top to bottom: The cw output of a ring dye laser (Sirah, Matisse DR) was pulse-amplified to obtain nanosecond pulses which were difference frequency-mixed with and further amplified by the fundamental of a pulsed Nd:YAG laser (Spectra-Physics, Quanta Ray Pro-230) in two LiNbO₃ crystals (Sirah, Opanir). Depending on the desired wavelength, either the signal or the idler pulse were used for vibrational excitation.

in a five-stage Sirah Pulsed Amplifier 5X giving nearly FOURIER transform limited 8 ns pulses with ~20 mJ. These were then overlapped with the fundamental output (1064 nm) of an injection seeded Nd:YAG laser (Spectra-Physics, Quanta Ray Pro-230) for difference frequency mixing in a LiNbO₃ crystal. Finally, the mid-IR pulse (~1.2 – 1.6 μm, ~3 mJ per pulse) was parametrically amplified with the Nd:YAG fundamental resulting in one signal pulse (i. e., the incoming mid-IR pulse got amplified to 20 – 30 mJ) and one idler pulse around 3.4 μm with 5 – 10 mJ of pulse energy.

With a software-based PID controller the wavelength of the final output pulse could be locked to within ±1 pm. For this purpose, a calculated idler or signal wavelength based on the actual wavelength of the pulse-amplified Matisse output and the 532 nm output of the Nd:YAG laser read out by a wavemeter (HighFinesse, Ångstrom WS/7 Super Precision) were compared with the set value. As a result, corrections were applied to the Matisse DR wavelength by adapting the cavity length with a piezo-mounted mirror.

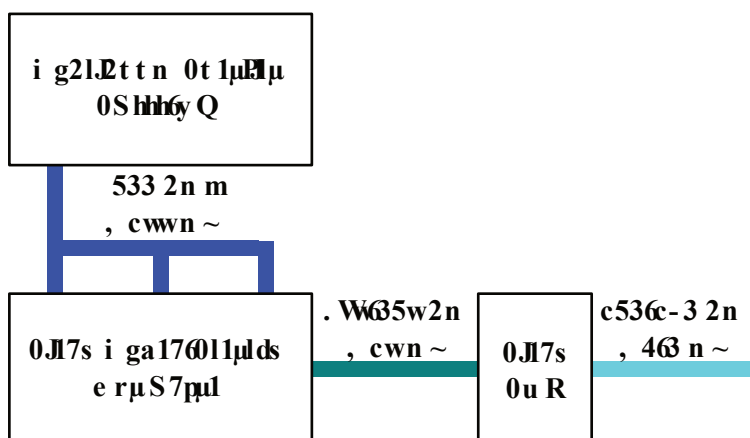


Figure 2.5 A simplified sketch illustrating the layout of the UV system. The dye was pumped by a 355 nm pulse from a Nd:YAG laser giving nanosecond pulses in the range of 470 – 530 nm. In a SHG unit these were frequency-doubled resulting in UV laser pulses with wavelengths of 235 – 265 nm and pulse energies of 1 – 5 mJ.

2.2.2 UV Laser Source

For detection of molecules I used resonance enhanced multi-photon ionization (REMPI) (see Sec. 2.3.2 for details). Its advantage over other ionization methods is the quantum state selectivity and the rather moderate UV wavelengths needed. Both spectral resolution for quantum state selectivity as well as sufficient photon flux for the multi-photon process were provided by the tunable nanosecond dye laser setup illustrated in Fig. 2.5 (Sirah, Cobra-Stretch). Pumped by a pulse of 355 nm (sum-frequency generation (SFG) of the first and second harmonic of a Nd:YAG laser, Continuum Surelite SLIII-EX, ~200 mJ/pulse) the dye laser generated nanosecond pulses in the range of 470 – 530 nm using solutions of pure or blended coumarin dyes (C460, C480, C503, and C540A) in three stages consisting of the oscillator and pre-/amplification. Small amounts of 1,4-diazabicyclo[2.2.2]octane (DABCO) were added to the solutions to improve the lifetime of the dyes [69]. In a second-harmonic generation (SHG) unit, the pulse frequency was doubled inside a beta barium borate (BBO) crystal (Sirah, SHG-215). Following the BBO was a compensator which in combination with a software-based manual calibration allowed to scan the wavelength of the dye laser over a range of several nanometer while maintaining sufficient pulse energy. With wavelengths in the range of 235 – 265 nm the final output pulses typically had energies of 1 – 5 mJ.

2.3 Methods

2.3.1 Surface Preparation

Every day, the surface was cleaned before any scattering experiments were carried out. As discussed in Sec. 2.1, over the course of one day of experiments adsorbates accumulate on the surface, possibly blurring the observed effects. For different sample materials several procedures have been developed to restore clean surface conditions.

In the case of Au(111) the procedure included Ar⁺ ion sputtering and thermal annealing of the crystal. In a first step, impurities on the surface were removed by ~20 – 30 min of sputtering using an Ar⁺ ion gun with an acceleration voltage of 3 kV at an Ar pressure of $\sim 2 \times 10^{-6}$ Torr. Using AES the cleanliness of the surface was confirmed. Since the surface structure was destroyed by the impact of the high-energy particles, it had to be restored afterwards. Heating the gold crystal to 700 °C for ~1 h (called *annealing*) mobilized the Au atoms on the surface enabling them to relax into the (111) surface structure (actually, in the case of bare Au(111) the preferred structure is the so-called *herringbone reconstruction* [70]), which involves complex, long-range rearrangements of Au atoms [71].

For the Ag(111) surface, the preparation procedures were in principle identical to those mentioned above. However, due to the lower melting point of silver (962 °C *versus* 1064 °C for gold [68]), the annealing temperature was reduced to 630 °C.

2.3.2 Resonance Enhanced Multi-Photon Ionization

Before molecules could be extracted by electric fields for detection on the MCPs they needed to be ionized. As mentioned above, a nowadays widespread method to ionize molecules is REMPI. As the name suggests it is a resonant, that is, state-selective process, based on the absorption of multiple photons by the molecule. Its basic principle, illustrated in Fig. 2.6 is rather simple: In a first step, m photons are absorbed to excite the molecule from the electronic ground state to an excited electronic state below the ionization threshold IE . Upon absorption of further n photons, the molecule is lifted above this threshold and an electron is kicked out of an orbital. The overall process is described in the $(m + n)$ -REMPI scheme. If the n photons are not supplied by the same radiation source (i. e., they have a different wavelength) they are marked with an index $(m + n')$ and the process is called two-color REMPI. Depending on the rotational constant B in diatomic molecules and the spectral laser resolution the rotational structure within vibrational levels can be resolved *via* REMPI as it is the case for HCl.

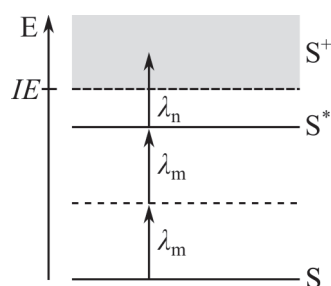


Figure 2.6 A simplified energy diagram illustrating the REMPI process. In this example, a molecule in electronic state S absorbs two photons with the wavelength λ_m upon which it is excited to electronic state S^* . Further absorption of one photon with the wavelength λ_n lifts the internal energy above the ionization threshold IE resulting in the ionization of the molecule. The $(2 + 1)$ photon scheme shown here is also applied in the case of HCl REMPI spectroscopy.

HCl REMPI

For state-selective detection of HCl molecules, a $(2 + 1)$ REMPI scheme was employed [72–75]. In Fig. 2.7, the electronic states involved in this scheme are illustrated. Their individual potential energy curves were calculated employing the RKR method [76] using vibrational and rotational constants obtained from the NIST database.⁴ By absorption of two photons, HCl is excited from its electronic ground state $X^1\Sigma^+$ with an equilibrium bond length of 1.28 Å to the $E^1\Sigma^+$ state which has an equilibrium bond length of 1.62 Å. Absorption of one more photon leads to ionization and possible fragmentation of the molecule (HCl⁺, Cl⁺ as well as H⁺ have been observed in literature [73, 77]). Independent of the probed vibrational state in the $X^1\Sigma^+$ state, all REMPI processes described in this thesis occurred *via* vibrational state $v = 0$ in the excited $E^1\Sigma^+$ state due to vertical FRANCK-CONDON transitions.

As can be seen in Fig. 2.7, there is a second excited electronic state $V^1\Sigma^+$ which is close in energy to the $E^1\Sigma^+$ state but has a much larger equilibrium bond length of 2.52 Å⁵. It has been argued that both excited states mix resulting in a combined state $B^1\Sigma^+$ that has two local minima [73]. Probing the $E^1\Sigma^+ \leftarrow X^1\Sigma^+$ transitions with the UV dye laser, I also observed spectral lines of transitions *via* higher vibrational states of the $V^1\Sigma^+$ state ($\sim v = 6 - 19$, depending on the probed vibrational state in $X^1\Sigma^+$). In some cases, further lines appearing in the spectra could not clearly be identified because they most probably belonged to transitions *via* some other electronic states.⁶

Some of these additional lines can be found in Fig. 2.8 which illustrates a typical REMPI spectrum of HCl molecules in $v = 0$ scattered from the Au(111) surface at a temperature of 953 K. Between Q branch lines of rotational states $J = 0 - 9$ (marked with vertical lines)

⁴ National Institute of Standards and Technology, <http://webbook.nist.gov/cgi/cbook.cgi?ID=C7647010&Units=SI&Mask=1000#Dia31>, accessed on 2017-03-22.

⁵ All equilibrium bond lengths were determined from the corresponding potential energy curves. They are in accordance with the NIST database values within 0.01 Å.

⁶ HCl exhibits several electronic states energetically close to the $E^1\Sigma^+$ and $V^1\Sigma^+$ states. A comprehensive overview of the corresponding transitions can be found in Ref. [73].

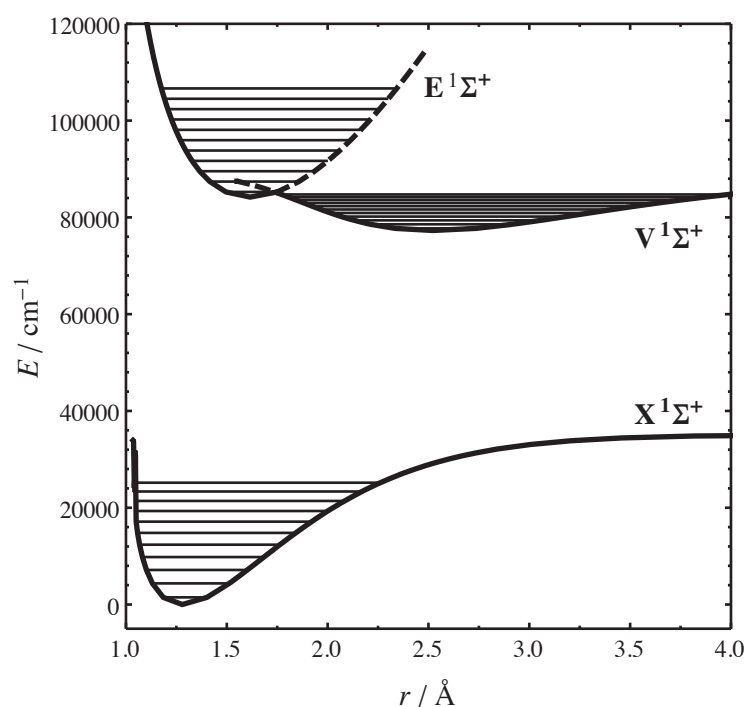


Figure 2.7 A potential energy diagram showing the electronic states of HCl important for the REMPI schemes employed in this thesis. The potentials were calculated with the RKR method [76] using vibrational and rotational constants obtained from the NIST database [78]. Also shown are vibrational levels $v = 0 - 10$ for each electronic state. While more sophisticated calculations might lead to slightly different potentials, the general characteristics are correctly reproduced (cf. Ref. [73]). Parts of the excited states' potentials are depicted with dashed lines to indicate the possible mixing.

there are lines not belonging to transitions *via* $E^1\Sigma^+$, some of them from transitions *via* $V^1\Sigma^+$ ($v = 11$).⁷

2.3.3 Time-of-Flight Techniques

As shortly mentioned in Sec. 2.2, the setup of two nanosecond lasers did not only allow the excitation of HCl molecules into higher vibrational states to increase their vibrational energy and their detection. By variation of the temporal delay between both laser pulses the *flight time* between the space volumes of excitation and detection could be changed. This IR-UV double resonance technique could thus be used for a variety of time-of-flight (TOF) experiments, the most prominent being the measurement of velocity distributions.

Molecules in a molecular beam do not have a single uniform velocity but exhibit a certain velocity distribution which depends on their final translational temperature. Fig. 2.9 illustrates the laser geometries that were used for measuring these distributions of the incident

⁷ The transitions were verified by comparison to theoretical simulations of the REMPI spectra. More details can be found in Sec. 3.1.

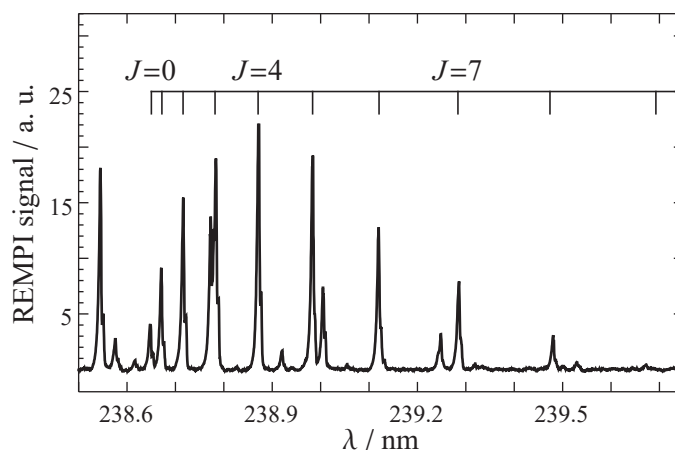


Figure 2.8 An example of a REMPI spectrum of HCl molecules in vibrational state $v = 0$. The spectrum was recorded scattering a molecular beam from the Au(111) surface at a temperature of 953 K. Individual rotational lines are marked on top. In addition to those lines stemming from the $E^1\Sigma^+(v=0) \leftarrow X^1\Sigma^+(v=0)$ Q branch transitions, there are a few lines from other transitions (e. g., *via* higher vibrational states of the $V^1\Sigma^+$ state).

as well as the scattered molecules. In the first case, the IR laser beam was positioned upstream from the detection region and its temporal delay was set to the maximum of the molecular beam pulse in time. Thereby, the IR laser pulse acted as a *tag* determining the starting point in time. Varying the UV laser pulse delay, the arrival time distributions of the molecules were scanned. Since the spatial distance between the two laser pulses was known, those could first be converted to velocity and further to kinetic energy distributions.

In Fig. 2.10 (a), representative TOF spectra of HCl molecules scattered from Au(111) in $v = 1, J = 5$ at two different mean translational incidence energies are shown. Being a density-sensitive method, REMPI signals S are proportional to the number density of the detected molecules and thus need to be converted to flux distributions. Further, TOF spectra represent the detection probability per differential time element that need to be converted to the velocity domain distribution $P(v)$ (see the appendix, Sec. A.2 for details on both conversions). Knowing the traveled distance l of the molecules, Eq. 2.3, which is a flowing three-dimensional MAXWELL-BOLTZMANN distribution $S(t)$ converted from velocity to time space (cf. Sec. A.2), could be fitted to the TOF data (solid lines in Fig. 2.10 a):

$$S(t) = A_t \left(\frac{l}{t}\right)^3 \exp\left[-\left(\frac{\left(\frac{l}{t}\right) - v_0}{\alpha}\right)^2\right] \frac{1}{l} \quad (2.3)$$

With v_0 and α the distributions in velocity space according to Eq. 2.4 are obtained:

$$P(v) = A_v v^3 \exp\left[-\left(\frac{v - v_0}{\alpha}\right)^2\right] \quad (2.4)$$

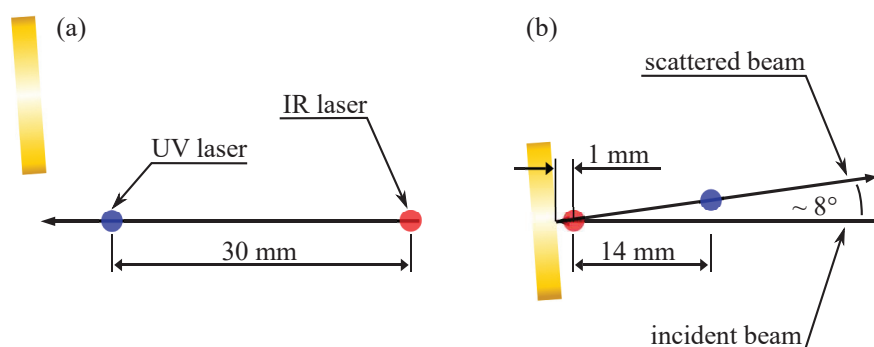


Figure 2.9 Typical laser geometries used for TOF experiments. Moving the surface out of the molecular beam and setting the IR-UV distance to 30 mm, the arrival time and thus the velocity distribution of the incident molecular beam was measured with high precision (a). Positioning the IR laser close to the surface (~ 1 mm) and tagging the molecules immediately before or after scattering from the surface (depending on which vibrational state was to be probed) the arrival time distribution of the scattered molecular beam was measured (b). The UV and IR laser, which intersected the molecular beam perpendicularly, are depicted by the blue and red spot, respectively.

From velocity distributions, the corresponding kinetic energy distributions were calculated following Eq. 2.5 (see Fig. 2.10 b):

$$P(E) = A_E \frac{2E}{m^2} \exp \left[- \left(\frac{\left(\sqrt{\frac{2E}{m}} - v_0 \right)^2}{\alpha} \right)^2 \right] \quad (2.5)$$

2.3.4 AUGER Electron Spectroscopy

AES was used for qualitative analysis of the surface after Ar^+ ion sputtering as well as for quantitative analysis of the amount of dissociated HCl in order to determine the dissociation probability (see Sec. 3.3). Due to the technique's low information depth of a few nanometer from the surface [79], it is generally well-suited for the detection of adsorbates. According to Ref. [80], the atomic concentration C_x of an element x present on the surface can be calculated as:

$$C_x = \frac{I_x}{S_x d_x} \bigg/ \sum_i \frac{I_i}{S_i d_i} \quad (2.6)$$

where

- I_x AUGER peak-to-peak height (APPH) of a peak
in the differential AUGER spectrum of x
- S_x relative elemental sensitivity factor for x
- d_x instrument sensitivity for the peak

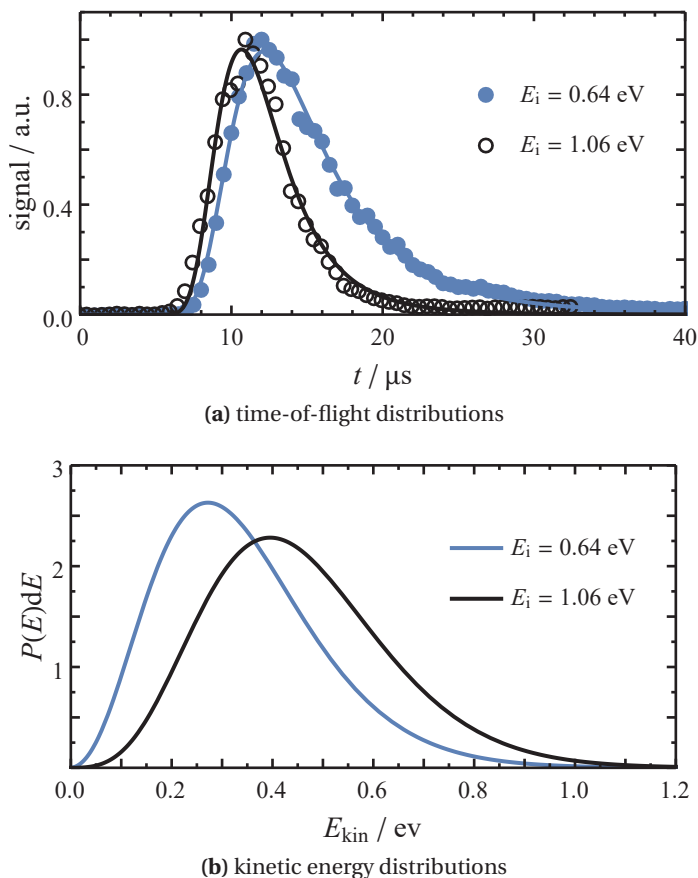


Figure 2.10 An example of a TOF spectrum and the resulting kinetic energy distribution of vibrationally elastically scattered HCl molecules in $v = 1, J = 5$. The arrival time distribution (a) was obtained scattering a molecular beam from the Au(111) surface at a temperature of 673 K (symbols represent experimental data, solid lines depict fits of Eq. (2.3) to these points). In (b), kinetic energy distributions were calculated from the fits in (a) according to Eq. (2.5).

While I_x was determined from the measured AUGER spectra, S_x can be found in databases [80]. Since both chlorine and gold were detected within a single AUGER spectrum in the dissociation studies, all d_i were the same and thus cancelled each other out. Fig. 2.11 a) shows an representative AUGER spectrum of the clean Au(111) surface recorded in derivative mode⁸ while b) shows a surface covered by $\Theta = 0.3$ ML of chlorine. Red, dashed lines mark the two peaks that are important for the studies of HCl dissociation: One at 181 eV, which also appears in the pure Cl spectrum and can thus be used for its quantitative analysis, and one large peak around 239 eV, which purely stems from Au atoms and thus can be used as a reference (for further details see Sec. 3.3).

⁸ All spectra shown in this thesis have been recorded this way.

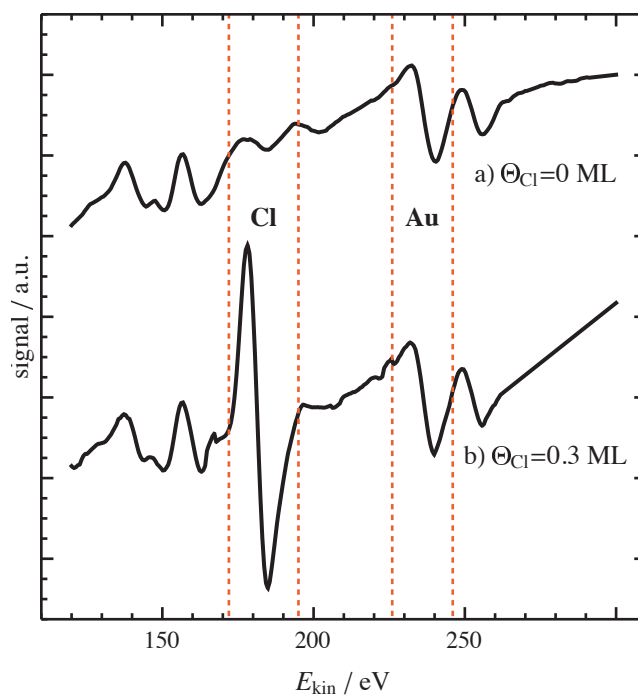


Figure 2.11 An example of derivative AUGER spectra of a clean Au(111) surface without detectable amounts of chlorine (a) and with a coverage of $\Theta = 0.3 \text{ ML}$ (b). Red, dashed lines mark the two peaks that are important for the studies of HCl dissociation: The one at 181 eV is already present for clean Au(111) and grows with increasing coverage of Cl while the one at 239 eV stays approximately constant. Their intensity ratio will be used to determine the Cl coverage on the Au(111) surface (see Sec. 3.3).

RESULTS

3 Scattering HCl from Au(111)

Scattering HCl molecules from a Au(111) surface was the first system that was actually studied in the same used apparatus when it was built several years ago. As mentioned in the introduction (Sec. 1), Ran *et al.* observed HCl($v = 0 \rightarrow 1$) vibrational excitation [30, 44, 45] that Lykke and Kay had previously not been able to detect [43]. In the following sections I will present my results on this scattering system that include:

- Vibrational excitation from $v = 0 \rightarrow 1$ and $v = 1 \rightarrow 2$
- Translational inelasticity
- Dissociative adsorption on the surface

For each of these processes I will compare my own to previous results and theoretical predictions where possible.

3.1 Vibrational Excitation

As presented in Sec. 1, vibrational inelasticity that occurs during scattering processes on metal surfaces can be a fingerprint of electronically nonadiabatic interactions. On the one hand it can be observed in the form of vibrational relaxation, which in general requires excitation of molecules to higher vibrational states before they collide with the surface. Starting from lower vibrational states, vibrational excitation can be studied in the form of the vibrational excitation probability $P_{v'',v'}$ which is defined as the number N of molecules scattered into the vibrational state of interest v' divided by the number of molecules scattered into all vibrational states v_i . If vibrational relaxation from higher vibrational states can be neglected (which will be discussed later on) the number of molecules that underwent a certain change in vibrational state¹ can be approximated by the number of

¹ In contrast to computational simulations, I was not able to observe the actual transition process or to follow the fate of individual molecules in my experimental work.

molecules that can be found in the final vibrational state after the scattering event:

$$P_{v'',v'} = \frac{N_{v'' \rightarrow v'}}{\sum_i N_{v'' \rightarrow v_i}} \approx \frac{N_{v'}}{\sum_i N_{v_i}} = \frac{\sum_J n_{v'}(J)}{\sum_i \sum_J n_{v_i}(J)} \quad (3.1)$$

Thus, the number of molecules in the involved vibrational states need to be determined after the scattering. Practically, a state's population is obtained from integrated state-specific REMPI spectra $I_v = \sum_J \sum n_v(J)$ where $n_v(J)$ is the population in one rotational state. However, using REMPI the molecules' density and not the actual flux is detected. Furthermore, the ionization volume of the REMPI laser pulse only includes a small fraction of the spatial and temporal extend of the scattered molecular pulse. To account for these limitations, the recorded raw signals $SIG_v(J_\Sigma, J, \theta_v, \tau_v)$ for each vibrational state need to be corrected for several factors that must be independently determined:

$$n_v(J) = \frac{SIG_v(J_\Sigma, J, \theta_v, \tau_v) \times \langle u_v \rangle}{S(J_\Sigma, J) \times \Theta_v(\theta_v) \times Q(v_\Sigma, v) \times \sigma_{v_\Sigma}(\lambda_{MPL,v}) \times \Delta_v(\tau_v) \times \Gamma_v \times \Pi(\pi_v)} \quad (3.2)$$

Mostly sticking to established nomenclature [25], the individual correction factors and variables are defined as follows:

$SIG_v(J_\Sigma, J, \theta_v, \tau_v)$	raw signal strength
Σ	excited $E^1\Sigma^+$ state
$\langle u_v \rangle$	average speed of the scattered molecules that is used for density-to-flux conversion
$S(J_\Sigma, J)$	rotational line strength factor
$\Theta_v(\theta_v)$	angular distribution of the scattered molecules
$Q(v_\Sigma, v)$	Franck-Condon factor
$\sigma_{v_\Sigma}(\lambda_{MPL,v})$	wavelength dependent ionization cross section of the intermediate state
$\Delta_v(\tau_v)$	temporal distribution of the scattered molecules
Γ_v	detector gain function
$\Pi(\pi_v)$	laser power correction function

These correction functions need to be evaluated at the corresponding values for the vibrational state v , rotational state J , scattering angle θ_v , time delay between nozzle opening and laser pulse τ_v , REMPI wavelength $\lambda_{MPL,v}$, and the laser power π_v . To circumvent dealing with corrections that are difficult to determine I measured machine-specific detection sensitivity factors that include $S(J_\Sigma, J)$, $Q(v_\Sigma, v)$, and $\sigma_{v_\Sigma}(\lambda_{MPL,v})$ in a single value.

To do so I excited HCl molecules in the incident beam from various rotational states J in a lower vibrational state ($v'' = 0$ or 1) to a higher vibrational state ($v' = 1$ or 2) *via* $R(J)$

transitions with the IR laser temporarily and spatially overlapped with the REMPI.² By comparing integrated REMPI signals of the J states in v'' with and without IR excitation a number proportional to the amount of molecules that had been excited from v'' to v' was obtained. A REMPI scan of the corresponding $J + 1$ state in v' then gave a number proportional to the amount of molecules actually detected in v' . Assuming that the lifetime of the vibrationally excited state is long enough and temporal as well as spatial spreads of the molecular packet are negligible³, a comparison of the laser power corrected signal losses in v'' and gains in v' directly yields the ratio of the sensitivity factors ϕ_v for both states:

$$\frac{\phi_{v'}}{\phi_{v''}} = \frac{S(J_{\Sigma} + 1, J + 1) \times Q(v_{\Sigma}, v') \times \sigma_{v_{\Sigma}}(\lambda_{v'})}{S(J_{\Sigma}, J) \times Q(v_{\Sigma}, v'') \times \sigma_{v_{\Sigma}}(\lambda_{v''})} \propto \frac{\text{SIG}_{v'}^{\text{IR=on}}(J + 1)}{\text{SIG}_{v''}^{\text{IR=off}}(J) - \text{SIG}_{v''}^{\text{IR=on}}(J)} \quad (3.3)$$

In Fig. 3.1 examples of short, laser power corrected REMPI scans for these "hole-burning" experiments can be seen. Panels (a) and (c) show spectra of the lower vibrational states $v = 0$ and $v = 1$ with the depopulating laser turned off and on while the panels on the right-hand side, (b) and (d), show spectra of the respective upper vibrational state, $v = 1$ and $v = 2$, with the IR laser turned on. The losses in the lower and the gains in the corresponding upper vibrational states' signal, denoted by the green-shaded area, enter Eq. (3.3) as denominator and numerator, respectively. Evaluating short scans as those shown in Fig. 3.1 for several different J states, the values for the sensitivity factors were determined as

$$\left\langle \frac{\phi_{v=1}}{\phi_{v=0}} \right\rangle = 0.9 \pm 0.2$$

and

$$\left\langle \frac{\phi_{v=2}}{\phi_{v=1}} \right\rangle = 0.5 \pm 0.1$$

which can also be seen in Fig. 3.2. Since I could not identify any clear trend in the J state depending sensitivity factors, their average values were used for all J states.⁴

² To obtain an easily detectable population of molecules in $v'' = 1$ in the incident beam, the SiC extension of the nozzle was heated to 1060 K.

³ Given the minimal time delay between the IR and the REMPI laser of a few nanoseconds these seem to be fair assumptions.

⁴ One could argue that $\langle \phi_{v=2} / \phi_{v=1} \rangle$ was declining with increasing J . However, the data range is too limited to give a definitive answer here.

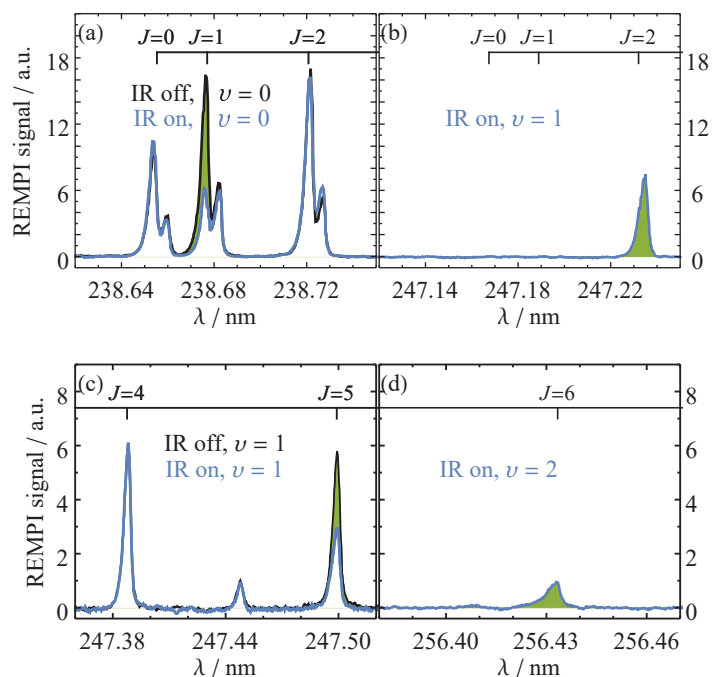


Figure 3.1 Short REMPI scans of HCl molecules for determination of sensitivity factors. Scans of $v = 0$ (a) and $v = 1$ (b) are shown in the upper panels, while in the lower panels scans of $v = 1$ (c) and $v = 2$ (d) can be seen. Black and blue lines denote scans with the IR laser turned off and on, respectively, whereas the green-shaded areas depict the losses in the lower and the gains in the respective upper vibrational state. With the IR turned off, there was zero signal in the scans of panel (b) and (d).

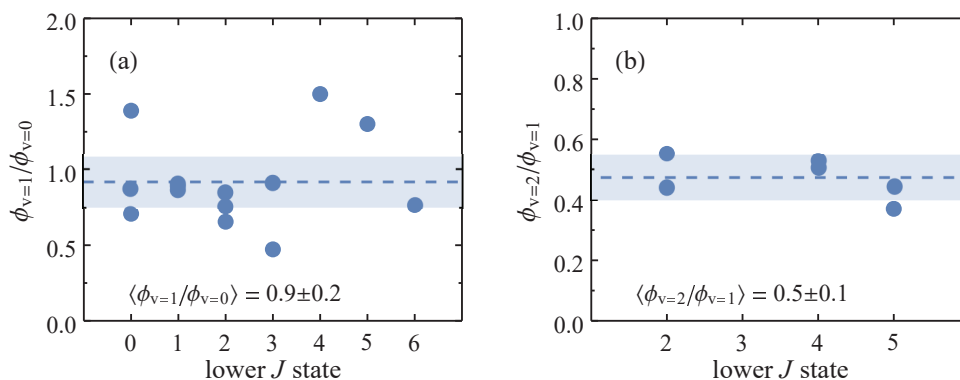


Figure 3.2 Relative detection sensitivity factors for different lower J states. In (a), $\phi_{v=1}/\phi_{v=0}$ is shown for the lower rotational states $J = 0 - 6$ whereas in (b), $\phi_{v=2}/\phi_{v=1}$ is shown for lower rotational states $J = 0 - 6$. While the dashed blue line denotes the mean value also noted down at the bottom of both panels, the blue-shaded area denotes the standard deviation of the mean. No systematic J dependence has been observed.

3.1.1 Excitation from $\nu = 0 \rightarrow 1$

Initially intended to be a mere starting point for the previously unstudied $\nu = 1 \rightarrow 2$ excitation, I shortly re-investigated the $\nu = 0 \rightarrow 1$ excitation of HCl molecules scattered from Au(111) to make sure that the experimental setup is working as desired and that the VEPs agree with those published by Ran *et al.* [30]. Without further manipulation, the incident molecular beam was scattered from the surface and detected in the direction of the specular scattering using the UV laser (cf. Fig. 2.9 in the introduction). The most important experimental parameters used for measuring the individual data sets are shown in Tab. 3.1.

Table 3.1 Experimental parameters for measuring the $\nu = 0 \rightarrow 1$ excitation of HCl on Au(111). $\langle E_i \rangle$ is the incidence translational energy, $U(\text{MCP})$ the detector voltage, $\langle E_L \rangle$ the approximate average laser power, and θ the approximate scattering angle. Shown are usual values that might have been adapted for individual measurements when needed.

Gas Mixture	$\langle E_i \rangle$ in eV	ν State	$U(\text{MCP})$ in V	$\langle E_L \rangle$ in mJ	θ in $^\circ$
8 % HCl in H ₂	0.67	$\nu = 0$	1300	~ 0.5	~ 15
		$\nu = 1$	1850	~ 1.5	~ 15
4 % HCl in H ₂	0.99	$\nu = 0$	1350	~ 0.7	~ 15
		$\nu = 1$	1850	~ 1.3	~ 15

For each gas mixture, REMPI scans of both vibrational states were carried out at several surface temperatures T_s . To avoid hysteresis effects due to the temperature change and intensity drifting over time, data was recorded with increasing/decreasing T_s first (300 K, 400 K, ..., 900 K). Then, T_s was changed in the opposite direction at intermediate steps (850 K, 750 K, ..., 350 K). In each case the laser power was measured parallel to the scanning of the UV laser to be able to correct for power fluctuations and to compare measurements in different laser power regimes.

In Fig. 3.3 representative REMPI spectra for an incidence energy of $\langle E_i \rangle = 0.67$ eV are shown. From these raw spectra (only corrected for laser power fluctuations/differences according to the laser power correction shown in the paragraph below) it can be directly seen that the signal in the incident vibrational state $\nu = 0$ stays approximately the same when the surface temperature T_s is increased from 323 K (top panel) to 953 K (bottom panel). However, the signal of $\nu = 1$ clearly increases with increasing surface temperature. Since according to Eq. 3.2 the REMPI signal is proportional to the population in the corresponding quantum state the vibrational excitation $\nu = 0 \rightarrow 1$ increases with T_s . Before Eqs. 3.1 and 3.2 can now be applied to calculate the actual VEPs, a number of correction factors and functions need to be determined and evaluated. Therefore, I will show examples of the correction functions introduced above for selected experimental conditions in the following paragraphs.

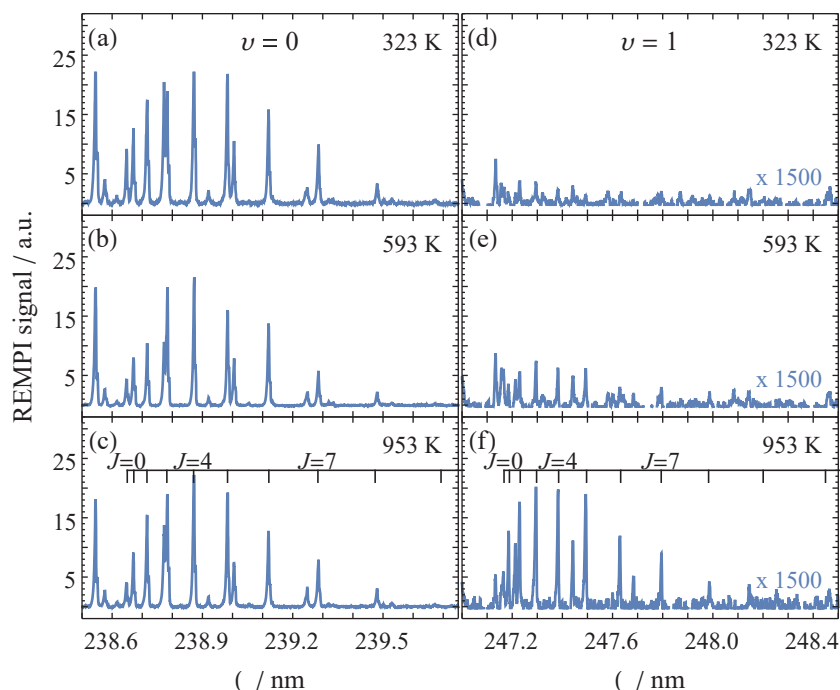


Figure 3.3 Representative REMPI spectra of HCl molecules scattered from Au(111) at three different surface temperatures. Shown are spectra in the wavelength range of $v = 0$ (a–c) and $v = 1$ (d–f) recorded at $\langle E_i \rangle = 0.67$ eV that have only been corrected for laser power. While the signal is arbitrarily scaled, the relative scale is the same for all six panels. The spectra for $v = 1$ are magnified by a factor of ~ 1500 relative to the spectra for $v = 0$. Additional lines not assigned to a certain J state belong to different transitions *via* the $V^1\Sigma^+$ state (see Sec. 2.3.2).

Average Velocity $\langle u_v \rangle$

Due to the low signal it was not possible to measure TOF spectra of molecules excited to $v = 1$ in comparison to those in $v = 0$. Instead, I assumed the velocity of molecules in $v = 0$ to be $\sim 22\%$ higher than that of molecules in $v = 1$. This number was the result of TOF measurements for the $v = 1 \rightarrow 2$ excitation and will be discussed in the according section.

Angular Distribution $\Theta_v(\theta_v)$

As described in detail in the appendix, Sec. A.3, angular distributions were measured by moving the UV laser on a vertical line parallel to the surface. Some problems associated with this simplified procedure are also discussed in Sec. A.3).

In Fig. 3.4 angular distributions for HCl molecules with an incidence energy of $E_i = 0.67$ eV scattered from the Au(111) surface in (a) $v = 0$ and (b) $v = 1$ are shown. In both cases the incident beam (denoted by red data points and the red dashed line) obviously has an effect on the angular distributions as the scattering data points measured at the same angle exhibit remarkable intensities. Even though the UV laser was tuned to a rotational state not populated in the incident beam ($J = 5$ in both vibrational states), its high flux compared to

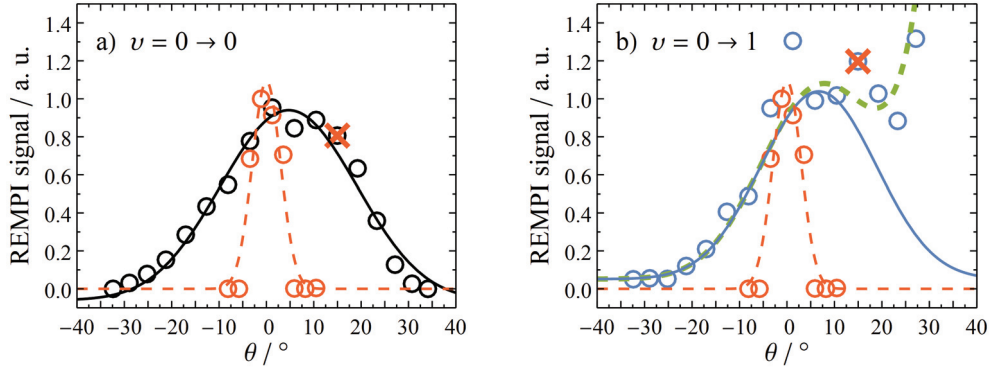


Figure 3.4 Angular distributions for molecules with $E_i = 0.67$ eV coming back in (a) $v = 0$ and (b) $v = 1$. While the solid lines denote a fit to the data according to $a \times \cos^n(\theta - \theta_0) + c$, red data points and the dashed line denote the incident molecular beam. The red crosses mark the data points at the angle at which the REMPI spectra for the VEPs were measured. In (b), the dashed green line denotes a fit that adds an exponential term to the cosine function (see text).

the scattered beam led to an above-average non-resonant background visible in the raw data. As a result, these data points were excluded from the cosine fit

$$f(\theta) = a \times \cos^n(\theta - b) + c \quad (3.4)$$

depicted by the solid black line in Fig. 3.4 (a). Most probably due to the high detector gain needed to detect vibrationally excited molecules, the angular distribution in panel (b) exhibits strong distortion in the range of $\theta \gtrsim 10^\circ$ where the ionization laser was closest to the detector. Therefore, the fitting function was modified by adding an exponential term that accounts for the steep rise with increasing scattering angle:

$$f(\theta) = a \times \cos^n(\theta - \theta_0) + c + \exp(-d(x - e)). \quad (3.5)$$

While the fit according to Eq. 3.5 is depicted by the dashed green line in Fig. 3.4, the solid blue line denotes a pure cosine function according to Eq. 3.4 with parameters a , b and c extracted from the fit. Comparing the cosine fits to $v = 0 \rightarrow 0$ and $v = 0 \rightarrow 1$ I consider two things to be especially noteworthy here: First, the fitted exponents are $n = 16$ for $v = 0$ (a) and $n = 22$ for $v = 1$ (b). Yet I would hesitate to call the latter distribution significantly narrower; it might only be an artifact from trying to disentangle the distortion mentioned above. In any case, however, the large n indicate direct scattering. Second, with an incidence angle close to 0° the center of both distributions suggests specular scattering with $\theta_0 = 5^\circ$ (a) and $\theta_0 = 7^\circ$ (b). For the correction of the REMPI spectra it is important to know what fraction $f(\theta_v)$ of the scattered molecules is detected by the UV laser at the position marked by red crosses ($\theta_v = 15^\circ$) in Fig. 3.4. More precisely, since for the VEP calculation the populations of $v = 0$ and $v = 1$ are compared, the ratio of those fractions directly shows

by how much the population in one state is over- or underestimated due to the choice of scattering angle. Since the exact angular distributions could not be determined due to the distortion explained above, $f(\theta_v)$ is calculated by dividing the signal I at $\theta_v = 15^\circ$ by the sum of signals at the rest of the measured angles (except for those where the incident beam or the detector distortion interfered with the signal):

$$f(\theta_v) = \frac{I(\theta_v)}{\sum_i I(\theta_i)}$$

For the angular distribution correction factors then follows that

$$\Theta_1(\theta_1) = \frac{f(\theta_1)}{f(\theta_0)} = 1.24 \quad \text{if} \quad \Theta_0(\theta_0) = 1.$$

That is, the relative fraction of all scattered molecules that is detected when recording the REMPI spectra is higher for $v = 1$ and thus this state's population is overestimated. The correction factors derived here were used for both incidence energies although they were determined only for $\langle E_i \rangle = 0.67$ eV.

Temporal Distribution $\Delta_v(\tau_v)$

While the angular distribution is used to correct for the spatial dilution of the molecular beam pulse, the temporal dilution needs to be corrected for with the knowledge of the temporal distribution of the pulse after scattering. For this purpose, the signal intensity was recorded while the time delay between the nozzle opening and the firing of the UV laser τ_v was scanned for different surface temperatures. As can be seen in Fig. 3.5, the temporal distributions of molecules in either vibrational state are very similar: While at the lower incidence energy of $\langle E_i \rangle = 0.67$ eV (panels a) and b)), the distributions of the $v = 0 \rightarrow 1$ channel are slightly broader, these distributions' tails decrease marginally faster at $\langle E_i \rangle = 0.99$ eV (panels c) and d)).

Similar to the angular correction, the temporal correction factors are calculated by dividing the signal intensity at the timing used for recording the REMPI spectra by the integral of the total distribution:

$$\Delta_v(\tau_v) = \frac{I(\tau_v)}{\int I(\tau)} \tag{3.6}$$

Again, it is convenient to define relative correction factors (setting $\Delta_0 = 1$) to visualize the width of the distributions. The resulting T_s dependent Δ_1/Δ_0 (which equal Δ_1 if $\Delta_0 = 1$) are shown in Fig. 3.6. At $\langle E_i \rangle = 0.67$ eV, $\Delta_1/\Delta_0 < 1$, and at $\langle E_i \rangle = 0.99$ eV, $\Delta_1/\Delta_0 > 1$ due to the distributions' different shapes mentioned above. Although there seems to be a trend of slightly increasing $\Delta_1/\Delta_0 < 1$ with increasing temperature, a close examination of the raw data and the limited number of data points in Fig. 3.6 left reasonable doubt. Thus, the

REMPI spectra were corrected with the average value of Δ_1/Δ_0 .

Detector Gain Γ_ν

While all corrections presented above introduce a certain error in the VEPs calculation the by far most influential factor is the detector gain. It was measured by filling the scattering chamber with a static background pressure of HCl, usually around $10^{-8} - 10^{-6}$ Torr depending on the gas mixture that was used (pure HCl or diluted in H_2). The UV laser was positioned at the usual scattering position and tuned to a wavelength corresponding to a rotational state J populated at room temperature (e. g. $J = 5$). Then, the exact pressure (i. e., the density of molecules) and the laser power were adjusted in a way that neither signals were saturated at higher MCP voltages nor did they vanish in the noise at lower voltages. With a single setting it was usually not possible to obtain a reasonable signal over the whole range of detector voltages which thus was split in two or even three parts with overlapping regions for subsequently scaling the individual regions. In Tab. 3.2 and Fig. 3.7 the MCP voltages with the corresponding detector gain Γ_ν and the inverted detector gain Γ_ν^{-1} are shown, where Γ_ν is the averaged, integrated oscilloscope trace of HCl^+ and H^+ ions (molecular fragments) relative to the highest detector gain at 1950 V. From both it can be seen that the dynamic range of the detection setup spans approximately four orders of magnitude. This high dynamic range probably is the reason why I was able to observe the $\nu = 0 \rightarrow 1$ channel at all whereas early studies failed to detect the excitation [43].

Further, as is especially obvious from the logarithmic plot in panel (b), the detector gain cannot be fitted with a simple exponential function. Thus, for correction of the VEP spectra the individual data points were used instead of a correction function.

Table 3.2 Normalized detector gain factor Γ_ν depending on MCP voltage for scattering HCl from Au(111).

$U(\text{MCP})$ in V	Γ_ν	Γ_ν^{-1}
1200	0.00016	6300.
1250	0.00050	2000.
1300	0.0014	700.
1350	0.0033	300.
1400	0.0067	150.
1450	0.014	73.
1500	0.028	35.
1550	0.048	21.
1600	0.081	12.
1650	0.13	7.5
1700	0.21	4.7
1750	0.29	3.5
1800	0.47	2.1
1850	0.63	1.6
1900	0.81	1.2
1950	1.0	1.0

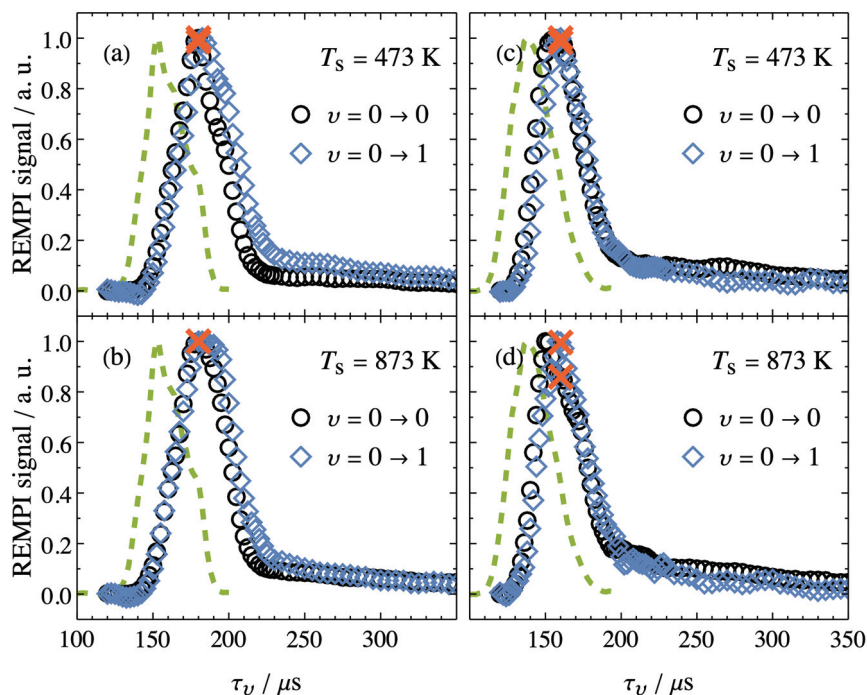


Figure 3.5 Temporal distributions for molecules with $\langle E_i \rangle = 0.67 \text{ eV}$ (a,b) and $\langle E_i \rangle = 0.99 \text{ eV}$ (c,d) coming back in $\nu = 0$ (black symbols) and $\nu = 1$ (blue symbols) at a surface temperature of $T_s = 473 \text{ K}$ (a,c) and $T_s = 873 \text{ K}$ (b,d). While the green dashed lines depict the respective incident molecules in $\nu = 0$, the timings at which the REMPI spectra were recorded are marked with red crosses. Here, τ_v is the time that has passed after the nozzle opened.

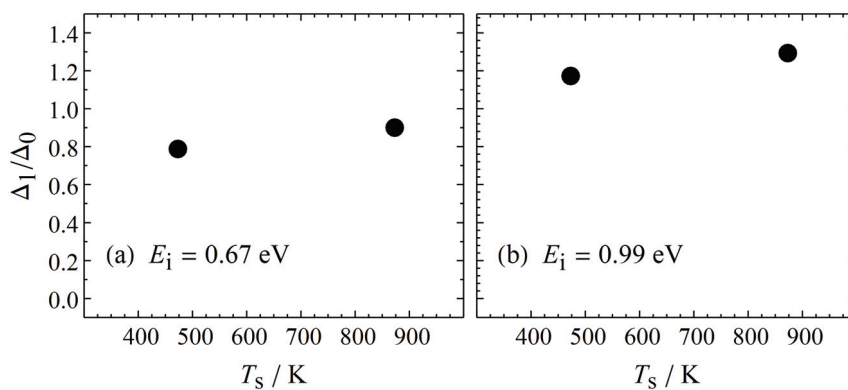


Figure 3.6 Ratio of the temperature dependent correction factors Δ_1/Δ_0 for different temporal dilution of molecules with $\langle E_i \rangle = 0.67 \text{ eV}$ (a) and $\langle E_i \rangle = 0.99 \text{ eV}$ (b) scattered from Au(111) in $\nu = 0$ and $\nu = 1$. Δ_1/Δ_0 is close to unity since the temporal distributions in Fig. 3.5 are quite similar in shape.

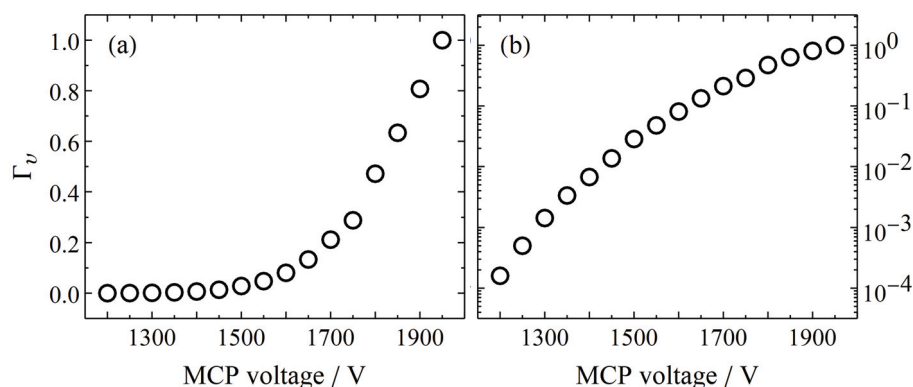


Figure 3.7 Normalized detector gain factor Γ_v depending on MCP voltage on a linear (a) and a logarithmic (b) scale.

Laser Power Correction $\Pi(\pi_v)$

Parallel to the REMPI signal the UV laser pulse energy was recorded while the wavelength was scanned. Since a (2 + 1) REMPI scheme was employed for the detection of individual ro-vibrational states (see Sec. 2.3.2), the ion signal strongly depended on the photon flux and thus on the pulse energy. Compared to the detector gain curve, this dependence was measured on the scattered molecules instead of background gas and the laser pulse energy was varied instead of the MCP voltage. The integral of the averaged oscilloscope trace of HCl^+ and H^+ ions is plotted against the laser pulse energy π_v in Fig. 3.8 for molecules in $v = 0$ (a) and $v = 1$ (b) (it is important to note here, that π_v was measured after the laser pulse has passed both entrance and exit windows and thus was lower than the direct laser output). Additionally shown in red is a simple power law fit that does represent the data quite well. Since different regimes of π_v needed to be used for measuring the REMPI spectra, both data and fit were normalized to the measured intensity at $\pi_v = 1$ mJ. Thereby, the pulse energy dependencies of molecules in $v = 0$ and $v = 1$ can directly be compared:

$$\Pi(\pi_0) = \pi_0^{1.61} \quad \text{and} \quad \Pi(\pi_1) = \pi_1^{1.26}$$

The larger exponent for $v = 0$ and thus stronger dependence on the laser energy can be explained by statistical effects: Depending on the number of photons hitting the molecular beam, the number of molecules in the detection volume, and their interaction probability (i. e., the absorption cross section), an increase in laser power can result in different signal dependencies. For a three-photon process, $\Pi(\pi)$ can theoretically range from π^3 to π^0 , depending on the ratio of the aforementioned values and the laser energy range that is investigated.⁵ While in the former case, a large excess of detectable molecules results in basically every photon being absorbed and thus in a strong dependence on the photon flux,

⁵ I carried out simple statistical simulations for conformation.

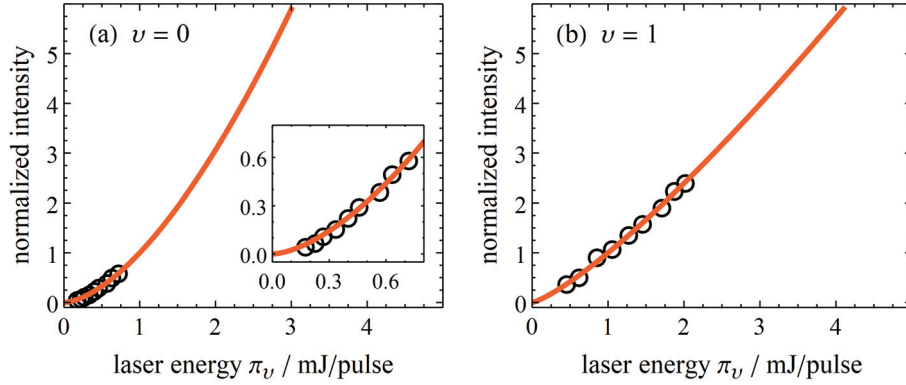


Figure 3.8 Signal intensity depending on the laser pulse energy π_v for molecules in $v = 0$ (a) and $v = 1$ (b). Depicted by red solid lines are fits according to $\Pi(\pi_0) = \pi_0^{1.61}$ (a) and $\Pi(\pi_1) = \pi_1^{1.26}$ (b). In both cases, data is normalized to the intensity at $\pi_v = 1$ mJ.

in the latter case, every molecule is ionized so that additional photons cannot result in a further signal increase. For $v = 0 \rightarrow 1$, due to the small excitation probability the population in $v = 1$ was much smaller than in $v = 0$ while at the same time the laser power and thus number of photons was higher. This resulted in the smaller laser power dependence given above.

Calculation of Vibrational Excitation Probabilities

With all necessary corrections at hand, the $v = 0 \rightarrow 1$ VEPs for scattering HCl molecules from Au(111) can now be calculated. First, the general definition of the VEP in Eq. 3.1 is adapted:

$$P_{0,1} = \frac{N_{0 \rightarrow 1}}{\sum_i N_{0 \rightarrow v_i}} \approx \frac{N_1}{\sum_i N_{v_i}} \approx \frac{N_1}{N_1 + N_0} \quad (3.7)$$

The approximation introduced in the last step of Eq. 3.7 is made under the assumptions that, first, no other states than $v = 0$ were populated in the incident beam (or rather, populations of higher states were below the detection limit). Thus, all population detected in $v = 1$ originated from excitation. Second, excitation into higher vibrational states was assumed to be negligible. Both assumptions are reasonable since no other states than those mentioned above could be detected. The (relative) populations N_0 and N_1 were calculated according to Eqs. 3.1 and 3.2 which led to the temperature and incidence energy dependent VEPs shown in Fig. 3.9. As seen for other molecule-surface systems and also for HCl/Au(111) in the previous publication (see Sec. 1.2), VEPs increase with increasing surface temperature as well as increasing incidence kinetic energy. Opposed to all other systems which showed vibrational excitation due to nonadiabatic interactions, the VEPs here cannot be fitted successfully with a pure exponential function as shown in Eq. 1.1.

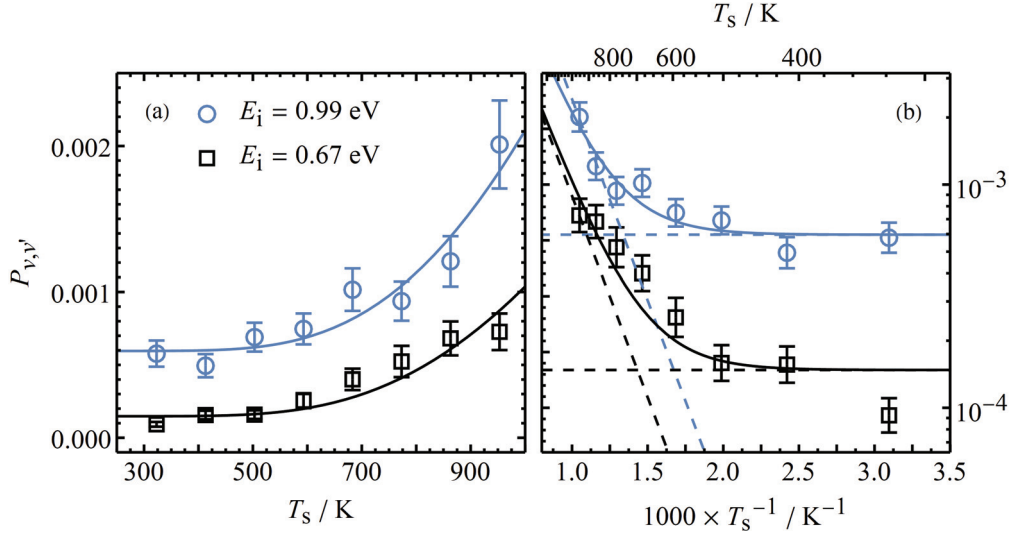


Figure 3.9 Vibrational excitation probabilities for $\nu = 0 \rightarrow 1$ excitation of HCl molecules scattered from Au(111). The solid lines in both panels depict fits to the data according to Eq. 3.8 while the dashed lines in (b) visualize the individual exponential (inclined line) and constant terms (horizontal line).

Instead, a constant $A^{\text{ad.}}(E_i)$ needs to be added to account for the non-zero intercept with the y -axis:

$$P_{v'',v'}(E_i, T_s) = A^{\text{ad.}}(E_i) + A^{\text{nonad.}}(E_i) \times \exp\left[\frac{-E_{v'',v'}}{k_B T_s}\right] \quad (3.8)$$

In contrast to the exponential prefactor $A^{\text{nonad.}}$, which has been attributed to the *non-adiabatic* interaction strength, the surface temperature independent $A^{\text{ad.}}$ is supposed to be a measure of *adiabatic* vibrational excitation. The necessity of this additional constant is obvious if the solid line denoting Eq. 3.8 in the logarithmic ARRHENIUS-like plot in Fig. 3.9 (b) is compared to the purely exponential term depicted by the dashed line whose negative slope is determined by the vibrational spacing of the $\nu = 0 \rightarrow 1$ excitation. While the latter might be used to fit data above ~ 800 K and the VEPs start approaching a constant value below ~ 500 K, the in-between transition region is only represented well by a combination of both.⁶ According to the derived values for $A^{\text{ad.}}$ and $A^{\text{nonad.}}$ in Tab. 3.3, the nonadiabatic interaction is approximately two orders of magnitude stronger than the adiabatic one. However, comparing this work's VEP values in

Table 3.3 Interaction strength constants $A^{\text{ad.}}$ and $A^{\text{nonad.}}$ for $\nu = 0 \rightarrow 1$ excitation on Au(111).

$\langle E_i \rangle / \text{eV}$	$A^{\text{ad.}}$	$A^{\text{nonad.}}$
0.67	1.5×10^{-4}	5.7×10^{-2}
0.99	6.0×10^{-4}	9.6×10^{-2}

⁶ As will be shown later on, neither the transition nor the constant value region have been observed for other, extensively studied systems as NO/Au(111).

general to those previously published shows that the former are higher by a factor of ~ 50 . Therefore I will take a closer look at how the older values were determined and at what might be the reason for this discrepancy.

Comparison to Previous Work

Since the actual formula which was used to calculate VEPs was not provided in the original publications [30, 44], Daniel Matsiev's PhD thesis needs to be revisited [81]. There, on p. 92 his definition of the excitation probability can be found:

$$P_v = \underbrace{\frac{N_{v=1 \leftarrow 0}}{N_{v=0}}}_I = \underbrace{\frac{N_{v=1}^S - N_{v=1}^I}{N_{v=1}^I}}_{II} \times \underbrace{\frac{N_{v=1}^I}{N_{v=0}}}_{III} \times \underbrace{W_A \times W_T}_{IV}, \quad (3.9)$$

where N_v denotes the population in vibrational state v in the incident (superscript I) or the scattered (superscript S) beam. Compared with my own definition (see Eq. 3.7) the denominator in term I does not consist of the sum of all states but only the population in $v = 0$. Since other states are barely populated, this is a fair assumption. Terms II and III describe the actual excitation and their origin is more easily understood if they are slightly rearranged:

$$\underbrace{\frac{N_{v=1}^S - N_{v=1}^I}{N_{v=1}^I}}_{II} \times \underbrace{\frac{N_{v=1}^I}{N_{v=0}}}_{III} = \underbrace{\frac{N_{v=1}^S - N_{v=1}^I}{N_{v=0}}}_{A} \times \underbrace{\frac{N_{v=1}^I}{N_{v=1}^I}}_B$$

Here, term A can be identified as the gain in molecules in $v = 1$ divided by the number of molecules in $v = 0$, thus it is directly linked to term I. If the fraction in A is expanded with the fraction in B and rearranged, we get back to terms II and III. While the former (term II) basically describes the normalization of the gain in $v = 1$ to the population of $v = 1$ in the incident beam, the latter (term III) denotes the theoretical thermal population in $v = 1$ or rather the BOLTZMANN factor for $v = 1$ and $v = 0$. The idea behind this formulation was to actually measure REMPI spectra of molecules in $v = 1$ only ($N_{v=1}^S$ and $N_{v=1}^I$) and to calculate term III from theory. In this way, no correction factors due to different sensitivities to molecules in different vibrational states were needed. The only corrections here can be found in part IV of Eq. 3.9 which describe the angular (spatial) and temporal dilution of the scattered relative to the incident beam.

In principal, this approach seems to be not only valid but also rather clever. However, the problem why the calculated VEPs are so low is the scaling with the supposed thermal population of $v = 1$ in the incident beam (term III). A reference value for $N_{v=1}^I$ was determined from REMPI spectra of the incident beam like that shown in Fig. 3.10 (a). By assuming that its intensity corresponded to a thermal population it was used to scale the intensity of the scattered beam in Fig. 3.10 (b). However, I propose that the assignment

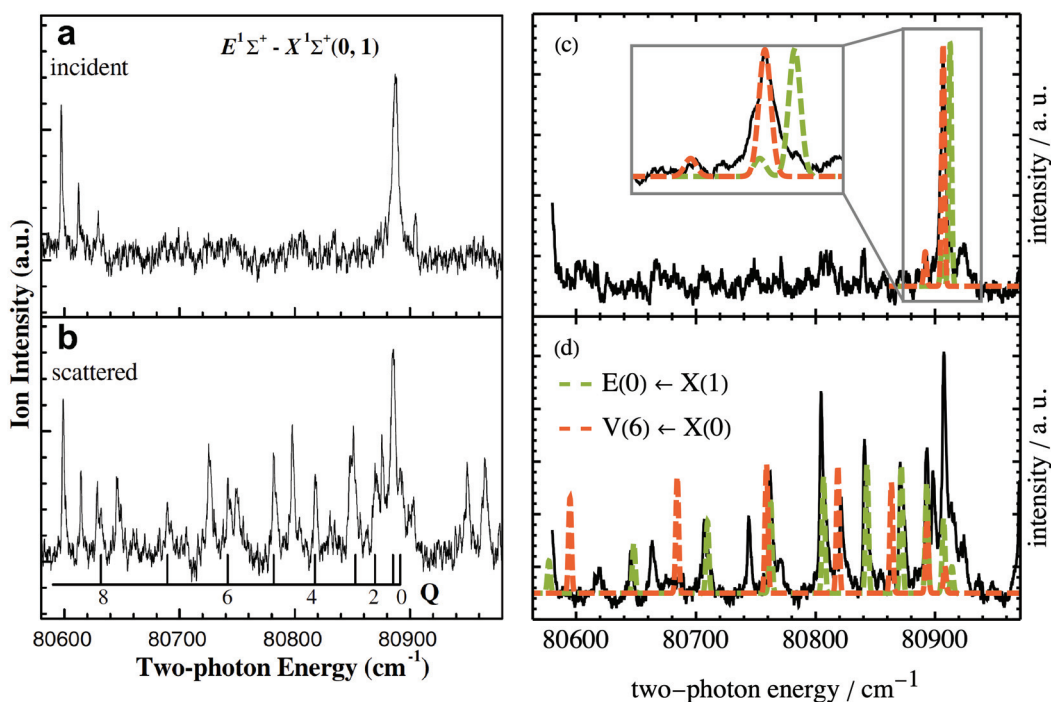


Figure 3.10 Erroneous line assignment that led to VEP values being too low in previous publication [44]. While panels (a) and (b) on the left hand side were directly taken from Ref. [44], panels (c) and (d) show similar (but not exactly the same) REMPI spectra from the same set of measurements as those in (a) and (b) (see text/footnote). In Ref. [44], the REMPI spectrum of the incident beam in (a) was used to calibrate the VEPs determined from the scattered intensity in (b), see text and Eq. 3.9. In (c) and (d), the dashed lines depict simulations of REMPI spectra at a rotational temperature $T_{\text{rot}} = 10\text{ K}$ and 500 K , respectively, for transitions from $v = 1$ via the E state (green) and from $v = 0$ via the V state (red). While lines originating from the E state transition are indeed seen in the scattered beam (d), the lines in the incident beam in this wavelength range actually stem from the V state transitions (c).

of the intense line in (a) is wrong: it most probably does not stem from the Q branch of the $E^1\Sigma^+ \leftarrow X^1\Sigma^+(0,1)$ transition as indicated on the top of panel (a), but from the $V^1\Sigma^+ \leftarrow X^1\Sigma^+(6,0)$ transition. This can be seen from the REMPI spectra in panels (c) and (d) where spectral simulations are superimposed on the raw data.⁷ For the incident beam, where due to the noise in the baseline the only populated rotational state that can clearly be identified is $J = 0$, assigning certain transitions is difficult. If only those via the E state are taken into account, the line in (a) and (c) could easily be assigned to $E^1\Sigma^+ \leftarrow X^1\Sigma^+(0,1)$. If, however, transitions via the V state are additionally considered and the x -axis is zoomed in (see the inset in (c)) it can be seen that both transitions from $J = 0$ are very close in

⁷ A trained eye will immediately see that (c) and (d) are not exactly the same spectra as (a) and (b). That is due to the simple fact that I could only retrieve raw data for those spectra in (c) and (d) but not for (a) and (b) from the original measurement data archive. However, the spectra in (c) and (d) stem from the same set of measurements as (a) and (b) and serve the purpose of visualizing the erroneous assignment.

energy. Yet, the position of the $J = 0$ line does fit the V transition better. Additionally, the energetic gap between $J = 0$ and $J = 1$ for the $V^1\Sigma^+ \leftarrow X^1\Sigma^+(6,0)$ transition and the relative intensities of the two rotational states do fit with a small spectral shoulder in the zoomed-in spectrum in panel (c) that can be assigned to $J = 1$ (simulation temperature is 10 K). This problem with overlapping lines from low J states was mentioned before by Rohlfiing *et al.* [74]. Nevertheless, a comparison in (d) with both simulated spectra shows that in the scattered beam, there was indeed measurable population in $v = 1$ that was detected *via* the E state. Given the increased number of populated rotational states, most of the lines in (d) can be assigned to $E^1\Sigma^+ \leftarrow X^1\Sigma^+(0,1)$ transitions while the relative intensity of $V^1\Sigma^+ \leftarrow X^1\Sigma^+(6,0)$ transitions was too weak in this case (red simulation does not have as much corresponding spectral lines). Since the erroneous assignments discussed above only affect the correct scaling of the population scattered in $N_{v=1}^S$, it should be possible to preserve the temperature and incidence energy dependence of the previous work and scale its VEPs by a constant so that they match the new data of this work.

In order to find this constant, the old data is analyzed in the same way as described above for the new VEPs. That is, the surface temperature dependence is fitted by Eq. 3.8 and parameters $A^{\text{ad.}}$ and $A^{\text{nonad.}}$ are extracted. The advantage of these parameters over the basic VEPs is that they are independent of the surface temperature and thus comparisons between different systems or measurements are more reliable. They are, however, still dependent on the incidence kinetic energy of the molecules. This dependence is shown in Fig. 3.11 where blue symbols depict the parameters from the new measurements. Shown as dashed blue lines are simple linear fits to this data which are allowed to have an offset (or threshold) or forced to go through zero for the adiabatic and nonadiabatic interactions, respectively. In a second step, $A^{\text{ad.}}$ and $A^{\text{nonad.}}$ from the old data are scaled to these fits by a least squares method that leads to

an upscaling factor of $f_{\text{up}} = 55$.⁸ The resulting values for $A^{\text{ad.}}$ and $A^{\text{nonad.}}$ are included in Fig. 3.11 as open black symbols. Additionally, applying f_{up} to the old VEP data it can be

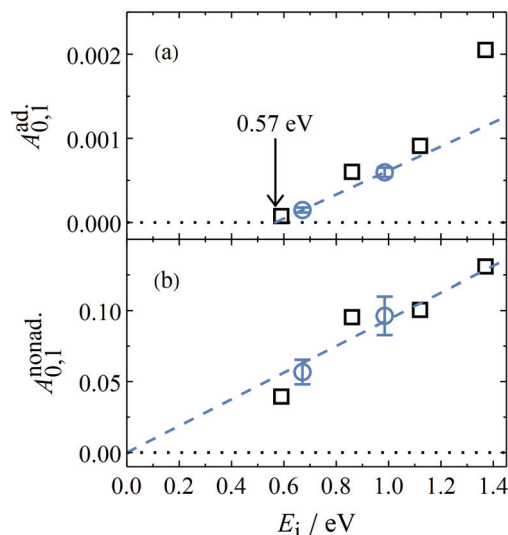


Figure 3.11 Interaction strength constants $A^{\text{ad.}}$ (a) and $A^{\text{nonad.}}$ (b) for $v = 0 \rightarrow 1$ excitation on Au(111) plotted against the incidence energy E_i . While blue symbols depict this work's data, old data that has been upscaled is depicted by black symbols (see text). The dashed lines indicate linear fits and in (a) an energetic threshold is depicted by the black arrow.

⁸ The data points at $\langle E_i \rangle = 1.37$ eV have been omitted since the value for $A^{\text{ad.}}$ obviously deviates from the linear behavior.

added to a comparison of $\nu = 0 \rightarrow 1$ excitation. As can be seen from Fig. 3.12, old and new excitation probabilities match nicely when scaled correctly. That is, surface temperature as well as incidence energy dependence are consistent on an absolute scale.

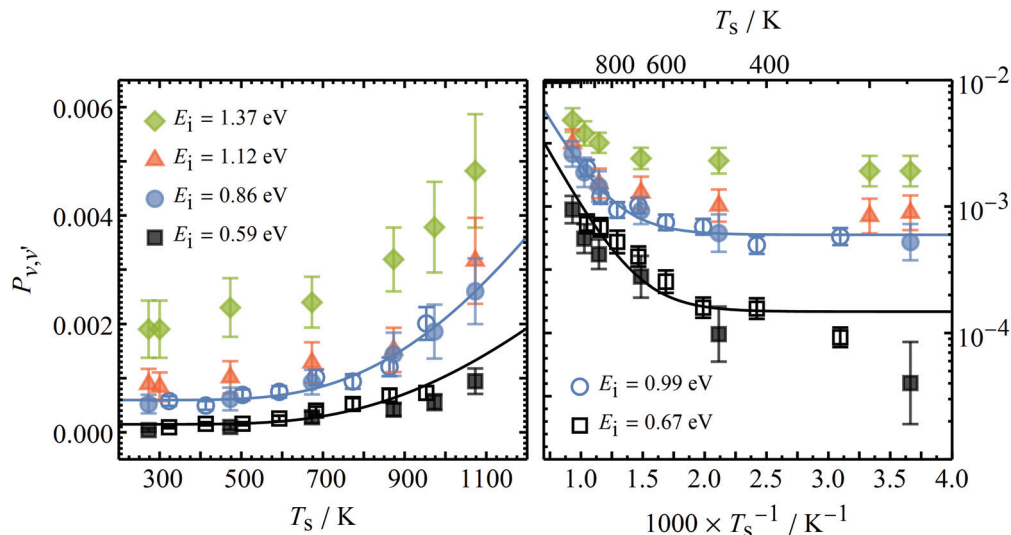


Figure 3.12 Vibrational excitation probabilities for $\nu = 0 \rightarrow 1$ excitation of HCl molecules scattered from Au(111). In addition to the newly determined VEPs depicted by open symbols, filled symbols represent the up-scaled VEPs from previous work. The solid lines in both panels depict fits to the new data according to Eq. 3.8.

3.1.2 Excitation from $\nu = 1 \rightarrow 2$

Although the repetition of the $\nu = 0 \rightarrow 1$ excitation probabilities measurements have turned out to be more important than they were supposed to be, they were intended to be the basis for measuring the previously unexamined $\nu = 1 \rightarrow 2$ excitation which will be discussed in the following section.

The general procedure for measuring this "hot band" excitation was very similar to the one describe in the previous section. However, in this case molecules in the incident molecular beam were excited to $\nu = 1$ prior to the surface collision with the IR laser system (see Sec. 2.2) tuned to the $R(0)$ transition at $\lambda = 3440.866$ nm ($\tilde{\nu} = 2906.245$ cm $^{-1}$). After the collision HCl molecules were detected in $\nu = 1$ and $\nu = 2$ using the UV laser system. As before, the most important experimental parameters are shown in Tab. 3.4. In comparison to the $\nu = 0 \rightarrow 1$ excitation (see Tab. 3.1) both the detector voltage (i. e. detector gain) as well as the laser power needed to be increased to obtain a reasonable signal intensity. All in all the intensity of the initial vibrational state's signal was approximately 20 times lower than in the case of $\nu = 0 \rightarrow 1$ excitation. That is due to the fact that only a small portion of the incoming molecular pulse was excited by the IR laser.

In Fig. 3.13 representative REMPI spectra for an incidence energy of $\langle E_i \rangle = 0.67$ eV are

Chapter 3. Scattering HCl from Au(111)

Table 3.4 Experimental parameters for measuring the $\nu = 1 \rightarrow 2$ excitation of HCl on Au(111). $\langle E_i \rangle$ is the incidence translational energy, $U(\text{MCP})$ the detector voltage, $\langle E_L \rangle$ the approximate average laser power, and θ the approximate scattering angle. Shown are usual values that might have been adapted for individual measurements when needed.

Gas Mixture	$\langle E_i \rangle$ in eV	ν State	$U(\text{MCP})$ in V	$\langle E_L \rangle$ in mJ	θ in $^\circ$
8% HCl in H ₂	0.64	$\nu = 1$	1400	$\sim 0.8 - 1.2$	~ 15
		$\nu = 2$	1950	$\sim 3.0 - 4.0$	~ 15
8% HCl in H ₂	0.67	$\nu = 1$	1400	$\sim 1.0 - 1.4$	~ 15
		$\nu = 2$	1950	$\sim 3.0 - 4.0$	~ 15
4% HCl in H ₂	0.94	$\nu = 1$	1450	$\sim 0.7 - 0.9$	~ 15
		$\nu = 2$	1950	$\sim 3.0 - 4.0$	~ 15
2.5% HCl in H ₂	0.99	$\nu = 1$	1400	$\sim 0.6 - 0.9$	~ 15
		$\nu = 2$	1950	$\sim 2.5 - 3.5$	~ 15
2% HCl in H ₂	1.06	$\nu = 1$	1500	$\sim 0.8 - 1.1$	~ 15
		$\nu = 2$	1950	$\sim 2.5 - 3.5$	~ 15

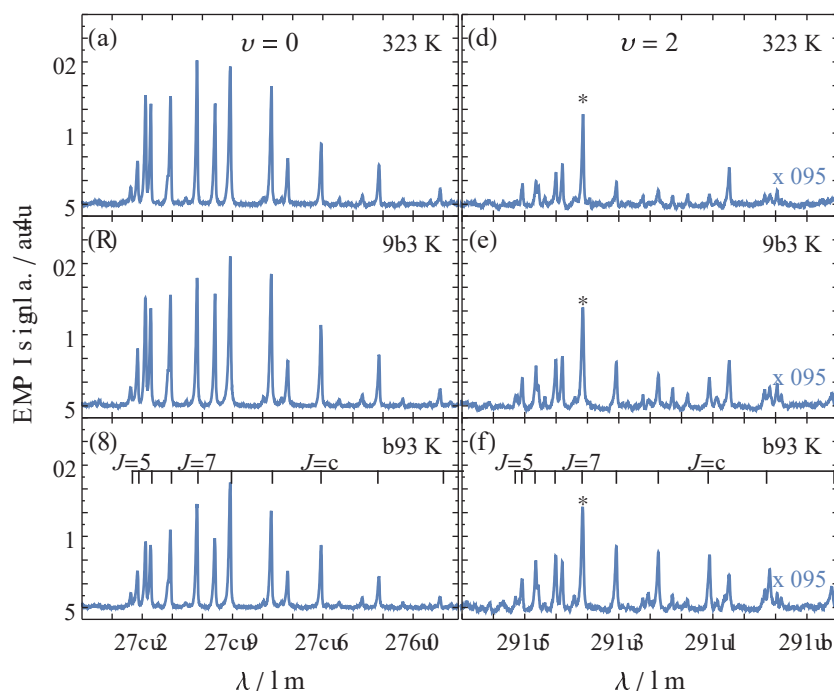


Figure 3.13 Representative REMPI spectra of HCl molecules scattered from Au(111) at three different surface temperatures. Shown are spectra in the wavelength range of $\nu = 1$ (a–c) and $\nu = 2$ (d–f) recorded at $\langle E_i \rangle = 0.67$ eV that have only been corrected for laser power. While the signal is arbitrarily scaled, the relative scale is the same for all six panels. The spectra for $\nu = 2$ are magnified by a factor of ~ 150 relative to the spectra for $\nu = 1$. Additional lines not assigned to a certain J state belong to different transitions *via* the $V^1\Sigma^+$ state (see Sec. 2.3.2). The line marked with an asterisk overlaps with the $J = 4$ line of $\nu = 2$.

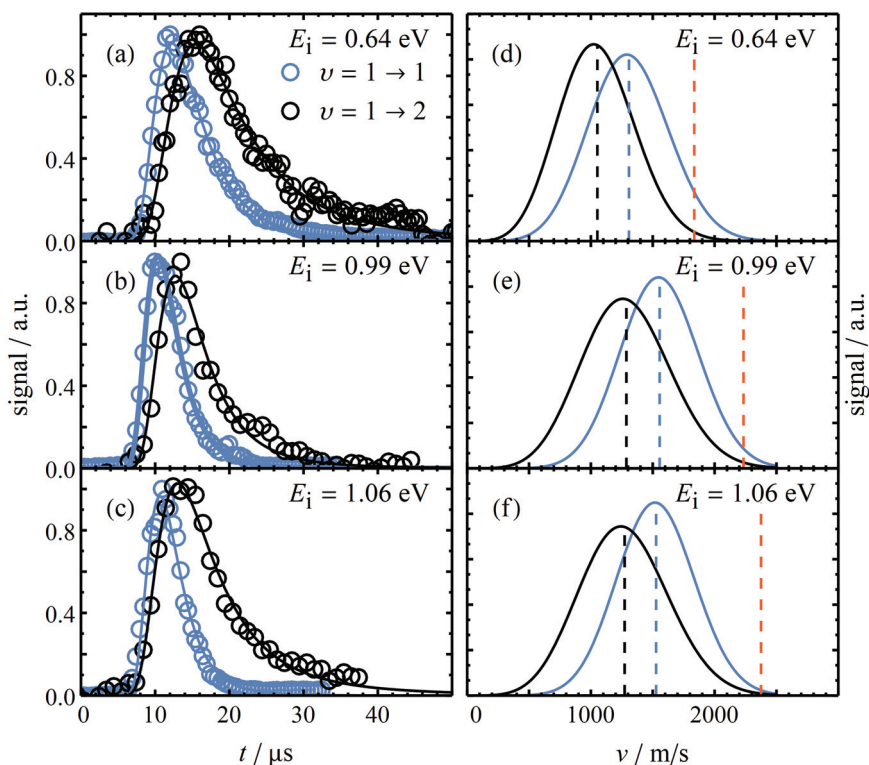


Figure 3.14 TOF raw data (a–c) and corresponding velocity distributions (d–f) for the $\nu = 1 \rightarrow 1$ and $\nu = 1 \rightarrow 2$ scattering channels on Au(111) at three representative incidence energies. Here, t is the time after the IR laser pulse. The mean velocities depicted by dashed blue ($\nu = 1 \rightarrow 1$, $J = 5$), black ($\nu = 1 \rightarrow 2$, $J = 5$) and red (incident beam, $J = 0$) vertical lines are also summarized in Tab. 3.5.

shown. Again, it can already be seen from these raw spectra (only corrected for laser power fluctuations/differences) that the signal in the incident vibrational state $\nu = 1$ stays approximately the same when the surface temperature T_s is increased from 323 K (top panel) to 953 K (bottom panel). As seen for the $\nu = 0 \rightarrow 1$ excitation, the signal of the upper vibrational state $\nu = 2$ increases with increasing surface temperature. Thus the vibrational excitation $\nu = 1 \rightarrow 2$ increases with T_s as well. In the following paragraphs I will show examples of the correction functions introduced in the previous section for selected experimental conditions.

Average Velocity $\langle u_\nu \rangle$

As explained in detail in Sec. A.2, REMPI is a detection method sensitive to the molecules' density. However, for a comparison of populations, i. e. the number of molecules in certain states coming from the surface, the required quantity is flux. Since density detection is biased towards slower molecules and the conversion factor between density and flux is velocity, the latter was determined for molecules leaving the surface in vibrational states

Table 3.5 Mean velocities $\langle u_v \rangle$ for the $v = 1 \rightarrow 1$ and $v = 1 \rightarrow 2$ scattering channels on Au(111) as well as the incident beam at three representative incidence energies.

$\langle E_i \rangle$ in eV	$\langle u_1 \rangle$ in m/s	$\langle u_2 \rangle$ in m/s	$\frac{\langle u_1 \rangle}{\langle u_2 \rangle}$	$\langle u_i \rangle$ in m/s
0.64	1307	1052	1.24	1835
0.99	1555	1286	1.21	2234
1.06	1527	1273	1.20	2375
<i>avg.</i>			1.22	

$v = 1$ and $v = 2$ by means of the TOF technique explained in Sec. 2.3.3.

In short, the IR laser pulse that excited HCl molecules to $v = 1$ prior to the collision was used as a *tag* and the delay between the IR and UV (the *probe*) laser pulses was scanned. In Fig. 3.14 a) – c) the signal intensities of $v = 1, J = 5$ and $v = 2, J = 5$ depending on the delay between tag and probe are shown for three representative incidence energies. Knowing the traveled distance these TOF distributions were converted to the velocity distributions $P(u)$ ⁹ in Fig. 3.14 d) – f) which represent flowing three-dimensional MAXWELL-BOLTZMANN distributions (cf. Eq. 2.4 in Sec. A.2). From these velocity distributions the mean velocities $\langle u_v \rangle$ were calculated according to Eq. 3.10

$$\langle u_v \rangle = \int u \times P(u) \, du. \quad (3.10)$$

Depicted by the dashed vertical lines in Fig. 3.14 d) – f), the resulting values for $\langle u_v \rangle$ are summarized in Tab. 3.5. On average, the mean velocities for molecules scattered back in $v = 1$ were 22 % higher than those of molecules scattered back in $v = 2$. Therefore, the correction factors for the VEP calculation are

$$\langle u_1 \rangle = 1.22 \quad \text{and} \quad \langle u_2 \rangle = 1.00.$$

Angular Distribution $\Theta_v(\theta_v)$

In Fig. 3.15 angular distributions for HCl molecules with an incidence energy of $\langle E_i \rangle = 0.67$ eV scattered from the Au(111) surface in (a) $v = 1$ and (b) $v = 2$ are shown. As seen above, the incident beam (denoted by red data points and the red dashed line) has an effect on the angular distributions as the scattering data points measured at the same angle exhibit intensities above expectations. Even though there was no detectable population of $v = 1$ or $v = 2$ in the incident beam, its high flux compared to the scattered beam led to an above-average non-resonant background visible in the raw data. As a result, these data

⁹ Here, u is used as the variable denoting the velocity to avoid confusing the usual v with the frequently appearing v denoting the vibrational state.

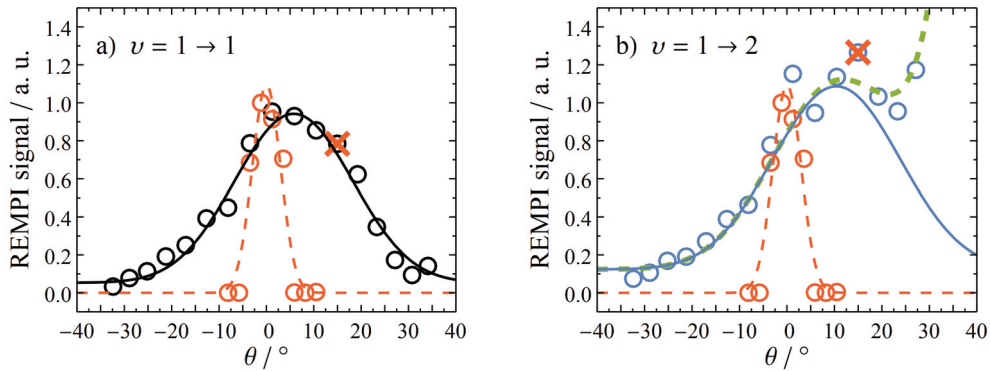


Figure 3.15 Angular distributions for molecules with $\langle E_i \rangle = 0.67 \text{ eV}$ coming back in (a) $\nu = 1$ and (b) $\nu = 2$. While the solid lines denote a fit to the data according to $a \times \cos^n(\theta - \theta_0) + c$, red data points and the dashed line denote the incident molecular beam. The red crosses mark the data points at the angle at which the REMPI spectra for the VEPs were measured. In (b), the dashed green line denotes a fit that adds an exponential term to the cosine function (see text).

points were excluded from the cosine fit (see Eq. 3.4) depicted by the solid black line in Fig. 3.15 (a). As described for the $\nu = 0 \rightarrow 1$ excitation, due to the high detector gain the angular distribution in panel (b) again exhibited strong distortion in the range of $\theta \gtrsim 10^\circ$ where the ionization laser was closest to the detector. Thus, a fit according to Eq. 3.5 is depicted by the dashed green line in Fig. 3.15 while the solid blue line denotes a pure cosine function according to Eq. 3.4 with parameters a , b and c extracted from the former fit. As seen before, the fitted exponents n indicate direct scattering with values of $n = 21$ for $\nu = 1$ (a) and $n = 18$ for $\nu = 2$ (b). The centers of both distributions suggest specular scattering with $\theta_0 = 6^\circ$ (a) and $\theta_0 = 10^\circ$ (b).

Since the angular distributions are very similar to those of the $\nu = 0 \rightarrow 1$ excitation, the angular correction factors are determined in the same way which results in

$$\Theta_2(\theta_2) = \frac{f(\theta_2)}{f(\theta_1)} = 1.25 \quad \text{if} \quad \Theta_1(\theta_1) = 1.$$

That is, they are basically the same as for $\nu = 0 \rightarrow 1$. Although they were explicitly determined only for $E_i = 0.67 \text{ eV}$, the correction factors derived here were used for all incidence energies.

Temporal Distribution $\Delta_\nu(\tau_\nu)$

While the angular distribution is used to correct for the spatial dilution of the molecular beam pulse, the temporal dilution needs to be corrected for with the knowledge of the temporal distribution of the pulse after scattering. For this purpose, the signal intensity was recorded while the time delay τ_ν between the nozzle opening and the firing of the

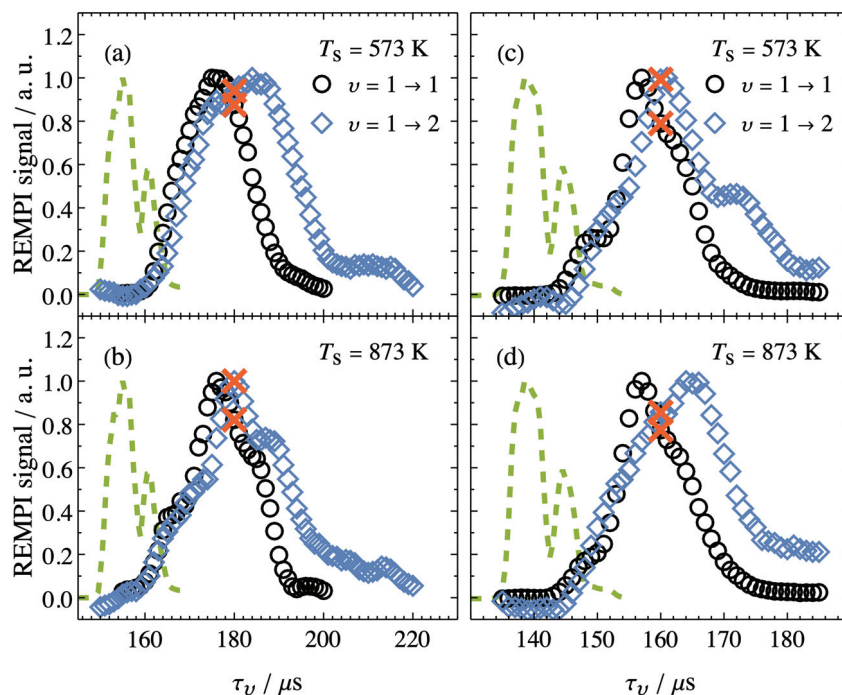


Figure 3.16 Temporal distributions for molecules with $\langle E_i \rangle = 0.67 \text{ eV}$ (a,b) and $\langle E_i \rangle = 0.99 \text{ eV}$ (c,d) coming back in $\nu = 1$ (black symbols) and $\nu = 2$ (blue symbols) at a surface temperature of $T_s = 573 \text{ K}$ (a,c) and $T_s = 873 \text{ K}$ (b,d). While the green dashed lines depict the respective incident molecules in $\nu = 1$, the timings at which the REMPI spectra were recorded are marked with red crosses. Here, τ_{ij} is the time that has passed after the nozzle opened.

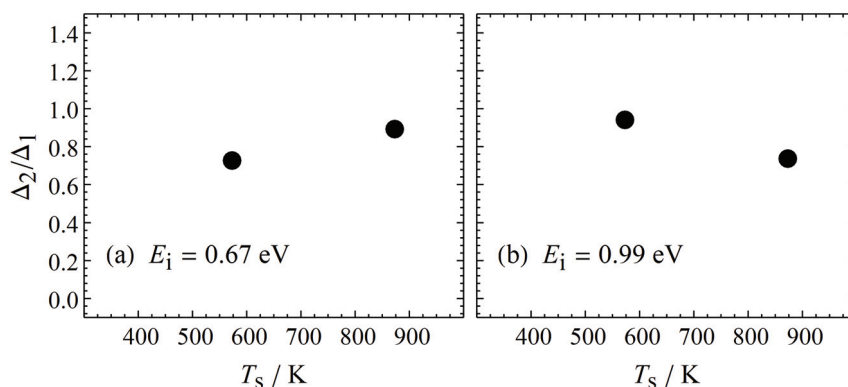


Figure 3.17 Ratio of the temperature dependent correction factors Δ_2/Δ_1 for different temporal dilution of molecules with $\langle E_i \rangle = 0.67 \text{ eV}$ (a) and $\langle E_i \rangle = 0.99 \text{ eV}$ (b) scattered from Au(111) in $\nu = 1$ and $\nu = 2$. Δ_2/Δ_1 is smaller than unity since the temporal distributions for $\nu = 2$ are broader.

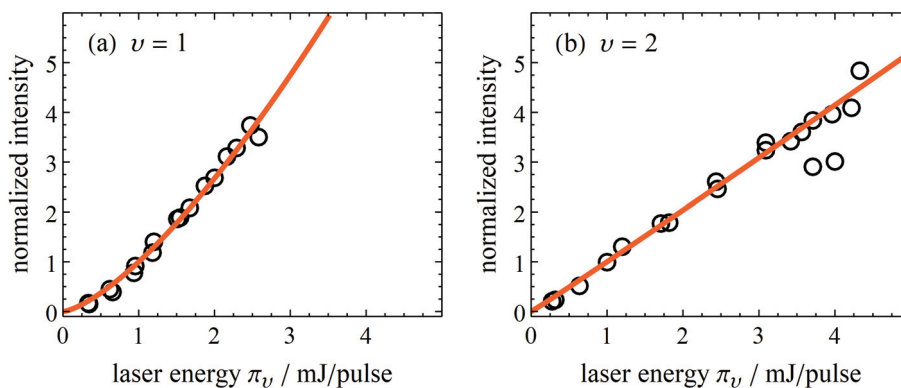


Figure 3.18 Signal intensity depending on the laser pulse energy π_v for molecules in $v = 1$ (a) and $v = 2$ (b). Depicted by red solid lines are fits according to $\Pi(\pi_1) = \pi_1^{1.42}$ (a) and $\Pi(\pi_2) = \pi_2^{1.02}$ (b). In both cases, data is normalized to the intensity at $\pi_v = 1$ mJ. The red line depicts a simple power law fit.

UV laser was scanned for different surface temperatures. As can be seen in Fig. 3.16 for representative incidence energies of $\langle E_i \rangle = 0.67$ eV and 0.99 eV, the temporal distributions of molecules in different final vibrational states differed in peak position, width and slightly in the general shape of the pulse. While the latter does not seem to follow an obvious trend with surface temperature or incidence energy, the scattered molecules in $v = 2$ exhibited broader distributions with later peak arrival times (similar as for the $v = 0 \rightarrow 1$ excitation). Again, it is convenient to define relative correction factors (setting $\Delta_1 = 1$) to visualize the different widths of the distributions. The resulting T_s dependent Δ_2/Δ_1 are shown in Fig. 3.17. Since there is no identifiable trend in the temporal distributions (possibly due to limited data), the REMPI spectra were corrected with the average value of Δ_2/Δ_1 .

Laser Power Correction $\Pi(\pi_v)$

In Fig. 3.18 the laser energy dependent signal intensity is shown for scattered molecules in $v = 1$ (a) and $v = 2$ (b). Depicted by a red solid line is a simple power law fit that does represent the data quite well. Since different regimes of π_v needed to be used for measuring the REMPI spectra, both data and fit were normalized to the measured intensity at $\pi_v = 1$ mJ. Thereby, the pulse energy dependencies of molecules in $v = 1$ and $v = 2$ can directly be compared:

$$\Pi(\pi_1) = \pi_1^{1.42} \quad \text{and} \quad \Pi(\pi_2) = \pi_2^{1.02}$$

The larger exponent for $v = 1$ and thus stronger dependence on the laser energy can be explained by the same statistical effects as given for the $v = 0 \rightarrow 1$ channel in Sec. 3.1.1. These effects might also explain why the correction functions derived here are lower than those for $v = 0 \rightarrow 1$ excitation for both the lower as well as the upper vibrational state.

Calculation of Vibrational Excitation Probabilities

Since the detector gain was assumed to be the same for the $\nu = 0 \rightarrow 1$ and the $\nu = 1 \rightarrow 2$ excitation, it was adopted from those measurements. Before the $\nu = 1 \rightarrow 2$ VEPs for scattering HCl molecules from Au(111) can be calculated, the general definition of the VEP in Eq. 3.1 needs to be adapted again:

$$P_{1,2} = \frac{N_{1 \rightarrow 2}}{\sum_i N_{1 \rightarrow \nu_i}} \approx \frac{N_2}{\sum_i N_{\nu_i}} \approx \frac{N_2}{N_2 + N_1} \quad (3.11)$$

The most important approximation introduced in the last step of Eq. 3.11 is that there is no significant relaxation from the prepared $\nu = 1$ state during the collision. This assumption is necessary since it would not be possible to measure any relaxation into $\nu = 0$ due to the enormous background of incident molecules in the vibrational ground state. However, in private communication with Igor Rahinov, who published results on the translational energy transfer in the HCl($\nu_1 = 2$)/Au(111) system [82], the relaxation probability of $\nu = 2 \rightarrow 1$ was reported to be around 30 %. As will be discussed later on, vibrational inelasticity during scattering events is expected to be enhanced by increased incidence vibration. Thus, I expect the $\nu = 1 \rightarrow 0$ relaxation to also exhibit a probability of 30 % or less. That is, if the aforementioned approximation is wrong, Eq. 3.11 will probably overestimate the VEPs by 30 % at most. Two minor approximations in Eq. 3.11 include the omission of $\nu = 0 \rightarrow 1$ excitation, which would falsely increase the amount of detected molecules in $\nu = 1$, and the excitation into vibrational states higher than $\nu = 2$. While the former process certainly occurred, it did not influence the $\nu = 1 \rightarrow 2$ measurements due to the low MCP voltage used here (1400 V *vs.* 1850 V). On the other hand, the latter process is even less likely to have influenced the $\nu = 1 \rightarrow 2$ VEPs because the energetic gap to the excitation of higher vibrational states is too large in the case of HCl.

The (relative) populations N_1 and N_2 are calculated according to Eqs. 3.1 and 3.2 leading to the temperature and incidence energy dependent VEPs shown in Fig. 3.19. As seen above, VEPs increase with surface temperature as well as incidence kinetic energy. Similar to the case of $\nu = 0 \rightarrow 1$ excitation, the VEPs here cannot be fitted successfully with a pure exponential function as shown in Eq. 1.1 but with an additional offset as in Eq. 3.8 instead. This is obvious from the logarithmic plot in Fig. 3.19 (b) where the exponential term, whose negative slope is determined by the vibrational spacing of the $\nu = 1 \rightarrow 2$ excitation, and the constant are depicted by the dashed lines. According to the derived values for $A^{\text{ad.}}$ and $A^{\text{nonad.}}$ in Tab. 3.6, the nonadiabatic interaction is approximately two orders of magnitude stronger than the adiabatic one but the difference between the two shrinks with increasing incidence energy. Interestingly, a comparison of both excitation channels reveals that the probabilities for the $\nu = 1 \rightarrow 2$ excitation are approximately 20 times higher than those for the $\nu = 0 \rightarrow 1$ channel.¹⁰ According to Tabs. 3.3 and 3.6 this difference predominantly

¹⁰It needs to be pointed out that even at $T_s = 950$ K the component $A^{\text{ad.}}$ still accounts for at least 25 % of the total VEP which explains the rapid deviation from the declining slope with decreasing temperature.

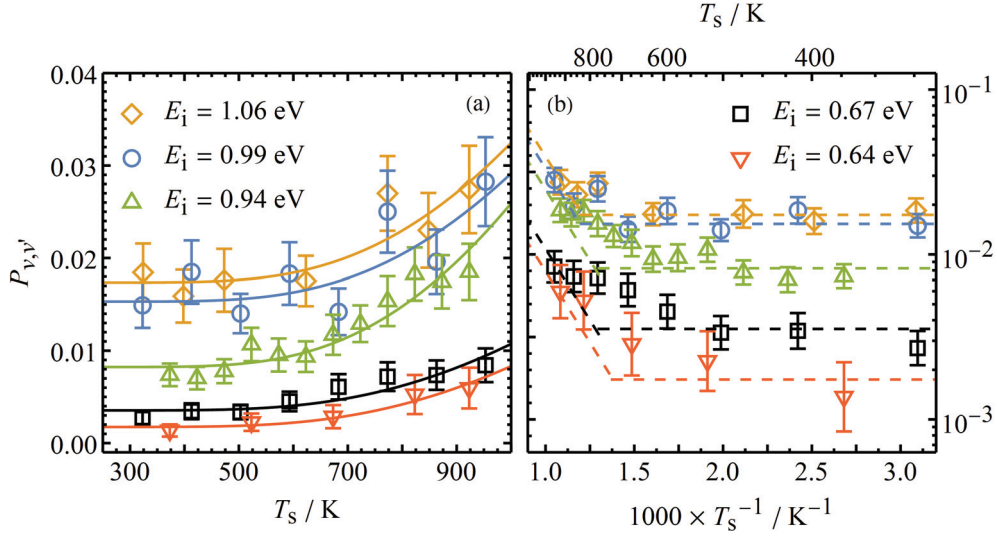


Figure 3.19 Vibrational excitation probabilities for $v = 1 \rightarrow 2$ excitation of HCl molecules scattered from Au(111). In panel (a) the solid lines depict fits to the data according to Eq. 3.8 while the dashed lines in (b) visualize the individual exponential (inclined lines) and constant terms (horizontal lines). Even though the legend was split, both panels include all five incidence energies.

arises from the mechanical contributions and only to a lesser extent from the electronic interactions. To facilitate this comparison, parameters quantifying the adiabatic and nonadiabatic interaction strength which are independent of surface temperature as well as incidence kinetic energy can be determined. In Fig. 3.20, $A^{\text{ad.}}$ (a) and $A^{\text{nonad.}}$ (b) are plotted against the corresponding $\langle E_i \rangle$ where dashed lines indicate linear fits to the data. The slopes of these fits, which represent incidence energy independent quantities, are gathered together with their counterparts for the $v = 0 \rightarrow 1$ excitation in Tab. 3.7. Whereas $\frac{dA^{\text{nonad.}}}{dE_i}$ increases by a factor of 8.5 when going from $v = 0 \rightarrow 1$ to $v = 1 \rightarrow 2$, $\frac{dA^{\text{ad.}}}{dE_i}$ even goes up by a factor of 24. Therefore, while both interactions are promoted by incident vibrational energy, it seems to affect the adiabatic part more strongly. These effects are even more impressive if compared to the classical LANDAU-TELLER theory for mechanical excitation of vibrations during collisions [83, 84]. There, the excitation probability is proportional to $(v'' + 1)$ within the harmonic oscillator framework:

$$P_{v'',v'} \propto (v'' + 1) \quad (3.12)$$

According to Eq. 3.12, $P_{1,2}$ would have been expected to be twice as large as $P_{0,1}$, which is in stark contrast to my experimental results. Considering these findings the next logical step was to excite HCl molecules to $v = 2$ prior to the collision and look for $v = 3$ coming back after scattering.

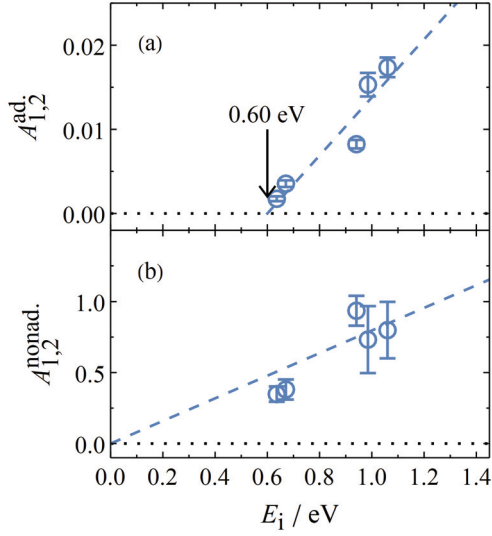


Figure 3.20 Interaction strength constants $A^{\text{ad.}}$ (a) and $A^{\text{nonad.}}$ (b) for $\nu = 1 \rightarrow 2$ excitation on Au(111) plotted against the incidence energy $\langle E_i \rangle$. The dashed lines indicate linear fits and in (a) an energetic threshold is depicted by the black arrow.

Table 3.6 Interaction strength constants $A^{\text{ad.}}$ and $A^{\text{nonad.}}$ for $\nu = 1 \rightarrow 2$ excitation on Au(111).

$\langle E_i \rangle / \text{eV}$	$A^{\text{ad.}}$	$A^{\text{nonad.}}$
0.64	1.7×10^{-3}	3.5×10^{-1}
0.67	3.5×10^{-3}	3.8×10^{-1}
0.94	8.2×10^{-3}	9.4×10^{-1}
0.99	1.5×10^{-2}	7.3×10^{-1}
1.06	1.7×10^{-2}	8.0×10^{-1}

Table 3.7 $\frac{dA^{\text{ad.}}}{dE_i}$ and $\frac{dA^{\text{nonad.}}}{dE_i}$ derived from Figs. 3.11 and 3.20.

$\nu \rightarrow \nu'$	$\frac{dA^{\text{ad.}}}{dE_i} / \frac{1}{\text{eV}}$	$\frac{dA^{\text{nonad.}}}{dE_i} / \frac{1}{\text{eV}}$
$0 \rightarrow 1$	1.4×10^{-3}	9.4×10^{-2}
$1 \rightarrow 2$	3.4×10^{-2}	8.0×10^{-1}

3.1.3 Excitation from $v = 2 \rightarrow 3$

Similar to the experimental procedure for studying the $v = 1 \rightarrow 2$, HCl molecules in the incident molecular beam were excited to $v = 2$ prior to the surface collision with the IR laser system (see Sec. 2.2) tuned to the $R(0)$ transition at $\lambda = 1758.196 \text{ nm}$ ($\tilde{\nu} = 5687.647 \text{ cm}^{-1}$). After the collision HCl molecules were detected using the UV laser system.

In first tests, detecting HCl($v = 2$) in the scattered beam this laser's wavelength was scanned over the range of the Q branch of the $E(0) \leftarrow X(2)$ transitions to assure the correct tuning of the pump laser. Here, the molecular beam was produced from the same 2.5 % mixture of HCl in H_2 with an incidence energy of $\langle E_i \rangle = 0.99 \text{ eV}$ that was also used for the $v = 0 \rightarrow 1$ and $v = 1 \rightarrow 2$ excitation. As can be seen in Fig. 3.21 (a), those Q branch transitions were successfully identified. Therefore, I searched for HCl molecules in $v = 3$ by scanning the corresponding wavelength range. Indeed, there were several REMPI lines that can be seen in Fig. 3.21 (b). However, these lines appeared to be rather independent of surface temperature in opposite to what I expected based on the other excitation studies. A closer look at their exact positions on the wavelength scale and a comparison with the spectral simulation mentioned above (Sec. 3.1.1) revealed the reason for this behavior. As shown in Fig. 3.21 (b), the mainly observable spectral lines belonged to transitions from ubiquitous $v = 0$ via $v = 7$ (dashed green lines) and $v = 8$ (dashed red lines) in the V state. In contrast to that, the simulation of the $E(0) \leftarrow X(3)$ transitions (solid blue lines) does not have any matching counterparts in the experiment.

The non-existence of $E(0) \leftarrow X(3)$ lines in Fig. 3.21 raises the question whether there was really no $v = 2 \rightarrow 3$ excitation (that is, possible signals of excitation remained below the detection limit) or the excitation signals were simply missed due to wrong experimental settings. First of all, as suggested in the previous paragraph, on several days different surface temperatures ranging from room temperature to 970 K and various wavelength ranges were tested. In all of these experiments the transitions via the V state could easily be seen and their signals barely changed with temperature. This is in accordance with the assumption that the transitions originate at $v = 0$, the population of which is supposed to vary only slightly with temperature. Furthermore, extending the scan range revealed more lines that matched the aforementioned transitions and thus additionally confirmed the assignment. Since I detected molecules in $v = 2$ and in $v = 0$ in the wavelength range where $v = 3$ is expected, it can safely be assumed that the $v = 2 \rightarrow 3$ excitation probabilities are simply too low to be detected in our setup. In the following paragraph I will thus try to estimate an upper limit for the $v = 2 \rightarrow 3$ VEPs based on comparisons with $v = 1 \rightarrow 2$ data. First, the experimental conditions under which the REMPI spectra of the scattered molecular beam were recorded need to be examined. In Tab. 3.8 the used average laser power $\langle \pi_v \rangle$, detector voltage $U(\text{MCP})$ and the resulting signals for the most intense spectral lines are gathered. For detection of the lower vibrational state in the $v = 2 \rightarrow 3$ excitation, the laser power needed to be increased by a factor of two and the detector voltage by 100 V in comparison to $v = 1 \rightarrow 2$. Assuming that the detector gain and laser power corrections

are approximately the same for both vibrational excitations, the detection sensitivity thus needed to be increased by a factor of ~ 13 to obtain the same signal intensity as for the lower vibrational state of the $\nu = 1 \rightarrow 2$ excitation. If additionally the lower laser power used for the attempted detection of $\nu = 3$ is taken into account, the effective detection sensitivity for this state was ~ 21 times lower. What signal intensity would have been observable

with such a low detectivity? Since the gas mixture (i. e., the concentration of HCl), the nozzle settings and detection geometries were the same, the molecular fluxes and thus the oscilloscope signals should have been comparable. As can be seen from the last row in Tab. 3.8, the integrated signal of $\nu = 2$ had a maximum value of ~ 18 . If we assume the VEP to be the same for both excitation channels and take the lower detectivity into consideration, the $\nu = 3$ signal would have been slightly below 1. In Fig. 3.21 (b) the dotted blue line depicts a signal level one unit above the baseline. At least a regular pattern of rotational lines as shown in the simulation should have been distinguishable from the noise. Therefore, I conclude that the VEPs of the $\nu = 2 \rightarrow 3$ excitation can be as large as those of $\nu = 1 \rightarrow 2$ at most. That is, in contrast to changing the incident vibrational state from $\nu_i = 0$ to $\nu_i = 1$, there is no substantial increase in VEPs going to $\nu_i = 2$.¹¹

Table 3.8 Comparison of experimental conditions for $\nu = 1 \rightarrow 2$ and $\nu = 2 \rightarrow 3$ excitation on Au(111).

	$\nu = 1 \rightarrow 2$		$\nu = 2 \rightarrow 3$	
	$\nu = 1$	$\nu = 2$	$\nu = 2$	$\nu = 3$
T_s / K	923	923	313	923
$\langle \pi_\nu \rangle / \text{mJ}$	~ 0.9	~ 3.2	~ 1.8	~ 2.0
$U(\text{MCP}) / \text{V}$	1400	1950	1500	1950
signal / a. u.	~ 2	~ 18	~ 2	< 1

¹¹That is, assuming the detection probabilities decrease by the same amount going from $\nu = 2$ to $\nu = 3$ as they decreased going from $\nu = 1$ to $\nu = 2$ (see the detection sensitivities described at the very beginning of this section). Depending on the FRANCK-CONDON overlap of $X(3)$ and $E(0)$, this doesn't necessarily need to be the case. However, based on calculated FRANCK-CONDON factors in Ref. [81], which have comparable values for $E(0) \leftarrow X(2)$ and $E(0) \leftarrow X(3)$, it still seems to be a fair assumption.

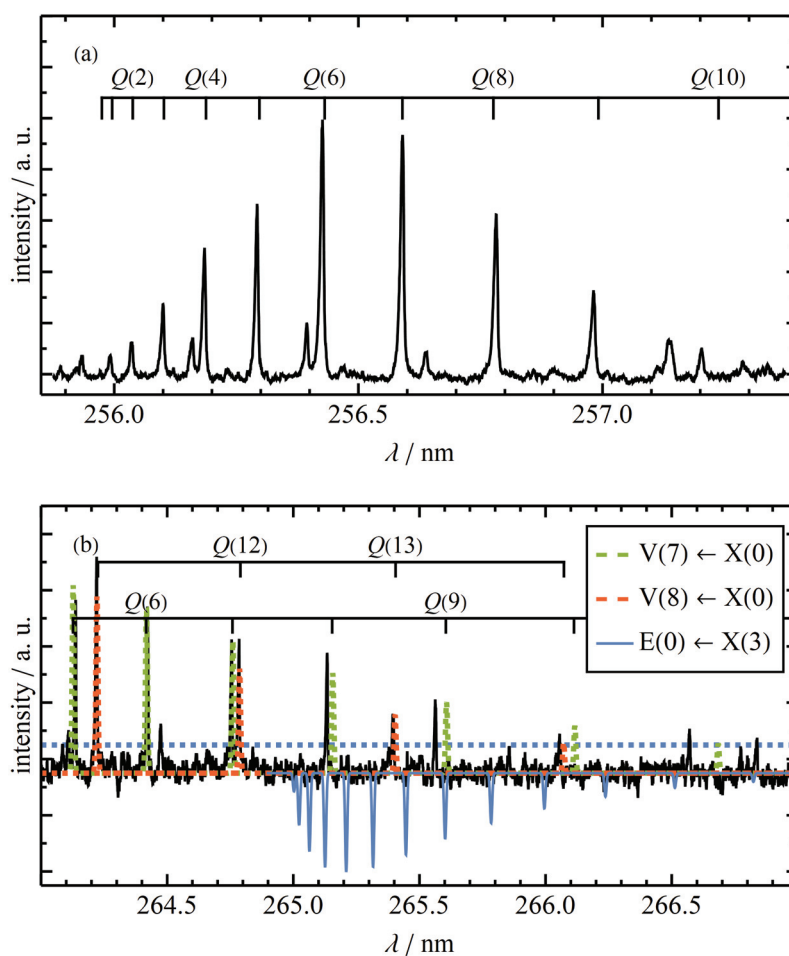


Figure 3.21 REMPI spectra of the scattered molecular beam in the wavelength ranges where transitions from (a) $v = 2$ and (b) $v = 3$ are expected. While the former can clearly be identified (see the indicated Q branch transitions), the latter are absent from the spectrum if compared to the simulation (solid blue lines). Instead, lines from $v = 0$ via $v = 7$ (dashed green lines) and $v = 8$ (dashed red lines) in the V state can be seen. The horizontal, dashed blue line indicates the approximate signal level expected if the VEP for $v = 2 \rightarrow 3$ was the same as for $v = 1 \rightarrow 2$. Incidence energy was $\langle E_i \rangle = 0.99$ eV and $T_s = 923$ K.

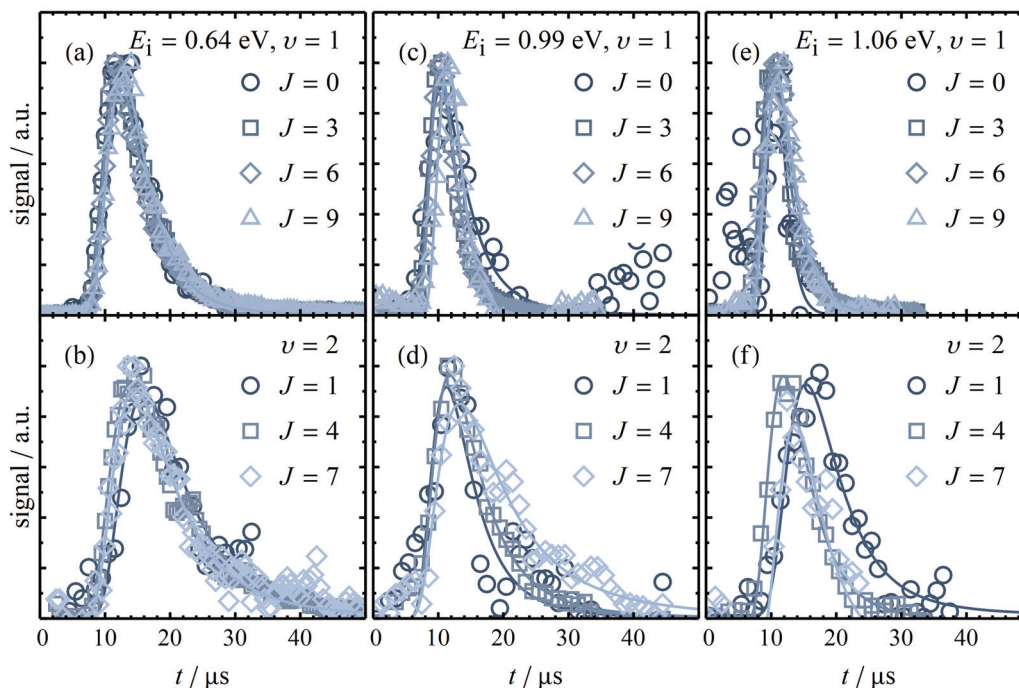


Figure 3.22 TOF distributions of HCl molecules scattered from Au(111) in different rovibrational states. For three different incidence energies distributions are shown for four and three rotational states for $\nu = 1$ (a,c,e) and $\nu = 2$ (b,d,f), respectively. Depicted by solid lines are fits to the data according to Eq. 2.3. There is no clear trend within the data for one E_i and ν state but with increasing E_i molecules tended to arrive earlier. Furthermore, the distributions for excited molecules in $\nu = 2$ peaked later and were generally broader in time (cf. Fig. 3.14).

3.2 Translational Inelasticity

Velocity distributions of HCl gas mixtures scattered from Au(111) were not only determined for density-to-flux corrections of the REMPI spectra (see previous sections) but also to investigate the transfer of molecular kinetic energy to or from the surface and the intramolecular coupling of vibrational to translational energy and translational to rotational energy (T-V and T-R coupling, respectively).

As shortly described in Sec. 3.1.2, using the IR laser system HCl molecules were excited to $\nu = 1, J = 1$ prior to the collision at a distance of approximately 1 mm from the surface. After scattering, molecules in $\nu = 1$ and $\nu = 2$ were detected in several J states *via* REMPI using the UV laser system. Scanning the temporal delay between the IR and UV pulses the molecules' density at the detection spot depending on their flight time was recorded. Examples of the thus obtained TOF spectra are shown in Fig. 3.22 for three incidence energies and several J states. Knowing the traveled distance l of the molecules, Eq. 2.3 which is a flowing three-dimensional MAXWELL-BOLTZMANN distribution $S(t)$ converted from velocity to time space (see Sec. A.2 for further details) could be fitted to the TOF data (solid

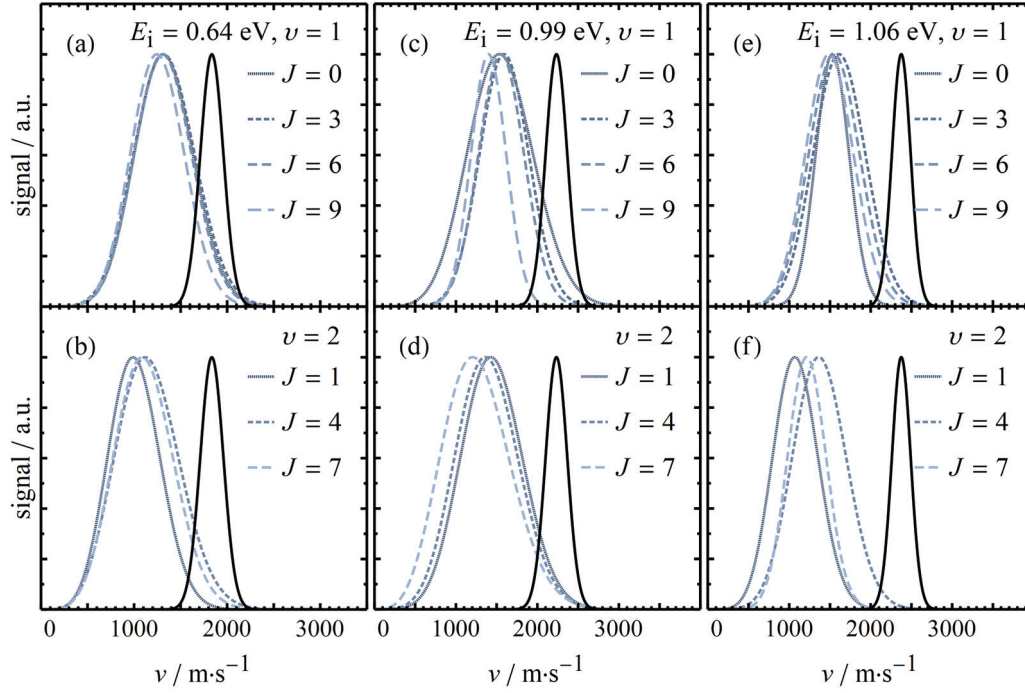


Figure 3.23 Velocity distributions of HCl molecules scattered from Au(111) at $T_s = 673$ K in different ro-vibrational states converted from the TOF data in Fig. 3.22. For three different incidence energies distributions are shown for four and three rotational states for $\nu = 1$ (a,c,e) and $\nu = 2$ (b,d,f), respectively. Depicted by the solid black lines are the velocity distributions of the corresponding incident beams. Neglecting the respective lowest J , distributions for molecules in higher rotational states were shifted to lower velocities. Similarly, molecules in $\nu = 2$ tended to be slower than in $\nu = 1$. As expected, the velocity distribution shifted to higher velocities when $\langle E_i \rangle$ was increased from 0.64 eV to 0.99 eV. However, there was no clear difference between the $\nu = 1$ scattered distributions of 0.99 eV and 1.06 eV although the incident distributions were distinguishable. In the case of $\nu = 2$, distributions at $E_i = 0.99$ eV were broader than at 1.06 eV but the peak velocities were approximately the same. Mind the different x -scales for different incidence energies.

lines in Fig. 3.22):

$$S(t) = A_t \left(\frac{l}{t}\right)^3 \exp \left[- \left(\frac{\left(\frac{l}{t}\right) - v_0}{\alpha} \right)^2 \right] \frac{1}{l}$$

With v_0 and α the distributions in velocity space according to Eq. 2.4 are easily obtained:

$$P(v) = A_v v^3 \exp \left[- \left(\frac{v - v_0}{\alpha} \right)^2 \right]$$

Fig. 3.23 shows these velocity distributions $P(v)$ for the same J states as in Fig. 3.22. For three different incident energies, blue lines depict the scattered distributions while the solid black lines denote those of the respective incident beams for comparison. As ex-

pected, distributions of scattered molecules were shifted to higher velocities increasing $\langle E_i \rangle$ from 0.64 eV to 0.99 eV. At least in $\nu = 1$, a further increase to 1.06 eV barely changed the distributions although there was a clear difference between the incident distributions. Scattered distributions in $\nu = 2$ were slightly broader for 0.99 eV but the peak velocities were approximately the same as for 1.06 eV. Within one gas mixture, distributions of molecules in higher rotational states were shifted to lower velocities (neglecting the respective lowest rotational states, see below). In a similar way, molecules in $\nu = 2$ in general exhibited distributions shifted to lower velocities compared to $\nu = 1$. An overview of the fitting parameters for the velocity ν_0 and width parameter α for all detected states is given in Tab. 3.9.

Table 3.9 Fitting parameters of velocity distributions obtained from fitting Eq. 2.3 to the data in Fig. 3.22. Velocity ν_0 and width parameter α are given in m/s.

J	0.64 eV				0.99 eV				1.06 eV			
	$\nu = 1$		$\nu = 2^*$		$\nu = 1$		$\nu = 2^*$		$\nu = 1$		$\nu = 2^*$	
	ν_0	α	ν_0	α	ν_0	α	ν_0	α	ν_0	α	ν_0	α
0	1040	488	-	-	1122	647	-	-	1442	298	-	-
1 [§]	1077	763	671	457	1401	701	1043	604	1245	954	808	417
2	1053	495	529	538	1360	495	914	593	1353	515	979	463
3	1014	515	533	548	1400	451	476	811	1394	483	916	525
4 [‡]	999	511	671	578	1335	481	923	630	1250	557	1054	528
5	983	514	628	519	1323	481	846	588	1294	476	858	564
6	1043	477	489	539	1387	415	729	647	1334	470	930	515
7	1004	486	698	530	1425	428	490	757	1330	483	951	430
8	1010	460	-	-	1335	470	-	-	1332	449	-	-
9	1002	449	-	-	1292	317	-	-	1290	445	-	-
10	919	479	-	-	1163	439	-	-	1062	706	-	-

* Since the signal was much lower for $\nu = 2$ in general, less J states could be detected.

[§] $\nu = 1, J = 1$ spectra contain contributions from the incident beam and thus values for the width α are higher than expected.

[‡] $\nu = 2, J = 4$ is spectrally overlapped with another transition and thus ν and α have to be taken with a pinch of salt.

From velocity distributions the corresponding kinetic energy distributions were easily

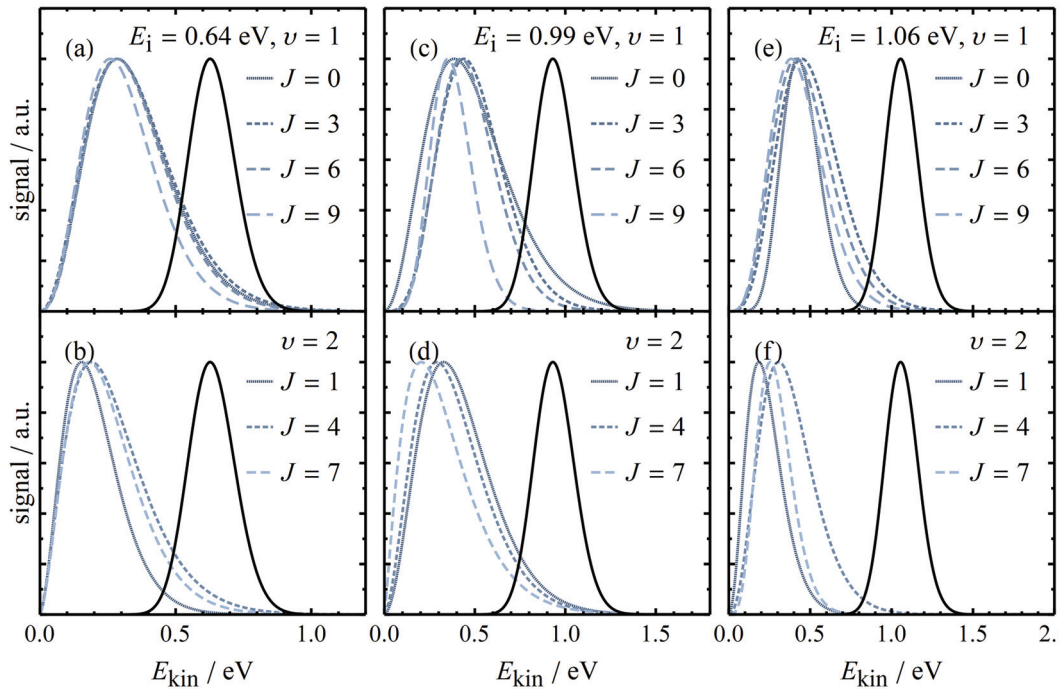


Figure 3.24 Kinetic energy distributions of HCl molecules scattered from Au(111) in different ro-vibrational states converted from the velocity distributions in Fig. 3.23. For three different incidence energies distributions are shown for four and three rotational states for $\nu = 1$ (a,c,e) and $\nu = 2$ (b,d,f), respectively. Depicted by the solid black lines are the kinetic energy distributions of the corresponding incident beams. Neglecting the respective lowest J , distributions for molecules in higher rotational states were shifted to lower energies. Similarly, molecules in $\nu = 2$ tended to have less energy than in $\nu = 1$. As expected, the distributions shifted to higher kinetic energies when $\langle E_i \rangle$ was increased from 0.64 eV to 0.99 eV. However, there was no clear difference between the $\nu = 1$ scattered distributions of 0.99 eV and 1.06 eV although the incident distributions were distinguishable. In the case of $\nu = 2$, distributions at $\langle E_i \rangle = 0.99 \text{ eV}$ were broader than at 1.06 eV but the peak energies were approximately the same. Mind the different x -scales for different incidence energies.

calculated following Eq. 2.5:

$$P(E) = A_E \frac{2E}{m^2} \exp \left[- \left(\frac{\left(\sqrt{\frac{2E}{m}} \right) - v_0}{\alpha} \right)^2 \right]$$

In Fig. 3.24 the resulting $P(E)$ are shown. Since the molecular mass m is the same in all cases, the observations here are the same as stated for the velocity distributions. Interestingly, there were no molecules that gained net energy in a way that would have given them more energy than the maximal available incident kinetic energy. To investigate the interactions between rotational and translational energy, in Fig. 3.25 the mean kinetic energy of scattered molecules is plotted against the rotational energy of their particular J state as open symbols. Additionally, two kind of lines are shown. Dashed lines exhibit a slope of -1

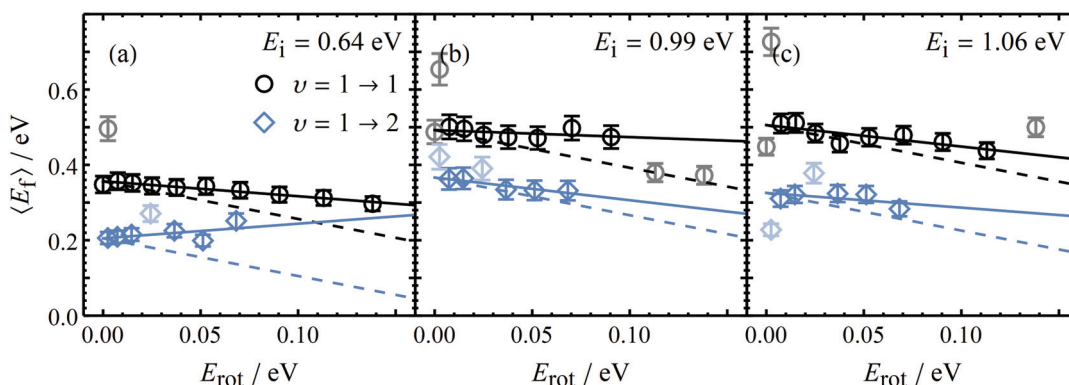


Figure 3.25 Mean final kinetic energy $\langle E_f \rangle$ in dependence on the final rotational energy E_{rot} of HCl molecules scattered from Au(111) at $T_s = 673$ K. For three different incidence energies data is shown for vibrationally elastic (open black symbols) and inelastic (open blue symbols) scattering. While the solid lines depict linear fits to these data, dashed lines exhibit a slope of -1 which corresponds to a complete conversion of kinetic to rotational energy. Pale symbols were excluded from the fits due to either poor signal-to-noise ratios (lowest and highest rotational energy), contributions from the incoming beam ($v = 1, J = 1$) or spectral overlap with other states ($v = 2, J = 4$). Except for the case of $\langle E_i \rangle = 0.64$ eV all fitted slopes m were $-1 < m < 0$.

which corresponds to a theoretically complete conversion of kinetic to rotational energy. Solid lines, on the other hand, denote linear fits according to Eq. 3.13 to the data:

$$\langle E_f \rangle = \langle E_f \rangle^{\text{el.}} + m \times E_{\text{rot}} \quad (3.13)$$

where $\langle E_f \rangle$ is the mean final kinetic energy, $\langle E_f \rangle^{\text{el.}}$ is the mean final kinetic energy in the rotationally elastic case, where no rotational de-/excitation had occurred, and m is the slope, i. e. a measure of the conversion efficiency of translational to rotational energy. The fitted values for m given in Tab. 4.7 were generally in the range of $-1 < m$ (except for $\langle E_i \rangle = 0.64$ eV, $v = 1 \rightarrow 2$),

which means scattered molecules must have gained final rotational energy from the surface during scattering. It must be noted, though, that the errors in m were rather large in most cases which impedes a more detailed analysis. However, from the values for $\langle E_f \rangle^{\text{el.}}$, which were assigned a much smaller error, it can clearly be seen that molecules that had experienced vibrational excitation during scattering exhibited a lower final kinetic energy.

Table 3.10 Resulting parameters of fitting Eq. 3.13 to the data in Fig. 3.25. E_i is the incidence translational energy and T_s the surface temperature. $\langle E_f \rangle^{\text{el.}}$ is the fitted translational energy in the case of rotationally elastic scattering and m is the slope of the fit.

$\langle E_i \rangle$ in eV	$v \rightarrow v'$	$\langle E_f \rangle^{\text{el.}}$ in eV	m
0.64	$1 \rightarrow 1$	0.36 ± 0.01	-0.40 ± 0.03
	$1 \rightarrow 2$	0.21 ± 0.01	$+0.39 \pm 0.29$
0.99	$1 \rightarrow 1$	0.49 ± 0.01	-0.19 ± 0.17
	$1 \rightarrow 2$	0.37 ± 0.01	-0.60 ± 0.16
1.06	$1 \rightarrow 1$	0.51 ± 0.01	-0.57 ± 0.15
	$1 \rightarrow 2$	0.33 ± 0.01	-0.39 ± 0.32

3.3 Dissociation

As pointed out in the introduction, shortly before the start of these studies a series of theoretical papers was published by Zhang and co-workers describing the determination of a PES for the dissociation of HCl and DCl molecules on Au(111) using PW91-DFT plus neural networks, as well as the actual quantum dynamics calculations on these reactions [58–60]. In these computational studies, relatively large initial dissociation probabilities S_0 were reported for incidence kinetic energies higher than the minimum energy path barrier of 0.64 eV calculated therein. However, in previous work on scattering HCl from Au(111) no indication of dissociating molecules had been provided [30, 43]. To shed light on these issues and test the applicability of adiabatic calculations in the case of a molecule/surface system with reported nonadiabatic interactions, experiments on the dissociation of HCl on Au(111) were carried out.

Since our apparatus had not been used for these kind of studies before, a method for determining the initial dissociation probabilities had to be found first. One famous approach was developed by King and Wells [85]. In principle, it relies on the different sticking properties of the studied molecule on the target surface and a non-reactive flag that temporarily blocks the molecular beam. When the molecules' partial pressure is monitored while the flag is moved in and out of the way of the molecular beam traveling towards the surface, its change can give information about S_0 . However, after first proof-of-principle tests this method had to be discarded because the observed pressure rise in the surface chamber with an opened slide valve seemed to be independent of the Au(111) surface being in or out of the molecular beam path. This could be due to dissociation probabilities being so small that their effect vanished in the noise of the overall signal or to HCl molecules sticking around on other parts of the chamber so that they did not get efficiently pumped. A second method that had regularly been used is to measure the atomic concentration of a certain element after a defined exposure to the molecular beam *via* AUGER spectroscopy. Beck and co-workers applied this methodology to determine the sticking of CH₄ on Ni(100) [86] and D₂O on Ni(111) [87], for example. Since it is not a dynamic measurement like the King and Wells experiment, it is crucial that molecules are strongly adsorbed or chemisorbed, i. e., they do not desorb before they can get detected with the AUGER spectrometer. This implies that a potential surface temperature as well as measurement time dependence of the coverage needs to be taken into consideration.

The same would also be applicable to approaches based on temperature programmed desorption (TPD), where the relative coverage on the surface is determined by integrating thermal desorption spectra in dependence on the exposure. However, accurate TPD experiments usually require mass spectrometers with specific geometries to maximize the detection sensitivity and minimize background signals (cf. Ref. [88]). Thus, as mentioned in the introduction (Sec. 2.3.4) AUGER spectroscopy was the method we chose to examine the dissociative adsorption of HCl molecules on Au(111).

3.3.1 Initial Experiments

As implied in the previous sections, diluting approximately 1 - 8 % HCl in H_2 resulted in molecular beams with incident translational energies in the range of 0.64 - 1.06 eV that offered good signal strengths for scattering experiments (it needs to be mentioned, though, that for mixtures exceeding $\sim 5\%$ of HCl clustering was observed in the TOF mass spectrum). According to the first theoretical publications available at the time of these experiments, for incidence energies between 0.8 and 1.0 eV the dissociation probability should rise from ~ 0.10 to ~ 0.25 . Assuming the reaction products Cl and H to be stable on the surface and the incident flux of molecules to be $\sim 0.5\%$ of a monolayer (ML) per pulse (i. e. 30 ML/min), chlorine should at least be detectable on the surface after several minutes of dosing. Thus, before systematically studying the dissociation probabilities, I examined the general applicability of AUGER spectroscopy for HCl/Au(111) and potential experimental conditions.

In Fig. 3.26, AUGER spectrum (b) was recorded after exposing the Au(111) surface to a molecular beam of HCl in H_2 with an incidence energy of $\langle E_i \rangle \approx 0.8$ eV for 30 min (≈ 900 ML). Surprisingly, in comparison with spectrum (a), which was recorded on the just cleaned surface, there was no change in the intensity of the chlorine peak around $E_{kin} \approx 180$ eV marked by the dashed red vertical lines. Apart from technical errors several reasons seemed to be plausible: First, E_i dependent values for S_0 could be much lower than predicted so that even a dosage of ~ 900 ML resulted in coverage too low to be detected. Since vibrational energy was predicted to enhance the reactivity even stronger than translational energy [58], parts of the incident molecular beam were excited to $v = 1$ ($\Delta E_{vib} = +0.36$ eV, spectrum c) and even $v = 2$ ($\Delta E_{vib} = +0.70$ eV, spectrum d). In these experiments, the incidence energies, dosing times t_D and dosage D were

$\langle E_i \rangle \approx 0.8$ eV / $t_D = 80$ min / $D = 2400$ ML and $\langle E_i \rangle = 0.99$ eV / $t_D = 180$ min / $D = 5400$ ML, re-

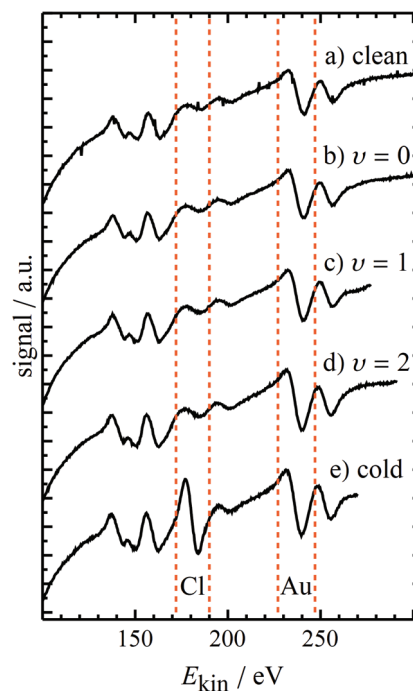


Figure 3.26 Stacked representative AUGER spectra of the Au(111) surface after different dosing conditions. From top to bottom: a) The freshly cleaned surface. b) The surface had been exposed to a molecular beam of ground state HCl with $\langle E_i \rangle \approx 0.8$ eV for 30 min. c) Exposure to the same gas mixture for 80 min. This time, a small portion of the molecules had been excited to $v = 1$. d) Exposure to a molecular beam with $\langle E_i \rangle \approx 0.99$ eV for 180 min, where a small portion had been excited to $v = 2$. e) Exposure to the same gas mixture for 30 min. Here, molecules were in the vibrational ground state and the surface was cooled to ~ 83 K while it was kept at room temperature during all other dosing experiments. The spectral peaks of Cl and Au that were used in the analysis are marked by dashed red lines. Except for spectrum e) there was no visible change in the chlorine peak.

spectively, $\sim 0.5\%$ of which were vibrationally excited according to hole-burning experiments. Even though the reaction probability in the latter case had been predicted to be $S_0 = 0.6$, there still was no change in the Cl signal. To check whether the AUGER detection worked in general, the surface was also dosed with the same gas mixture but without vibrational excitation at a temperature of $\sim 83\text{ K}$ to at least physically adsorb HCl molecules. As can be seen from Fig. 3.26 spectrum e), the cold surface indeed exhibited an obvious increase in the chlorine peak intensity after dosing for 30 min ($D \approx 900\text{ ML}$). Thus, HCl must have been physisorbed to the surface most probably without dissociating.

Having confirmed that the general detection method worked, I needed to test whether predicted values for S_0 might be too low. For this I had to increase the incidence translational energy of the HCl molecules beyond what could be done by seeding in H_2 .

3.3.2 Increasing the Incidence Energy

As mentioned in the introduction (Sec. 2.1), I used a heated nozzle extension to increase the energy of the incident molecules. A SiC tube with a length of $\sim 13\text{ mm}$ was mounted on the exit of the home-built, solenoid-driven valve. Through two small clamps carefully attached to both ends of the SiC a current could be applied while the temperature was monitored *via* a K -type thermocouple attached to the clamp on the tube's exit. At the same time, the nozzle housing was water-cooled so that its temperature remained below 70°C . Being resistively heated by the flow of electrons, the semiconductor tube gained thermal energy that was transferred to the molecules in the molecular beam. With this setup a nozzle tip temperature of $\sim 1000\text{ K}$ could be reached.

Initially, the hot nozzle was characterized by measuring the velocity and ro-vibrational distributions of the resulting molecular beams at different temperatures of the SiC tube. Fig. 3.27 shows the relative population in vibrational state $v = 1$ in the incident beam that was determined according to the procedure for calculating the VEPs described in Sec. 3.1. For comparison, the red dashed lines depict the thermal population expectation following Eq. 3.14:

$$\frac{N_1}{\sum_i N_{v_i}} = \frac{\exp[-E_1 / (k_B \times T)]}{\sum_i \exp[-E_{v_i} / (k_B \times T)]} \quad (3.14)$$

where E_{v_i} is the vibrational energy according to

$$E_{v_i} = \omega_e(v_i + 0.5) - \omega_e x_e(v_i + 0.5)^2 + \omega_e y_e(v_i + 0.5)^3. \quad (3.15)$$

Here, the values for $\omega_e = 2990.946\text{ cm}^{-1}$, $\omega_e x_e = 52.8186\text{ cm}^{-1}$ and $\omega_e y_e = 0.2243\text{ cm}^{-1}$ were taken from the NIST data base [89]. As can be seen from Fig. 3.27 the measured population increased faster with nozzle temperature T_N than Eq. 3.14. Additionally, for moderate values of T_N the data was below the expectation. On the one hand, the latter might be explained

by worse signal-to-noise ratios for lower populations that could be underestimated by the shown error bars. In general, it was more difficult to reliably determine small populations in $\nu = 1$. On the other hand, there could have been a certain degree of vibrational cooling in the expansion coming from the SiC tube leading to populations below the thermal expectation (even though unlikely for diatomic molecules [66, 67], it has been observed for small organic molecules [90]). At temperatures below $T_N \approx 550\text{K}$ no signal from HCl molecules in $\nu = 1$ could be detected. Since it is rather unlikely that there is vibrational heating in a supersonic expansion, vibrational populations above the thermal expectation led to the conclusion that the temperature read out from the thermocouple might not have been the actual temperature at the tip of the SiC tube. According to the STEFAN-BOLTZMANN law the radiant emittance of a black body is proportional to T^4 . Since the thermocouple was attached to the end of a small clamp on the SiC tube, its effective temperature might have been lower than the tip's. Thus, the measured population was fitted with a modified thermal expectation (dashed black line in Fig. 3.27) where the T in Eq. 3.14 was replaced by

$$T_{\text{true}} = T_{\text{read}} + A_T \times (T_{\text{read}} - 298\text{K})^n \quad (3.16)$$

That is, at nozzle tip temperatures above room temperature, where the tip was a net emitter of radiance, a certain proportion A_T of the excess temperature $T_{\text{read}} - 298\text{K}$ needed to be added to obtain the true temperature. If the exponent was chosen to be $n = 4$ as a tribute to the STEFAN-BOLTZMANN law, the resulting $A_T = 8.5(9) \times 10^{-10}\text{K}^{-3}$. However, other combinations of values for n around 4 and resulting values for A_T did not make a significant difference in the limited temperature range of interest. Since vibrational degrees of freedom are usually not effectively cooled in supersonic expansions for diatomic molecules with high vibrational frequencies, this modified temperature was used to obtain the true tip temperature from the measured one.

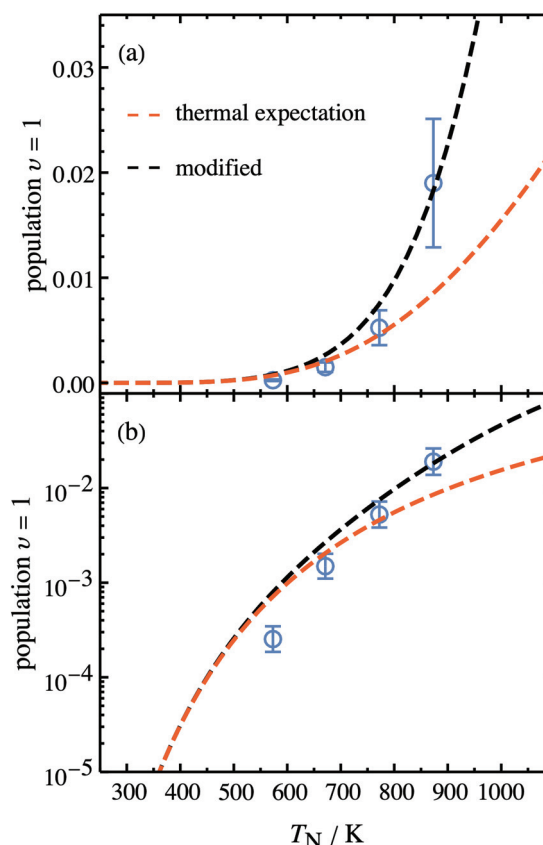


Figure 3.27 Population in vibrational state $\nu = 1$ in the incident molecular beam at different nozzle temperatures. Depicted by open symbols are populations determined as mentioned in Sec. 3.1 in a linear (a) and a logarithmic plot (b). While the red dashed line shows the theoretical thermal expectation, the black dashed line denotes a fit applying a modified expectation function (see text). At higher temperatures the theoretically predicted populations are too low but the modified function fits well.

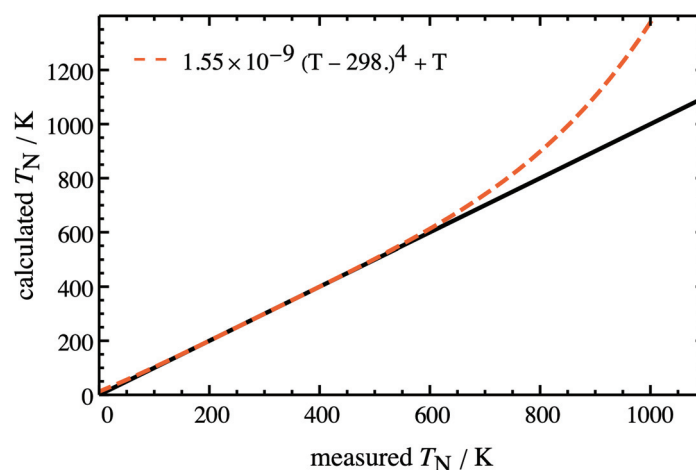


Figure 3.28 Calibration of the measured nozzle tip temperature T_N with the vibrational state distribution shown in Fig. 3.27. While the solid black line denotes the case where $T_{\text{true}} = T_{\text{read}}$, the dashed red line denotes the modified temperature derived from the vibrational state distribution. It starts to significantly deviate from the measured temperature at $T_{\text{read}} \gtrsim 600$ K.

The relationship between these two is already given in Eq. 3.16 and illustrated in Fig. 3.28. Beneath vibrational populations, TOF distributions and the resulting velocity as well as kinetic energy distributions were also determined for different nozzle temperatures. In Fig. 3.29, examples for T_N in the range of 423 - 1267 K are shown (T_N was calculated according to Eq. 3.16). As expected, with increasing T_N the flight time between the IR tag and the UV detection decreased (panel a). From these flight times the velocity distributions shown in panel b and the resulting energy distributions shown in panel c were calculated according to Sec. 2.3.3. In both cases, the distributions' maxima as well as the relative widths increased with nozzle temperature.

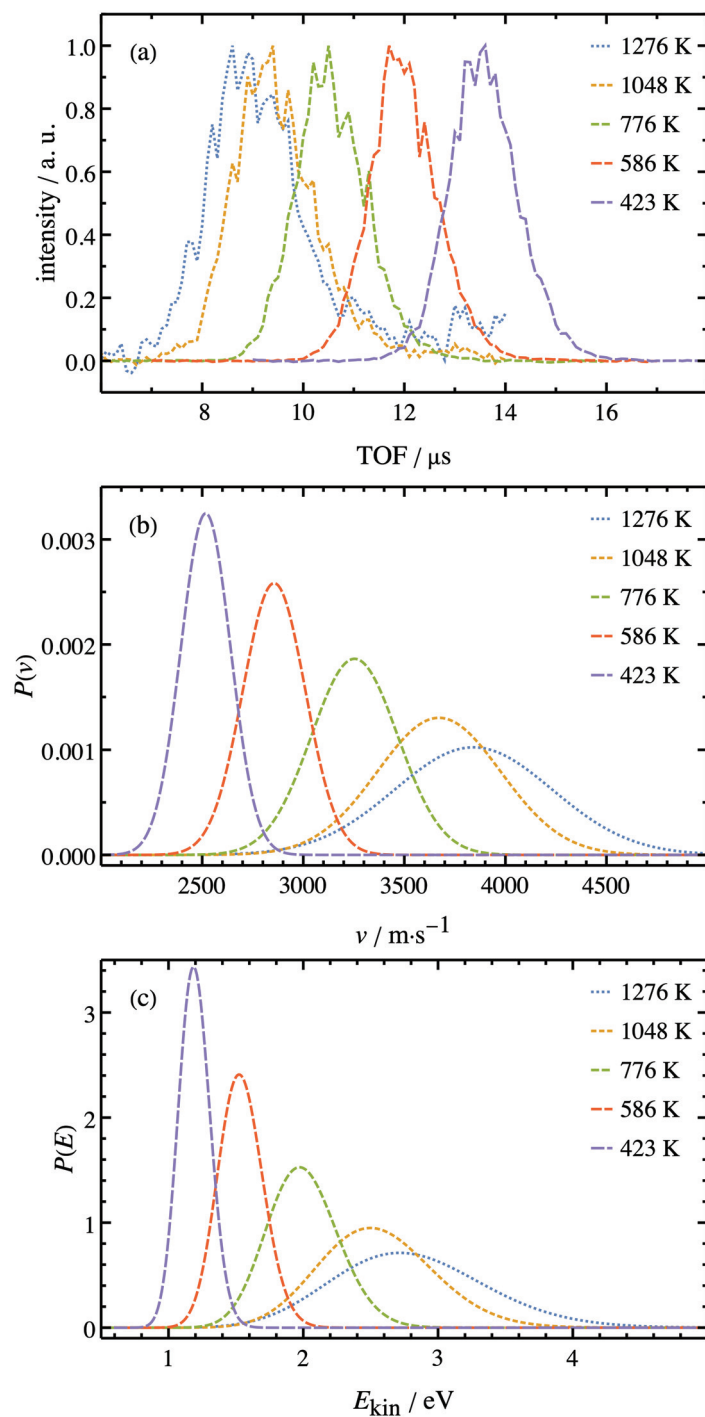


Figure 3.29 Characterization of the incident molecular beam coming from the heated nozzle. In panel (a), the TOF distributions for nozzle temperatures in the range of 423–1276 K are depicted by differently dashed lines. From the raw data it can easily be seen that the distributions shift to shorter flight times with increasing nozzle temperature. Since the flight distance was the same in all cases, the most probable velocity of the respective distributions shifted to higher values while the relative width of the distributions increased (panel b). Of course, the same was true for the kinetic energy distributions in panel (c).

3.3.3 Determination of Surface Coverage

General Procedure

With mean incidence energies reaching ~ 2.6 eV for $T_N = 600$ K, chlorine was observed in the AUGER spectra after dosing the surface with the molecular beam. In Fig. 3.30, the spectral peak at 181 eV assigned to chlorine on the surface can be seen to increase with increasing dose. Before going into details about the calculation of the actual coverage, I will shortly describe the general procedure of dosing the surface with the molecular beam and obtaining the AUGER spectra.

First, the surface was cooled down to a temperature of $T_s = 173$ K/ -100°C by filling the sample holder with liquid nitrogen and at the same time applying a certain current through the crystal to maintain a steady temperature. With the slide valve that prevented the molecular beam from entering the surface chamber being closed, the cold crystal was then positioned so that the molecular beam would approximately hit the middle of the surface. For a series of measurements the surface was tilted by an angle of $32^\circ < \theta < 50^\circ$ to reduce the normal component of the mean incidence energy. After the nozzle tip had also obtained the temperature that corresponded to the desired mean incidence energy (see. Fig. 3.29), the slide valve was opened for a certain dosing time so that the molecular beam hit the surface. During exposure to HCl the partial pressure rise of H_2 was monitored *via* the residual gas analyzer (RGA) to obtain a measure for the dose.¹² Upon closing the slide valve again, the surface was quickly transferred to the AUGER spectrometer. Here, two so-called line scans were carried out: First, at several vertical positions around the surface center AUGER spectra were recorded. At the vertical position with the highest peak intensity for Cl, a more detailed line scan at ~ 9 horizontal positions

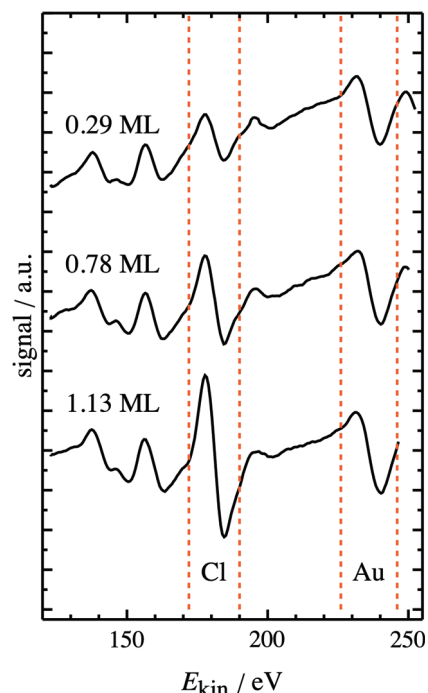


Figure 3.30 Stacked representative AUGER spectra of the Au(111) surface after different dosings at $\langle E_i \rangle = 2.56$ eV measured at the surface center. From top to bottom, the dose applied to the surface *via* the incident molecular beam increases from 0.29 - 1.13 ML. The spectral peaks of Cl and Au that were used in the analysis are marked by dashed red lines. As can be seen from the Cl peak, the amount of Cl on the surface increases with dose. For comparison with a clean Au(111) surface see Figs. 2.11 and 3.26. See the text for how the spectra were analyzed to obtain the actual Cl coverage.

¹²HCl could not be monitored directly because its signal's response to opening and closing the slide valve was too slow. Probably HCl molecules adsorbed to the walls of the chamber and could not get efficiently pumped. See the following sections for further information.

was carried out. In combination with the dose applied to the surface, the evaluation of thus obtained AUGER spectra revealed the initial dissociation probabilities of HCl on the Au(111) surface.

Determining the Dose

As mentioned above, the dose was monitored *via* the pressure rise of H_2 in the surface chamber. Fig. 3.31 shows an example where the pressure rose to $\sim 2.5 \times 10^{-9}$ Torr during dosing (see Fig. 3.30 for the resulting AUGER spectrum). From this pressure rise the actual dose in monolayer (ML) needed to be determined. First, the total number of H_2 molecules entering the surface chamber $N_{\text{inc.}}(H_2)$ was calculated according to Eq. 3.17,

$$N_{\text{inc.}}(H_2) = \int p_{H_2}(t) dt \times \frac{r_{H_2}}{k_B \times T} \quad (3.17)$$

where $\int p_{H_2}(t) dt$ is the time integrated pressure rise as shown in Fig. 3.31, r_{H_2} is the pumping speed in the surface chamber for H_2 , k_B is the BOLTZMANN constant, and $T = 300\text{K}$ the temperature inside the surface chamber. Since there was no specific H_2 pumping speed supplied by the manufacturer of the surface chamber TMP, it was estimated based on its N_2 pumping speed ($r_{N_2} = 345\text{L/s}$) and rates for both molecules for a comparable pump to be $r_{H_2} = 243\text{L/s}$. Second, the area upon which this number of molecules was impinging needed to be determined. For simplification, the incident beam was approximated by a cylinder with a "flat top" intensity profile, i. e. the distribution of molecules was assumed to be uniform throughout its cross section. The diameter of this cylinder was determined similar to the measurements of angular distributions of scattered molecules as shown in Sec. A.3. Moving the UV laser set to a fixed ro-vibrational REMPI transition vertically through the incident beam, its density profile was obtained essentially assuming an infinitesimal small laser beam (i. e., no deconvolution was carried out in this case). In Fig. 3.32, the measured density distribution along the (vertical) z axis is depicted by black open symbols connected by a solid black line as a guide to the eye. Additionally shown as a solid blue line is the 2D representation of a cylinder, the diameter of which was calculated by assuming the cylinder's integral and height to be the same as the actual density distribution's integral and maximum.

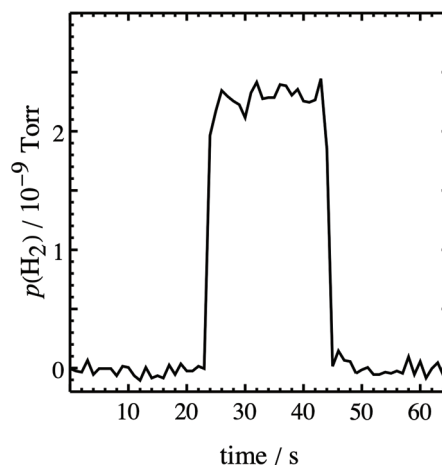


Figure 3.31 Example of the H_2 pressure rise during dosing the Au(111) surface with the molecular beam. Opening the slide valve resulted in a pressure rise of $\sim 2.5 \times 10^{-9}$ Torr (pressure values are baseline corrected). The overall dose corresponded to 0.29 ML, cf. Fig. 3.30.

The thus obtained value of $d = 2.2$ mm was used for calculating the area which was hit by the incident molecular beam according to $A = \pi (d/2)^2$. Since the partial pressure of H_2 was measured, the dose of H_2 needed to be converted to the HCl dose. This was done by using the known ratio of concentrations $c(H_2)$ and $c(HCl)$ that were given by the mixing ratio of the two gases. However, there were two more correction factors that needed to be applied to the H_2 dose. First, a comparison of the ion gauge pressure corrected for the H_2 sensitivity factor supplied by the manufacturer and the pressure reading from the RGA at different leak-in rates showed that the values given by the latter were a factor of $f_{IG} \approx 1.8$ higher. That is, the actual pressure rise in the dosing experiments and thus the dose could have been overestimated by the same. However, since the ion gauge itself was not manually calibrated, it was difficult to judge this correction's accuracy.

However, there was a second uncertainty associated with the determination of the actual HCl dose. As shown for example by Scoles [66], in binary gas mixtures a separation of the components in the molecular beam can occur. Due to their smaller perpendicular velocities heavier particles will concentrate along the center line of the beam when passing a skimmer. Additional separation can be caused by different cross sections for scattering with background gas molecules, for example. Thus, in a series of experiments the enrichment factors from the prepared gas mixture to surface chamber HCl concentration were determined. As stated above, it was not possible to measure the partial pressure rise of HCl directly. Since a particle's mass is the important parameter for its perpendicular velocity, Ar ($M = 40$ amu) was chosen as a replacement for HCl ($M = 36$ amu) since its partial pressure as measured by the RGA could easily be tracked. The enrichment factors were determined the following way: First, a gas mixture of Ar in H_2 was prepared in the same way it was done for HCl. This gas mixture was then introduced into the surface chamber in two different ways: It was either expanded from the pulsed nozzle in the source chamber or directly leaked into the surface chamber *via* the leak valve while the partial pressures for Ar and H_2 were monitored with the RGA. In Fig. 3.33, the partial pressure rise in the surface chamber is shown for both operation modes. Each individual "block" corresponds to a certain repetition rate in the range of 10 – 50 Hz in the case of the molecular beam or a certain leak rate in the case

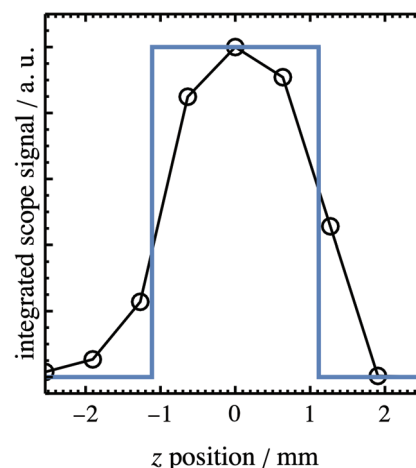


Figure 3.32 Density distribution measured vertically across the incident molecular beam. While the open black symbols denote the integrated scope signal at the corresponding vertical z position relative the the molecular beam's center, the solid blue line is the 2D representation of a cylinder with the same integral and height as the measured distribution. Its diameter which was used for calculating the dose on the surface was determined to be $d = 2.2$ mm. The solid black line is a guide to the eye.

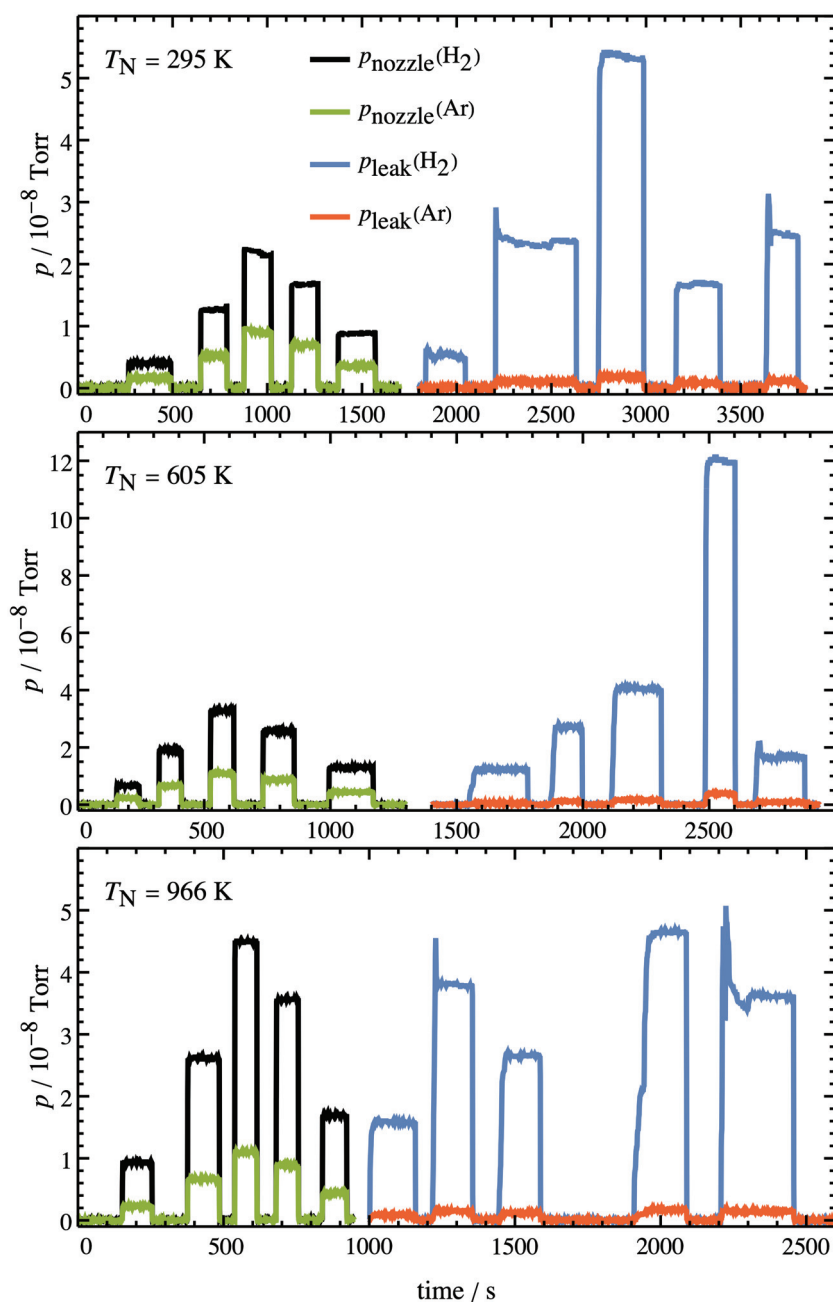


Figure 3.33 Experimental determination of heavier species enrichment at the centerline of the molecular beam. Depicted by solid lines are the pressure *vs* time curves recorded by the RGA in the surface chamber. Shown in black and green are the partial pressures of H₂ and Ar, respectively, obtained with the molecular beam entering the surface chamber. For every pressure rise, the pulsed valve was operated at a nozzle tip temperature of 295 - 966 K and a repetition rate in the range of 10 – 50 Hz leading to different maximal pressures. In blue and red the partial pressures of H₂ and Ar introducing the gas mixture through the leak valve at different leak rates are shown. It is immediately obvious that the partial pressure ratio $p(\text{Ar})/p(\text{H}_2)$ was significantly higher in the molecular beam than in the leaked-in gas mixture. Additionally, it can be seen to decrease with increasing nozzle temperature T_N .

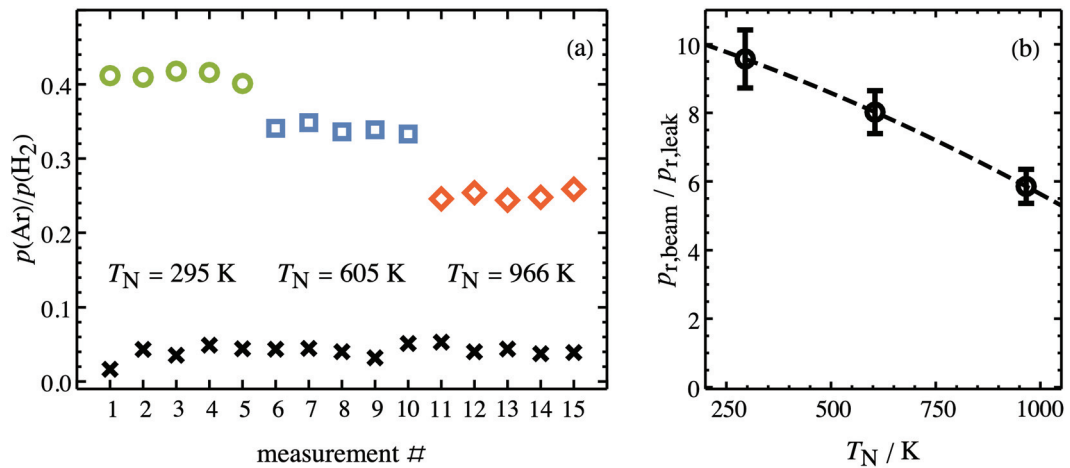


Figure 3.34 Panel (a): pressure ratios $p(\text{Ar})/p(\text{H}_2)$ at different nozzle temperatures. While the pressure ratios in the molecular beam are depicted by open symbols, the ratios measured from the leak valve are depicted by black crosses. In contrast to the latter case, where the ratio showed little deviation over 15 measurements, the pressure ratio from the heated nozzle decreased with increasing nozzle temperature. As can be seen from the leak valve data, the pressure ratio there nicely reproduced the mixing ratio of the gas mixture: $\langle p(\text{Ar})/p(\text{H}_2) \rangle = 0.043(2)$. In panel (b), the enrichment factor in the molecular beam depending on the nozzle temperature is shown. Depicted by open black symbols is the ratio of the pressure ratios in the molecular beam $p_{r,\text{beam}}$ and the ones coming from the leak valve $p_{r,\text{leak}}$. That is, $f_e = p_{r,\text{beam}}/p_{r,\text{leak}}$ is the enrichment factor of HCl molecules in the molecular beam. It decreased from a nearly tenfold enrichment at room temperature to $f_e = 5.9(5)$ at $T_N = 966 \text{ K}$. The dashed black line is a polynomial fit to the data that was used to calculate f_e at intermediate temperatures.

of the leak valve. Without further analysis it can be seen that the partial pressure ratio $p(\text{Ar})/p(\text{H}_2)$ was significantly higher in the molecular beam than in the leaked-in gas mixture. Further, this ratio decreased with increasing nozzle temperature T_N . From the average pressure rise in the Ar and H_2 channel the pressure ratios $p(\text{Ar})/p(\text{H}_2)$ shown in Fig. 3.34 (a) coming from the leak valve (black crosses) and from the pulsed valve at different nozzle temperatures were calculated. While the ratio in the leaked-in gas mixture nicely reproduced the prepared mixture, $\langle p(\text{Ar})/p(\text{H}_2) \rangle = 0.043(2)$, the ratios in the molecular beam were several times higher. This becomes obvious when the ratio of the pressure ratios is constructed as in panel (b). Here, the enrichment factor $f_e = p_{r,\text{beam}}/p_{r,\text{leak}}$ can be seen to decrease from $f_e = 9.6(9)$ at a room temperature nozzle to $f_e = 5.9(5)$ at $T_N = 966 \text{ K}$. Thus, calculating f_e confirms the significant enrichment of heavier particles along the centerline of the molecular beam which cannot be neglected.

Finally, the overall incoming dose was calculated according to Eq. 3.18:

$$\phi_{\text{HCl}} = \frac{N_{\text{inc.}}(\text{H}_2)}{A_{\text{MB}}} \times \frac{c(\text{HCl})}{c(\text{H}_2)} \times \frac{f_e}{f_{\text{IG}}} \times \frac{1}{N_{\text{ML}}} \quad (3.18)$$

Here, $N_{\text{inc.}}(\text{H}_2)$ is the number of incident H_2 molecules as calculated in Eq. 3.17, A_{MB} the

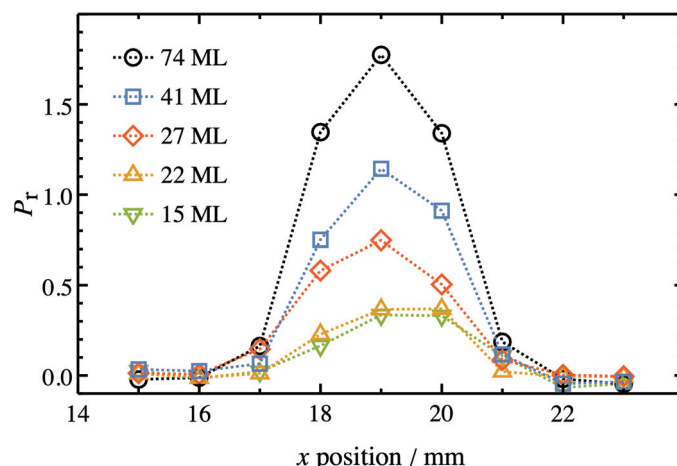


Figure 3.35 Representative AUGER line scans. Shown is the APPH ratio P_T depending on the surface position in x direction (manipulator moving perpendicular to the AUGER electron beam) for five different doses in the range of 15 - 74 ML (calculated according to Eq. 3.18) at an incidence energy of 1.55 eV. As expected, P_T increased for higher applied doses. The values of the x position correspond to the reading of the micrometer screw moving the manipulator that contained the surface.

cross-sectional area of the incident molecular beam, $c(\text{HCl})$ and $c(\text{H}_2)$ are the concentrations in the prepared gas mixture, f_e is the enrichment factor of HCl, f_{IG} the pressure correction from the ion gauge compared to the RGA, and N_{ML} is the number of Cl atoms per monolayer on the Au(111) surface. The latter was assumed to be equal to the density of Au atoms on the un-reconstructed (111) surface which is $1.39 \times 10^{15} \text{ cm}^{-2}$ according to my own calculations and Ref. [91].

Determining the Coverage

Now that the dose applied to the Au(111) surface was known, the corresponding coverage needed to be determined. Since there was no absolute calibration of the AUGER signals, the most important information from the recorded spectra was the AUGER peak-to-peak height (APPH). That is, for both the Cl and the Au peak of the differential AUGER spectra the maxima and minima were determined and their signal differences (i. e. the peak-to-peak heights) were used to obtain a ratio P_T independent of the absolute signal strength. After dosing the surface, P_T was measured for ~ 9 horizontal positions in a line scan once the most intense vertical AUGER signal (i. e., the vertical center position of the Cl coverage) had been found. As can be seen from Fig. 3.35, where representative line scans for an incident energy of 1.55 eV and different doses are shown, P_T increased with the applied dose as expected. However, the observed distribution of Cl atoms on the surface as indicated by P_T was a convolution of the incident electron beam from the AUGER spectrometer and the actual Cl density distribution.

In a first step, the width of the electron beam was determined by measuring the surface current in dependence on the x position on the surface. That way, a surface profile was recorded that could be compared to the known geometry of the Au(111) crystal. Assuming the electron beam to exhibit a GAUSSIAN intensity distribution, a full width at half maximum (FWHM) of 1.1 mm gave the best fit when the convolution of the electron beam GAUSSIAN and the actual surface profile was compared to the profile derived from the surface current. Then, the line scans were fitted with a convolution of the electron beam as determined above and a cylindrical function. Although the fitting was carried out in two dimensions, both individual functions were treated and convoluted in three dimensions to account for the Cl coverage on the surface, not only on the line that had been scanned.¹³ The resulting cylindrical function represented an averaged Cl coverage on the surface, in accordance with the initial assumption of an "flat top" incident beam. Its diameter, however, was generally larger than the 2.2 mm of the incident beam, an observation for which I think diffusion of Cl atoms on the surface might be one reason. Yet, by calculating the cylinders three-dimensional integral the height of a cylinder with the diameter of 2.2 mm could easily be calculated. This height now represented the artificially homogenized Cl coverage on the surface (or rather the P_T that can be converted to coverage) caused by an incident beam with a diameter of 2.2 mm.

For those experiments, where the surface was tilted to decrease the normal component of the incidence energy, the procedure to determine the average coverage was slightly modified. Instead of using a cylindrical function convoluted with the electron beam to fit the line scans an elliptical function was used. Here, the ellipse's semi-minor axis b corresponded to the radius of the cylindrical function while its semi-major axis a was elongated by the cosine of the tilting angle θ : $a = b / \cos(\theta)$. That way, I was able to account for the "broadened" line scan due to the tilted surface.¹⁴ The further analysis followed the procedure for the un-tilted surface.

Since the APPH ratio P_T is a measure of but not equal to the surface coverage, it needed to be converted for calculating dissociation probabilities. Recapitulating Sec. 2.3.4, the atomic concentration C_x of an element x present on the surface can be calculated as given in Eq. 2.6:

$$C_x = \frac{I_x}{S_x d_x} \bigg/ \sum_i \frac{I_i}{S_i d_i}$$

where I_x is the APPH of a peak as mentioned above and S_x the relative elemental sensitivity factor. Since the instrument sensitivities d_x canceled each other out, Eq. 2.6 could be

¹³ Assuming the Cl coverage to exhibit cylindrical symmetry around the surface center.

¹⁴ Since the overall coverage was taken into account and not just P_T at one particular spot, there was not need to correct for the reduced exposure to HCl molecules at a certain point on the surface due to the tilt.

re-written for the specific case of Cl on Au as

$$C_{\text{Cl}} = \frac{I_{\text{Cl}}}{S_{\text{Cl}}} \bigg/ \left(\frac{I_{\text{Cl}}}{S_{\text{Cl}}} + \frac{I_{\text{Au}}}{S_{\text{Au}}} \right) = \frac{P_{\text{r}} \times S_{\text{Au}}}{P_{\text{r}} \times S_{\text{Au}} + S_{\text{Cl}}} \quad (3.19)$$

where P_{r} was the aforementioned APPH ratio of the Cl peak at 181 eV and the Au peak at 239 eV. While the elemental sensitivity factors were extracted from an AUGER database[80] to be $S_{\text{Cl}} = 1.03$ and $S_{\text{Au}} = 1.79 \times 10^{-2}$, some kind of calibration to obtain the actual surface coverage from the atomic concentrations was still needed. Evaluating the APPH ratios reported by Spencer and Lambert [92] I calculated a saturation value of $P_{\text{r,sat.}} = 8.8$. Assuming this value to correspond to a chlorine coverage of $\Theta_{\text{Cl}} = 1 \text{ ML}^{15}$, the saturation concentration was determined *via* Eq. 3.19 to be $C_{\text{Cl,sat.}} = 0.13$. Using this as a reference, the chlorine coverage on the surface could be calculated from the AUGER spectra according to Eq. 3.20:

$$\Theta_{\text{Cl}} = \frac{C_{\text{Cl}}}{C_{\text{Cl,sat.}}} = \frac{P_{\text{r}} \times S_{\text{Au}}}{0.13 (P_{\text{r}} \times S_{\text{Au}} + S_{\text{Cl}})} \quad (3.20)$$

N.B. As can be seen from Fig. 3.26, P_{r} is not zero in the case of a clean surface because there also is a small intrinsic Au peak at $E_{\text{kin}} = 181 \text{ eV}$. Its APPH of ~ 0.15 was subtracted from every APPH value measured for Cl.

3.3.4 Initial Sticking Probabilities

Following the procedure described in the previous section in general, the coverage of Cl atoms on the Au(111) was determined for 4 – 5 different doses at normal incidence energies of 0.51 – 2.56 eV. Tab. 3.11 summarizes the incident beam conditions that were used in the dosing experiments. In one series of measurements, which will from now on be referred to as data set one (DS1), a gas mixture of 4 % HCl in 96 % of H_2 was used and the temperature of the nozzle tip T_{N} was varied to change the mean incidence energy. In a second series, data set two (DS2), T_{N} was held at a constant temperature of $T_{\text{N}} = 1042 \text{ K}$. To vary the mean incidence energy, the surface was tilted by θ relative to the incident beam during dosing. That way, the "normal component" of $\langle E_{\text{i}} \rangle$ was lowered according to Eq. 3.21:

$$\langle E_{\perp} \rangle = \langle E_{\text{i}} \rangle \times \cos^2(\theta) \quad (3.21)$$

Although energy in general is a scalar, the incidence translational energy is calculated based on the molecules' velocity. If interaction with the surface is assumed to occur only for the perpendicular component of the incident velocity and thus momentum, $v_{\perp} = v_{\text{i}} \times \cos(\theta)$,

¹⁵This assumption will be discussed later on.

the cosine factor needs to be squared going from velocity to energy.¹⁶

Table 3.11 Incident beam conditions for the dosing experiments. Given are the corrected nozzle temperature T_N , mean incidence energy $\langle E_i \rangle$, incident angle θ_i , normal component of the mean incidence energy $\langle E_\perp \rangle$, lower limit of the initial sticking probability S_0^{low} , and the respective upper limit S_0^{up} .

Gas mix [†]	T_N / K	$\langle E_i \rangle / \text{eV}$	$\theta_i / ^\circ$	$\langle E_\perp \rangle / \text{eV}$	S_0^{low}	S_0^{up}
(1)	296	0.94(5)	0	0.94(5)	$2.4(3) \times 10^{-5}$	$6.1(7) \times 10^{-5}$
(1)	403	1.18(8)	0	1.18(8)	$7.1(35) \times 10^{-5}$	$1.8(9) \times 10^{-4}$
(1)	495	1.29(9)	0	1.29(9)	$3.0(26) \times 10^{-4}$	$7.8(67) \times 10^{-4}$
(1)	616	1.55(10)	0	1.55(10)	$3.1(2) \times 10^{-3}$	$8.4(7) \times 10^{-3}$
(1)	739	1.80(12)	0	1.80(12)	$1.2(3) \times 10^{-2}$	$3.2(5) \times 10^{-2}$
(1)	898	2.12(14)	0	2.12(14)	$2.2(10) \times 10^{-2}$	$6.0(29) \times 10^{-2}$
(1)	961*	2.31(14)	0	2.31(14)	$2.5(4) \times 10^{-2}$	$7.0(15) \times 10^{-2}$
(1)	1141*	2.48(16)	0	2.48(16)	$3.9(16) \times 10^{-2}$	$1.0(4) \times 10^{-1}$
(1)	1042	2.56(15)	0	2.12(15)	$5.6(18) \times 10^{-2}$	$1.6(6) \times 10^{-1}$
(2)	1042	1.23(8)	50	0.51(3)	$1.2(13) \times 10^{-4}$	$3.1(34) \times 10^{-4}$
(2)	1042	1.23(8)	40	0.72(5)	$3.8(15) \times 10^{-4}$	$1.0(4) \times 10^{-3}$
(1)	1042	2.50(15)	50	1.03(6)	$3.1(6) \times 10^{-3}$	$8.5(3) \times 10^{-3}$
(1)	1042	2.45(15)	44	1.27(8)	$8.9(11) \times 10^{-3}$	$2.5(4) \times 10^{-2}$
(1)	1042	2.50(15)	40	1.47(9)	$1.8(2) \times 10^{-2}$	$4.8(8) \times 10^{-2}$
(1)	1042	2.45(15)	32	1.76(11)	$3.2(2) \times 10^{-2}$	$8.8(8) \times 10^{-2}$

[†] (1): 4 % HCl + 96 % H₂; (2): 6 % HCl + 20 % Ne + 74 % H₂

* As figured out in hindsight, the nozzle was not running under optimal conditions for these dosing experiments. Even though T_N was high, the mean incidence energy was slightly lower than expected.

For comparison with previous and future work, the quantity of interest when studying dissociation on surfaces is the initial sticking probability S_0 . It describes the probability of a single (or the first) molecule dissociating on the surface and is usually determined from the dependency of surface coverage on the applied dose. In Fig. 3.36 representative plots for four different incident conditions are shown. While open symbols denote the coverage and dose data calculated according to Eqs. 3.20 and 3.18, respectively, the black dashed lines are fits to that data following the bounded growth model in Eq. 3.22 (as used

¹⁶It needs to be pointed out that the absence of interaction with the parallel momentum of the molecules is assumed but not proven at this point. See the discussion in further sections.

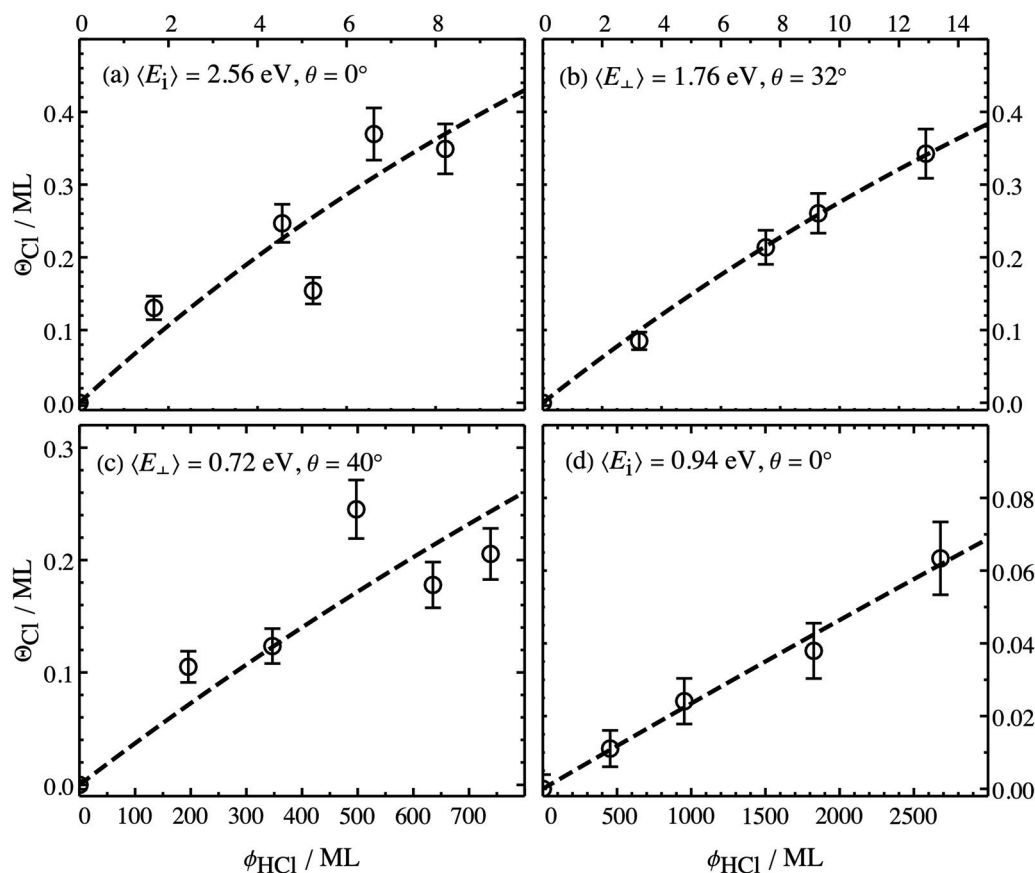


Figure 3.36 Representative plots of the Cl coverage Θ_{Cl} on the surface *vs.* the applied dose ϕ_{HCl} . Open symbols denote the data calculated according to Eqs. 3.18 and 3.20, the dashed lines show fits according to Eq. 3.22. While in some cases, see panel (b) and (c), the fit was excellent, in other cases, see panel (a) and (d), the data exhibited more scatter. As can be seen from a comparison of dose, coverage, incidence energy, and incidence angle in all panels, there was no systematic trend in the fit quality.

in Ref. [93], for example):

$$\Theta_{\text{Cl}} = 1 - \exp(-S_0 \times \phi_{\text{HCl}}) \quad (3.22)$$

Here, the coverage approaches an asymptotic maximum value due to the exponentially lowered number of unoccupied binding sites on the surface. Assuming the asymptote to be equal to a coverage of $\Theta_{\text{Cl}} = 1$, the only fit parameter was S_0 which corresponds to the initial slope of the dashed line. The four plots in Fig. 3.36 were intentionally chosen to cover high and low incidence energies and angles. As can be seen from a comparison of all panels, the fit quality did not systematically depend on the experimental conditions but exhibited random magnitudes of scatter.

Although I paid attention to a number of necessary corrections to coverage and dose, mainly two uncertainties remained. First, as mentioned above, the ion gauge was not

calibrated prior to the experiments which limits the correction's reliability. Second, the surface temperature played an important role in the detected coverage after dosing. In Fig. 3.37 the measured chlorine coverage after the surface had been dosed at a range of different surface temperatures is shown as open symbols. Dose and incidence energy $\langle E_i \rangle \approx 2.2$ eV were the same for all experiments so that the observable decrease in Θ_{Cl} was supposed to be due to the increasing T_s only. Except for one potential outlier at ~ 170 K all data points could be nicely fit with a linear function shown as a red dashed line. As seen in Fig. 3.26, at the lowest accessible surface temperatures around ~ 80 K a chlorine containing compound stuck on the surface even at very low incidence energies, most probably HCl remaining in a weakly-bound physisorption state. That is, the difference in coverage between $T_s \approx 80$ K, $\Theta_{\text{Cl}} \approx 0.25$ ML, and $T_s = 173$ K, $\Theta_{\text{Cl}} \approx 0.18$ ML, could partly be due to a loss in physisorbed HCl at elevated T_s .

Indeed, further temperature dependent experiments, where the surface was kept at $T_s \approx 80$ K and the number of HCl molecules leaving the surface in $v = 0, J = 0$ was monitored with the REMPI laser over a few minutes, showed that even at $T_s \approx 80$ K there was an exponential decay of the presumably physisorbed HCl on the experimental timescale of tens of seconds. Since the origin of the difference between coverages obtained at the lowest $T_s \approx 80$ K and $T_s = 173$ K, which was used in the dissociation experiments, was not entirely clear, the ratio of these coverages was only taken as an upper limit for the correction factor $f(T_s) = 0.25/0.18 = 1.4$ with which the coverage from Eq. 3.20 was multiplied. If, however, the additional coverage detected at $T_s \approx 80$ K was only due to physisorbed HCl, the lower limit correction factor could be taken as $f(T_s) = 1$.

Depending on whether both uncertain corrections were applied or not, respective upper and lower limits of S_0 were determined (see Tab. 3.11). In Fig. 3.38, both are shown on a linear and logarithmic scale (see panel (a) and (b), respectively). While the data set where the incidence angle was kept constant at $\theta_i = 0^\circ$ and the nozzle temperature T_N was varied in the range of 296 – 1141 K is depicted by open black symbols, open blue symbols depict the data set where the nozzle temperature was kept constant at $T_N = 1042$ K while the effective mean incidence energy $\langle E_i \rangle$ was varied by changing the gas mixture and θ_i (assuming normal energy scaling according to Eq. 3.21). Both sets shared the data point at the highest $\langle E_i \rangle = 2.56$ eV. In contrast to the symbols, which denote the lower limit of S_0 , the correspondingly colored dashed lines denote the upper limit applying both ion gauge as well as surface temperature corrections as discussed above. The lightly colored areas thus indicate the range of possible values between both limits. As expected, S_0 increased with $\langle E_i \rangle$. However, it did not increase strictly exponentially but its slope started to level off at $\langle E_i \rangle > 2$ eV. Further, at comparable incidence energies the data set with a fixed high nozzle temperature exhibited significantly higher S_0 . Not surprisingly, the ratio of S_0 at fixed $T_{N,\text{fix}}$ to S_0 at varied $T_{N,\text{var}}$ was highest where the temperature ratio also was highest. With increasing $T_{N,\text{var}}$ the values for S_0 converged. Thus, not only the mean incidence energy played an important role in the dissociation but also further nozzle temperature

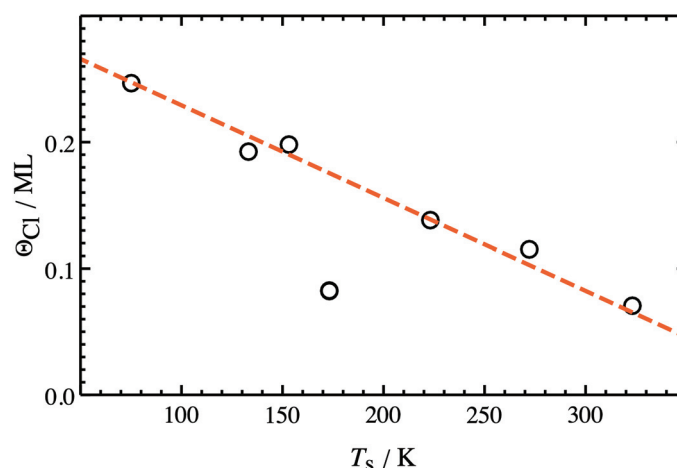


Figure 3.37 Chlorine coverage depending on the surface temperature during dosing. Depicted by open black symbols is the coverage determined after dosing at different surface temperatures. Under otherwise identical experimental conditions (i. e., the same dose at $E_i \approx 2.2$ eV) the resulting coverage can be seen to decrease with increasing T_s . Except for one outlier at ~ 170 K all data points could be nicely fit with a linear function shown as a red dashed line.

dependent properties of HCl molecules. Considering the incident beam characterization, the most obvious candidate was the T_N dependent vibrational population.

It has been theoretically and experimentally established that late barrier reactions like the dissociation of HCl on Au(111) [60] are enhanced more strongly by vibrational than by translational excitation prior to the collision [61]. Thus, it is likely that at higher T_N the increased population in $v = 1$ lead to enhanced dissociation on the surface. Such behavior had also been predicted in the quantum dynamics study by Liu and co-workers [58]. In order to account for these effects a fitting routine was developed. Here, it is important to mention that not only the vibrational population varies with the nozzle temperature but also the width of the incidence energy distribution. At the same mean incidence energy $\langle E_i \rangle$ the fraction of molecules with $E_i > \langle E_i \rangle$ is larger at higher T_N so that the reactivity is enhanced. That is, the significance of the parameter $\langle E_i \rangle$ to judge the reactivity at different experimental conditions is limited. Thus, for a comparing fit of both data sets in Fig. 3.38 the widths α and energies E_0 from fitting incident velocity distributions as seen in Fig. 3.29 needed to be taken into consideration.

In general, every determined S_0 represented a value averaged over the incidence vibrational population and translational energy distribution which can be expressed by Eq. 3.23:

$$S_0(E) = \sum_{i=0}^1 f(v=i) \int_0^{\infty} S_0^{v=i}(E') g[E', E_0(E), \alpha(E)] dE' \quad (3.23)$$

Here, the relative vibrational population $f(v=i)$ (determined as in Fig. 3.27 and Eq. 3.14) is multiplied with the integral over the product of the sticking probability $S_0^{v=i}(E')$ at

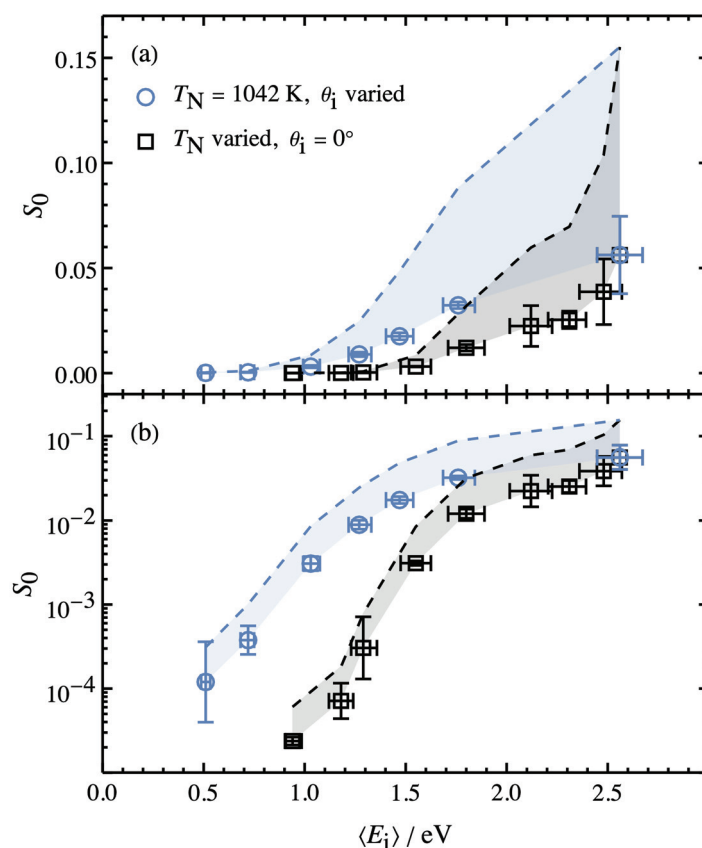


Figure 3.38 Initial sticking probability S_0 depending on the mean incidence energy $\langle E_i \rangle$ shown on (a) linear and (b) logarithmic scale. While the data set where the incidence angle was kept constant at $\theta_i = 0^\circ$ and the nozzle temperature T_N was varied in the range of 296 – 1141 K is depicted by open black symbols, open blue symbols depict the data set where the nozzle temperature was kept constant at $T_N = 1042 \text{ K}$ while the effective mean incidence energy was varied by changing the gas mixture and θ_i (assuming normal energy scaling). Both sets shared the data point at the highest $\langle E_i \rangle = 2.56 \text{ eV}$. In contrast to the symbols, which denote the lower limit of S_0 , the correspondingly colored dashed lines denote the upper limit applying both ion gauge as well as desorption corrections as discussed in the text. The lightly colored area between lower and upper limit thus indicates the range of values for S_0 .

one vibrational state i and translational energy E' and the corresponding distribution of incidence energies g depending on the energy $E_0(E)$ and the distribution width $\alpha(E)$. Assuming vibrational states $\nu \geq 2$ to be negligible, only reactivity from $\nu = 0$ and $\nu = 1$ was supposed to contribute to the sum in Eq. 3.23. In order to construct the functional form of $S_0(E)$ for fitting, $S_0^{\nu=i}(E')$ was represented by an S-shaped error function [94]

$$S_0^{\nu=i}(E') = \frac{A_i}{2} \left[1 + \operatorname{erf} \left(\frac{E - E_{0,i}}{W_i} \right) \right] \quad (3.24)$$

where A_i is the asymptotic value for S_0 , $E_{0,i}$ the function's inflection point (comparable to an energetic barrier) and W_i a measure for its width. Further, the incidence energy distribution was given the familiar shape of

$$g[E', E_0(E), \alpha(E)] = C \times \left(\frac{2E'}{m_{\text{HCl}}^2} \right) \times \exp \left[- \left(\frac{\sqrt{2E'/m_{\text{HCl}}} - \sqrt{2E_0/m_{\text{HCl}}}}{\alpha} \right)^2 \right] \quad (3.25)$$

where C is a normalization constant. To obtain a continuous function as in Eq.3.23, the discrete values of $E_0(E)$ and $\alpha(E)$ determined for the experimental conditions given in Tab. 3.11 needed to be parameterized to obtain continuous functions of E . On the one hand, for DS1 the E_0 and especially α dependence on $\langle E_i \rangle$ was well represented by a simple linear fit. On the other hand, for DS2 the parametrization required some additional steps: Since the surface was tilted, the whole incidence energy distribution got compressed. Thus, new effective parameters for E_0 and α had to be determined in the case of DS2 including the compression factor of $\cos^2(\theta)$. These effective parameters then also exhibited a linear dependence on $\langle E_i \rangle$ that could be used for the fitting of $S_0(E_i)$. In order to fit Eq.3.23 to the data, a least-square

fitting routine was used where the individual deviations were weighted with the square of the error associated with the calculated values for S_0 . The total error was simultaneously minimized with respect to the parameters $E_{0,0}$, $E_{0,1}$, W_0 , and W_1 . A_i was assumed to be equal to 1 since the reactivity should not be greater than unity. While Tab. 3.12 contains the resulting fit parameters, in Fig. 3.39 the results of the fitting are shown visually. As can be seen from

Table 3.12 Derived fit parameters according to Eq. 3.23 for the lower and upper limit. All parameters are given in units of eV.

limit	$E_{0,0}$	W_0	$E_{0,1}$	W_1
lower	4.1	1.1	1.2	0.1
upper	3.1	0.8	1.0	0.2

linear as well as logarithmic scales, the calculated data for S_0 could not be satisfactorily fit with the procedure employing Eq. 3.23. In comparison to the lower limit data, the upper limit fit is even worse. I suppose one of the main reasons for the poor fit quality is the role of the vibrationally excited states as their population is the main difference between DS1 and DS2. Even assuming the reactivity $S_0^{\nu=1}(E) = 1$, except for contributions from slightly different incidence energy distributions the difference between S_0 in both data sets cannot be higher than the difference in $f(\nu = 1, E)$ which is < 0.02 at all $\langle E_i \rangle$. Thus, the

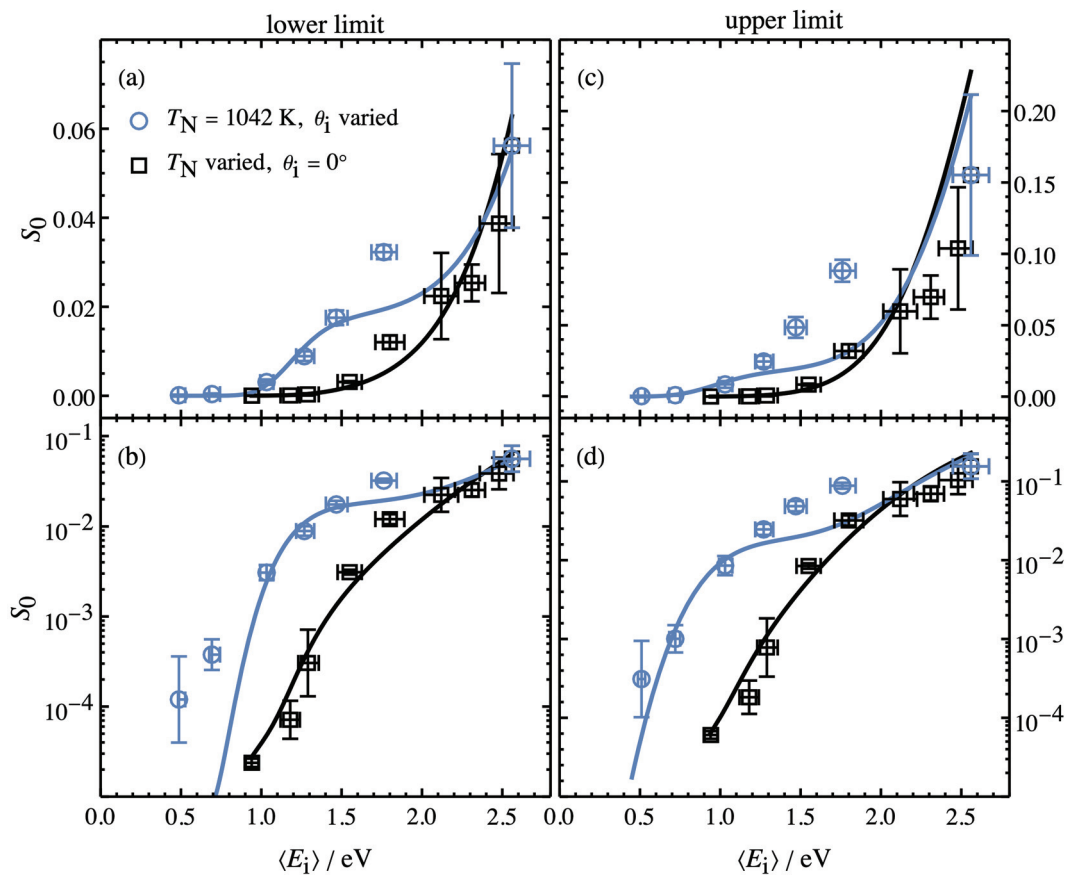


Figure 3.39 Fitting of the initial sticking probability S_0 for the lower (a,b) and upper (c,d) limit shown on linear (top) and logarithmic (bottom) scale. While DS1 is depicted by open black symbols, open blue symbols depict DS2. Both sets shared the data point at the highest $\langle E_i \rangle = 2.56 \text{ eV}$. Solid lines show a simultaneous weighted least-square fit of Eq. 3.23 to both data sets. As can be seen on both scales, neither the lower nor the upper limit can be satisfactorily fit within the limitations given in the text.

differences between the fits for DS1 and DS2 also could not be larger than <0.02 as can be seen from Fig. 3.39. To improve the fit quality, either the model in Eq. 3.23 or the constraints in the fitting parameters needed to be changed. This will be further elaborated on in the discussion section.

3.3.5 Potential Problems

At the beginning of the section on dissociation I mentioned that using AUGER spectroscopy to determine dissociation probabilities requires stable reaction products on the surface to prevent recombinative desorption. As can be seen in Refs. [58, 95, 96], the dissociation products H and Cl were calculated to be metastable on Au(111). One result supposedly due to these characteristics has already been discussed in the form of the surface temperature dependence of the chlorine coverage (see Fig. 3.37). Apart from thermal recombinative desorption, electron stimulated desorption (ESD) and ELEY-RIDEAL reactions can lead to loss of surface Cl.

Electron Stimulated Desorption

ESD is known to deplete Cl coverage on the Au(111) surface [91, 92]. Since its rate depends on the actual experimental parameters like the beam energy and current, it needed to be determined for the conditions used in the dissociation experiments.

In Fig. 3.40, the APPH ratio P_r of Cl and Au depending on the irradiation time and three different electron beam currents measured as surface current I_s is depicted by open symbols. All three curves are normalized to the initial peak ratio for the sake of comparability. As can be seen from the dashed lines, the decay of P_r could be fitted with a simple monoexponential decay:

$$f_{I_s}(t) = a \times \exp(-k \times t) + b(I_s)$$

where b was the zero-coverage value of 0.15 scaled by the same normalization factor as the corresponding curve. From the inverse of the fitted rate constants k kinetic lifetimes τ of P_r were determined to be 2.0×10^4 s, 8.7×10^2 s, and 5.6×10^2 s for surface currents of $1 \mu\text{A}$, $4 \mu\text{A}$, and $8 \mu\text{A}$, respectively. Since the beam intensity for detection of Cl in the dissociation experiments was chosen so that $I_s \approx 1 \mu\text{A}$, there was no significant loss of Cl during the measurement of the AUGER spectra which usually took less than 60 s ($f_{1\mu\text{A}}(60\text{ s}) = 0.997 f_{1\mu\text{A}}(0\text{ s})$). This was confirmed for every line scan by repeating the first measurement at the end of the scan and comparing the peak ratios.

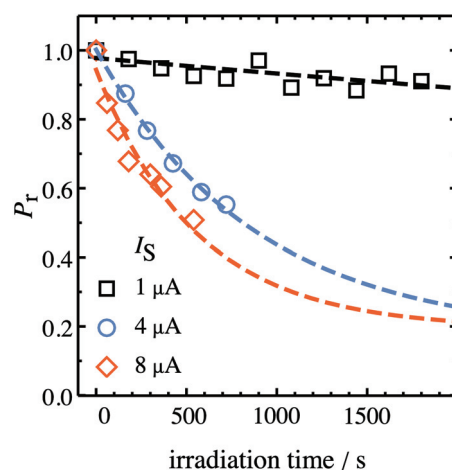


Figure 3.40 ESD kinetics at a beam energy of 3 kV. Depicted by open symbols is the dependence of the APPH ratio P_r of Cl and Au (normalized for the sake of comparability) depending on the irradiation time and three different electron beam currents measured as surface current I_s . Dashed lines denote an exponential decay fit to the data. As expected, higher beam currents lead to accelerated loss of Cl.

Atom Formation in the Hot Nozzle

Since the nozzle was heated to more than 1000 K there could have been thermal dissociation of molecules in the incident beam. Two reactions are conceivable: dissociation of HCl molecules and/or of H₂ seed gas molecules. The influence of the former is not easily predictable. On the one hand, nascent Cl atoms will most probably have a higher sticking probability on the surface than HCl molecules. Thus, high amounts of Cl atoms would artificially increase the coverage on the surface. On the other hand, for every Cl atom there would be one incident H atom that could in principle remove Cl atoms from the surface in ELEY-RIDEAL (or LANGMUIR-HINSHWOOD) type surface reactions. Since reaction cross sections are unknown, it is difficult to judge the overall effect of a possible thermal dissociation of HCl. The influence of dissociated H₂ molecules, however, should result in a net loss of Cl atoms from the surface due to the reactions mentioned above.

On the basis of these considerations, the incident beam coming from the hot nozzle was examined for Cl and H atoms. First, a gas mixture of 4% HCl in H₂ as used in the dissociation experiments was expanded from the heated nozzle and examined with the UV laser as well as the RGA that was mounted in-line with the incident beam in this case. At a corrected nozzle tip temperature of $T_N \approx 1200$ K the UV laser was scanned over the range of the Cl atom REMPI lines [72] for the excited spin-orbit state transition $4p^2P_{1/2} \leftarrow 3p^2P_{1/2}$ at $\nu_{Cl^*} = 235.12$ nm and the ground state transition $4p^2D_{3/2} \leftarrow 3p^2P_{3/2}$ at $\nu_{Cl} = 235.26$ nm¹⁷. Additionally, a second UV laser set to a wavelength of 205 nm for photodissociation of HCl molecules was spatially and temporarily overlapped with the detection laser to obtain comparative spectra (to be precise, the photodissociation laser fired 50 ns earlier than the detection laser). In comparison to the spectra with the photodissociation laser turned on, where the lines mentioned above could easily be observed, there was no detectable Cl signal when the laser was blocked. This observation was in line with results from RGA measurements where the ratio of the ³⁵Cl and the H³⁵Cl signal in the incident beam was found to be independent of the nozzle tip temperature. I thus concluded that there were no Cl atoms formed in the incident beam due to thermal dissociation of HCl.

For H₂ and the formation of H atoms, the case could not that easily be solved. First of all, the LYMAN- α (~ 243.2 nm 2-photon-wavelength) as well as the LYMAN- β (~ 205.2 nm 2-photon-wavelength) transitions were detected in the incident beam and their intensities also seemed to increase with T_N . However, signal at the corresponding wavelengths was also detected when the molecular beam was blocked or at positions vertically off the incident beam, at least some of which could be attributed to background from ion gauge and possibly AUGER filaments. Thus, not only the existence but the effect of possible H atom formation in the incident beam was checked. To do so, the surface was dosed with an incident beam energy of ~ 2.5 eV to establish a chlorine coverage of approximately 0.25 ML at $T_s = 130$ K. Then, the same surface spot was dosed with a pure H₂ beam expanded from

¹⁷The wavelength given by the UV laser was not calibrated in this case, thus there is a small offset compared to literature values.

Chapter 3. Scattering HCl from Au(111)

the nozzle at $T_N \approx 1200$ K. After dosing for the same time, the coverage was measured again. While it did decrease slightly, the magnitude of the loss could be explained by the ESD described in the section above. Neither ELEY-RIDEAL nor LANGMUIR-HINSHWOOD reaction fingerprints were observed. Thus, although the formation of H atoms in the incident beam could not be completely ruled out, if existent they did not seem to influence the detected Cl coverage.

3.3.6 Associative Desorption

REMPI-TPD

As has been shown throughout the previous sections, depending on surface and nozzle tip temperature the surface contained different chlorine (and hydrogen) species after dosing with HCl molecules seeded in H₂. One way to gain further knowledge about the nature of these species was to conduct TPD measurements. Since the UHV chamber was not equipped for standard TPD experiments employing specially prepared (i. e., masked) mass spectrometers, REMPI was chosen as a method to detect desorbing species while heating the surface.

The general procedure for these REMPI-TPD measurements was the following. First, the sample holder containing the gold crystal was cooled with liquid nitrogen so that the thermocouple attached to the surface displayed a temperature of $T_s < 78\text{K}$ ¹⁸. Then, the surface was dosed with the molecular beam at a certain T_N to either physisorb or chemisorb HCl molecules. While the surface was subsequently heated with a temperature ramp of $\sim 2\text{K/s}$, one or two UV lasers aligned close to the surface were fired. While the UV laser described in Sec. 2.2 was used to detect desorbing HCl molecules state-selectively *via* (2 + 1) REMPI around 238.7 nm, H₂ was detected simultaneously *via* (2 + 1) REMPI using the third harmonic of a second pulsed dye laser around 201.7 nm.

In Fig. 3.42 (a), such REMPI-TPD spectra are shown for dosing the Au(111) surface at $T_s \approx 75\text{K}$ with the nozzle tip at room temperature for time spans of 1 - 4 min. As expected, the area under the curves and thus the HCl coverage increased with dosing time. However, the signal saturated rather quickly indicating a large sticking coefficient. Judging from the peak shape, the curves could result from 1. order desorption kinetics which would fit a simple desorption process of physisorbed HCl molecules (it was difficult to estimate the peak position shift because of the rapid saturation, though). In panel (b), the surface was now dosed with a nozzle tip temperature of $T_N = 1250\text{K}$ which corresponded to an incidence energy of $\langle E_i \rangle = 2.5\text{eV}$. Based on the results in Fig. 3.38, the dissociation probability was approximately three orders of magnitude higher at this $\langle E_i \rangle$ but still far below unity. Accordingly, the curves' integral did not saturate in the examined dosing time range of 1 - 10 min. Additionally, while the peak positions were similar to those in panel (a), their shape rather resembled those of 2. order processes. Thus, the surface was dosed again for 4 min with HCl molecules at $\langle E_i \rangle = 2.5\text{eV}$. This time, however, the exponential decay of the HCl $v = 0, J = 0$ REMPI signal was recorded while the surface was maintained at $T_s \approx 75\text{K}$. After approximately 5 min the signal had vanished and the surface temperature was raised, leading to the TPD spectrum depicted by the dashed blue line in panel (c). The sum of the accordingly scaled, dashed black and blue curves was equal to the red dashed curve. That is, the TPD spectrum resulting from the hot nozzle dosing could be split into

¹⁸At these low temperatures, the true temperature might deviate from the one read-out from the K -type thermocouple.

contributions presumably stemming from physisorbed and chemisorbed (more strongly bond) HCl species.

As mentioned above, not only HCl but also H_2 and Cl desorption was observed. In Fig. 3.41 (a), H_2 TPD spectra are depicted by dashed black and red lines while the dashed blue and green lines depict the simultaneously measured HCl spectra from $\nu = 0, J = 1$ and $\nu = 0, J = 0$, respectively. While for H_2 the curve integral was higher for $J = 1$, it was the other way around for HCl. In any case, the H_2 desorption peak temperature of ~ 78 K was much lower than the 110 K previously reported after dosing a Au(111) surface with H atoms [97]. In panel (b), spectra recorded by applying Cl atom REMPI are depicted by the blue and black curve for surface dosing temperatures of $T_s \approx 78$ K and $T_s \approx 173$ K, respectively. The high temperature peak at ~ 800 K, which had previously been reported as the single peak for low Cl_2 exposures [91, 92], was only seen in the latter case.

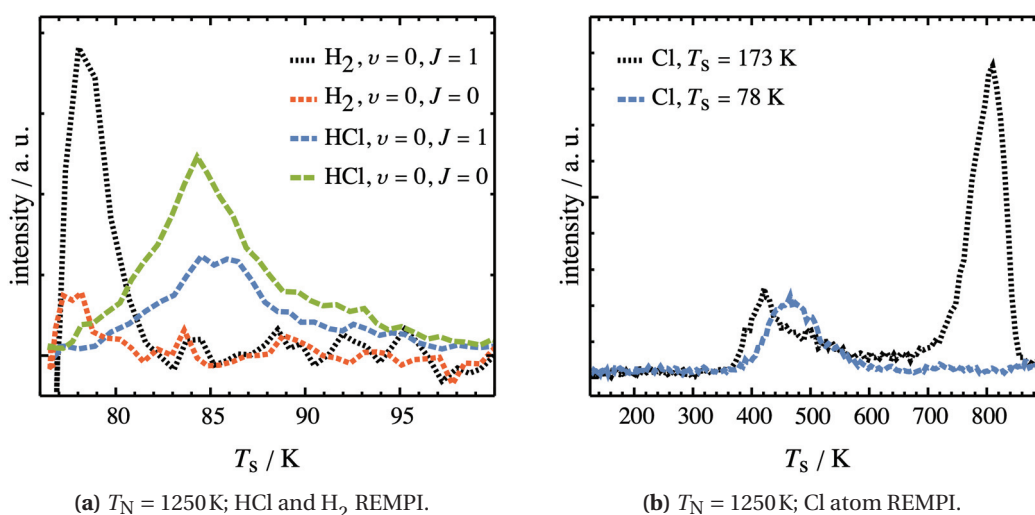


Figure 3.41 REMPI-TPD spectra of HCl, H_2 , and Cl after dosing the Au(111) surface with HCl molecules from the nozzle at $T_N = 1250$ K with $\langle E_i \rangle = 2.5$ eV. In panel (a), simultaneously recorded spectra for H_2 and HCl (detected by two different UV laser systems operating around 201.7 nm and 238.7 nm, respectively) are depicted by dashed black and red and dashed blue and green lines for $\nu = 0, J = 1$ and $\nu = 0, J = 0$, respectively. While for H_2 the curve integral was higher for $J = 1$, it was the other way around for HCl. In panel (b), spectra recorded by applying Cl atom REMPI are depicted by the blue and black curve for dosing at surface temperatures of $T_s \approx 78$ K and $T_s \approx 173$ K, respectively. The high temperature peak at ~ 800 K was only seen in the latter.

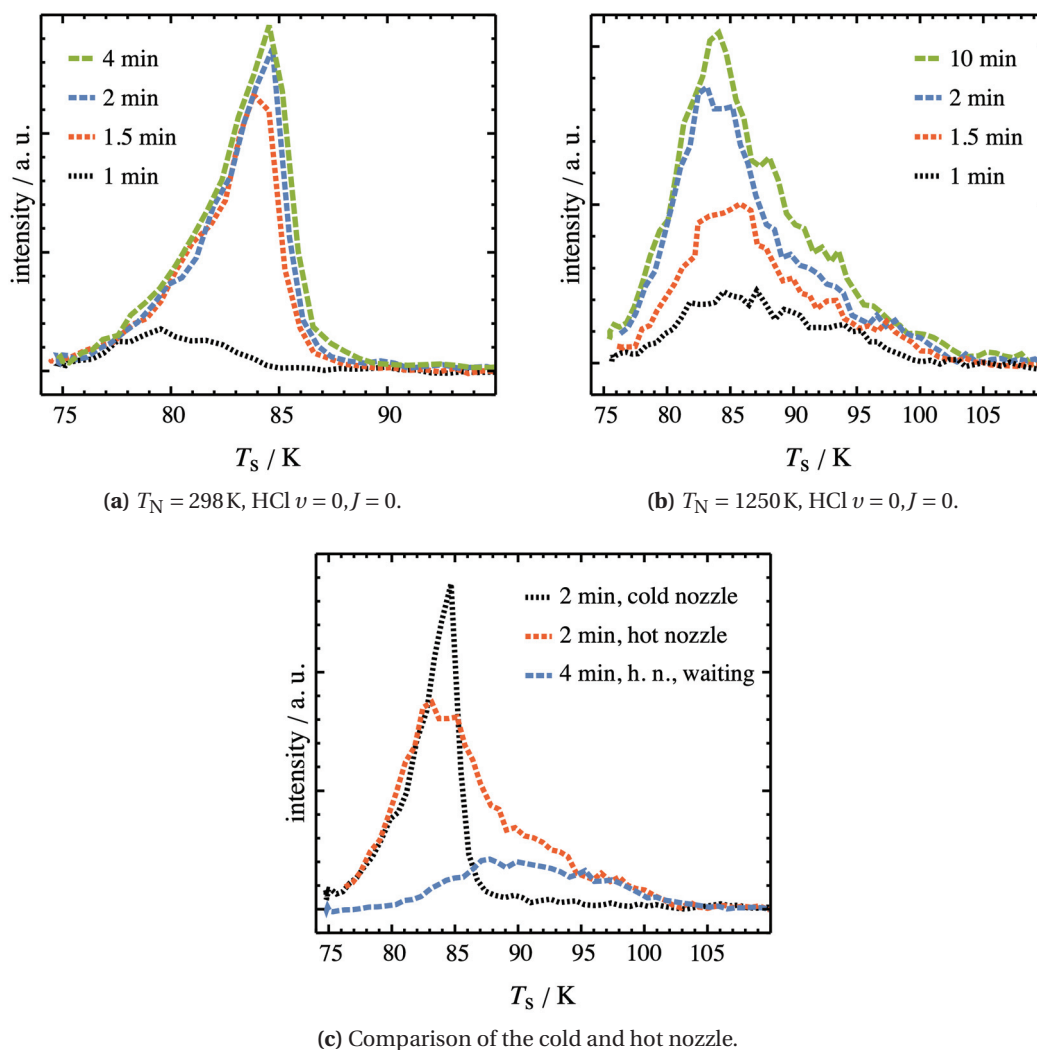


Figure 3.42 REMPI-TPD spectra of HCl after the surface ($T_s \approx 75\text{ K}$) had been dosed with nozzle temperatures of (a) $T_N = 298\text{ K}$ ($\langle E_i \rangle = 0.9\text{ eV}$) and (b) $T_N = 1250\text{ K}$ ($\langle E_i \rangle = 2.5\text{ eV}$) for the times specified in the individual panels. As can be seen from the increase in intensity, the coverage on the surface increased with dosing time. Moreover, peak positions and shapes were different for low and high incidence energies. In panel (c), the two curves from (a) and (b) for a dosing time of 2 min are compared to a REMPI-TPD curve where the surface had been dosed with $\langle E_i \rangle = 2.5\text{ eV}$ for 4 min whereupon the exponential decay of the HCl $\nu = 0, J = 0$ REMPI signal was recorded while the surface was maintained at $T_s \approx 75\text{ K}$. After approximately 5 min the signal had vanished and the surface temperature was raised leading to the TPD spectrum depicted by the dashed blue line. The sum of the accordingly scaled, dashed black and blue curves was equal to the red dashed curve.

Analysis of the REMPI-TPD Spectra

Although the REMPI-TPD data presented in the previous section was not as sophisticated as most published spectra recorded with specifically designed TPD experiments in terms of temperature calibration or signal-to-noise ratio, I will at least try to get an estimate on the activation energies of the underlying desorption reactions. In a general picture, the rate of desorption, which is proportional to the detected molecules per time interval, can be described by the POLANYI-WIGNER model [98]:

$$-\frac{d\Theta}{dt} = \nu_n \Theta^n \exp\left(-\frac{E_a}{k_B T}\right) \quad (3.26)$$

where Θ is the surface coverage, ν is the (reaction order dependent) pre-exponential factor, n the reaction order and E_a the activation energy for desorption. Taking the logarithm of Eq. 3.26 leads to the following form:

$$\ln\left(-\frac{d\Theta}{dt}\right) = \ln(\nu_n) + n \times \ln(\Theta) - \frac{E_a}{k_B T} \quad (3.27)$$

which can easily be rearranged to:

$$\ln\left(-\frac{d\Theta}{dt}\right) - n \times \ln(\Theta) = \ln(\nu_n) - \frac{E_a}{k_B T} \quad (3.28)$$

as shown by Parker *et al.* [99]. That is, with the correct choice of n Eq. 3.28 leads to a linearization of the recorded TPD spectra. Even without exactly knowing the coverage or desorption rate, the reaction order and the activation energy can in principle be determined [99]. In contrast, since ν is contained in the ordinate, a vertical shift of the curve will also alter the pre-exponential factor which thus eludes determination without exact signal calibration. Because of the limited REMPI-TPD data available, I will thus try to estimate reaction orders and extract desorption barriers that can be compared to previously published values.

In Fig. 3.43, the analysis of TPD spectra recorded after dosing the cold surface with a room temperature nozzle ($\langle E_i \rangle \approx 0.9$ eV, panels (a) and (b)) and with a hot nozzle ($\langle E_i \rangle \approx 2.5$ eV, panels (c) and (d)) as in Fig. 3.42 is shown. In the first case, the data could be linearized according to Eq. 3.28 when a desorption order of one was assumed. Due to the sharp drop in intensity after the peak, the linearization primarily worked for the rising edge of the spectrum.¹⁹ Based on the analysis of several spectra, an activation energy of $E_a = 0.24(1)$ eV was determined for the desorption process observed in panel (a).

Employing the thus derived activation energies, TPD spectra were simulated for comparison with the experimentally obtained ones. In the case of presumably physisorbed HCl, this was done the following way. First, a set of differential equations describing the

¹⁹As Parker *et al.* state in their publication, the method "is most sensitive to the choice of n in the region *near the desorption peak maximum*" [99].

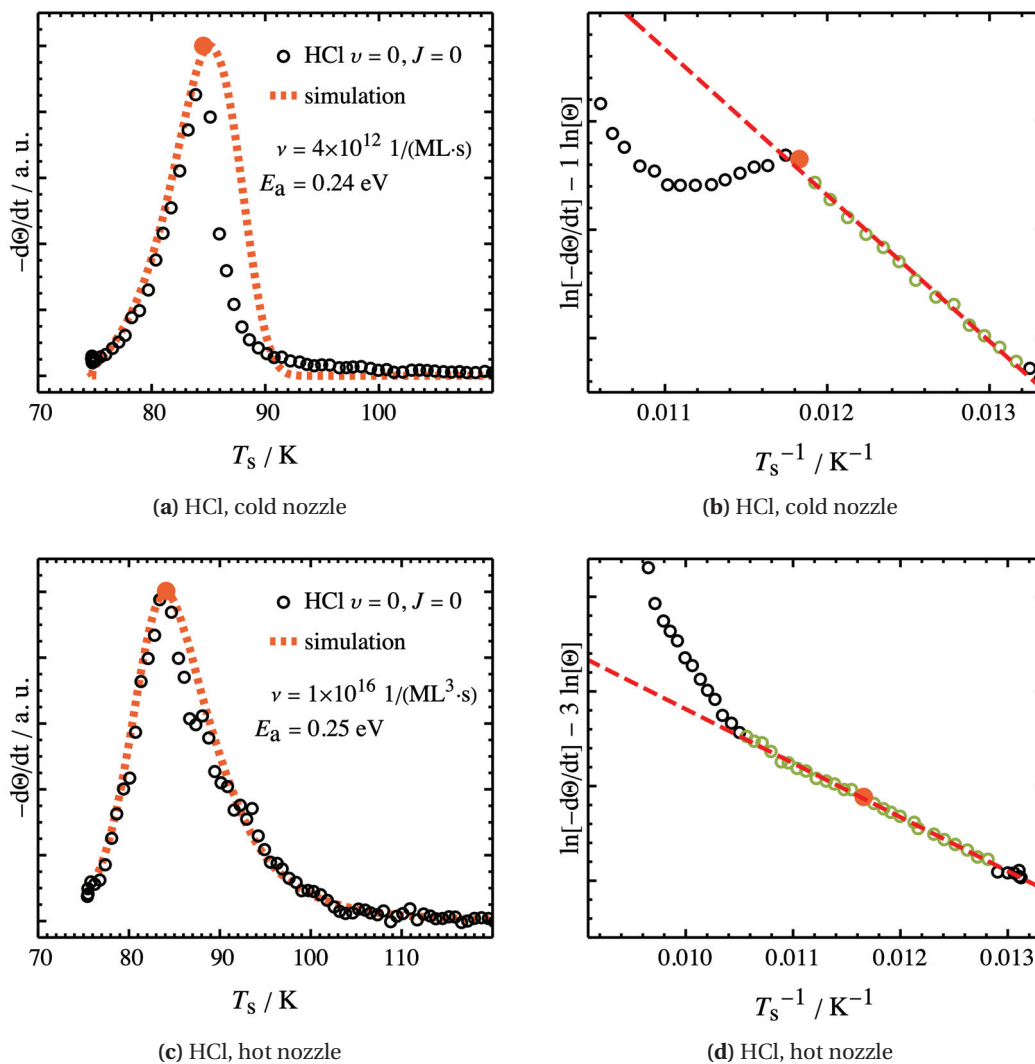


Figure 3.43 REMPI-TPD spectra of HCl($v=0, J=0$) as shown in Sec. 3.3.6. In panels (a) and (c), black symbols depict the measured TPD while dashed red lines depict simulated spectra after the surface had been dosed with a cold (i. e., room temperature) and hot nozzle, respectively. In panels (b) and (d), the analysis of the spectra according to Eq. 3.28 is shown. While black symbols depict the logarithmized data, green symbols depict those data points included in the fit, the single red symbol depicts the peak of the spectrum (in all panels) and the dashed red line shows the fit from which E_a was derived. Assuming the desorption of a single species, the TPD spectra are compared to a simulated spectrum assuming first order (a) and third order (c) desorption. For the simulations, E_a was taken from the fits on the right hand side and ν was manually fitted to match the experimental TPD spectrum (actual values given in panel (a) and (b)).

desorption kinetics was established:

$$[\text{HCl}_{\text{ad}}]' = -k \times [\text{HCl}_{\text{ad}}]$$

$$[\text{HCl}_{\text{g}}]' = k \times [\text{HCl}_{\text{ad}}]$$

where $[\text{HCl}_{\text{ad}}]$ is the concentration or rather coverage of adsorbed HCl molecules in units of ML and $[\text{HCl}_{\text{g}}]$ the concentration of gaseous HCl in ML. The rate constant k was given as:

$$k = \nu \times \exp\left(-\frac{E_a}{k_B T_s(t)}\right)$$

In order to numerically solve the system of differential equations in the time domain, T_s was taken to be the time dependent surface temperature based on the actual experimental heating rate (to ensure the best possible comparability with experiment). With the boundary conditions of $[\text{HCl}_{\text{g}}]_0 = 0$ and $[\text{HCl}_{\text{ad}}]_0 = \Theta$, where Θ was some presumed coverage in ML, and assuming a value for ν the differential equations were solved with MATHEMATICA's built-in `NDSolve` function²⁰. Assuming that due to high pumping speeds there was no build-up of HCl pressure in the surface chamber, the TPD spectrum was obtained *via* differentiation of the numerical solution. For simulations of higher order desorption processes, the kinetic rate equations needed to be adapted, of course.

To most accurately simulate the observed spectrum in panel (a), a pre-exponential factor of $\nu = 4 \times 10^{12} \text{ ML}^{-1} \text{ s}^{-1}$ needed to be assumed. While the rising edge was well represented, the simulation overestimated the falling edge of the spectrum. However, the latter also consisted of very few data points and thus this side of the recorded spectrum was less reliable (e. g., due to laser fluctuations). Interestingly, the spectra after hot-nozzle dosing could best be linearized choosing $n = 3$ which basically led to the same activation energy of $E_a = 0.25(1) \text{ eV}$.²¹ Assuming $\nu = 1 \times 10^{16} \text{ ML}^{-3} \text{ s}^{-1}$ led to an almost perfect simulation of the experimental TPD. However, one has to be careful here: For $n = 3$, peak position and width depend on ν *and* the coverage on the surface. That is, without knowing the exact coverage, the above value for ν could only be used for the simulation of the spectrum but is not necessarily close to the true value. In any case, the determined (and more robust) activation energies are very similar to previously published values based on experimental data by Lykke and Kay ($E_a = 0.23 \text{ eV}$ [43]) and the theoretically determined physisorption well by Füchsel *et al.* ($E_a = 0.217 \text{ eV}$ [100]). Yet, while $n = 1$ is reasonable for the desorption of physisorbed molecules, it seems less obvious why the desorption of molecules dosed with the hot nozzle should follow a third order process. This would, in first approximation,

²⁰WOLFRAM MATHEMATICA version 11.3.

²¹In this case, HCl molecules were assumed to have dissociated prior to the desorption and thus the coverages of H and Cl atoms entered the kinetic differential equations. $n = 3$ was chosen to be the sum of the individual exponents for $[\text{H}_{\text{ad}}]$ and $[\text{Cl}_{\text{ad}}]$. Since only one recombination reaction was considered in the simulation and the starting coverages were assumed to be the same for both atoms, it did not matter which species was given an exponent of $n = 1$ or $n = 2$.

require the interaction of three particles during the rate-limiting step of the desorption process.

However, as shown in Fig. 3.42, the TPD spectrum of HCl which was obtained after dosing the surface with the hot nozzle exhibited two contributions: one from supposedly physisorbed HCl and one that became apparent after letting the former molecules desorb from the still cold surface. This process is visualized in Fig. 3.44. Here, HCl molecules in $\nu = 0, J = 0$ desorbing from the surface at $T_s \approx 77\text{K}$ were detected after the surface had been dosed with the hot nozzle ($\langle E_i \rangle \approx 2.5\text{eV}$). As can be seen from the black symbols in panel (a), the corresponding REMPI signal decayed over a time of $\sim 300\text{s}$. Assuming that the origin of this signal was a first order desorption process, the time dependent coverage Θ would be:

$$\Theta(\text{HCl}) = A \times \exp(-k \times t) \quad (3.29)$$

where differentiation leads to

$$-\frac{d\Theta}{dt} = -k \times A \times \exp(-k \times t) = A' \times \exp(-k \times t) \quad (3.30)$$

Fitting of the exponential decay in Eq. 3.30 to the arbitrarily scaled data in Fig. 3.44 (a) led to the function depicted by the solid red line with a rate constant of $k = 1.58(2) \times 10^{-2} \text{s}^{-1}$. Rearranging the classic ARRHENIUS equation in Eq. 3.31, the activation energy E_a can be calculated from the temporal decay:

$$k = \nu \times \exp\left(-\frac{E_a}{k_B T_s}\right) \quad (3.31)$$

$$E_a = -\ln(k/\nu) \times k_B T_s \quad (3.32)$$

Assuming $\nu = 4 \times 10^{12} \text{ML}^{-1} \text{s}^{-1}$ (as obtained from Fig. 3.43) and entering the surface temperature $T_s = 77\text{K}$, the resulting activation energy obtained from Eq. 3.32 was $E_a = 0.22\text{eV}$. Considering that ν was only estimated, this value is identical to those obtained from the first order TPD analysis as well as the previously published physisorption wells [43, 100]. Fig. 3.44 (b) shows the TPD spectrum obtained after the signal in (a) had vanished. In comparison to Fig. 3.42 (c) the shape of the leading and falling edges look slightly different. Indeed, this spectrum could be linearized according to Eq. 3.28 if a second order process was assumed with $n = 2$, which resulted in an activation energy of $E_a = 0.20(2)\text{eV}$. Assuming ν and initial coverages of H and Cl atoms, which for a second order process also cannot be determined at the same time from a single TPD curve, the spectrum could successfully be simulated (dotted red line). That is, the supposedly third order spectrum in Fig. 3.43 (c) most probably resulted from the superposition of individual first order and second order spectra. Indeed, it could be represented by a weighed sum of the simulated spectra shown in Fig. 3.43 (a) and Fig. 3.44 (b). In conclusion, I would thus argue that there were two differently adsorbed species of HCl on the Au(111) surface which desorbed at similar

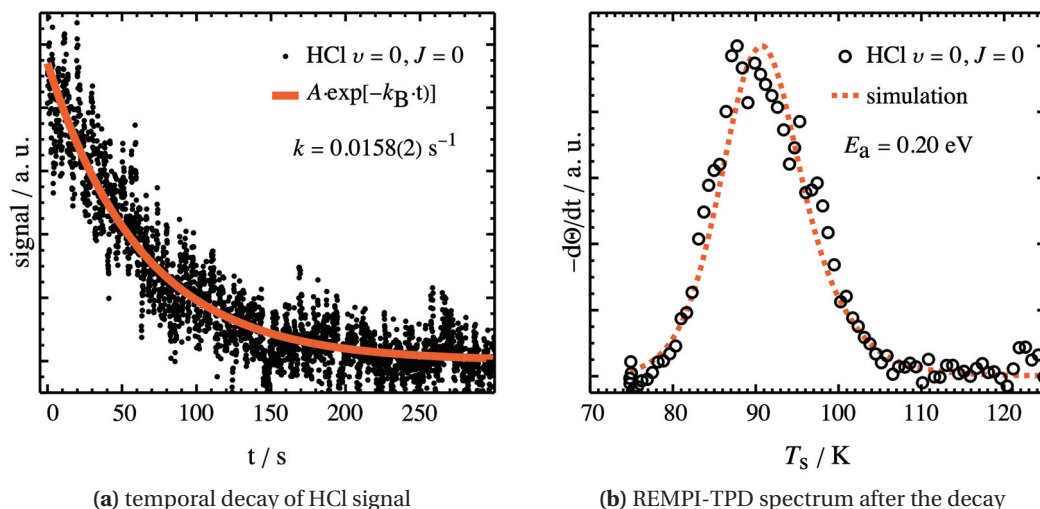


Figure 3.44 Temporal decay of the HCl($v = 0, J = 0$) signal and subsequent REMPI-TPD spectrum of HCl($v = 0, J = 0$). In panels (a), black symbols depict the REMPI signal of HCl molecules detected in $v = 0, J = 0$ in front of the Au(111) surface over a time of 300 s after the surface had been exposed to the incident HCl beam with $\langle E_i \rangle \approx 2.5$ eV at $T_s \approx 77$ K. The solid red line depicts a fit to this data according to Eq. 3.30 which resulted in a rate constant of $k = 1.58(2) \times 10^{-2} \text{ s}^{-1}$. In panel (b), black symbols depict the TPD spectrum obtained after the signal shown in (a) had vanished. In comparison to Fig. 3.42 (c) the shape of the leading and falling edges look slightly different. Indeed, this spectrum could be linearized according to Eq. 3.28 if a second order process was assumed with $n = 2$, which resulted in an activation energy of $E_a = 0.20(2)$ eV (linearization not shown here). The dotted red line depicts a simulated spectrum assuming ν and initial coverages of H and Cl atoms. Since for a second order process the latter also cannot be determined at the same time from a single TPD curve, their absolute values are not given here.

T_s and with similar values for E_a .

In contrast to the spectra in Figs. 3.43 and 3.44, where the surface temperature during dosing was ~ 77 K, the dosing T_s in Fig. 3.45 was 170 K. Thus, the TPD spectra in this figure were recorded after dosing the surface with a hot nozzle ($\langle E_i \rangle \approx 2.5$ eV) at the same T_s as for the dissociation experiments. That is, HCl molecules should have dissociated leaving H and Cl atoms behind on the surface, but due to the slightly elevated temperature no HCl molecules in a physisorbed state were expected to be present. Further, at this temperature the H_2 recombinative desorption was supposed to have removed H atoms stemming from the HCl dissociation. To test whether Cl atoms were remaining on the surface, the REMPI wavelength was tuned to the detection of the spin-orbit ground state of Cl atoms that were reported to desorb from Au(111) in atomic form [91, 92].

While the spectrum in Fig. 3.45 panel (a) was only seen under these dosing conditions, the feature in panel (c), which at $T_s = 170$ K partly overlapped with the spectrum in (a), was also seen for $T_s \approx 77$ K. As one would expect for desorption of Cl atoms, the spectrum in (a) could be linearized around the peak when $n = 1$ was assumed. With the E_a of 2.06(2) eV

derived in panel (b), a pre-exponential factor of $\nu = 1.6 \times 10^{12} \text{ ML}^{-1} \text{ s}^{-1}$ could be used to fit the spectrum in panel (a) (for $n = 1$ only the peak intensity but not its position depend on the coverage). Both Kastanas and Koel as well as Spencer and Lambert also observed the Cl desorption peak around 800 K with more traditional TPD methods based on mass spectrometry [91, 92]. Assuming $\nu = 1 \times 10^{13} \text{ s}^{-1}$ both groups estimated the desorption barrier using a REDHEAD and leading edge analysis to be $E_a = 2.08 \text{ eV}$ and $E_a = 2.25 \text{ eV}$, respectively. Especially the former barrier energy derived by Kastanas and Koel is identical to the one determined here.

In the aforementioned publications a second peak at around 650 – 750 K was observed for a mass of 70 amu which was attributed to desorption of Cl_2 molecules. This peak could not be observed in the REMPI-TPD spectra I recorded for which only Cl atoms were detected. However, as mentioned above a small second peak around 430 K was observed monitoring the Cl transition, see Fig. 3.45 panel (c). Linearizing this peak was not as straightforward since the signal-to-noise ratio (S/N) ratio was subpar. The best fit was obtained assuming $n = 2$ which lead to a desorption energy of $E_a = 0.31(2) \text{ eV}$. With $\nu = 3 \times 10^6 \text{ ML}^{-2} \text{ s}^{-1}$ the peak position and width could satisfactorily be simulated although the S/N as well as the coverage dependence of the simulation left room for interpretation. Given the small intensity of the TPD peak it could be due to Cl desorbing from nearby surfaces of the sample holder which also warmed up. Based on its seemingly second order kinetics, it could also be that accidentally a transition of recombined HCl or Cl_2 was hit with the REMPI wavelength. In addition to recording the TPD spectra, the oscilloscope signal was also monitored at the peak temperature. While for the assigned Cl peak the mass spectrum clearly showed both isotopes at the expected ratio of 3 : 1, the unassigned peak resulted from a broad, unresolved mass peak at approximately the same mass.

Unable to unravel the mystery of the presumed second order peak around 430 K, I marked it as "unknown species" in Fig. 3.45. The most important results from this and all other REMPI-TPD spectra analyses discussed here are summarized in Tab. 3.13.

Table 3.13 Summary of the REMPI-TPD analysis. Given are the peak temperature T_p of the REMPI-TPD spectra, the determined reaction order n , the supposed species, activation energy E_a , pre-factor ν and the corresponding figure.

T_p / K	n	supposed species	E_a / eV	$\nu^\dagger / \text{s}^{-1}$	Fig.
85	1	physisorbed HCl	0.24(1)	4×10^{12}	3.43
90	2	chemisorbed HCl	0.20(2)		3.44
800	1	chemisorbed Cl	2.06(2)	2×10^{12}	3.45
430	2	unknown	0.31(2)		3.45

[†] Since the peak position and width of first order TPD spectra is independent of the coverage, in this case ν can be given either in units of $\text{ML}^{-1} \text{ s}^{-1}$ or s^{-1} .

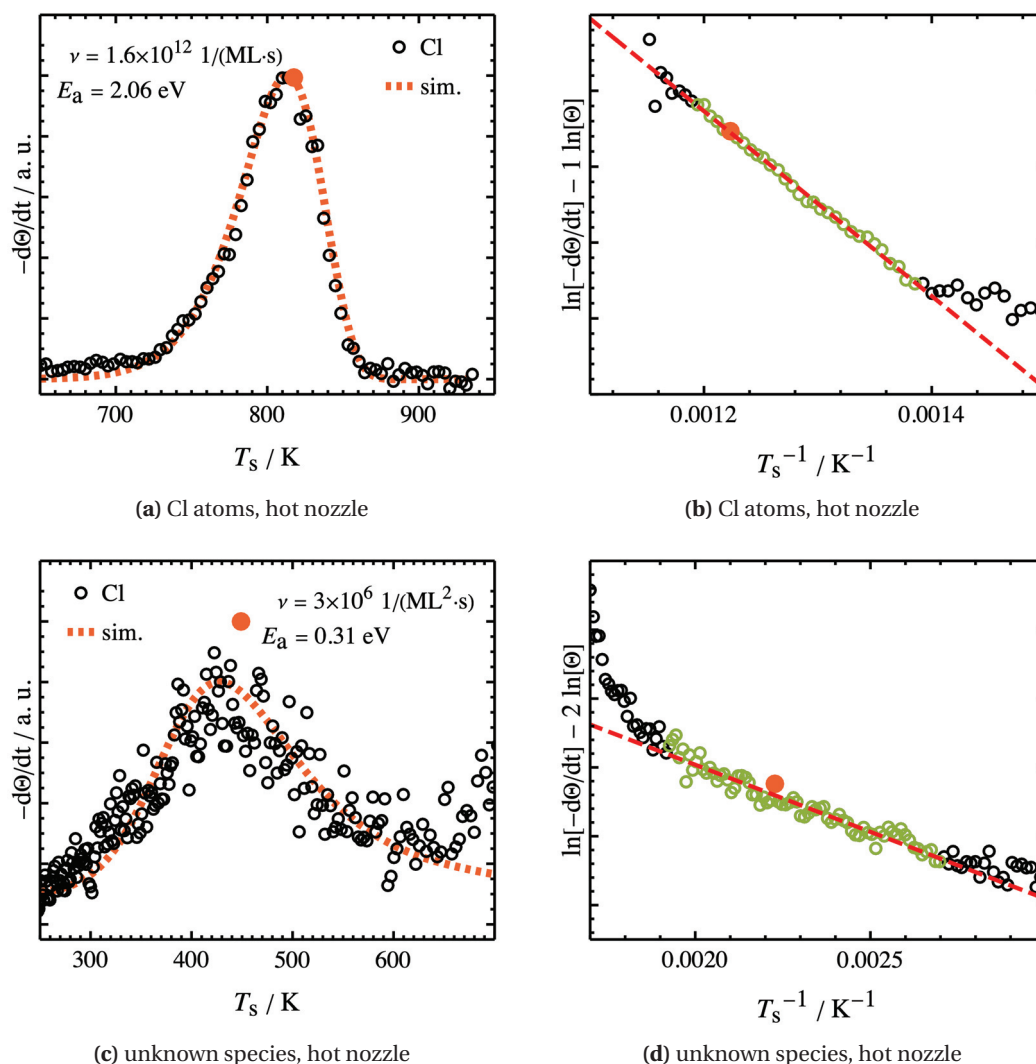


Figure 3.45 REMPI-TPD spectra of Cl atoms in the spin-orbit ground state as shown in Sec. 3.3.6. In panels (a) and (c), black symbols depict the measured TPD while dashed red lines depict simulated spectra after the surface had been dosed with a hot nozzle. In panels (b) and (d), the analysis of the spectra according to Eq. 3.28 is shown. While black symbols depict the logarithmized data, green symbols depict those data points included in the fit, the single red symbol depicts the peak of the spectrum (in all panels) and the dashed red line shows the fit from which E_a was derived. Assuming the desorption of a single species, the TPD spectra are compared to a simulated spectrum assuming first order (a) and third order (c) desorption. For the simulations, E_a was taken from the fits on the right hand side and ν was manually fitted to match the experimental TPD spectrum (actual values given in panel (a) and (b)). While both spectra were obtained with the REMPI laser tuned to the detection of the spin-orbit ground state of Cl, the origin of the spectrum in (c) remained unclear. That is, the actual species desorbing from the surface is unknown.

Cl₂ Recombination

In contrast to Cl atoms, Cl₂ molecules were not detected *via* REMPI-TPD. It was only in subsequent dynamic scattering experiments that I found evidence for the recombination of Cl₂ on the surface. In these experiments, a molecular beam of 3 % HCl in H₂ coming from the hot nozzle with an incidence energy of $\langle E_i \rangle = 2.5$ eV was scattered from the Au(111) surface at $T_s \approx 1073$ K which was mounted at an angle of $\theta_i = 26^\circ$ relative to the incident molecular beam (resulting in $\langle E_\perp \rangle = 2.0$ eV assuming normal energy scaling). Directly scattered and potentially desorbing reaction products were detected at a vertical position relative to the incident beam that corresponded to the surface normal. There, I detected an ion signal corresponding to a mass of ~ 70 amu in the spectral proximity of previously used HCl transitions at a UV laser wavelength of 239.666 nm. Scanning the surrounding wavelength range while recording the signal gated to the time corresponding to the mass of Cl₂ gave rise to the REMPI spectrum shown in Fig. 3.46. In the range of 238.2 – 250.5 nm (2 + 1) REMPI transitions of Cl₂ *via* [²Π_{3/2}]_g 5s and [²Π_{1/2}]_g 5s RYDBERG states were reported [101]. Depicted by the solid black and blue lines are individual wavelength scans that were stitched together since the UV laser could not be scanned for the entire range at once. Additionally shown as solid red lines are the transitions given in literature for jet-cooled ³⁵Cl₂. Colored pairs of numbers below the spectrum indicate the corresponding vibrational transitions $v' \leftarrow v''$ in the form of (v', v'') where the color denotes the intermediate RYDBERG state as given in the plot legend.

The following can be seen from a comparison of both spectra: First, Cl₂ coming from the hot surface lead to a massively increased transition line density, most probably due to the increased number of populated states. Second, even though this phenomenon hampered the assignment of the recorded spectral lines, some prominent features of the reported cold spectrum could be identified (mind the possible small shift in absolute wavelength between both spectra). Two of the most intense lines were used for the subsequently described experiments: $\lambda_1 = 239.666$ nm and $\lambda_2 = 247.350$ nm. In Fig. 3.47, arrival time distributions of Cl₂ molecules at the laser detection spot depending on different experimental parameters are shown. In panel a), the recorded signal of Cl₂ desorbing from the surface at $T_s = 1073$ K in dependence on the laser-nozzle delay τ is shown as a solid blue line in comparison to the incident HCl beam as a solid red line and the scattered HCl beam as a dashed black line. Under these conditions, the Cl₂ signal was approximately eight times less intense than the HCl signal and started to appear later at the detector. It was highly dependent on the normal incidence energy of the HCl molecules and increased strongly when the latter was varied from 0.68 – 2.0 eV (panel b). Moreover, the peak of the Cl₂ signal shifted to earlier times and the peak normalized distribution became narrower (see inset of panel b). While the signal intensity also depended on the scattering angle and was maximal around the surface normal (which corresponded to 26°, see the dashed green line in panel c), the width was independent of θ_{scat} . However, both were dependent on the surface temperature (panel d): with increasing T_s , the peak intensity increased

while its width decreased, which can be explained by a reduced residence time at elevated temperatures. Taken together, these findings confirmed the origin of the Cl_2 to be on the surface: As one would expect based on the results obtained from AUGER measurements, the dissociation of HCl molecules on Au(111) which is the basic prerequisite for formation of Cl_2 molecules on the surface, strongly depended on $\langle E_i \rangle / \langle E_{\perp} \rangle$ (or more directly on T_N). Additionally, the Cl_2 signal intensity predictably varied with the detection angle relative to the surface normal and the surface temperature. Since further no Cl or H atoms could be detected in the incident beam, I thus claim that the Cl_2 signal was a dynamic fingerprint of the HCl dissociation on Au(111).

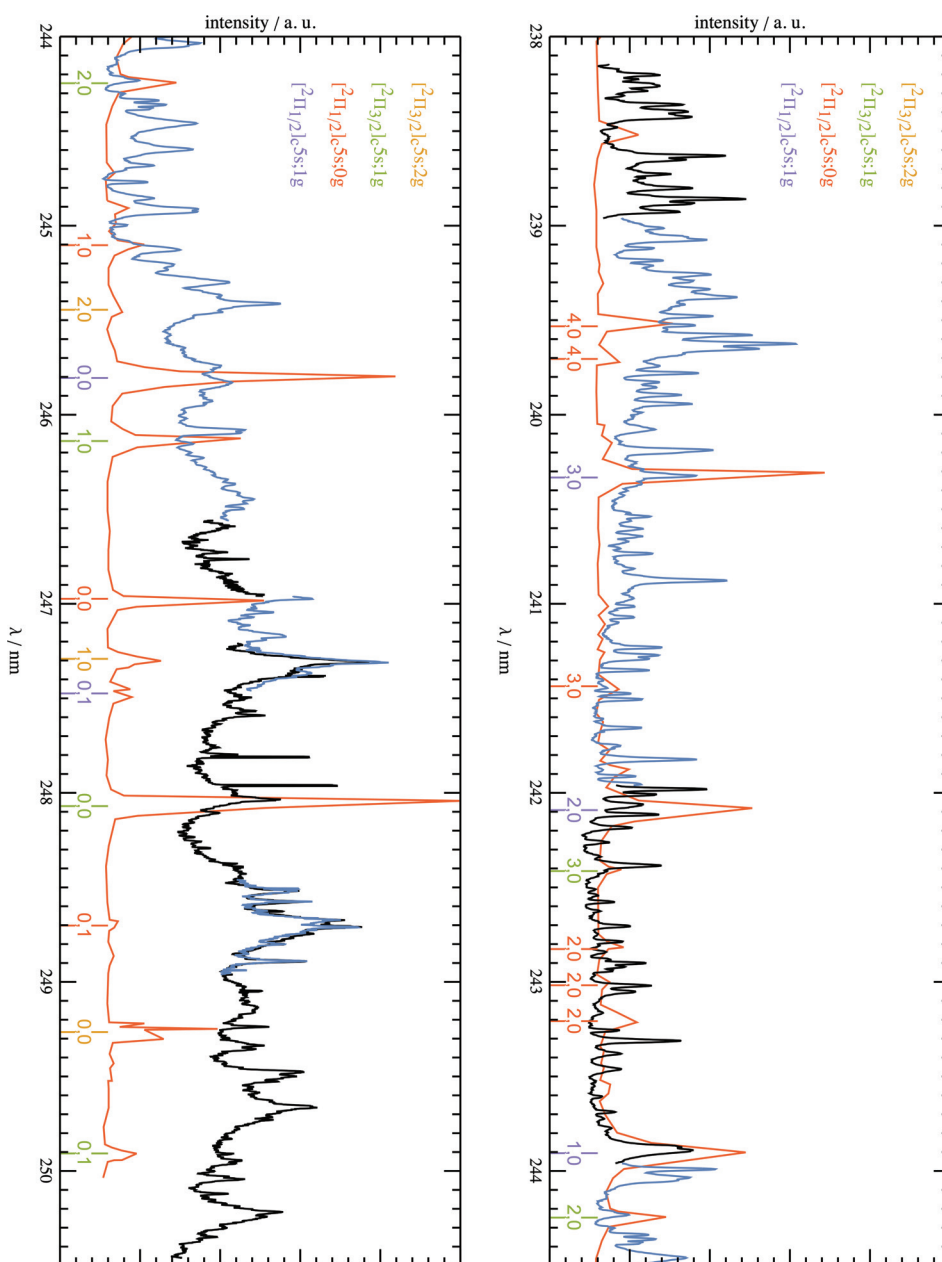


Figure 3.46 REMPI spectrum in a wavelength range of 238.2 – 250.5 nm where (2+1) REMPI transitions of Cl_2 via 5s RYDBERG states were reported [101]. Depicted by the solid black and blue lines are individual wavelength scans that were stitched together since the UV laser could not be scanned for the entire range at once. The data was recorded when the molecular beam containing HCl molecules with an incidence energy of $\langle E_i \rangle = 2.5$ eV was scattered from the surface at $T_s \approx 1073$ K. Additionally shown as solid red lines are the transitions given in literature for jet-cooled $^{35}\text{Cl}_2$. Colored pairs of numbers below the spectrum indicate the corresponding transitions in the form of (v', v'') where the color denotes the intermediate RYDBERG state as given in the plot legend. The spectrum of Cl_2 coming from the hot surface exhibits a much higher line density, probably due to the increased number of populated states.

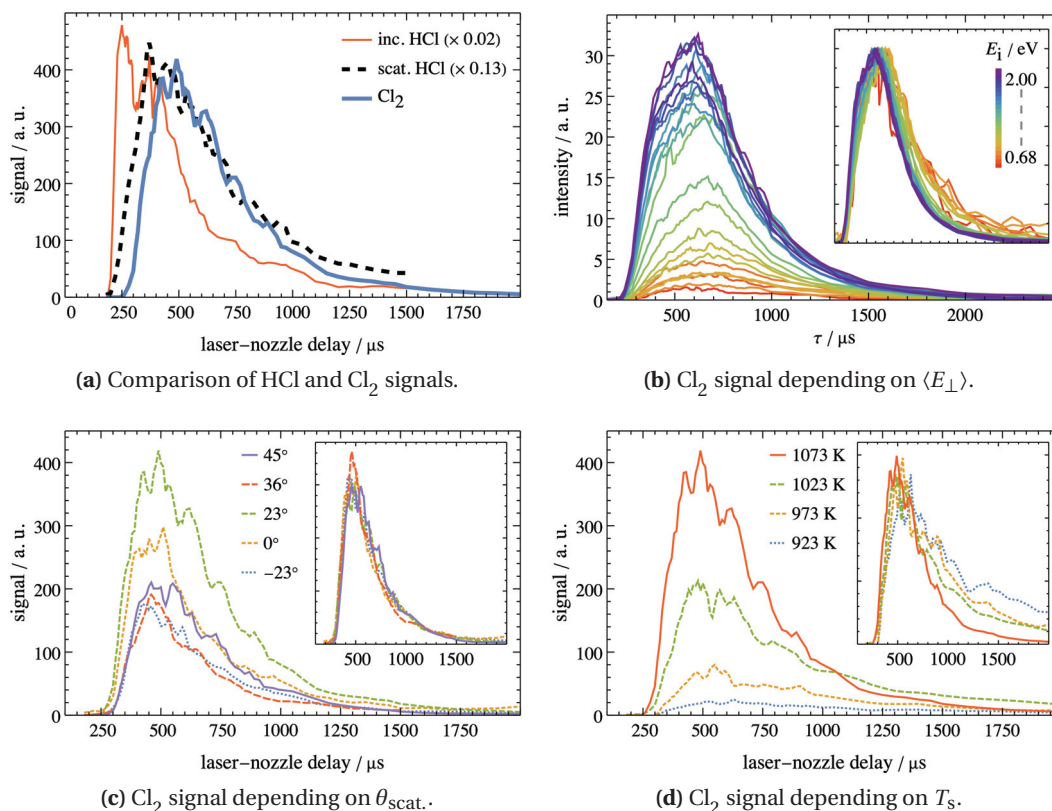


Figure 3.47 Arrival time distributions of Cl₂ at the laser detection spot depending on different experimental parameters. In panel a), the recorded signal of Cl₂ desorbing from the surface at 1073 K in dependence on the laser-nozzle delay τ is shown as a solid blue line in comparison to the incident HCl beam as a solid red line and the scattered HCl beam as a dashed black line. The incident beam is rather broad due to the nozzle tip being heated. As can be read from the plot legends, Cl₂ signal was approximately eight times less intense than the HCl signal and started to appear later at the detector. The Cl₂ signal was highly dependent on the incidence energy of the HCl molecules and increased strongly when the latter was changed from 0.68 – 2.0 eV (panel b). Moreover, the peak of the Cl₂ signal shifted to earlier times and the peak normalized distribution became narrower (see inset of panel b). While the signal intensity also depended on the scattering angle and was maximal around the surface normal (which corresponded to 26°, see the dashed green line in panel c), the width was independent of $\theta_{\text{scat.}}$. However, both were dependent on the surface temperature (panel d): with increasing T_s , the peak intensity increased while its width decreased.

4 Scattering HCl from Ag(111)

While HCl molecules had been scattered from Au(111) before, to the best of my knowledge no reports exist on scattering HCl from Ag(111). Nevertheless, in the past fruitful comparisons of scattering NO and CO from Au(111) and Ag(111) were drawn [34, 102, 103]. There, larger nonadiabatic interactions were observed in the case of Ag(111) which was associated with its lower work function of $\phi = 4.7$ eV compared to $\phi = 5.3$ eV for Au(111). I thus considered a comparison of the previously obtained data for Au(111) with Ag(111) to be worthwhile.

4.1 Vibrational Excitation

The general considerations and procedures for measuring VEPs for HCl scattering from Ag(111) were the same as for scattering from Au(111). The reader is thus referred to Sec. 3.1 for further information about the rationale behind the VEP calculation.

4.1.1 Excitation from $\nu = 0 \rightarrow 1$

As described before, the incident molecular beam was scattered from the surface and detected in the direction of the specular scattering using the UV laser. The most important experimental parameters used for measuring the individual data sets are shown in Tab. 4.1. In Fig. 4.1 representative REMPI spectra for an incidence energy of $\langle E_i \rangle = 0.66$ eV are shown. As seen for Au(111), the signal in the incident vibrational state $\nu = 0$ remains approximately the same when the surface temperature T_s is increased from 400 K (top panel) to 900 K (bottom panel).¹ However, the signal of $\nu = 1$ grows with increasing surface temperature. Since according to Eq. 3.2 the REMPI signal is proportional to the population in the corresponding quantum state, the vibrational excitation $\nu = 0 \rightarrow 1$ increases with T_s .

¹ Overall, the integrals of the spectra decline slightly with temperature. This decrease is much less pronounced than the increase in $\nu = 1$.

Table 4.1 Experimental parameters for measuring the $\nu = 0 \rightarrow 1$ excitation of HCl on Ag(111). $\langle E_i \rangle$ is the incidence translational energy, $U(\text{MCP})$ the detector voltage, $\langle E_L \rangle$ the approximate average laser power, and θ the approximate scattering angle. Shown are usual values that might have been adapted for individual measurements when needed.

Gas Mixture	$\langle E_i \rangle$ in eV	ν State	$U(\text{MCP})$ in V	$\langle E_L \rangle$ in mJ	θ in $^\circ$
8% HCl in H ₂	0.66	$\nu = 0$	1400	~1.1	~22
		$\nu = 1$	1950	~2.4	~22
6% HCl in H ₂	0.86	$\nu = 0$	1400	~1.0	~22
		$\nu = 1$	1950	~2.3	~22
3% HCl in H ₂	1.00	$\nu = 0$	1400	~1.3	~22
		$\nu = 1$	1950	~2.7	~22
2% HCl in H ₂	1.15	$\nu = 0$	1500	~0.7	~17
		$\nu = 1$	1950	~2.3	~17

In the following paragraphs I will show examples of the correction factors and functions for selected experimental conditions needed to calculate the VEPs.

Average Velocity $\langle u_\nu \rangle$

As explained for $\nu = 0 \rightarrow 1$ excitation on Au(111), I was unable to measure TOF spectra of molecules excited to $\nu = 1$ due to the low signal levels. Thus, I again had to assume that the velocity of molecules in $\nu = 0$ was ~22% higher than that of molecules in $\nu = 1$ (see Sec. 3.1.2).

Angular Distribution $\Theta_\nu(\theta_\nu)$

Figures 4.2 and 4.3 show angular distributions for HCl molecules with incidence energies of $\langle E_i \rangle = 0.66 - 1.24$ eV scattered from the Ag(111) surface at different temperatures in $\nu = 0$ and $\nu = 1$. For all incidence energies and detected vibrational states, probable distortions can be seen for scattering angles lower than approximately -10° . Since they seem to be present at every experimental condition (see Tab. 4.1) I assign them to problems with the experimental setup and not to actual features of the angular distributions.² A similar peculiarity can be seen for angles greater than $\sim 10^\circ$. On this side of the surface normal, however, a second distinct bump or peak is only visible for molecules scattered in $\nu = 1$. This might either be due to the much higher MCP voltage used here or could resemble a real feature of the scattering dynamics. Interestingly, in his work on HCl recombinative desorption from Au(111) Charles Rettner saw angular distributions for

² It must be noted though that on this side of the surface normal no distortion was seen on Au(111). There, similar oddities appeared at detection spots on the other side, i. e. closer to the detector (see Fig. 3.4).

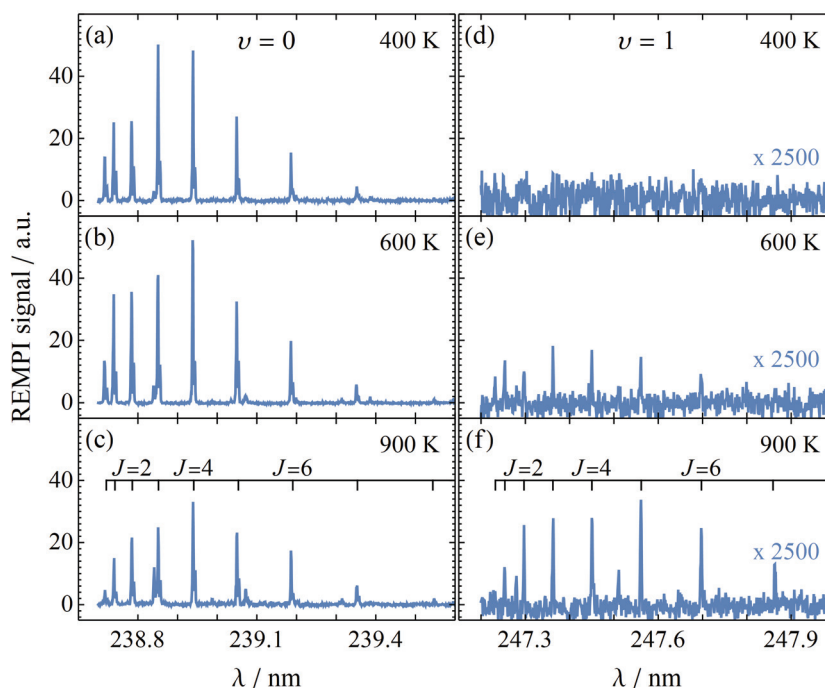


Figure 4.1 Representative REMPI spectra of HCl molecules scattered from Ag(111) at three different surface temperatures. Shown are spectra in the wavelength range of $\nu = 0$ (a–c) and $\nu = 1$ (d–f) recorded at $\langle E_i \rangle = 0.66$ eV that have only been corrected for laser power. While the signal is arbitrarily scaled, the relative scale is the same for all six panels. The spectra for $\nu = 1$ are magnified by a factor of ~ 2500 relative to the spectra for $\nu = 0$. Additional lines not assigned to a certain J state belong to different transitions *via* the $V^1\Sigma^+$ state (see Sec. 2.3.2).

certain desorbing vibrational states with what he described as a "doughnut" shape [104]. That is, the distribution had a minimum at $\theta = 0$ and two maxima around -25° and 25° . Although that distribution was assigned to molecules in $\nu = 0$ and not $\nu = 1$, the mere observation of HCl angular distributions that do not follow cosine behavior is noteworthy. Additionally, similar observations were made in a theoretical study of this surface reaction [105]. Independent of the shapes' origin, Figs. 4.2 and 4.3 show fits to the data as solid lines. Here, only the "core" data around $\theta = 0$ was considered in the fitting process. Based on the fitted exponents given in Tab. 4.2 I have observed direct scattering under all conditions. Since the cosine function did not reproduce the experimental data properly, the correction factors for the VEP calculation were determined in the same way as the for scattering from Au(111). That is, the signal intensity detected at the same angle where also the VEP measurements were carried out were divided by the sum of the intensity at all angles. The resulting correction factors are shown in the last column of Tab. 4.2. In general, these corrections are close to unity since the angular distributions are not too different for both vibrational states. However, the values for molecules in $\nu = 1$ are lower than those for $\nu = 0$ because the detection angle of $\sim 15^\circ$ is located in a "dip" resulting in a relatively lower contribution to the overall angular distribution. This is clearly visible in Fig. 4.2 (f) and

Fig. 4.3 (b), for example.

Table 4.2 Cosine fitting parameters of angular distributions for the $\nu = 0 \rightarrow 1$ excitation of HCl on Ag(111). $\langle E_i \rangle$ is the incidence translational energy, $U(\text{MCP})$ the detector voltage, and T_s the surface temperature. n is the fitted exponent of the cosine function (Eq. 3.4) and θ_0 the angle where the distribution peaks. *c-fac.* is the correction factor for the VEP calculation (see text).

$\langle E_i \rangle$ in eV	ν State	$U(\text{MCP})$ in V	T_s in K	n	θ_0 in $^\circ$	c-fac.
0.66	$\nu = 0$	1400	500	19	2	1
			900	13	2	1
	$\nu = 1$	1950	500	15	-1	0.84
			900	16	1	0.78
0.86	$\nu = 0$	1450	500	21	-1	1
	$\nu = 1$	1950	500	13	2	0.91
1.00	$\nu = 0$	1400	900	13	3	1
	$\nu = 1$	1950	900	14	3	0.67
1.15	$\nu = 0$	1550	350	13	2	-
		1500	650	13	2	-
		1500	900	15	2	-
	$\nu = 1$	1950	900	-	-	-

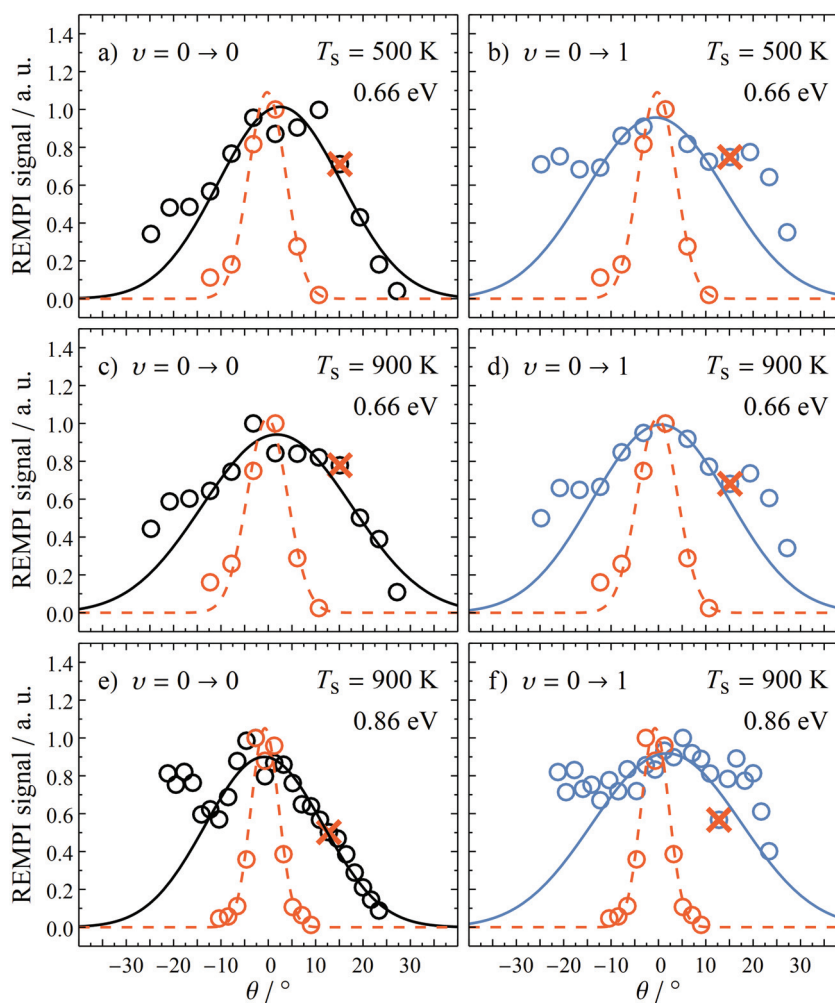


Figure 4.2 Angular distributions for molecules with $\langle E_i \rangle = 0.66\text{ eV}$ coming back from the surface at $T_s = 500\text{ K}$ in (a) $\nu = 0$ (black) and (b) $\nu = 1$ (blue) and at $T_s = 900\text{ K}$ in (c) $\nu = 0$ and (d) $\nu = 1$. In e) and f), the incidence energy was $\langle E_i \rangle = 0.86\text{ eV}$ and $T_s = 900\text{ K}$. In all panels, the solid lines depict a fit to the data according to $a \times \cos^n(\theta - \theta_0) + c$ while red data points and the dashed line depict the incident molecular beam. The red crosses mark the data points at the angle at which the REMPI spectra for the VEPs were measured.

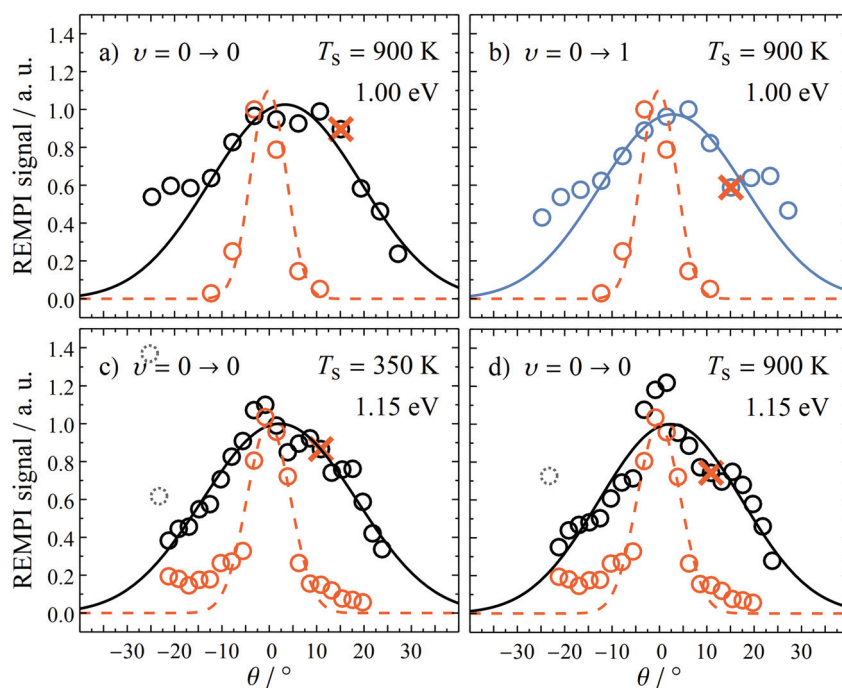


Figure 4.3 Angular distributions for molecules with $\langle E_i \rangle = 1.00$ eV coming back from the surface at $T_s = 900$ K in (a) $\nu = 0$ (black) and (b) $\nu = 1$ (blue). In (c) and (c), the incidence energy was $\langle E_i \rangle = 1.15$ eV while the surface temperature was $T_s = 350$ K and $T_s = 900$ K, respectively. At $\langle E_i \rangle = 1.15$ eV no angular distribution could be measured for $\nu = 0 \rightarrow 1$ because the S/N was too low (probably due to the low concentration of HCl in the gas mixture). In all panels, the solid lines depict a fit to the data according to $a \times \cos^n(\theta - \theta_0) + c$ (for which the data points with a dotted outline in (c) and (d) were omitted) while red data points and the dashed line depict the incident molecular beam. The red crosses mark the data points at the angle at which the REMPI spectra for the VEPs were measured.

Temporal Distribution $\Delta_\nu(\tau_\nu)$

As before, the signal intensity was recorded while the time delay τ_ν between the nozzle opening and the firing of the UV laser was scanned for different surface temperatures. For incidence energies of $\langle E_i \rangle = 0.66$ eV, 0.86 eV, and 1.00 eV the temporal distributions of molecules in different final vibrational states were similar in shape but exhibited slightly more intensity at the second (and in some cases third) peak visible in all arrival time distributions (Figs. 4.4, 4.5, and 4.6 a–c). At the highest incidence energy of $\langle E_i \rangle = 1.15$ eV the distributions were slightly different in shape and exhibit deviating peak positions, see Fig. 4.6 d–f. Since the distributions shifted towards a better overlap at higher temperatures (Fig. 4.6 f) one reason for the deviations might be the worse S/N for this highly diluted gas mixture especially at low temperatures for $\nu = 1$. Multiple peaks could be attributed to their counterparts in the incident beam (dashed green line) which were also separated by approximately the same time span of $\sim 100\mu\text{s}$ and were probably caused by a faulty nozzle controller. Only for $\langle E_i \rangle = 0.86$ eV there was no distinct second peak in the incident beam due to a new nozzle controller used in these experiments. Yet there was a broader shoulder/second peak and a small third peak in the temporal distributions of the scattered molecules for $\nu = 0$ as well as $\nu = 1$.

Temporal correction factors are calculated by dividing the signal intensity at the timing used for recording the REMPI spectra by the integral of the total distribution (see Eq. 3.6). Again, for a better comparability relative correction factors are defined (setting $\Delta_0 = 1$). The resulting T_s dependent Δ_1/Δ_0 are shown in Fig. 4.7. In general, Δ_1/Δ_0 seems to increase with the surface temperature. Except for $\langle E_i \rangle = 1.15$ eV, where the raw data is not convincing, it is above unity since the distributions are slightly broader for molecules in $\nu = 0$. Since the temporal corrections were not measured at every

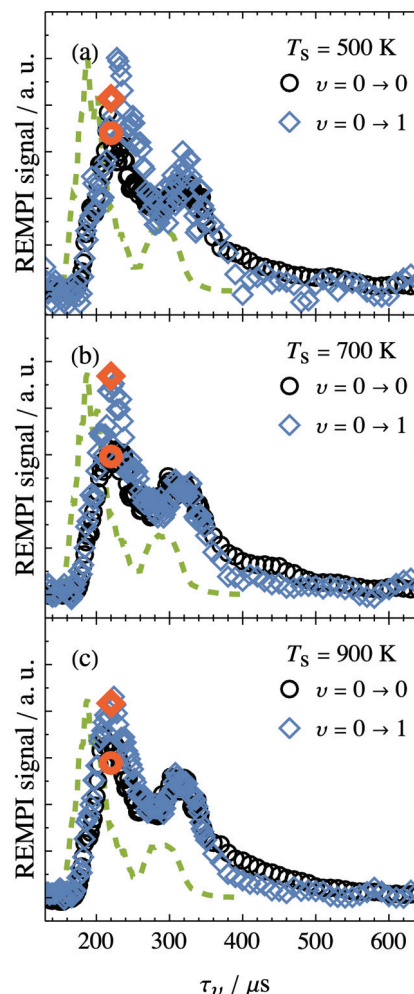


Figure 4.4 Temporal distributions for molecules with $\langle E_i \rangle = 0.66$ eV coming back in $\nu = 0$ (black symbols) and $\nu = 1$ (blue symbols) at surface temperatures of $T_s = 500$ K (a), 700 K (b), and 900 K (c). All distributions were normalized to their respective integral. While the timings at which the REMPI spectra were recorded are marked with red symbols, the incident beam is shown as a dashed green line. Here, τ_ν is the time that has passed after the nozzle opened.

T_s at which VEPs were determined, the intermediate corrections were interpolated.

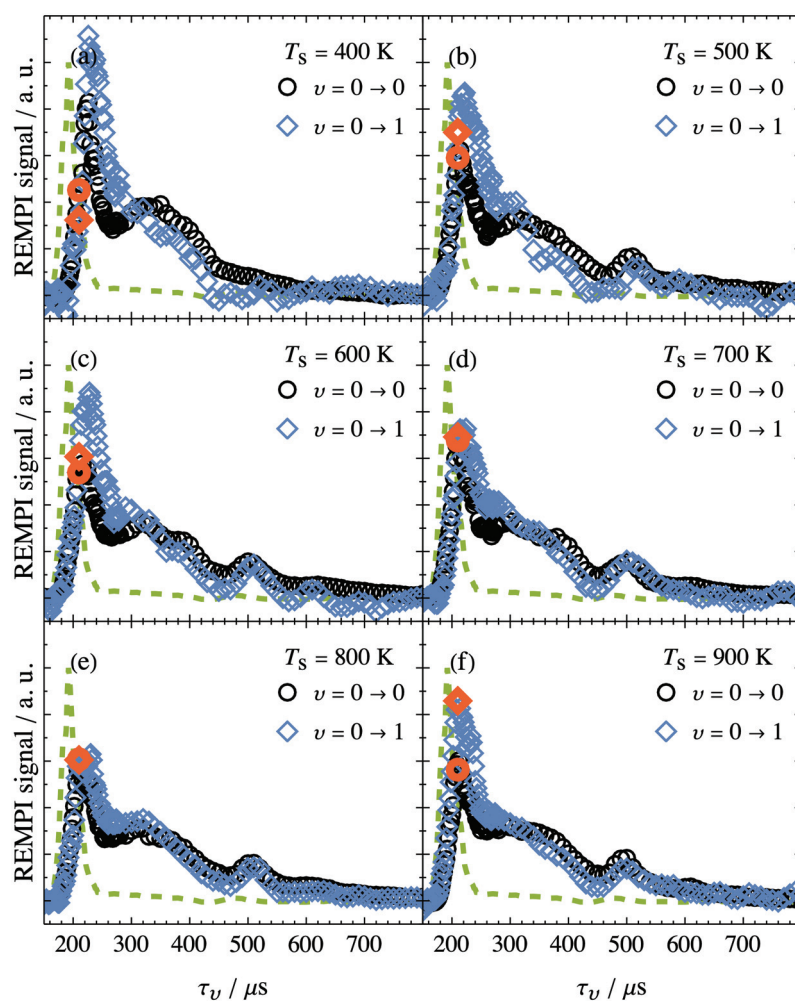


Figure 4.5 Temporal distributions for molecules with $\langle E_i \rangle = 0.86$ eV coming back in $v = 0$ (black symbols) and $v = 1$ (blue symbols) at surface temperatures of $T_s = 400 - 900$ K. All distributions were normalized to their respective integral. While the timings at which the REMPI spectra were recorded are marked with red symbols, the incident beam is shown as a dashed green line. Here, τ_ν is the time that has passed after the nozzle opened.

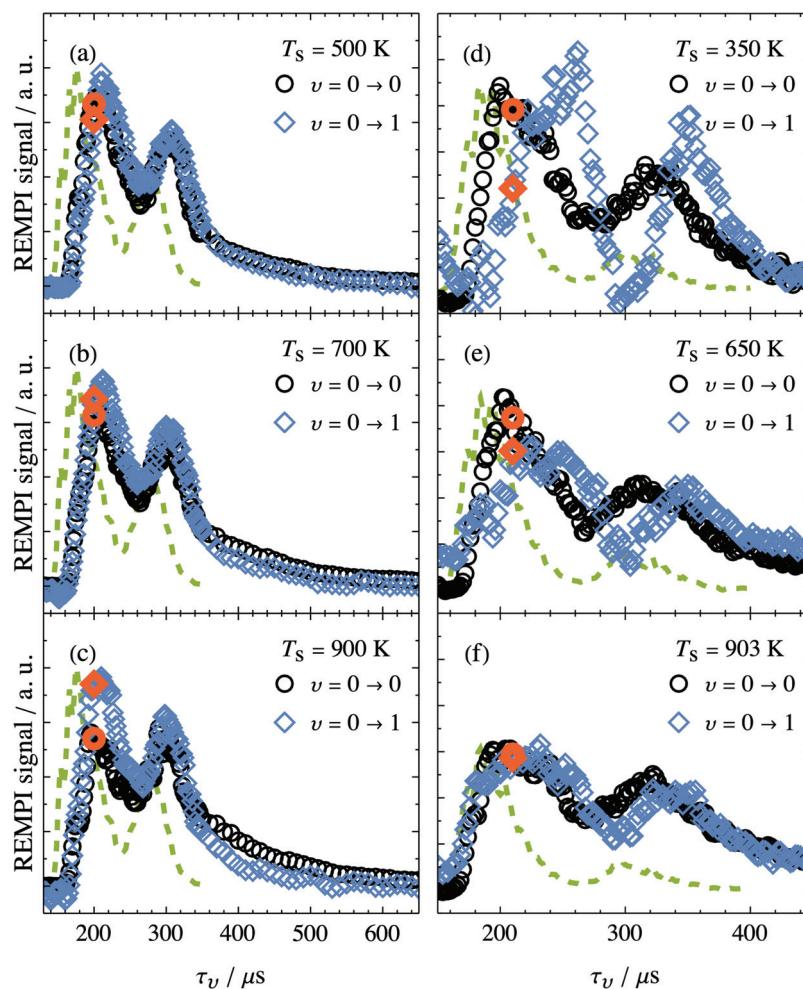


Figure 4.6 Temporal distributions for molecules with $\langle E_i \rangle = 1.00\text{ eV}$ (a–c) and 1.15 eV (d–e) coming back in $v = 0$ (black symbols) and $v = 1$ (blue symbols) at surface temperatures of $T_s = 400 - 900\text{ K}$. All distributions were normalized to their respective integral. While the timings at which the REMPI spectra were recorded are marked with red symbols, the incident beam is shown as a dashed green line. Here, τ_v is the time that has passed after the nozzle opened.

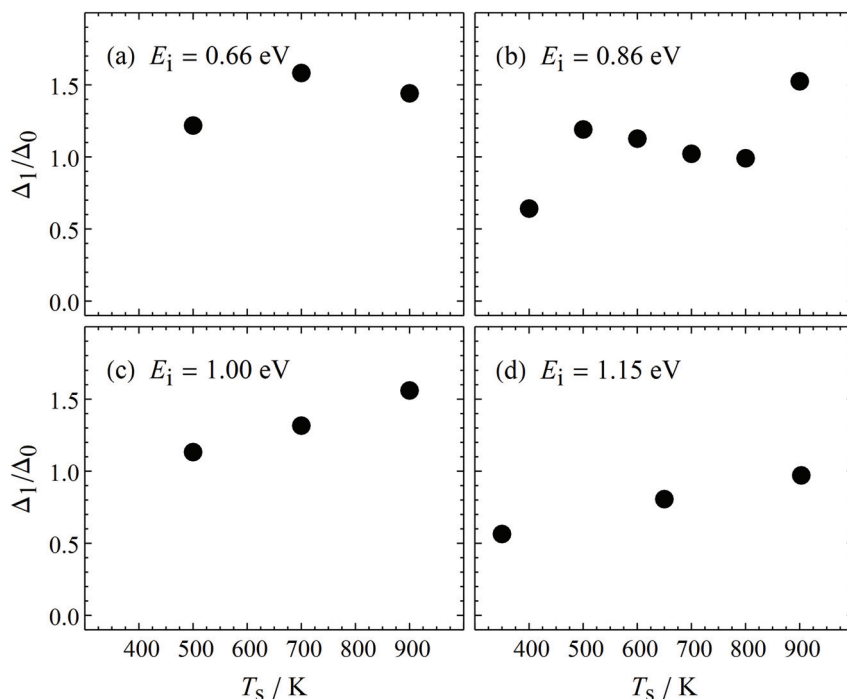


Figure 4.7 Ratio of the temperature dependent correction factors Δ_1/Δ_0 for different temporal dilutions of molecules with $\langle E_i \rangle = 0.66 - 1.15$ eV scattered from Ag(111) in $\nu = 0$ and $\nu = 1$ at different surface temperatures. In general, Δ_1/Δ_0 seems to increase with T_s since the temporal distributions of molecules in $\nu = 1$ tend to broaden more with temperature than those of $\nu = 0$.

Detector Gain Γ_ν

Since a considerable amount of time had passed between the measurements of vibrational excitation on Au(111) and Ag(111) I re-investigated the dependence of the detected signal intensity on the detector voltage. In contrast to previous experiments I did not use a static pressure of background gas but the actual molecular beam of HCl in H_2 for these measurements. Yet the same limitations also applied here: It was not possible to cover the whole range of detector voltages with one set of experimental conditions since either the signal saturated or vanished in the noise. Thus, the range $U(\text{MCP}) = 1200 - 1950$ V was divided into two or three overlapping parts that were scaled afterwards.

In Tab. 4.3 and Fig. 4.8 the MCP voltages with the corresponding detector gain Γ_ν and the inverted detector gain Γ_ν^{-1} are shown, where Γ_ν is the averaged, integrated oscilloscope trace of HCl^+ and H^+ ions (molecular fragments) relative to the highest detector gain at 1950 V. From both it can be seen that the dynamic range of the detection setup spans approximately four orders of magnitude. In comparison to the previous curve (Tab. 3.2 and Fig. 3.7) the deviations at $U(\text{MCP}) = 1200$ V and $U(\text{MCP}) > 1600$ V are less than 10 %. In between, the old gain values were up to 83 % higher (maximum deviation at 1350 V). It has

to be noted that in contrast to scattering from Au(111) the different data sets were fitted with the sum of two logistic functions and subsequently averaged.

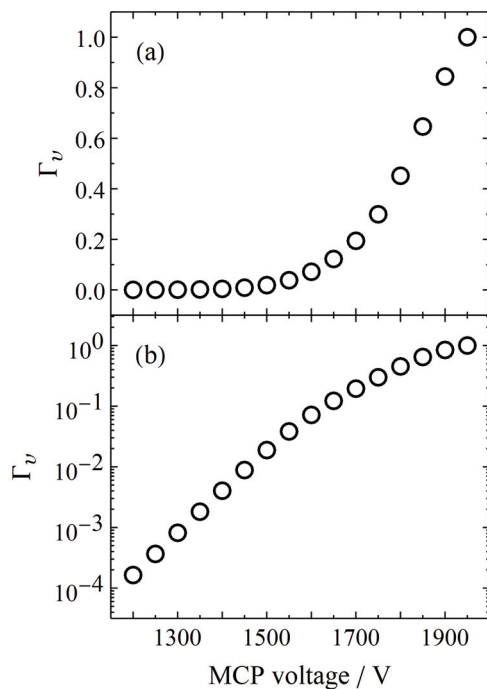


Figure 4.8 Normalized detector gain factor Γ_v depending on MCP voltage on a linear (a) and a logarithmic (b) scale.

Table 4.3 Normalized detector gain factor Γ_v depending on MCP voltage for scattering HCl from Ag(111).

$U(\text{MCP})$ in V	Γ_v	Γ_v^{-1}
1200	0.00016	6100.
1250	0.00037	2700.
1300	0.00082	1200.
1350	0.0018	550.
1400	0.0040	250.
1450	0.0088	110.
1500	0.019	53.
1550	0.038	26.
1600	0.072	14.
1650	0.12	8.2
1700	0.19	5.1
1750	0.30	3.3
1800	0.45	2.2
1850	0.65	1.5
1900	0.84	1.2
1950	1.0	1.0

Laser Power Correction $\Pi(\pi_v)$

In Fig. 4.9 the laser energy dependent signal intensity is shown for scattered molecules in $v = 0$ (black and grey) and $v = 1$ (dark and light blue) for $\langle E_i \rangle = 0.66 - 1.15$ eV. Compared to the laser power dependencies measured for scattering from Au(111), there are two differences. First, except for $\langle E_i \rangle = 1.15$ eV the ion signals for both H^+ and HCl^+ were detected and analyzed independently. Second, instead of a power law a sigmoidal fit according to Eq. 4.1 was applied because it reproduced the raw data better in most cases.

$$\Pi(\pi_v) = \frac{a}{1 + \exp[b \cdot \pi_v + c] + d} \quad (4.1)$$

Since different regimes of π_ν needed to be used for measuring the REMPI spectra, both data and fit were normalized to the measured intensity at $\pi_\nu = 1.2$ mJ and $\pi_\nu = 1.4$ mJ for (a)–(b) and (c)–(d), respectively. For the correction of the VEP calculation only the ν state depending changes in intensity relative to those fixed values are important. Yet, as noted for HCl/Au(111), the slopes and curvatures of the curves in Fig. 4.9 can be explained by the same statistical effects as given for the $\nu = 0 \rightarrow 1$ channel in Sec. 3.1.1. Only for the highest incidence energy of 1.15 eV shown in panel (d), which was obtained by the highest dilution of HCl in H_2 and where only the HCl^+ signal was recorded, the results are not that unambiguous. It might well be that the ionization step of the (2 + 1) REMPI process was actually not saturated as suggested by the plateau of the fitting function for $\pi_\nu > 2$ mJ/Pulse. However, since for measuring the VEP data only laser powers were used in the range where actual data points are available in panel (d), the fits were sufficient as correction functions.

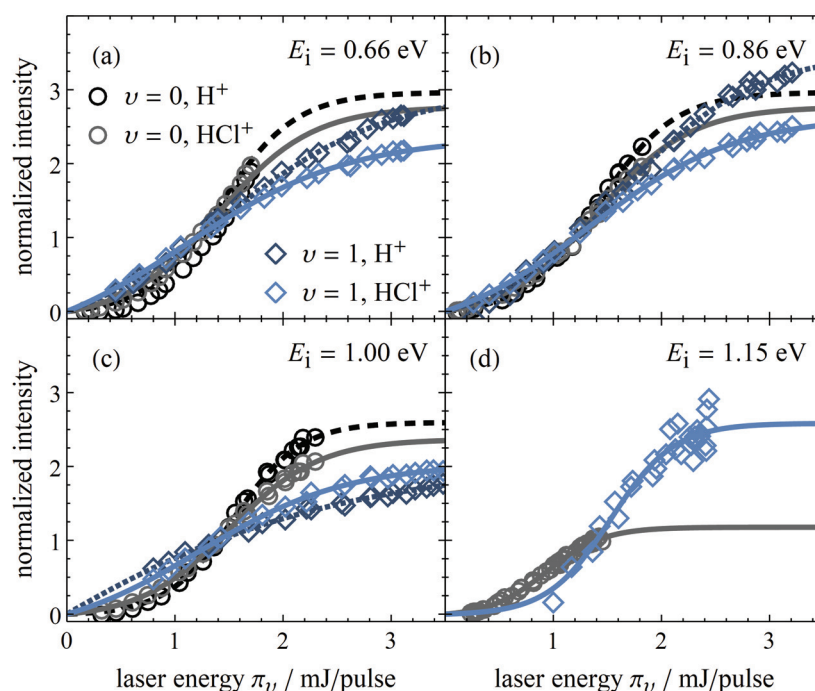


Figure 4.9 Signal intensity depending on the laser pulse energy π_ν for molecules in $\nu = 0$ and $\nu = 1$ at all four incidence energies. Shown is the raw data for $\nu = 0$ depicted by open symbols (black and grey) and for $\nu = 1$ (dark and light blue) as well as sigmoidal fits to this data (solid and dashed lines). While in (a) and (b), data is normalized to the intensity at $\pi_\nu = 1.2$ mJ, in (c) and (d) it is normalized to the intensity at $\pi_\nu = 1.4$ mJ.

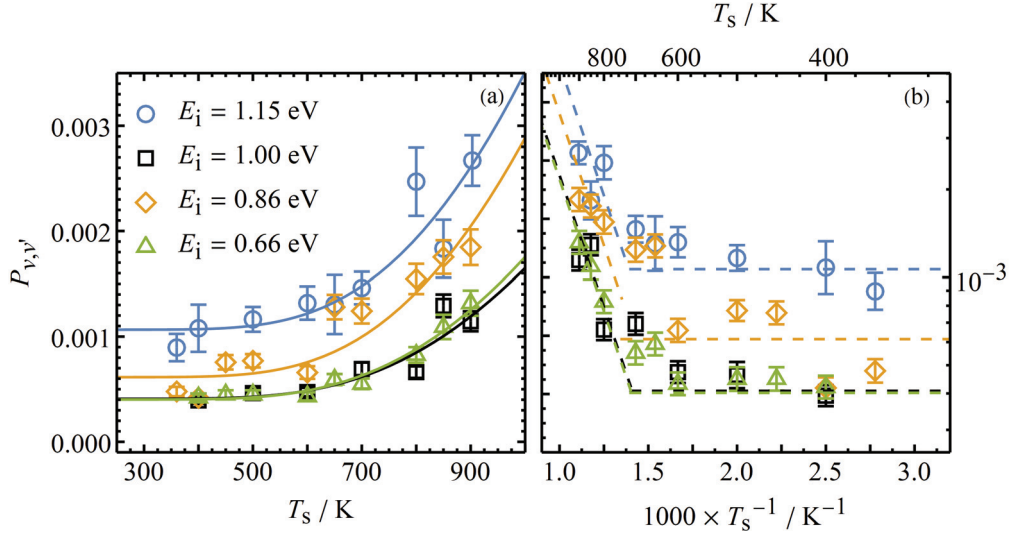


Figure 4.10 Vibrational excitation probabilities for $\nu = 0 \rightarrow 1$ excitation of HCl molecules scattered from Ag(111). The solid lines in both panels depict fits to the data according to Eq. 3.8 while the dashed lines in (b) visualize the individual exponential (inclined line) and constant terms (horizontal line).

Calculation of Vibrational Excitation Probabilities

In Sec. 3.1 the general approach of calculating excitation probabilities was presented. For the case of $\nu = 0 \rightarrow 1$ excitation, the VEP was defined in Eq. 3.7 as

$$P_{0,1} \approx \frac{N_1}{N_1 + N_0} \quad (3.7 \text{ revisited})$$

where N_i is the population in the corresponding vibrational state. Calculating the (relative) populations N_0 and N_1 according to Eqs. 3.1 and 3.2 leads to the temperature and incidence energy dependent VEPs shown in Fig. 4.10. As seen on Au(111), the excitation probabilities increase with incidence energy as well as surface temperature. One exception here is the data set recorded at $\langle E_i \rangle = 1.00$ eV. Although the set by itself is consistent concerning the T_s dependence, its absolute scaling seems to be incorrect with regard to the other data sets.

As on Au(111), the VEPs cannot be fitted with a single exponential function (Eq. 1.1). Instead, an additional offset as in Eq. 3.8 is needed which can be seen in the logarithmic plot in Fig. 4.10 (b). Here the exponential term, whose negative slope is determined by the vibrational spacing of the $\nu = 0 \rightarrow 1$ excitation, and the constant are depicted by the dashed lines. Again, based on $A^{\text{ad.}}$ and $A^{\text{nonad.}}$ in Tab. 4.4, the nonadiabatic interaction is approximately two orders of magnitude stronger than the adiabatic one. This can also be seen from the incidence energy independent quantities $\frac{dA^{\text{nonad.}}}{dE_i}$ and $\frac{dA^{\text{ad.}}}{dE_i}$ in Tab. 4.5 which resemble the slopes of linear fits to the data (see dashed lines in Fig. 4.11). While $\frac{dA^{\text{ad.}}}{dE_i}$ is the same as for scattering from Au(111), $\frac{dA^{\text{nonad.}}}{dE_i}$, i. e. the nonadiabatic interaction strength,

is larger on Ag(111). Interestingly, the energetic threshold for the electronically adiabatic excitation at $\langle E_i \rangle = 0.37 \text{ eV}$ approximately corresponds to the vibrational spacing of the $\nu = 0 \rightarrow 1$ excitation.

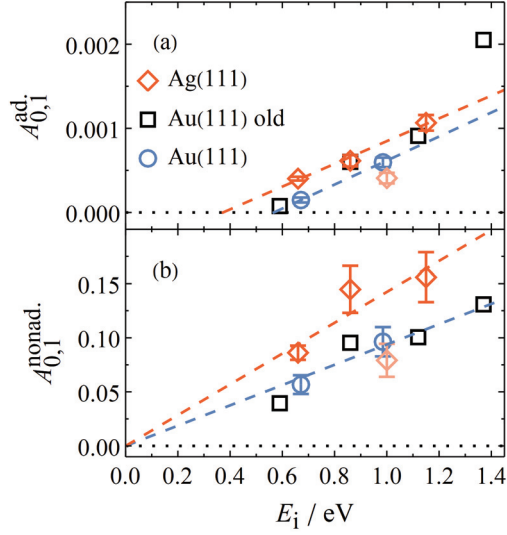


Figure 4.11 Interaction strength constants $A^{\text{ad.}}$ (a) and $A^{\text{nonad.}}$ (b) for $\nu = 0 \rightarrow 1$ excitation on Ag(111) plotted against the incidence energy E_i . The dashed lines indicate linear fits for which the semitransparent data at $\langle E_i \rangle = 1.00 \text{ eV}$ was omitted (see text). While the intersection with the x -axis is not marked here, the threshold is at $\langle E_i \rangle = 0.37 \text{ eV}$ which is very close to the vibrational spacing.

Table 4.4 Interaction strength constants $A^{\text{ad.}}$ and $A^{\text{nonad.}}$ for $\nu = 0 \rightarrow 1$ excitation on Ag(111).

$\langle E_i \rangle / \text{eV}$	$A^{\text{ad.}}$	$A^{\text{nonad.}}$
0.66	4.0×10^{-4}	8.6×10^{-2}
0.86	6.1×10^{-4}	1.4×10^{-1}
1.00	4.1×10^{-4}	7.9×10^{-2}
1.15	1.1×10^{-3}	1.6×10^{-1}

Table 4.5 $\frac{dA^{\text{ad.}}}{dE_i}$ and $\frac{dA^{\text{nonad.}}}{dE_i}$ derived from Figs. 4.10 and 4.11.

$\nu \rightarrow \nu'$	$\frac{dA^{\text{ad.}}}{dE_i} / \frac{1}{\text{eV}}$	$\frac{dA^{\text{nonad.}}}{dE_i} / \frac{1}{\text{eV}}$
$0 \rightarrow 1$	1.4×10^{-3}	1.4×10^{-1}

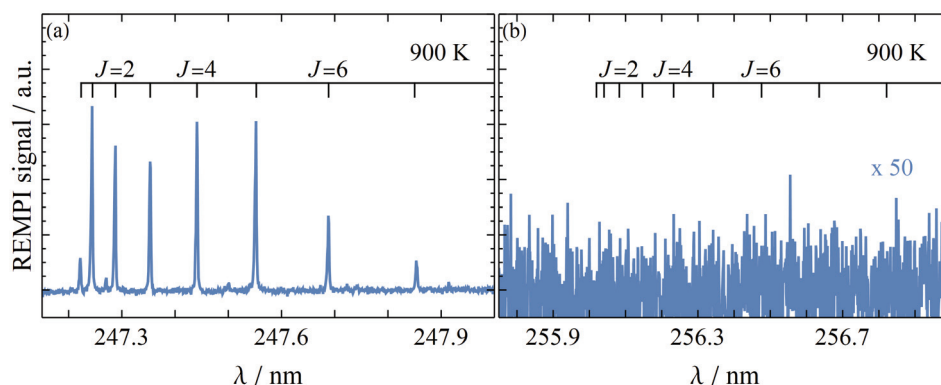


Figure 4.12 Representative REMPI spectra of HCl molecules scattered from Ag(111) at a surface temperatures of $T_s = 900$ K. Shown are spectra in the wavelength range of $v = 1$ (a) and $v = 2$ (b) recorded at $\langle E_i \rangle = 0.79$ eV that have only been corrected for laser power. While the signal is arbitrarily scaled, the relative scale is the same for both panels. The spectrum for $v = 2$ is magnified by a factor of ~ 50 relative to the spectrum for $v = 1$.

4.1.2 Excitation from $v = 1 \rightarrow 2$

Following the results on Au(111), I expected to detect HCl $v = 1 \rightarrow 2$ excitation on Ag(111) *via* molecules leaving the surface in $v = 2$ if they get excited to $v = 1$ prior to the collision. However, I could not detect HCl molecules in vibrational state $v = 2$ *via* REMPI for any of the experimental conditions mentioned above in Tab. 4.1. Fig. 4.12 shows a representative comparison of a REMPI spectrum for molecules scattered elastically in $v = 1$ (a) and the wavelength range where spectral lines of molecules in $v = 2$ are expected (b). As can be seen from the comb of rotational states above the spectrum in panel (b), not a single J state could be detected. Instead, the S/N in the spectra for $v = 2$ was much worse than for the measurements on Au(111). One reason could have been that at 900 K the vapor pressure of solid silver is approximately two orders of magnitude larger than that of gold (cf. Ref. [68]). High numbers of Ag atoms hitting the MCP might have contributed to the increased noise masking the actual signal.

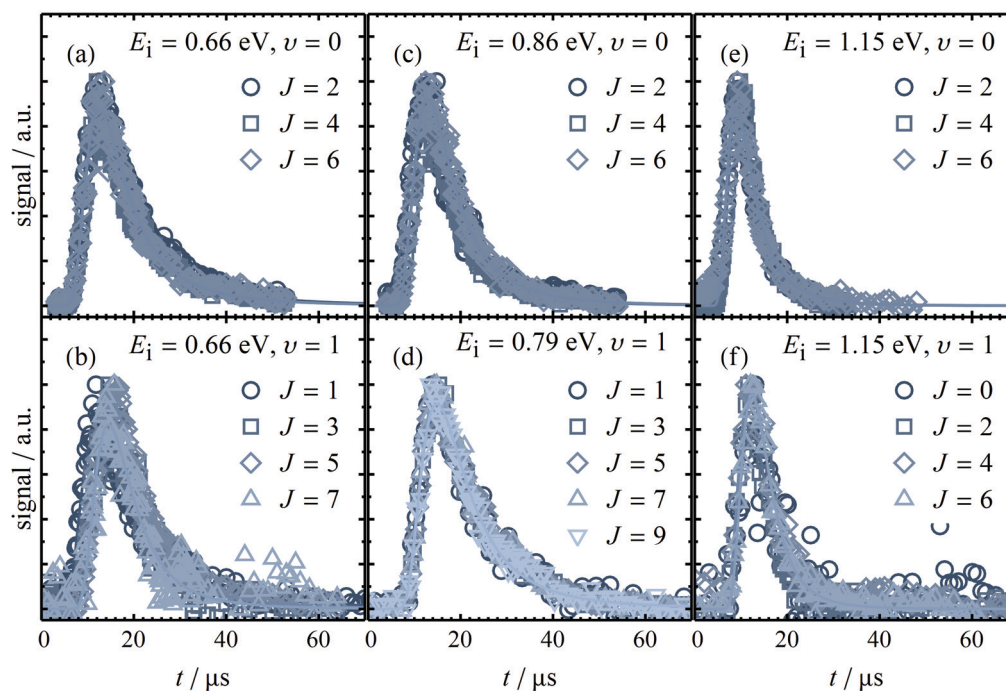


Figure 4.13 TOF distributions of HCl molecules scattered from Ag(111) at $T_s = 900\text{K}$ in different ro-vibrational states. For three different incidence energies, distributions of several rotational states are shown for $\nu = 0 \rightarrow 0$ (a,c,e) and $\nu = 1 \rightarrow 1$ (b,d,f) scattering. The incidence energy in panel (d) was slightly differing from panel (c) because a different gas mixture had to be used. Depicted by solid lines are fits to the data according to Eq. 2.3 in the appendix. There is no clear trend within the data for one $\langle E_i \rangle$ and ν state but with increasing $\langle E_i \rangle$ molecules tended to arrive earlier.

4.2 Translational Inelasticity

Since I did not detect any molecules being excited from $\nu = 1$ to $\nu = 2$, velocity distributions of HCl molecules having experienced vibrational excitation could not be determined. Thus, differences in the transfer of molecular kinetic energy to or from the surface and the intramolecular coupling of vibrational to translational energy could also not be investigated. However, I examined kinetic energy transfer to the Ag(111) surface and translational to rotational energy coupling for $\nu = 0 \rightarrow 0$ and $\nu = 1 \rightarrow 1$ scattering, i. e., for vibrationally elastic channels. To do so, I either tagged HCl molecules after they had hit the surface ($\nu = 0 \rightarrow 0$) or in front of the surface right before the collision ($\nu = 1 \rightarrow 1$). The used laser geometry can be seen in Fig. 2.9.

Figure 4.13 shows time-of-flight distributions for both scattering channels with incidence energies of 0.66 – 1.15 eV at a surface temperature of $T_s = 900\text{K}$.³ In each panel data for 3 – 5 J states is given as open symbols while solid lines denote fits to the data according to

³ In panel (d) of Fig. 4.13 a gas mixture had to be used which differed slightly in concentration from the one in panel (c). Thus the incidence energy was somewhat lower.

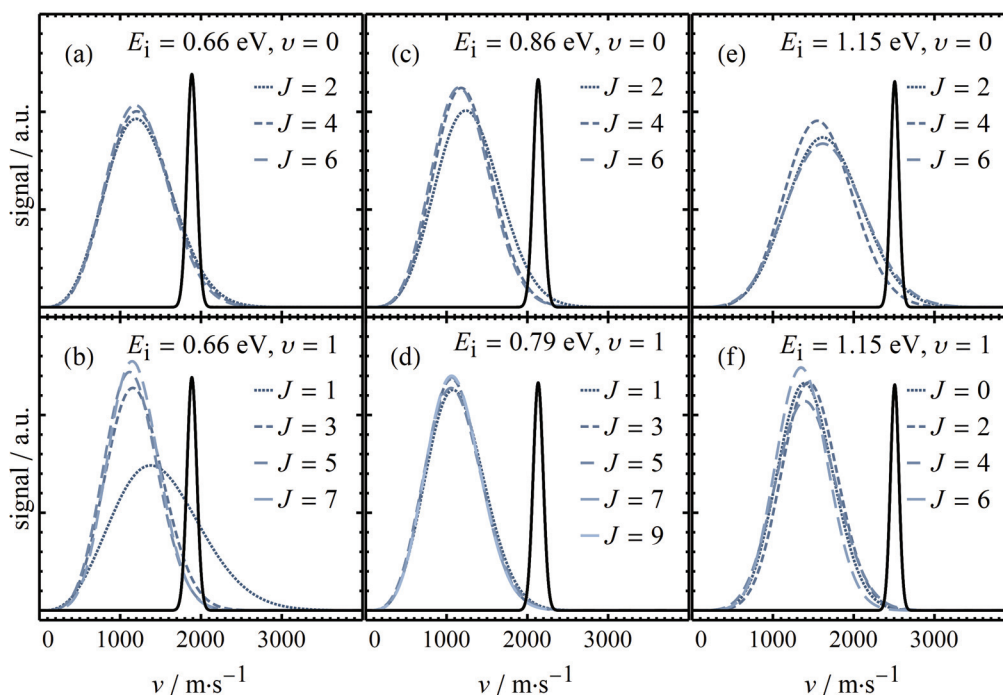


Figure 4.14 Velocity distributions of HCl molecules scattered from Ag(111) at $T_s = 900$ K in different ro-vibrational states. For three different incidence energies, velocity distributions of several rotational states for $v = 0 \rightarrow 0$ (a,c,e) and $v = 1 \rightarrow 1$ (b,d,f) scattering are depicted by dashed blue lines. Additionally, the distributions of the incident beams are shown as solid black lines. The incidence energy in panel (d) was slightly differing from panel (c) because a different gas mixture had to be used. There is no clear trend within the data for one $\langle E_i \rangle$ and v state but with increasing $\langle E_i \rangle$ velocities were shifted to higher values.

Eq. 2.3 in the appendix. Since the curves for individual rotational states for one given incidence energy and scattering channel overlap almost perfectly, the final rotational energy did not seem to significantly influence the molecules' arrival time. However, comparing panels (a), (c) and (e) or (b), (d) and (f) molecules tend to arrive earlier with increasing incidence energy. Judging from the TOF distributions only, there was no remarkable difference between the $v = 0 \rightarrow 0$ and $v = 1 \rightarrow 1$ scattering channels. Knowing the traveled distance of the molecules, the flight time distributions were converted to velocity distributions as done before in Sec. 3.2. In Fig. 4.14 the results for several rotational states are depicted by dashed blue lines. From these velocity distributions, two observations become more obvious.

First, the velocity distributions for the $v = 1 \rightarrow 1$ channel exhibited a smaller width (which can also be seen in Tab. 4.6 where all fitting parameters are gathered). Considering the slightly different measuring procedures, this finding is counterintuitive: Since HCl molecules were excited to $v = 1$ before the collision and not afterwards, I rather expected the distributions to be broader due to interactions with the surface.

Second, although there was no clear J state dependence of the most probable velocity v_0 within one scattering channel, on average the velocity was lower for $v = 1 \rightarrow 1$. Further,

from Fig. 4.14 and Tab. 4.6 it becomes obvious that measurements of TOF distributions of $\nu = 1, J = 1$ were flawed. As can be seen for $\langle E_i \rangle = 0.66$ eV and 1.15 eV (table only), the velocity distributions were much broader and while the fitted value for ν_0 was exceptionally low for $\langle E_i \rangle = 0.66$ eV the actual distribution was shifted to higher velocities far beyond the distribution of the incident beam. The reason for these problems was that substantial population in $\nu = 1, J = 1$ arose from two different processes. Due to the temporal spread of the incident beam, the same IR laser pulse excited HCl molecules from $\nu = 0, J = 0$ to $\nu = 1, J = 1$ either prior to their collision with the surface, which were then also scattered back in $\nu = 1, J = 1$, or after they had been elastically scattered in the vibrational ground state ($\nu = 0 \rightarrow 0$). While the former was the intended process used to study $\nu = 1 \rightarrow 1$ translational inelasticity, the latter resulted in molecules which by mistake had shorter flight distances to the detection spot. Thus, they arrived earlier in the TOF spectra resulting in artificially high velocities and generally broadened velocity distributions.

Table 4.6 Fitting parameters of velocity distributions obtained from fitting Eq. 2.3 to the data in Fig. 4.13. Velocity ν_0 and width parameter α are given in m/s.

J	0.66 eV		0.86 eV		0.79 eV		1.15 eV					
	$\nu = 0$		$\nu = 1$		$\nu = 0$		$\nu = 1$		$\nu = 0$		$\nu = 1$	
	ν_0	α	ν_0	α	ν_0	α	ν_0	α	ν_0	α	ν_0	α
0	-	-	-	-	-	-	542	623	-	-	1074	542
1*	-	-	95	1085	-	-	539	623	-	-	840	1130
2	481	756	664	616	660	691	581	584	1178	829	1146	534
3	503	746	697	595	467	734	489	641	1225	768	992	624
4	580	707	649	603	723	601	504	623	1204	739	1006	602
5	636	666	713	547	764	588	528	607	1161	693	986	572
6	600	679	676	570	679	605	586	579	1112	875	1068	503
7	-	-	807	510	-	-	594	575	-	-	1044	549
8	-	-	-	-	-	-	600	572	-	-	-	-

* $\nu = 1, J = 1$ spectra contain contributions from the incident beam. Thus values for the width α are higher than expected and peak velocities can be incorrect.

These observations can naturally also be made in Fig. 4.15 where the kinetic energy distributions converted from the data in Fig. 4.14 and Tab. 4.6 are shown. Here, distributions for several rotational states are again depicted by dashed blue lines while the respective incident beam is given as a solid black line. As described for the velocity space, there was no obvious dependence on the rotational state apart from the anomaly for $\nu = 1, J = 1$ explained above.

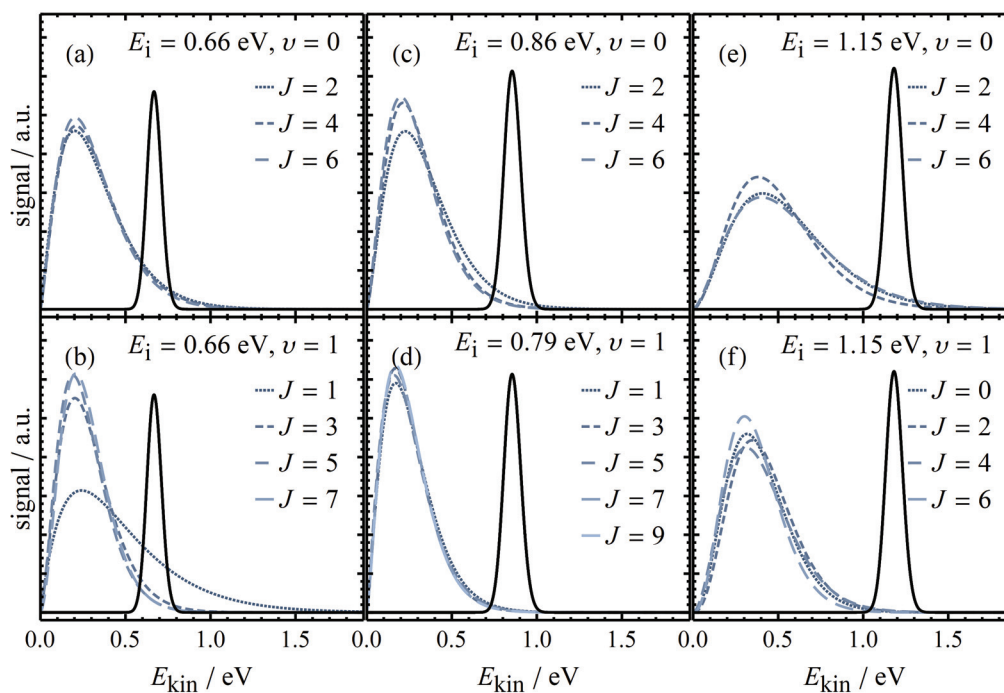


Figure 4.15 Kinetic energy distributions of HCl molecules scattered from Ag(111) at $T_s = 900$ K in different ro-vibrational states. For three different incidence energies, kinetic energy distributions of several rotational states for $\nu = 0 \rightarrow 0$ (a,c,e) and $\nu = 1 \rightarrow 1$ (b,d,f) scattering are depicted by dashed blue lines. Additionally, the distributions of the incident beams are shown as solid black lines. The incidence energy in panel (d) was slightly differing from panel (c) because a different gas mixture had to be used. There is no clear trend within the data for one $\langle E_i \rangle$ and ν state but for $\langle E_i \rangle = 1.15$ eV the distributions of the scattered molecules were substantially broader and shifted to higher energies. Comparing $\langle E_i \rangle = 0.66$ eV and 0.79 eV/ 0.86 eV shows no clear difference in width or peak position.

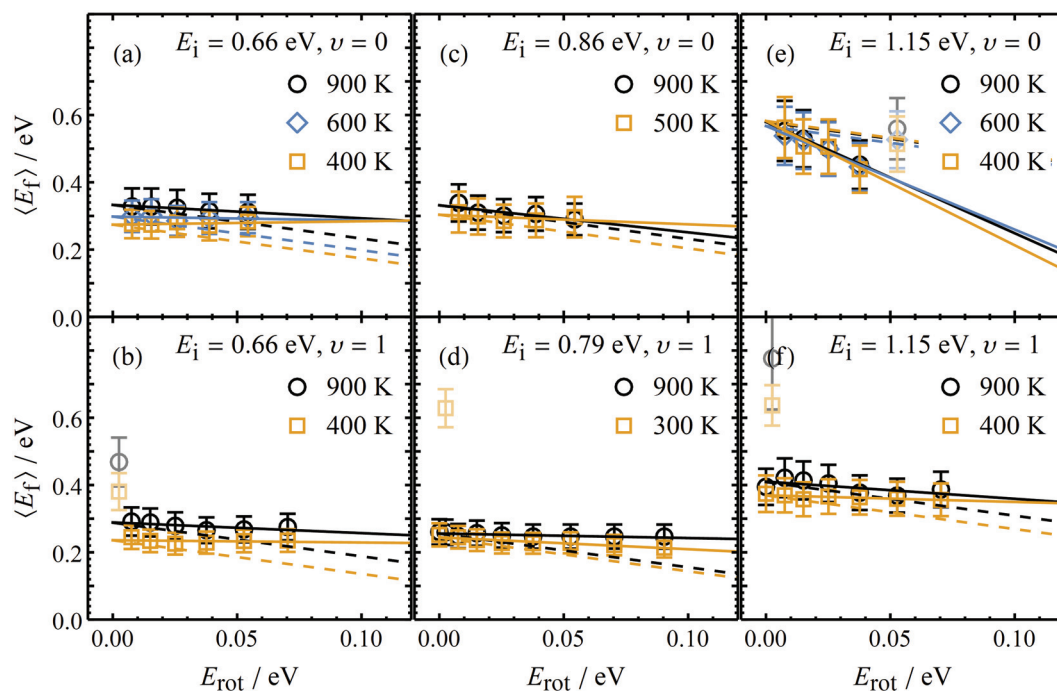


Figure 4.16 Mean final kinetic energy $\langle E_f \rangle$ in dependence on the final rotational energy E_{rot} of HCl molecules scattered from Ag(111). For incidence energies in the range of $\langle E_i \rangle = 0.66 - 1.15$ eV data is shown for $\nu = 0 \rightarrow 0$ (a,c,e) and $\nu = 1 \rightarrow 1$ (b,d,f) scattering by open symbols. While the solid lines depict linear fits to these data, dashed lines exhibit a slope of -1 which corresponds to a complete conversion of kinetic to rotational energy. Pale symbols were excluded from the fits due to either poor S/N (lowest and highest rotational energy) or contributions from the incoming beam ($\nu = 1, J = 1$, see text above). Except for the case of $\langle E_i \rangle = 1.15$ eV, $\nu = 0 \rightarrow 0$, all fitted slopes m were $-1 < m < 0$.

To further investigate the interactions between rotational and translational energy, in Fig. 4.16 the mean kinetic energy of scattered molecules is plotted against the rotational energy of their particular J state for different surface temperatures as open symbols. Additionally, two kind of lines are shown. Dashed lines exhibit a slope of -1 which corresponds to a theoretically complete conversion of kinetic to rotational energy. Solid lines, on the other hand, denote linear fits according to Eq. 3.13 to the data. The fitted values for m given in Tab. 4.7 are generally in the range of $-1 < m < 0.1$ except for $\langle E_i \rangle = 1.15$ eV, $\nu = 0 \rightarrow 0$. Further, in most data sets m decreased with increasing surface temperature, potentially indicating a more efficient conversion of translational to rotational energy. Since $-1 < m$ in almost all cases, scattered molecules must have gained final rotational energy from the surface during scattering.

4.2. Translational Inelasticity

Table 4.7 Resulting parameters of fitting Eq. 3.13 to the data in Fig. 4.16. $\langle E_i \rangle$ is the incidence translational energy and T_s the surface temperature. $\langle E_f \rangle^{\text{el.}}$ is the fitted translational energy in the case of rotationally elastic scattering and m is the slope of the fit.

$\langle E_i \rangle$ in eV	$v \rightarrow v$	T_s in K	$\langle E_f \rangle^{\text{el.}}$ in eV	m
0.66	0 \rightarrow 0	400	0.27 ± 0.01	$+0.10 \pm 0.15$
		600	0.30 ± 0.01	-0.11 ± 0.18
		900	0.33 ± 0.01	-0.40 ± 0.06
	1 \rightarrow 1	400	0.24 ± 0.01	-0.07 ± 0.14
		900	0.29 ± 0.01	-0.32 ± 0.16
	0.86	0 \rightarrow 0	500	0.30 ± 0.01
900			0.33 ± 0.01	-0.80 ± 0.30
0.79	1 \rightarrow 1	300	0.24 ± 0.01	-0.35 ± 0.06
		900	0.26 ± 0.01	-0.13 ± 0.05
1.15	0 \rightarrow 0	400	0.58 ± 0.02	-3.69 ± 0.84
		600	0.57 ± 0.01	-3.08 ± 0.38
		900	0.58 ± 0.01	-3.31 ± 0.16
	1 \rightarrow 1	400	0.37 ± 0.01	-0.20 ± 0.07
		900	0.41 ± 0.01	-0.51 ± 0.25

4.3 Dissociation

Recently, in one of their follow-up publications, Liu *et al.* reported incidence energy depending dissociation probabilities of HCl molecules on Ag(111) to be even higher than those on Au(111) [106, 107]. This was in line with unpublished DFT calculations by Jan Altschäffel from our group that predicted the barrier to dissociation on Ag(111) to be ~ 0.1 eV lower than on Au(111) while the reaction products were calculated to be much more stable due to the strong Ag-Cl bond (FHI-aims code, RPBE functional). Thus, I tried to investigate the dissociation on Ag(111) applying the same methodology involving AUGER spectroscopy as described for the gold surface. Fig. 4.17 shows two AUGER spectra recorded after dosing the Ag(111) surface with HCl molecules with $\langle E_i \rangle = 0.9$ eV (a) and $\langle E_i \rangle = 2.2$ eV (b) at $T_s = 300$ K for at least 40 min (dose $D > 1000$ ML). In case (a), no chlorine peak could be observed in the AUGER spectrum (zooming into the suspected energy range, a very small peak could be assumed that more or less vanished in the spectral noise). Assuming dissociation probabilities close to those on Au(111) this was not surprising since under these conditions, no Cl signal was detected on Au(111) at first as well (cf. Fig. 3.26). When the incidence energy was increased to 2.2 eV by heating the nozzle tip, the chlorine peak emerged at the expected position. Its intensity, however, remained rather small

considering that incidence energy and dose should have resulted in a coverage at least close to saturation assuming similar behavior of Cl on Ag(111) as on Au(111) based on the aforementioned DFT calculations. If this signal was already the maximum in intensity, a detailed study of the incidence energy depending dissociation probability would be difficult. Looking back at Sec. 3.3, a much smaller Cl signal did make sense, though. On Au(111), the saturation APPH ratio of $P_{r,sat} = 8.8$ resulted from AUGER sensitivity factors of $S_{Cl} = 1.03$ and $S_{Au} = 1.79 \times 10^{-2}$. Since these factors were in fact determined against a silver standard, $S_{Ag} = 1$ and thus $S_{Ag}/S_{Au} = 56$. That is, in a simple picture AUGER spectroscopy is supposed to be more than 50 times as sensitive to silver as to gold. Indeed, assuming the same maximal coverage of 1 ML on the Ag(111) surface, the Cl/Ag peak ratio in spectrum

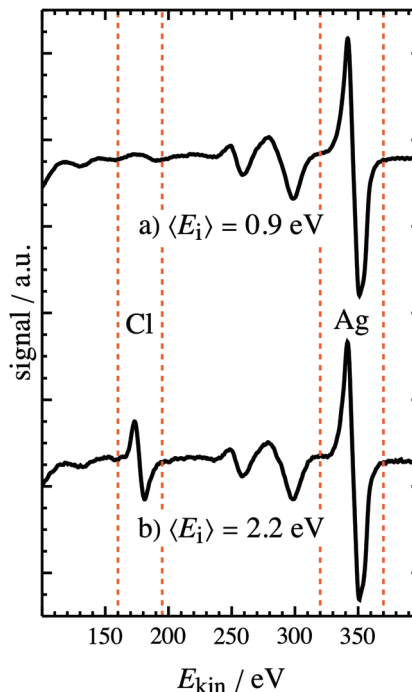


Figure 4.17 Stacked AUGER spectra of the Ag(111) surface after dosing it with HCl molecules with $\langle E_i \rangle = 0.9$ eV (a) and $\langle E_i \rangle = 2.2$ eV (b) at $T_s = 300$ K for at least 40 min (dose $D > 1000$ ML). The main peaks of Cl and Ag that could in principle be used in the analysis are marked by dashed red lines. While in case (a) there was no observable chlorine peak, a relatively small peak emerged in case (b) which was supposed to correspond to a coverage close to saturation.

(b) is smaller than the maximal APPH on Au(111) by a factor of 29. Thus, the dynamic range of the AUGER spectrometer would need to be improved or different scans with different gains would need to be carried out for the Cl and the Ag peak.

Here, it needs to be noted that the state of chlorine adsorbed on Ag(111) was reported to be much more complex than simply Cl atoms occupying certain binding sites on the surface. In an extensive study, Bowker and Waugh examined the adsorption of Cl₂ on Ag(111) and the subsequent desorption of chlorine species by AUGER, LEED, and TPD [108]. Concerning AUGER spectra, they found a P_T value of ~ 0.9 for a monolayer coverage of Cl at room temperature. However, P_T continued to increase with further Cl₂ exposure and was also highly surface temperature dependent. These findings were attributed to the formation of AgCl layers on the surface which was supported by several TPD peaks from different states of AgCl desorbing from the surface. Thus, it remained unclear whether HCl dissociation on Ag(111) could be meaningfully studied employing AUGER spectroscopy. Additionally, due to the unfavorable sensitivities a detailed analysis of the incidence energy dependent sticking probabilities was not feasible with this technique.

4.3.1 Cl₂ Recombination

While the AUGER studies remained unsuccessful, I was able to detect desorbing Cl₂ molecules in dynamic scattering experiments in the same way as on Au(111). The experimental conditions were similar to those described in Sec. 3.3.6: HCl molecules (6% in H₂) with an incidence energy of $\langle E_i \rangle = 2.1$ eV were scattered from the Ag(111) surface at $T_s \approx 900 - 1073$ K which was mounted at an angle of $\theta_i = 36^\circ$ relative to the incident molecular beam (resulting in $\langle E_\perp \rangle \approx 1.4$ eV assuming normal energy scaling).

In Fig. 4.18, arrival time distributions of Cl₂ at the laser detection spot depending on different experimental parameters are presented. In panel a), the recorded signal of Cl₂ desorbing from the surface at 1073 K in dependence on the laser-nozzle delay is shown as a solid blue line in comparison to the incident HCl beam as a solid red line and the scattered HCl beam as a dashed black line. As can be read from the plot legends, the Cl₂ signal peak was approximately five times less intense than the HCl signal peak and started to appear later at the detector. However, its peak intensity strongly increased with T_s while the distributions' width became narrower (see inset of panel b). Measured at $T_s = 1073$ K, the signal intensity also depended on the scattering angle and was maximal around the surface normal (which corresponded to $\sim 36^\circ$, see the dashed red and purple lines in panel c) while the width was more or less independent of θ_{scat} . (see inset of panel c), the measurement at $\theta_{\text{scat}} = 52^\circ$ is probably not very reliable due to the geometric constraints of the apparatus). Integrating the arrival time distributions for Ag(111) in panel c) and for Au(111) in Fig. 3.47 panel c) resulted in the area-normalized angular distributions shown in panel d). Meant as a guide to the eye, the dashed black and blue lines denote \cos^2 functions peaking at $\theta = 26^\circ$ and $\theta = 30^\circ$, respectively.

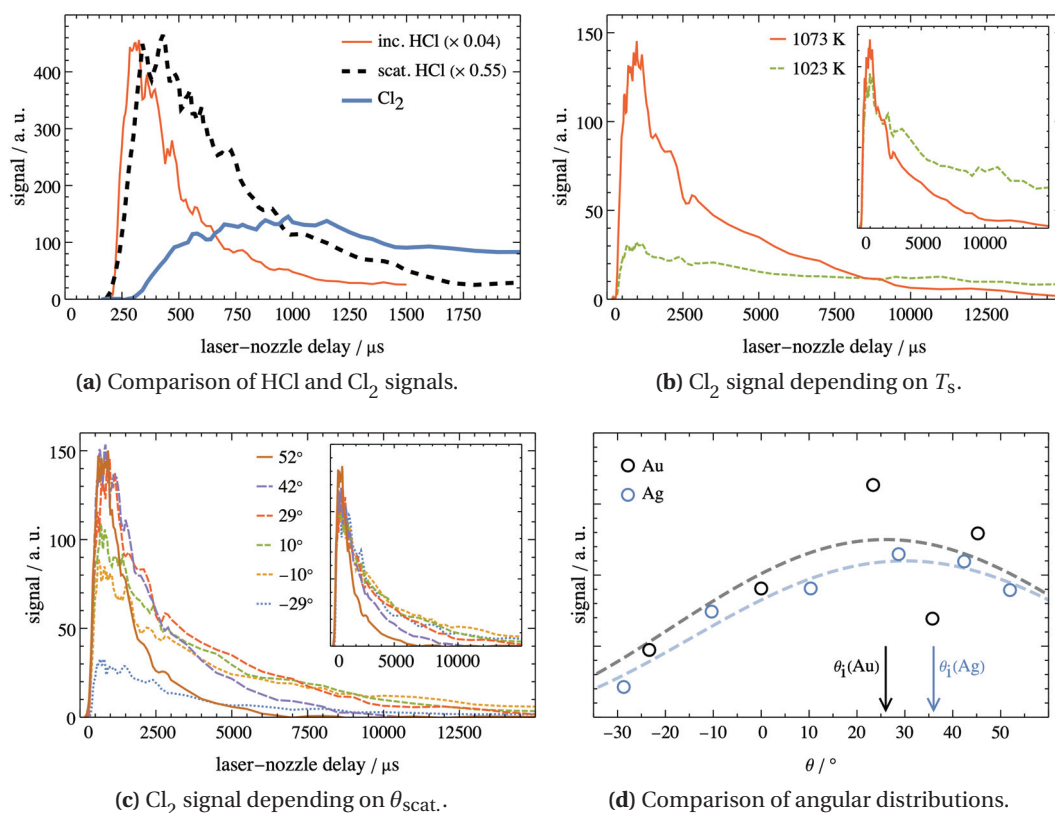


Figure 4.18 Arrival time distributions of Cl_2 at the laser detection spot depending on different experimental parameters. In panel a), the recorded signal of Cl_2 desorbing from the surface at 1073 K in dependence on the laser-nozzle delay is shown as a solid blue line in comparison to the incident HCl beam as a solid red line and the scattered HCl beam as a dashed black line. As can be read from the plot legends, Cl_2 signal peak was approximately six times less intense than the HCl signal and started to appear later at the detector. However, in panel b) it can be seen that its peak intensity strongly increased with T_s while the distributions' width became narrower (see inset). Further, as can be seen in panel c), the signal intensity measured at $T_s = 1073\text{ K}$ also depended on the scattering angle and was maximal around the surface normal (which corresponded to $\sim 36^\circ$ (see the dashed red and purple lines) while the width was more or less independent of $\theta_{\text{scat.}}$ (the measurement at $\theta_{\text{scat.}} = 52^\circ$ is probably not very reliable due to the geometric constraints of the apparatus). In panel d) area-normalized angular distributions derived by integrating the arrival time distributions for Ag(111) in panel c) and for Au(111) in Fig. 3.47 panel c) are shown. Meant as a guide to the eye, the dashed black and blue lines denote \cos^2 functions peaking at $\theta = 26^\circ$ and $\theta = 30^\circ$, respectively.

DISCUSSION

5 Discussion

Before going into details about the processes and phenomena examined in this thesis, I would like to summarize the main results of the vibrational excitation, translational inelasticity, and dissociation studies.

Vibrational Excitation Scattering HCl molecules from Au(111) and Ag(111), surface temperature and incidence translational energy dependent vibrational excitation from $v = 0 \rightarrow 1$ was observed in both cases. While the general trend with VEPs in the range of $\sim 1 \times 10^{-4} - 3 \times 10^{-3}$ was similar on both metals, the derived E_i independent electronically nonadiabatic interaction strength $A^{\text{nonad.}}$ was slightly higher for scattering from Ag(111) (1.4×10^{-1} vs. 9.4×10^{-2}). On the other hand, the adiabatic interaction strength $A^{\text{ad.}}$, approximately two orders of magnitude lower than the nonadiabatic one, was determined to be 1.4×10^{-3} on both surfaces (see Fig. 4.11 and Tabs. 4.4 and 4.5).

Further, scattering HCl molecules pre-excited to vibrational state $v = 1$ from Au(111), excitation to $v = 2$ was observed. Here, VEPs in the range of $\sim 1 \times 10^{-3} - 3 \times 10^{-2}$ were determined leading to $A^{\text{ad.}} = 3.4 \times 10^{-2}$ and $A^{\text{nonad.}} = 8.0 \times 10^{-1}$ (see Tab. 3.7). Thus, relative to $v = 0 \rightarrow 1$ excitation, the adiabatic interaction strength was enhanced by a factor of 24 while the nonadiabatic one was enhanced by a factor of 9. Opposed to Au(111), no $v = 1 \rightarrow 2$ excitation could be observed while scattering from Ag(111). On neither surface HCl molecules coming back in $v = 3$ could be detected after pre-collisional excitation to $v = 2$.

Translational Inelasticity Employing laser based TOF techniques the translational energy of HCl molecules after scattering from the metal surfaces could be determined for various ro-vibrational states. While for Au(111) translational inelasticity was examined for $v = 1 \rightarrow 1$ and $v = 1 \rightarrow 2$ scattering channels, due to the lack of molecules in $v = 2$ for Ag(111) only the $v = 0 \rightarrow 0$ and $v = 1 \rightarrow 1$ channels could be studied. With two exceptions, the mean final translational energy decreased very slightly with increasing rotational energy meaning that at least part of this energy must have been transferred from the surface to

Chapter 5. Discussion

the molecules. In all cases, the mean final translational energy for $\Delta J = 0$ was substantially lower than the mean incidence translational energy. This will further be discussed in the following sections.

Dissociation Measuring the chlorine coverage on the gold surface after dosing it with HCl molecules, initial sticking probabilities for the dissociation of HCl on Au(111) were determined in dependence on the incidence translational energy. For $\langle E_i \rangle = 0.9 - 2.6$ eV S_0 was found to be in the range of $2.4 \times 10^{-5} - 1.6 \times 10^{-1}$ (including lower and upper limit values). Using REMPI-TPD, desorbing HCl and H_2 molecules as well as Cl atoms could be detected while in further scattering experiments Cl_2 was seen to desorb from the surface. Although HCl dissociation on Ag(111) could not be studied by Auger spectroscopy, Cl_2 desorption was seen here as well.

5.1 Vibrational Excitation

5.1.1 Comparison of Different Systems

To the best of my knowledge there is no other molecule for which vibrational excitation probabilities for transitions not only from the vibrational ground state and but also from excited states were reported for comparable incidence energies.¹ Yet, in our group I have found older, so far unpublished raw data for the $\nu = 2 \rightarrow 3$ excitation of NO scattered from Au(111) at a mean incidence energy of 0.41 eV. Even though they might not be absolutely correct due to limited information about the actual experimental conditions, I was able to derive VEPs for this excitation process and compare them to values published for $\nu = 0 \rightarrow 1$ excitation. Fig. 5.1 (a) shows the VEPs depending on the surface temperature where black and blue symbols depict the data for $\nu = 0 \rightarrow 1$ and $\nu = 2 \rightarrow 3$ excitation, respectively. Solid lines denote fits to the data according to Eq. 5.1:

$$P_{\nu'',\nu'}(E_i, T_s) = A^{\text{nonad.}}(E_i) \times \exp\left[\frac{-E_{\nu'',\nu'}}{k_B T_s}\right] \quad (5.1)$$

In contrast to HCl, for NO (as well as other molecules like CO, see Sec. 1.2) no contribution to the excitation that could be assigned to electronically adiabatic interactions was found [25]. Thus, opposed to Eq. 3.8 there is only one exponential term in Eq. 5.1 and only $A^{\text{nonad.}}$ can be extracted. Although the energetic spacing between the incident vibrational levels $\nu = 2$ and $\nu = 0$ is 0.46 eV in the case of NO, the enhancement in $A^{\text{nonad.}}$ is less than a factor of two when going from $\nu_i = 0$ to $\nu_i = 2$. Comparing this to the 9 times enhancement for HCl incident in $\nu = 1$, which is 0.36 eV higher in vibrational energy than the ground state, the vibrational pre-excitation had much less effect in the case of NO scattering from Au(111) (see also Fig. 5.1 (b)).

I hypothesize the following qualitative explanation: Due to the relatively low lying barrier to dissociation [58, 60, 96, 100, 109], trajectories of incident HCl molecules sample geometries on the PES in the proximity of the transition state to dissociation. Since the dissociation is calculated to be a so-called late barrier reaction, vibrational excitation is supposed to be more efficient for approaching the barrier than translational energy [58, 60, 61]. Incident molecules that had been vibrationally pre-excited might thus have come closer to the transition state which is supposed to involve a considerable elongation of the HCl bond ($r = 1.9 - 2.2 \text{ \AA}$ [60, 100] instead of $r = 1.3 \text{ \AA}$ at equilibrium). Not able to surmount the barrier, the molecules roll back down the energetic hill while the stretched bond "snaps back", leaving HCl in a vibrationally excited state (vibrational excitation for nonreactive trajectories was shown by Díaz and Olsen for $\text{N}_2/\text{Ru}(0001)$ [110], for example). The vibrationally enhanced dissociation could also have contributed to the absence of vibrational excitation from $\nu = 2 \rightarrow 3$. With a vibrational energy of $E_{\text{vib}} = 0.70 \text{ eV}$ and inci-

¹ In Ref. [32], Wodtke *et al.* reported population ratios of $\text{NO}(\nu = 3)$ and $\text{NO}(\nu = 2)$ for $\langle E_i \rangle = 0.31 \text{ eV}$ and $\langle E_i \rangle = 0.62 \text{ eV}$ from which the VEP cannot be directly inferred.

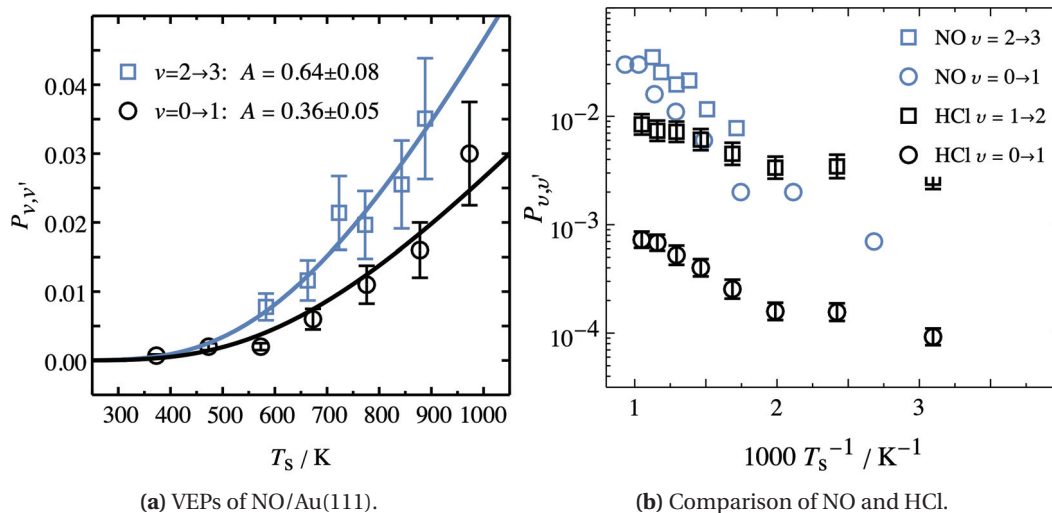


Figure 5.1 Comparison of vibrational excitation channels $\nu = 0 \rightarrow 1$ and $\nu = 2 \rightarrow 3$ of NO scattering from Au(111) at $\langle E_i \rangle = 0.41$ eV.

dence translational energy of $\langle E_i \rangle = 0.99$ eV, a considerable fraction of those HCl molecules might have simply dissociated on the surface instead of being further excited.²

Recently, Grotemeyer and Pehlke also showed that excited vibrational states enhance the nonadiabatic interactions of HCl scattering from Al(111) in TDDFT-MD simulations [111]. In this case, the enhancement was attributed to a large energy shift of the antibonding LUMO of HCl with increasing bond length, resulting in a stronger interaction with the metal's continuum of states. Again, this enhanced interaction might also take place in the case of bond elongation due to approaching the transition state to dissociation. Thus, this observation could also have implications for the dissociation of HCl molecules on Au(111), even more so for those in higher vibrational states.

In comparison, for NO scattering from Au(111) the barrier to dissociation was calculated to be $E_{\text{TS}} = 3.9$ eV [112]. From a purely energetical point of view, the vibrational energy of $E_{\text{vib}} = 0.46$ eV for $\nu = 2$ accounts for a much smaller fraction of the barrier energy than $E_{\text{vib}} = 0.36$ eV *vs.* $E_{\text{TS}} = 0.64 - 1.05$ eV in the case of HCl/Au(111).³ In other words, if due to the similar geometrical change in the molecules the reaction coordinate for both dissociations is assumed to be comparable, the curvature of the PES is higher if the transition state is much higher in energy. Thus, the same increase in energy would result in less progression on the reaction coordinate. It must be noted, though, that these arguments purely based on energetic considerations do not necessarily account for the complete picture: Vibrational energy should not only be seen as additional energy that can be converted on the PES. Vibrationally excited molecules can also have easier access to "parts of

² I will come back to this argument again in the discussion of the dissociation probabilities.

³ Yet, it must be noted that even though barrier height was calculated to be very different, the bond elongation is supposed to be approximately the same.

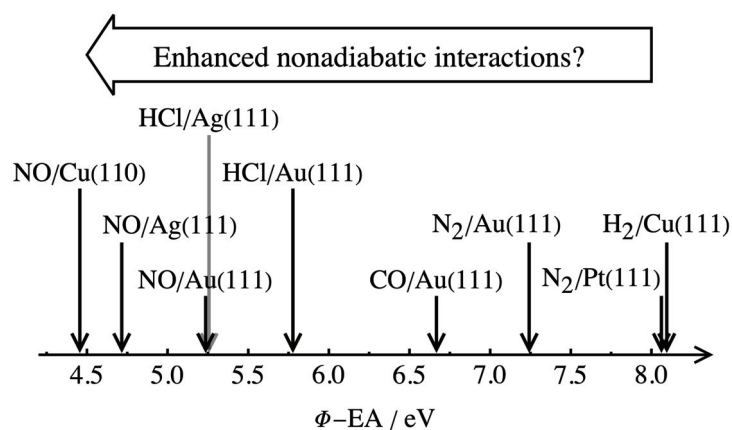


Figure 5.2 The difference of a metal's work function Φ and the molecule's electron affinity EA as a proxy of nonadiabatic interaction strength. Panel (a) resembles Fig. 1.4 complemented with the previously unstudied system HCl/Ag(111). The lower $\Phi - EA$ the higher is the expected nonadiabatic interaction strength.

the configuration space with lower barriers than the molecules in the vibrational ground state" [110]. Nevertheless, I propose that the qualitative explanations given above can at least partially explain the differences between the experimentally derived $v = 0 \rightarrow 1$ and $v = 1 \rightarrow 2$ excitation probabilities.

Taking the transition state to dissociation into account might also help to explain the differences between the excitation probabilities scattering from Au(111) and Ag(111). First of all, the calculated absolute values for $P_{0,1}$ were very similar for both surfaces and the $\langle E_i \rangle$ independent adiabatic interaction strengths $dA^{\text{ad.}}/d\langle E_i \rangle$ were even determined to be the same. On the other hand, the nonadiabatic interaction strength was slightly higher on Ag(111). Fig. 5.2 (a) basically re-capitulates Fig. 1.4 complemented with the previously unstudied system HCl/Ag(111). Based on the proposed proxy for nonadiabaticity, $\Phi - EA$, the interaction strength should be higher than on Au(111) and similar to that of the NO/Au(111) system. As shown in panel (b), where the actual determined, incidence energy independent nonadiabatic interaction strength $dA^{\text{nonad.}}/d\langle E_i \rangle$ for several systems is plotted against their $\Phi - EA$ as open black symbols, this was not the case. As long as only the excitations from the vibrational ground state are considered, vibrational excitation of HCl on Au(111) as well as Ag(111) was lower than expected based on this proxy. Including the $v = 1 \rightarrow 2$ excitation, shown as filled red symbols, HCl/Au(111) does fit much better into the general trend. The validity of this comparison is questionable, however, since for the other systems there is no reported excitation from higher vibrational states to compare to. Further, so far HCl is the only molecule for which adiabatic as well as nonadiabatic contributions to the vibrational excitation have been observed, which might add to the difficulties associated with the comparability.

Coming back to the direct comparison of HCl on gold and silver, not only the different

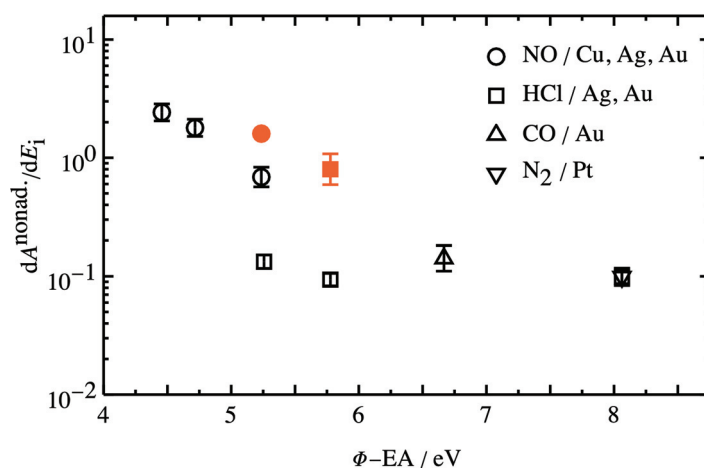


Figure 5.3 The difference of a metal’s work function Φ and the molecule’s electron affinity EA as a proxy of nonadiabatic interaction strength. Here the actual determined, incidence energy independent nonadiabatic interaction strength $dA^{\text{ad.}}/d\langle E_i \rangle$ for several systems in the ground vibrational state is plotted against their $\Phi - EA$ as open black symbols. Expecting a more or less monotonic dependence, vibrational excitation of HCl on Au(111) as well as Ag(111) was lower than expected based on this proxy. Including the excitations from higher vibrational states, shown as filled red symbols, HCl/Au(111) fits much better into the general trend. While the $dA^{\text{ad.}}/d\langle E_i \rangle$ were calculated from data in Refs. [12, 25, 28, 29, 33], values for work functions were gathered from Refs. [39–41] and electron affinities were taken from Ref. [42].

work functions of the surfaces but also the PES and transition states to dissociation exhibit slight differences. According to recent DFT calculations, on Ag(111) the transition state energy is $E_{\text{TS}} = 0.86$ eV while the bond is elongated to $r_{\text{TS}} = 1.89$ Å for the RPBE functional and $E_{\text{TS}} = 0.59$ eV and $r_{\text{TS}} = 1.85$ Å for PBE [106]. In comparison, the values for Au(111) are $E_{\text{TS}} = 1.05$ eV while the bond is elongated to $r_{\text{TS}} = 1.95$ Å for the RPBE functional and $E_{\text{TS}} = 0.76$ eV and $r_{\text{TS}} = 1.93$ Å for PBE [100]. That is, the transition state should be more accessible which is also reflected in reported higher dissociation probabilities [107]. Reconsidering the argumentation for the unobserved $v = 2 \rightarrow 3$ excitation in the case of Au(111), on Ag(111) the excitation to $v = 1$ might have been enough to dissociate most of the molecules instead of leaving them excited to $v = 2$. Unfortunately, it is difficult to quantitatively include the absolute dissociation probabilities calculated in Ref. [107] in the considerations to get an estimate of the enhancement. Both the reported dependence of S_0 on the DFT functional and the differences between theoretically and experimentally determined values impede a direct comparison.

5.1.2 Comparison with Theoretical Predictions

However, only considering the $\nu = 1 \rightarrow 2$ excitation on Au(111), Füchsel *et al.* [100] offered what they called absolute excitation probabilities calculated in the form of:

$$P_{\nu=1, j=1 \rightarrow \nu'} = \frac{N_{\text{sc}}(\nu')}{N_{\text{t}}} \quad (5.2)$$

where $N_{\text{sc}}(\nu')$ was the number of trajectories ending in ν' and N_{t} the total number of simulated trajectories. From these, they further calculated "scaled vibrational transition probabilities" according to:

$$T_{\nu=1 \rightarrow \nu'} = \frac{P(\nu = 1, j = 1 \rightarrow \nu')}{P(\nu = 1, j = 1 \rightarrow \nu' = 1) + P(\nu = 1, j = 1 \rightarrow \nu' = 2)} \quad (5.3)$$

which are supposed to be comparable to the VEP values I report here. Starting the simulation with all HCl molecules in $\nu = 1, j = 1$ with $\langle E_i \rangle = 0.94$ eV at $T_s = 575$ K and $\langle E_i \rangle = 0.94$ eV and 1.06 eV at $T_s = 900$ K, they obtained values for $T_{\nu=1 \rightarrow \nu'=2}$ that are 3 – 8 times higher than the VEPs I derived experimentally. At the same time, their values for $P_{\nu=1, j=1 \rightarrow \nu'=2}$ are ~ 3 times lower than those for $T_{\nu=1 \rightarrow \nu'=2}$ and are thus comparable to my VEPs. The reason for the difference between their values is that the relaxation channel (which amounted to 24 – 26%) and the dissociation channel (which amounted to 35 – 43%) were neglected for the calculation of $T_{\nu=1 \rightarrow \nu'=2}$ so that the denominator of Eq. 5.3 was only approximately one third of that of Eq. 5.2. Both of these channels were also not considered in Eq. 3.11 for calculating the $\nu = 1 \rightarrow 2$ VEPs (however, a maximal relaxation rate of 0.3 was estimated in Sec. 3.1.2).

One possible reason for the disagreement between experiment and theory that was also noted in Ref. [100] could be an underestimation of the dissociation barrier (also see the discussion in Sec. 5.3). As discussed above, a lower barrier might lead to higher vibrational excitation due to enhanced bond elongation and at the same time to higher dissociation probabilities. Both phenomena would act together to increase $T_{\nu=1 \rightarrow \nu'=2}$. Additionally, nonadiabatic interactions might not be adequately modeled in the simulations using EF in the independent atom approximation (IAA). To test this, the authors suggested further simulations employing theories beyond the IAA like orbital density friction and IESH. Beneath deviations from the absolute values, the simulations successfully captured the trend of increasing VEP with increasing $\langle E_i \rangle$. However, due to large error bars the effect of increasing VEP with increasing T_s could not be reliably reproduced.

5.1.3 Kinetic Approach

So far, in the analysis of the adiabatic and nonadiabatic contributions I relied on the previously established ARRHENIUS model that was fitted to the temperature dependent VEPs. One of the shortcomings of this procedure is that the different vibrational states and transitions needed to be treated individually. In the following paragraphs I will thus shortly introduce a kinetic model of the vibrational excitation processes along the lines of the model that was introduced for the vibrational excitation of NO/Au(111) [24, 47]. Taking into account vibrational states $v = 0 - 2$ HCl can be considered a three-state system with the following transition rates:

$$\begin{aligned} n'_{v=0} &= k_{2,0} \times n_{v=2} + k_{1,0} \times n_{v=1} - k_{0,1} \times n_{v=0} - k_{0,2} \times n_{v=0} \\ n'_{v=1} &= k_{2,1} \times n_{v=2} + k_{0,1} \times n_{v=0} - k_{1,2} \times n_{v=1} - k_{1,0} \times n_{v=1} \\ n'_{v=2} &= k_{0,2} \times n_{v=0} + k_{1,2} \times n_{v=1} - k_{2,1} \times n_{v=2} - k_{2,0} \times n_{v=2} \end{aligned} \quad (5.4)$$

where the rate constants $k_{v,v'}$ have the following form:

$$k_{v,v'} = \alpha_{v,v'} \frac{E_{v,v'}}{\exp(E_{v,v'} / (k_B T_s)) - 1} \quad (5.5)$$

with $\alpha_{v,v'}$ effectively being a coefficient incorporating the coupling between the electron affinity level and the vibrational DOF of HCl amongst others. The remaining part of $k_{v,v'}$ was derived from FERMI's Golden Rule involving the NEWNS-ANDERSON Hamiltonian and according to that formalism is valid for $k_B T_s \ll E_F$ (see Ref. [47] for further details). Based on the Rule's symmetry, $E_{v,v'} = -E_{v',v}$ and $\alpha_{v,v'} = \alpha_{v',v}$ (corresponding to microscopic reversibility) which simplifies the evaluation. Employing MATHEMATICA's built-in DSolve function, the differential equations could be solved analytically.

For the best possible simulation of the experimentally derived values, the boundary conditions for the solutions were chosen so that $n_{v=0}(t=0) = 1$ and $n_{v=1}(t=0) = n_{v=2}(t=0) = 0$ in the case of the $v = 0 \rightarrow 1$ excitation and $n_{v=0}(t=0) = 0.995$, $n_{v=1}(t=0) = 0.005$, and $n_{v=2}(t=0) = 0$ in the case of the $v = 1 \rightarrow 2$ excitation (since hole-burning experiments showed that $\sim 0.5\%$ of the incoming molecular pulse had been excited to $v = 1$ by the IR laser). With the resulting time-dependent populations in the three vibrational states the excitation probabilities according to Eqs. 3.7 and 3.11 were calculated as:

$$\begin{aligned} P_{0,1} &= \frac{n_{v=1}(t)}{n_{v=0}(t) + n_{v=1}(t)} \\ P_{1,2} &= \frac{n_{v=2}(t)}{n_{v=1}(t) + n_{v=2}(t)} \end{aligned} \quad (5.6)$$

As done before with Eq. 3.8, the $\langle E_i \rangle$ and T_s dependent experimental values for $P_{0,1}$ and $P_{1,2}$ were fitted with Eqs. 5.6. To facilitate the fitting procedure, the following approximations

were introduced in addition to those in the preceding paragraph. First, the interaction time with the surface t was replaced by $1/\sqrt{\langle E_i \rangle}$ since it should be inversely proportional to the molecules' velocity (and in this model the time is treated in arbitrary units). Second, $\alpha_{0,1}$, $\alpha_{1,2}$, and $\alpha_{0,2}$ were assumed to exhibit the same $\langle E_i \rangle$ dependence so that the latter two can be replaced by $\alpha_{1,2} = f_{1,2}\alpha_{0,1}$ and $\alpha_{0,2} = f_{0,2}\alpha_{0,1}$. That is, instead of fitting three coefficients for each data set, only $\alpha_{0,1}$ was fitted for every $\langle E_i \rangle$ and $f_{1,2}$ and $f_{0,2}$ were fitted globally to all data sets including both the $\nu = 0 \rightarrow 1$ and the $\nu = 1 \rightarrow 2$ excitation. Thus, the scaling factor $f_{1,2}$ should be a measure of the nonadiabatic interaction enhancement of higher incident vibrational states (as discussed above).

Third, since the kinetic model was specifically developed for nonadiabatic vibrational excitation, similar to Eq. 3.8 an adiabatic constant needed to be added to $P_{0,1}$ and $P_{1,2}$ in order to account for the horizontal offset. Unfortunately, even with these approximations I was not able to perform the fitting due to the immense complexity of the analytical solutions of the differential equations.⁴ Thus, I had to reduce the complexity of the fit by modifying the differential equations. Assuming the $\nu = 0 \rightarrow 2$ de-/excitation to be way less efficient than $\nu = 0 \rightarrow 1$ and $\nu = 1 \rightarrow 2$, I changed Eq. 5.4 to:

$$\begin{aligned} n'_{\nu=0} &= k_{1,0} \times n_{\nu=1} - k_{0,1} \times n_{\nu=0} \\ n'_{\nu=1} &= k_{2,1} \times n_{\nu=2} + k_{0,1} \times n_{\nu=0} - k_{1,2} \times n_{\nu=1} - k_{1,0} \times n_{\nu=1} \\ n'_{\nu=2} &= k_{1,2} \times n_{\nu=1} - k_{2,1} \times n_{\nu=2} \end{aligned} \quad (5.7)$$

Before continuing with the fit I checked the effect on $P_{0,1}$ and $P_{1,2}$ by filling in arbitrary values for the fitting parameters. Neglecting the two-quanta de-/excitation did not change the final equilibrium values for either excitation probability but only extended the time until equilibrium was obtained. It was thus considered to be an acceptable modification of the differential equations, the solutions of which could now easily be fitted to the data for Au(111) and Ag(111) previously shown in Figs. 3.9, 3.19 and 4.10. As can be seen in Fig. 5.5, where the data for $\nu = 0 \rightarrow 1$ and $\nu = 1 \rightarrow 2$ excitation on Au(111) and $\nu = 0 \rightarrow 1$ excitation on Ag(111) including the corresponding fits are shown, the kinetic model fits to the data cannot be distinguished from the previous fits. Being able to represent the same data equally well, the advantage of this new model fit is that, as mentioned above, both excitation channels on Au(111) were fitted with the same set of $\alpha_{0,1}$ coefficients and one single scaling factor $f_{1,2}$ that could account for the higher efficiency of the $\nu = 1 \rightarrow 2$ excitation. That is, due to the expanded data basis, the obtained efficiency might be more reliable. Fascinatingly, the fitting outcome was $f_{1,2} = 8.8$ which basically exactly reflects the ratio of the $\langle E_i \rangle$ independent $A_{1,2}^{\text{nonad.}}/A_{0,1}^{\text{nonad.}} = 8.5$ derived in Sec. 3.1.2 and discussed above. By varying the value of $f_{1,2}$ and leaving the remaining fitting parameters the same, I also confirmed that for $\nu = 1 \rightarrow 2$ the fit responds sensitively to this efficiency parameter. This puts the increasing

⁴ That is, the fitting procedure filled the RAM of the computer (to an equivalence of ~100GB according to the activity monitor) until the program kernel quit without results.

nonadiabatic interaction strength with increasing incident vibrational state on a firmer footing. In general, the results for Au(111) and Ag(111) should also be comparable. One has to keep in mind, though, that $\alpha_{0,1}$ is inversely proportional to the interaction time t which was artificially set to $1/\sqrt{\langle E_i \rangle}$. If the interaction time varied for different surfaces, it would need to be adapted correspondingly in the fit in order to obtain comparable values for $\alpha_{0,1}$. For the fits shown in Fig. 5.5, t was nevertheless taken to be the same for both surfaces. Further, since there was no $\nu = 1 \rightarrow 2$ excitation data for Ag(111), $f_{1,2}$ was simply assumed to be the same here as well. In Fig. 5.4, the resulting values for $\alpha_{0,1}$ are shown depending on the mean incidence translational energy. While open round symbols depict the data for Au(111), for Ag(111) it is depicted by filled squares. The colors of the symbols were chosen in correspondence with those used in Fig. 5.5.

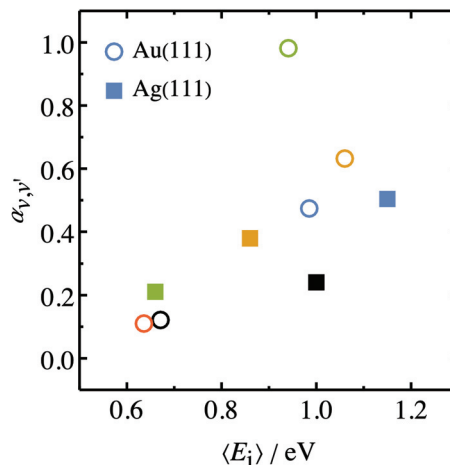


Figure 5.4 Comparison of the $\alpha_{0,1}$ values derived from the fitting of the kinetic model. While open round symbols depict the data for Au(111), for Ag(111) it is depicted by filled squares. The colors of the symbols were chosen in correspondence with those used in Fig. 5.5.

Based on the limited data available, $\alpha_{0,1}$ seems to be smaller for Au(111) at lower $\langle E_i \rangle$ while at higher $\langle E_i \rangle$ it seems to be *vice versa*. By comparison with Fig. 5.5 it can be seen that for the green circle and the black square the underlying VEP exhibited unusually high $\langle E_i \rangle$ dependence and unusually low overall values, respectively, which might explain why the symbols appear as outliers. In any case, the relatively clear increase ($\sim 2\times$) that I observed for $A_{0,1}^{\text{nonad.}}$ when going from Au(111) to Ag(111) was absent in the kinetic fit. While the fit on Ag(111) is insensitive to the assumed value of $f_{1,2}$ (since only $\nu = 0 \rightarrow 1$ excitation is fitted), it might well be possible that the interaction time t cannot be presumed to be the same on both surfaces. However, assuming the formation of a transient HCl anion, as it is generally done in the case of nonadiabatic vibrational relaxation [102, 113], the image charge stabilization should facilitate the electron transfer at greater distances from the surface for smaller work functions of the surface. That is, for comparable velocities of the molecules, a larger distance would result in longer interaction times in the case of Ag(111). Assuming larger values for t in the fitting process would in return result in even lower values for $\alpha_{0,1}$ which would further increase the discrepancy between the two analysis methods.

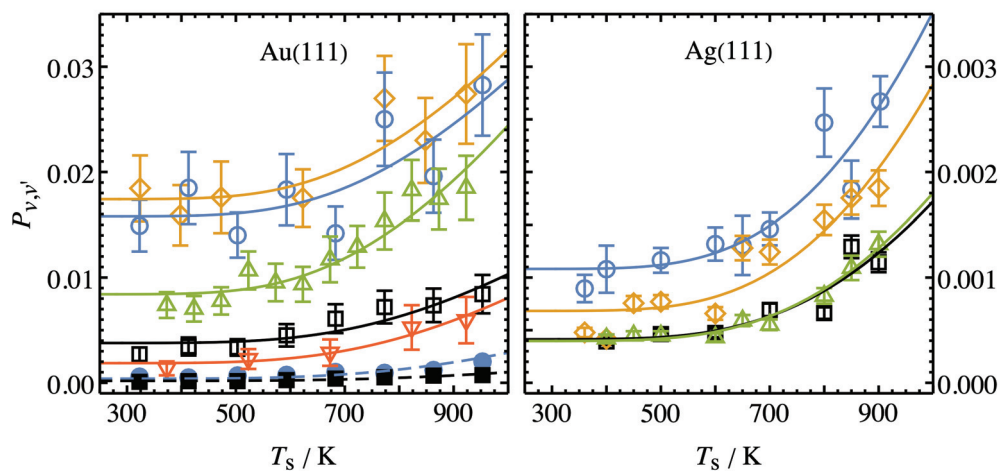


Figure 5.5 Kinetic model fit to the $P_{0,1}$ and $P_{1,2}$ data. For Au(111) (left panel), data and fits for $v = 0 \rightarrow 1$ as well as $v = 1 \rightarrow 2$ are shown in a single plot as filled symbols and dashed lines as well as open symbols and solid lines, respectively. As can also be seen for Ag(111) in the right panel, the kinetic model fits are indistinguishable from the previous ARRHENIUS model fits. Mind the different scales for Au(111) and Ag(111).

5.2 Translational Inelasticity

5.2.1 HCl/Au(111)

Surprisingly, in several molecule-surface systems studied so far, the transfer of translational energy from the molecule to the surface could successfully be described by a simple hard-cube model, the so-called BAULE limit [114]. Here, the theoretical energy that can be transferred to the surface only depends on the masses of the scattered molecules and the surface atoms so that the mean final translational energy $\langle E_f \rangle$ can be calculated as

$$\langle E_f \rangle = \langle E_i \rangle \frac{(m - M)^2}{(m + M)^2} \quad (5.8)$$

where m is the mass of the scattered particle and M the mass of one surface atom. Within this simplistic picture there is no other kind of energy transfer involving internal degrees of freedom, no impact parameter, and no energy transfer of from the thermally moving surface atoms to the scattered molecule, for example. Yet, for HCl scattered from Au(111) in $v = 0 \rightarrow 0$ and $v = 2 \rightarrow 2$ there was a remarkable agreement of $\langle E_f \rangle / \langle E_i \rangle$ with the calculated value of 0.477 if m was assumed to be 36 u and $M = 197$ u, i. e. the mass of a single gold atom [82, 115]. It must be noted, though, that this agreement was mostly true for the mean energy values. At a closer look at the individual translational energy distributions, the authors reported substantial energy transfer beyond the BAULE limit. Similar results were also reported for NO scattering from Au(111), where again the BAULE limit held true at least for mean values of the translational energy [116].

Basically describing the interaction between two isolated bodies, the hard-cube model relies on the scattering event being much faster than the energy redistribution by surface lattice vibrations which can be approximated by the DEBYE frequency [82]. If the surface atom motion is not decoupled from the surrounding atoms on this time scale, the scattered molecule can experience a higher effective surface mass which can lead to higher energy transfer. In this case, Eq. 5.8 can be modified by adding a factor N to the surface mass with which the BAULE limit can be fitted to experimental data:

$$\langle E_f \rangle = \langle E_i \rangle \frac{(m - N \times M)^2}{(m + N \times M)^2} \quad (5.9)$$

In Ref. [82], the authors gathered data from several previous studies of translational inelasticity, where this factor N was determined, which revealed that especially for systems with a small ratio of m/M the value for N was close to 1 – 2 (as HCl/Au(111) and NO/Au(111)). For systems with higher mass ratios N was seen to reach much higher values, e. g. $N = 25$ for Xe/C.

In Secs. 3.2 and 4.2 I calculated the mean final translational energy $\langle E_f \rangle$ for rotationally elastic scattering in dependence on $\langle E_i \rangle$ and the scattering channel in terms of the involved

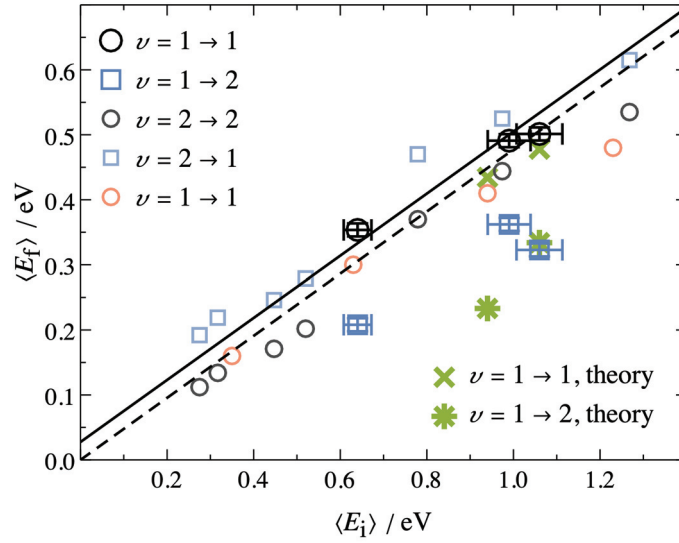


Figure 5.6 Baule limit for HCl/Au(111). Shown is comparison of $\langle E_f \rangle$ depending on $\langle E_i \rangle$ for various vibrational scattering channels of HCl from Au(111). Slightly larger symbols depict the data I measured myself in the vibrationally elastic ($\nu = 1 \rightarrow 1$) and inelastic ($\nu = 1 \rightarrow 2$) case at $T_s = 673$ K as black and blue symbols, respectively. Data taken from Ref. [82] measured at $T_s = 300$ K is depicted by smaller, paler symbols for $\nu = 2 \rightarrow 2$ (black, elastic) and $\nu = 2 \rightarrow 1$ (blue, inelastic) whereas pale red symbols depict data from a bachelor's thesis work conducted at $T_s = 673$ K in our group [117]. The dashed and solid black lines denote the simple BAULE limit according to Eq. 5.8 and the thermal limit according to Eq. 5.10. In addition, green symbols depict theoretical values from Ref. [100] calculated for $T_s = 900$ K.

vibrational states. While for Au(111) the $\nu = 1 \rightarrow 1$ and $\nu = 1 \rightarrow 2$ channels were examined, $\nu = 0 \rightarrow 0$ and $\nu = 1 \rightarrow 1$ were investigated in the case of Ag(111). First, I will concentrate on scattering from Au(111) and compare the current results to previously published ones before including the data on scattering from Ag(111).

In Fig. 5.6, $\langle E_f \rangle$ depending on $\langle E_i \rangle$ is plotted for both scattering channels. In addition, data for HCl/Au(111) taken from Ref. [82] is shown for vibrationally elastic $\nu = 2 \rightarrow 2$ and vibrationally inelastic $\nu = 2 \rightarrow 1$ scattering. Further data was taken from Ref. [117], a bachelor's thesis prepared in our group that also involved measuring the $\nu = 1 \rightarrow 1$ channel. As can be seen from the dashed black line, the classic simple BAULE limit according to Eq. 5.8 does represent the vibrationally elastic data relatively well, especially for $\langle E_i \rangle \lesssim 1$ eV. It needs to be noted, though, that not all measurements were carried out at the same surface temperature and that Eq. 5.8 does not consider the effects of surface temperature at all. However, since its first appearance the simple approach has been modified in several ways. For example, Grimmelmann *et al.* added possible influences of the incidence angle deviating from 0° and the surface temperature deviating from 0 K. Still assuming conservation of parallel momentum and single bounce collisions only, they obtained:

$$\langle E_f \rangle = \alpha_i \langle E_i \rangle + \alpha_s \langle E_s \rangle \quad (5.10)$$

where

$$\alpha_i = \left(1 - \frac{4\mu}{(\mu+1)^2} \cos^2(\theta_i) \right) \quad \text{with} \quad \mu = m/M$$

$$\alpha_s = \frac{\mu(2-\mu)}{(\mu+1)^2}$$

$$\langle E_s \rangle = 2k_B T_s$$

Thus, α_i corresponds to the factor in Eq. 5.8 accounting for the incidence angle and $\langle E_s \rangle$ is the mean surface energy of which the part α_s is transferred to the molecule. Since for the TOF experiments the incidence angle was close to zero, mainly $T_s > 0$ K contributed to deviations from Eq. 5.8. In Fig. 5.6, the solid black line depicts Eq. 5.10 with $\theta_i = 0^\circ$ and $T_s = 673$ K. Indeed, it does fit the data I measured for $\nu = 1 \rightarrow 1$ scattering better than the simple BAULE limit. However, the $\nu = 1 \rightarrow 1$ scattering data depicted by red symbols also was determined for $T_s = 673$ K and is better represented by Eq. 5.8.

It thus seems to be difficult to compare different data sets for vibrational elastic scattering even though the same methodology was used for determining the translational energies. Probably systematic errors in the measurements were larger than previously estimated. One observation, however, is rather obvious: Within one series of experiments, there were substantial differences between the vibrationally elastic and inelastic channels: While those molecules that had undergone vibrational relaxation ($\nu = 2 \rightarrow 1$) exhibited a higher $\langle E_f \rangle$ than those elastically scattered, molecules that had been vibrationally excited ($\nu = 1 \rightarrow 2$) exhibited a lower $\langle E_f \rangle$. The same observation was also made in very recent AIMDEF simulations, the results of which are shown as green symbols in Fig. 5.6. Considering that the theoretical results for vibrational excitation and dissociation probabilities strongly deviate from the experimental ones, not only the qualitative but even the quantitative agreement is remarkable. Although $\langle E_f \rangle$ for the elastic channel is slightly lower than the experimental values (even though the simulated surface temperature was higher at $T_s = 900$ K) it must be noted that in Ref. [100] the authors calculated values for $\langle E_f \rangle$ averaged over all rotational states ($\langle E_{\text{rot}} \rangle \approx 0.1$ eV). In contrast, the values I report here are for the rotationally elastic case at $J = 1$ which will naturally be higher in energy since no energy was lost to rotational excitation.

These differences between vibrationally elastic and inelastic channels were also seen in the case of NO/Au(111) where several vibrational excitation and de-excitation channels of $\nu_i = 2, 3$ were examined [116, 118]. There, over the range of $\Delta\nu = -2 - 1$ a difference $d\langle E_f \rangle / d(\Delta\nu) = -0.05$ eV was found for a fixed $\langle E_i \rangle = 0.63$ eV. That is, for every vibrational quanta lost or gained during the scattering process, a difference of 0.049 eV was seen in the

final translational energy which corresponds to $\sim 22\%$ of one vibrational quantum (this amount increased with $\langle E_i \rangle$). First, the authors ruled out several hypotheses also referring to the $\nu = 2 \rightarrow 1$ relaxation of HCl/Au(111) which I will briefly recall:

1. Coulomb attraction between transient anion and image charge accelerates the incident molecule leading to enhanced energy transfer.
2. Vibrational inelasticity *via* EHPs is enhanced at specific surface sites with a higher effective mass.
3. Specific orientations of the incident molecule enhance nonadiabatic interactions as well as translational energy transfer at the same time.

While these hypotheses could explain general differences between vibrationally elastic and inelastic channels, contradictory to the experimental findings they should have resulted in enhanced energy transfer and thus lower $\langle E_f \rangle$ for both vibrational relaxation as well as excitation. Since this was not the case, two other explanations can be considered: First, there is direct mechanical T-V coupling where translational can be converted to vibrational energy and *vice versa*. Since the VEP analyses revealed no electronically adiabatic contribution to the vibrational excitation of NO on Au(111) [25], that could be a minor effect only. Second, the T-V coupling could have occurred indirectly *via* coupling through EHPs. That is, vibrational as well as translational energy could be received from or transferred to the electronic bath of the surface. After first experimental evidence of T-EHP coupling in scattering Xe from InP(100) [119], it was recently shown that the translational energy loss of H atoms scattered from Au(111) is even dominated by EHP excitation [120] (interestingly, the relative average energy loss was constantly at 40 % over $\langle E_i \rangle = 1 - 3.5$ eV).

Therefore, it does seem reasonable to assume that also the translational degrees of freedom of NO molecules couple to EHP in the Au(111) surface. Such processes might also explain the increase of the assigned EHP mediated V-T coupling with $\langle E_i \rangle$ [116]: Faster molecules could penetrate further into the electron cloud of the surface, thus facilitating the nonadiabatic energy transfers. What remains unclear is the exact pathway through which the energy is channeled between vibration and translation. The vibrational excitation could only be observed at elevated surface temperatures where the amount of excited EHPs with $E \geq E_{\text{vib}}$ was large enough - how could the available surface energy not be enough to compensate the losses due to vibrational excitation and as a result draw translational energy in the range of only up to 34 % of E_{vib} ? Why did the final translational energy of the vibrationally inelastic channels exhibited the same increase with T_s no matter whether the vibrationally energy was transferred from or to the surface? While these questions remain, they do not rule out the possibility of an indirect T-V/V-T transfer.

For HCl/Au(111), the situation is slightly different. For the vibrational relaxation, $\nu = 2 \rightarrow 1$, the gain in translational energy was 0.08 eV (or 24 % of E_{vib}) independent of $\langle E_i \rangle$. For the

excitation, the loss in translational energy was 0.15 eV (42 % of E_{vib}) averaged over the three studied incidence energies. While relaxation in general was explained by nonadiabatic interactions, in the case of vibrational excitation I observed an additional adiabatic contribution. Could it thus be that for HCl/Au(111) direct mechanical T-V coupling was observed?

Going back to Fig. 3.20, the adiabatic and nonadiabatic components $A_{1,2}^{\text{ad.}}$ and $A_{1,2}^{\text{nonad.}}$ depending on $\langle E_i \rangle$ were shown. The former component determines the adiabatic, mechanical contribution to the vibrational excitation. Thus, considering the vibrationally excited molecules detected in the TOF measurements, the relative adiabatic contribution to the gained vibrational energy $\Delta E_{\text{ad.}}$ can be defined as:

$$\Delta E_{\text{ad.}}(E_i) = \frac{A^{\text{ad.}}(E_i)}{A^{\text{ad.}}(E_i) + A^{\text{nonad.}}(E_i) \times \exp[-E_{v,v'} / k_B T_s]} \quad (5.11)$$

Since linear relations were proposed for $A_{1,2}^{\text{ad.}}(E_i)$ and $A_{1,2}^{\text{nonad.}}(E_i)$, an analytical form of $\Delta E_{\text{ad.}}(E_i)$ parametrically depending on T_s can be obtained. Assuming only adiabatic T-V transfer to be responsible for the additional loss of $\langle E_i \rangle$ compared to the vibrationally elastic channel (for which the BAULE limit is considered to be correct), Eq. 5.10 can be extended to:

$$\langle E_f \rangle = \alpha_i \langle E_i \rangle + \alpha_s \langle E_s \rangle - \Delta E_{\text{ad.}}(\langle E_i \rangle) \quad (5.12)$$

In Fig. 5.7, the data from Fig. 5.6 for the $\nu = 1 \rightarrow 1$ and $\nu = 1 \rightarrow 2$ channels is shown again. Apart from the thermal BAULE limit according to Eq. 5.10, which is depicted by the solid black line, three additional lines are shown. First, the dashed black line depicts Eq. 5.12, i. e. the expected final translational energy if the adiabatic fraction of the gained vibrational energy is subtracted from the thermal BAULE limit. Clearly, this approach overestimates the energy loss which is due to the fact that at $T_s = 673$ K the adiabatic fraction $\Delta E_{\text{ad.}}(\langle E_i \rangle)$ was in the range of 0.65 – 0.89 for the given $\langle E_i \rangle$. To get closer to the measured values of $\langle E_f \rangle$, I will reconsider the findings and explanations for the vibrationally relaxation channel of $\nu = 2 \rightarrow 1$. There, $\langle E_f \rangle$ was on average 0.08 eV higher than for the elastic channel. If I now assume that this energy exclusively came from excited EHP (since the indirect coupling of V-T remained unclear) that would open up the possibility that also the $\nu = 1 \rightarrow 2$ channel, which exhibited nonadiabatic interactions with the surface, could have *gained* energy from EHPs. Further assuming the same nonadiabatic gain for both channels (0.08 eV) results in the dotted black line in Fig. 5.7, which is already close to the measured values of $\langle E_f \rangle$. Their agreement can be further improved by introducing a fit parameter N according to Eq. 5.9 that accounts for an effectively encountered surface mass differing from the mass of one gold atom. Implementing the resulting $N = 1.18$ leads to the dashed blue line.

To the best of my knowledge there is no reported example where molecules (or atoms) directly gained translational energy from EHPs. Usually, scattered particles get decelerated

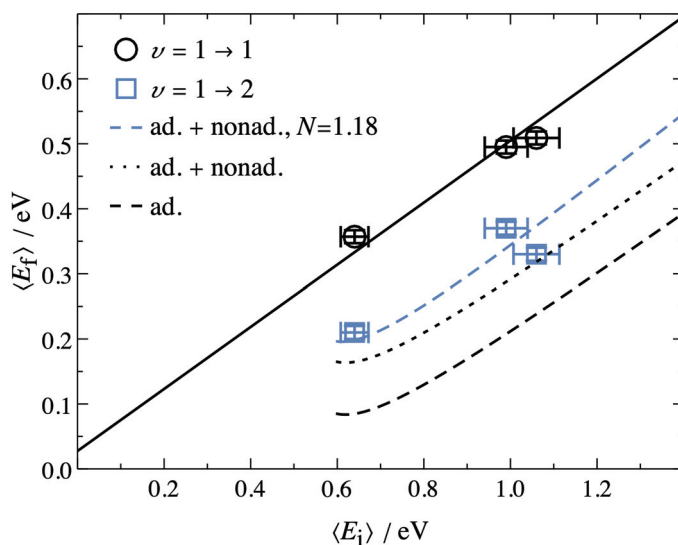


Figure 5.7 T-V coupling for HCl/Au(111). While the data from Fig. 5.6 for the $\nu = 1 \rightarrow 1$ and $\nu = 1 \rightarrow 2$ channels at $T_s = 673$ K is again shown as black and blue symbols, respectively, the solid black line denotes the thermal BAULE limit according to Eq. 5.10. In addition, the blue dashed, black dotted, and black dashed lines depict different modifications of the thermal BAULE limit accounting for different adiabatic and nonadiabatic contributions to the vibrational excitation in line with Eq. 5.12 (see text). These lines are only shown down to $\langle E_i \rangle = 0.6$ eV since below this point $A^{\text{ad.}}(E_i) < 0$ which leads to nonphysical results (the onset of which can be seen as the slight upward trend in the curves).

which in the terms of EF can be visualized as molecules diving into a viscous electron bath. A gain in $\langle E_f \rangle$ also seems to be unlikely in the light of the consistent results of NO/Au(111) where no hint for adiabatic effects could be found. Nevertheless, being unlikely does not make the proposed processes impossible. More extensive experimental work including more incidence energies and vibrational transitions of HCl (and ideally also other molecules and surfaces) are needed to shed more light on the underlying mechanisms of energy transfer.

5.2.2 HCl/Ag(111)

I will now compare the results obtained on Au(111) to those for HCl scattered from Ag(111). Since I could not detect the $\nu = 1 \rightarrow 2$ excitation on this surface I only examined the elastic $\nu = 0 \rightarrow 0$ and $\nu = 1 \rightarrow 1$ channels. In Fig. 5.8, the mean final translational energies $\langle E_f \rangle$ obtained from Tab. 4.7 depending on their respective mean incidence energy $\langle E_i \rangle$ are shown. While the $\nu = 0 \rightarrow 0$ channel is depicted by open red symbols for $T_s = 400 - 900$ K, the $\nu = 1 \rightarrow 1$ data is depicted by filled silver symbols for $T_s = 400$ K and 900 K. For comparison, data from Fig. 5.6 for the $\nu = 1 \rightarrow 1$ channel scattered from Au(111) at $T_s = 673$ K is depicted by filled golden symbols. Dashed and solid lines in the corresponding elemental colors show the simple and thermal BAULE limit (for $T_s^{\text{Au}} = 673$ K and $T_s^{\text{Ag}} = 900$ K), respectively.

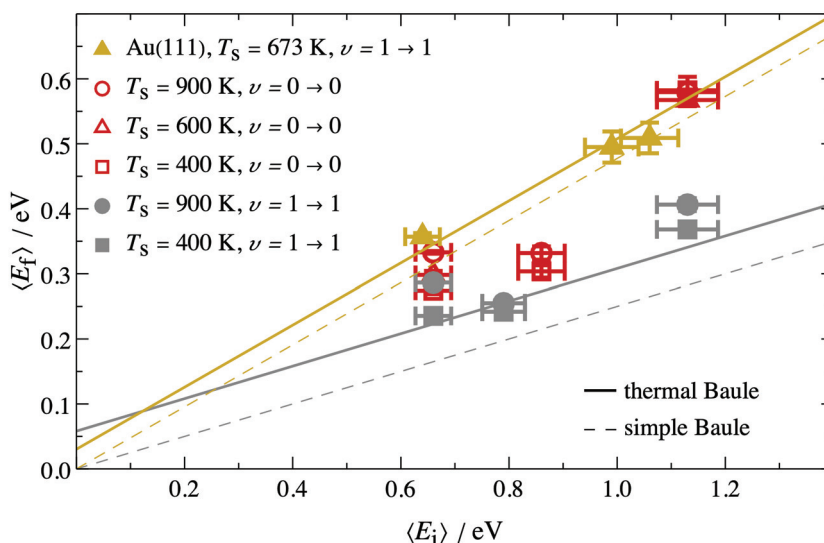


Figure 5.8 Testing the BAULE limit for HCl/Ag(111) in comparison to HCl/Au(111). Depicted by filled silver symbols are the mean final translational energies $\langle E_f \rangle$ for $\nu = 1 \rightarrow 1$ scattering of HCl from Ag(111) at $T_s = 400 \text{ K}$ and 900 K while open red symbols depict the data for $\nu = 0 \rightarrow 0$ at $T_s = 400 - 900 \text{ K}$. For comparison, data from Fig. 5.6 for the $\nu = 1 \rightarrow 1$ channel on Au(111) is depicted by filled golden symbols. Dashed and solid lines in the corresponding elemental colors show the simple and thermal BAULE limit (for $T_s^{\text{Au}} = 673 \text{ K}$ and $T_s^{\text{Ag}} = 900 \text{ K}$), respectively.

In contrast to HCl/Au(111), where the thermal model was in very good agreement with $\nu = 1 \rightarrow 1$, on Ag(111) the same channel lead to values of $\langle E_f \rangle$ slightly above the expectation. Interestingly, for the $\nu = 0 \rightarrow 0$ channel the disagreement is even higher. Unlike on Au(111), where all vibrationally elastic channels studied so far exhibited comparable values for $\langle E_f \rangle$, $\langle E_f \rangle$ of molecules in $\nu = 0 \rightarrow 0$ was significantly higher than in $\nu = 1 \rightarrow 1$ (although there is a notable deviation from a linear dependence for $\nu = 0 \rightarrow 0$ consisting of only three data points). There seem to be different scattering characteristics for both elastic channels which become obvious if again the number of surface atoms is used as a fitting parameter according to Eq. 5.9. While for $\nu = 1 \rightarrow 1$ the resulting mass is $M_{\text{eff}} = 1.1 \times M_{\text{Ag}}$ averaged over all T_s , this increases to $M_{\text{eff}} = 1.7 \times M_{\text{Ag}}$ in the case of $\nu = 0 \rightarrow 0$. Reconsidering the translational energy distributions in Fig. 4.15, the calculated higher $\langle E_f \rangle$ results from slightly increased peak energies as well as broader distributions extending to higher translational energies.

As can especially be seen for $\langle E_i \rangle = 0.66 \text{ eV}$ and 1.15 eV (Fig. 4.15 panel a) and e)), small fractions of the scattered molecules even exhibited E_{kin} beyond the incidence translational energy distributions (even though their contribution to the mean value will be minor). That is, they must have gained energy from the surface during the scattering event, a process that previously had not even been observed for the $\nu = 2 \rightarrow 1$ relaxation of HCl/Au(111). It was seen for NO/Au(111), however, when molecules relaxed from $\nu = 3 \rightarrow 2$ or $\nu = 3 \rightarrow 1$. For both systems, the fraction of molecules with $E_f >$

E_i is rather small. Yet, the effect was observable for two data sets measured several months apart with sufficient S/N so that I am rather confident it was not due to experimental errors. It needs to be pointed out, though, that for HCl/Ag(111) these high energy molecules only appeared at elevated surface temperatures (like $T_s = 900\text{K}$ as shown in Fig. 4.15). At $T_s = 400\text{K}$, the energy distributions were not as broad. Instead, at these relatively low surface temperatures the scattered TOF curves for $\langle E_i \rangle = 0.66\text{eV}$ and 0.86eV revealed a second component hidden under the trailing edges that could be fitted with a 3D MBD at $T \approx 300 - 400\text{K}$ (see Fig. 5.9). That is, among the scattered there were molecules whose translational energy had accommodated to the surface energy, probably due to TD. These components could only be observed for

1. the $\nu = 0 \rightarrow 0$ channel,
2. the lower T_s ,
3. and the lower two $\langle E_i \rangle$.

I guess that, first, the molecules incident in $\nu = 1$ vibrationally relaxed during trapping so that there was no slow $\nu = 1 \rightarrow 1$ TD component. Second, at higher surface temperatures MBDs shift to higher energies blending into the DS energy component. Even though they might be hidden underneath, it is not possible to distinguish them in these experiments. Third, if the TD component was due to physisorption, it is reasonable to assume that the trapping probability decreased with increasing $\langle E_i \rangle$. However, even $0.66 - 0.86\text{eV}$ seem to be rather high incidence energies for trapping/desorption.⁵ It must be noted that the TOF background correction in the case of $\langle E_i \rangle = 1.15\text{eV}$ was not as good as for the other two $\langle E_i \rangle$ so that TD components could have been overseen. If the TD component was due to chemisorption (i. e. dissociative adsorption), I would expect its intensity relative to the DS to increase which was not seen. In any case, even for $T = 900\text{K}$ the energetical MBD extends only to approximately 0.5eV and should not affect the high energy edge of the $\langle E_i \rangle$ distributions for the $\nu = 0 \rightarrow 0$ channel.

Coming back to the comparison of the $\nu = 0 \rightarrow 0$ and the $\nu = 1 \rightarrow 1$ channels, as mentioned

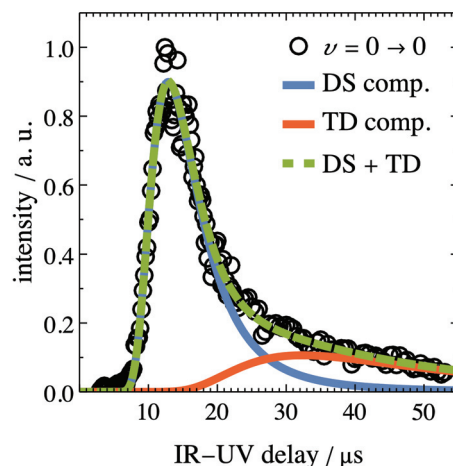


Figure 5.9 TOF distribution for HCl molecules with $\langle E_i \rangle = 0.66\text{eV}$ scattered from Ag(111) in $\nu = 0 \rightarrow \nu = 0, J = 2$ at $T_s = 400\text{K}$. While the black symbols depict the measured intensity, the solid blue and red, and the dashed green line depict the direct scattering (DS) and the trapping/desorption (TD) component, and the sum of both, respectively. The MAXWELL-BOLTZMANN distribution (MBD) was fitted with $T_s = 308\text{K}$ in a global fit including all examined J states. Pure DS fits were not able to satisfactorily reproduce the data.

⁵ Unfortunately, I could not find any publications reporting the desorption energy of HCl from Ag(111).

in Sec. 4.2 from an experimental point of view it is counterintuitive that the translational energy distributions of the former channel was broader. For obtaining $v = 0 \rightarrow 0$ TOF distributions, HCl molecules were IR-tagged after the surface collision while for $v = 1 \rightarrow 1$ they were tagged before. That is, in the latter case the bunch of tagged molecules had a longer flight path as well as interactions with the surface to spread out in time. There are two processes which might explain the findings. In the case of $v = 0 \rightarrow 0$ there could have been contributions from TD components on the lower energy side even for high surface temperatures which could simply not be disentangled from the DS component under these conditions. On the other hand, dissociation could have played a role in the $v = 1 \rightarrow 1$ channel. As seen for HCl/Au(111), vibrational excitation presumably increased the dissociation probability (cf. Fig. 3.39). Maybe molecules in the higher energy side of the incident $v = 1$ translational energy distributions already had a significant dissociation probability so that they were removed from the scattered distributions. This might also explain the increasing difference between $v = 0 \rightarrow 0$ and $v = 1 \rightarrow 1$ with increasing $\langle E_i \rangle$: the relative amount of dissociating molecules should have increased with $\langle E_i \rangle$.

If thus the $v = 0 \rightarrow 0$ channel exhibited the "regular" behavior on Ag(111), the observed relatively high $\langle E_f \rangle$ above the BAULE limit would not have been without precedent. While, as stated above, for NO/Au(111) the hard-cube model held approximately true [116], it was recently reported that on Ag(111), $\langle E_f \rangle$ of scattered NO($v = 2 \rightarrow 2$) as well as CO($v = 2 \rightarrow 2$) stayed well above the calculated limit [103]. That study, which involved translational inelasticity measurements on Au(111) gradually covered by thin films of Ag(111), revealed three findings that were especially interesting in relation to my results: First, in contrast to the results on several layers of Ag(111), for the bare Au(111) surface the BAULE limit again successfully predicted $\langle E_f \rangle$ for NO($v = 2 \rightarrow 2$) and CO($v = 2 \rightarrow 2$). Second, the (change in) scattering behavior was explained with the (change in the) phonon structure, which evolved over three layers of Ag(111) on Au(111), by comparison to DFT calculations. That is, at least on Ag(111) the incident molecules seemed to interact with more than one silver atom. Third, a closer look reveals that for NO($v = 0 \rightarrow 0$) the values of $\langle E_f \rangle$ were repeatedly higher than for NO($v = 2 \rightarrow 2$), similar to what I discussed above.

Considering these findings I will complete this section with once again invoking nonadiabatic interactions. As I have presented above, these interactions were shown to be stronger on Ag(111) than on Au(111) and are enhanced for incident vibrational excitation. If one assumes EHPs to influence translational inelasticity, both observations can be made here as well: HCl as well as NO molecules incident in excited vibrational states do lose more translational energy during the scattering, an effect that is more pronounced on Ag(111) (for HCl, which exhibits weaker nonadiabatic interactions than NO, it seems to be absent on Au(111)). Although only tested for H and D atoms, the general loss of translational energy *via* EHPs was shown both experimentally and theoretically for several transition metals [121].

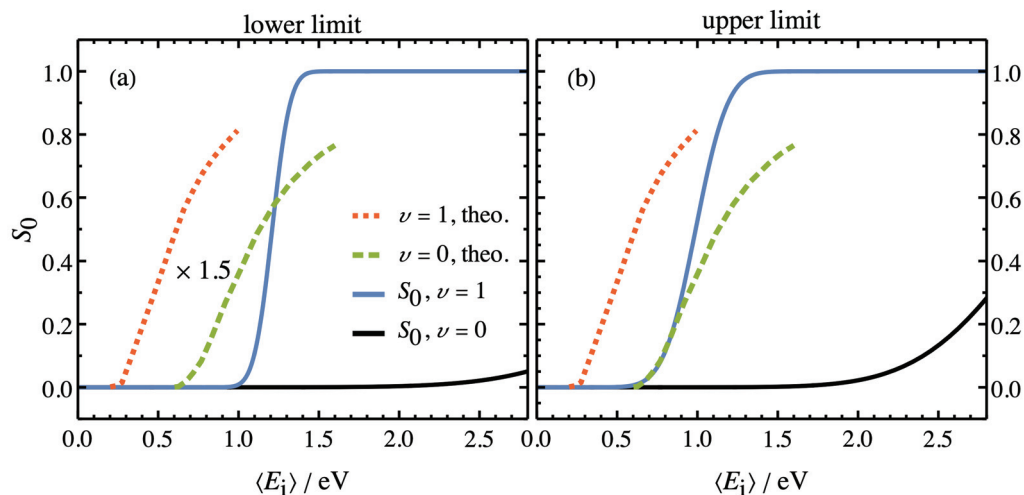


Figure 5.10 Comparison of the $S_0^{\nu=i}(\langle E_i \rangle)$, derived from the fits in Fig. 3.39 according to Eq. 3.23, with theoretical predictions of Liu *et al.* [58, 60]. In panel (a), the solid black and blue lines depict the experimentally derived lower limit curves for $\nu = 0$ and $\nu = 1$, respectively, while the theoretical curves taken from [58, 60] are depicted by the dashed green and red curves which have been multiplied by a factor of 1.5 for better comparability. Panel (b): The same as in (a), but experimentally derived curves are shown for the upper limit.

5.3 Dissociation

5.3.1 Comparison with Initial Theory

As stated in Sec. 3.3, among other things my work on the dissociation of HCl on Au(111) had been stimulated by the theoretical work of Liu *et al.* [58, 60]. Thus, the first thing to do is comparing the experimentally derived initial sticking probabilities depending on the incident vibrational state and mean translational energy $S_0^{\nu=i}(\langle E_i \rangle)$ with the reported theoretical values. The fitting parameters given in Tab. 3.12 characterize the inflection points $E_{0,0}$ and $E_{0,1}$ of the error functions describing $S_0^{\nu=i}(\langle E_i \rangle)$, which are comparable to energetic barriers, and the widths W_0 and W_1 , which are a measure of the curves' slope (i. e., how strongly S_0 increases with $\langle E_i \rangle$). In Fig. 5.10, solid black and blue lines depict the experimental curves for $\nu = 0$ and $\nu = 1$, respectively, in the lower and upper limit while the theoretical curves taken from [58, 60] are depicted by the dashed green and red lines. Before going into discussions, I need to recall that the derived fitting parameters in Tab. 3.12 could not satisfactorily represent the experimentally determined values. If theoretical and experimental results are nevertheless compared, three details are obvious:

1. The inflection points of the experimental curves are shifted to higher energies by ~ 0.6 eV and ~ 0.3 eV for the lower and upper limit, respectively. That is, the apparent barrier to dissociation should be much higher than predicted.

2. At least for $\nu = 1$ the slope of the curve is much steeper (the width is smaller). That is, the vibrationally excited molecules respond more strongly to an increase in $\langle E_i \rangle$.
3. The shift in E_0 between $\nu = 0$ and $\nu = 1$ is much larger in the experimental curves which means that here the vibrational efficacy was much higher.

Knowing that the fitting parameters are flawed, the validity of these observations might be limited. Therefore, experiment and theory can be compared in a different way where the theoretical, calculated curves can be adapted to the experimental situation. First, the digitized theoretical curves are fitted with error functions as in Eq. 3.24 to obtain continuous functions $S_{0,\text{theo}}^{\nu=i}(E)$. These are then inserted in Eq. 3.23 to obtain a modified fitting function for DS1 and DS2:

$$S_{0,\text{theo}}(E) = \sum_{i=0}^1 f(\nu = i) \int_0^{\infty} S_{0,\text{theo}}^{\nu=i}(E') g[E', E_0(E), \alpha(E)] dE' \quad (5.13)$$

That is, the sticking probabilities obtained from theory are averaged over the experimental vibrational state and translational energy distributions of the incident beam. The result of this procedure is shown in Fig. 5.11 as dashed black and blue lines, where the main difference between both curves is the fraction of molecules in $\nu = 1$ (varying with $\langle E_i \rangle$ for the black line and constant for the blue one). In an attempt to get the curves roughly scaled to the open symbols depicting the experimentally determined S_0 as in Fig. 3.39, they had to be multiplied with a factor of 0.1 and 0.25 for the lower and upper limit, respectively. Although the fitting described above is flawed, the results are not surprising keeping in mind the outcome of the fitting in Sec. 3.3.4. Apart from the expected overestimation of S_0 the most striking observation in Fig. 5.11 is the almost perfect overlap of both curves which makes them difficult to distinguish. While the overestimation is related to the overall shift to lower energies of the theoretical curves (first point of the list above), there are two possible explanations for the overlap:

1. Even though there are predicted differences between $S_0^{\nu=0}$ and $S_0^{\nu=1}$ they did not manifest in Fig. 5.11 because the population in $\nu = 1$ was simply too low to result in significant deviations of both curves.
2. Not only the absolute position but also the position difference on the energy axis of $S_0^{\nu=0}(\langle E_i \rangle)$ and $S_0^{\nu=1}(\langle E_i \rangle)$ is underestimated by theory.

On the one hand, an incorrectly determined population of $\nu = 1$ could be the reason for the lack of correspondence between theory and experiment in addition to the barrier shift. On the other hand, theory could have underestimated the difference in reactivity between both vibrational states. All of these cases can be tested if a fitting routine is developed as in Sec. 3.3.4 that includes the theoretical $S_{0,\text{theo}}^{\nu=i}(E)$ as well as a scaling factor for the

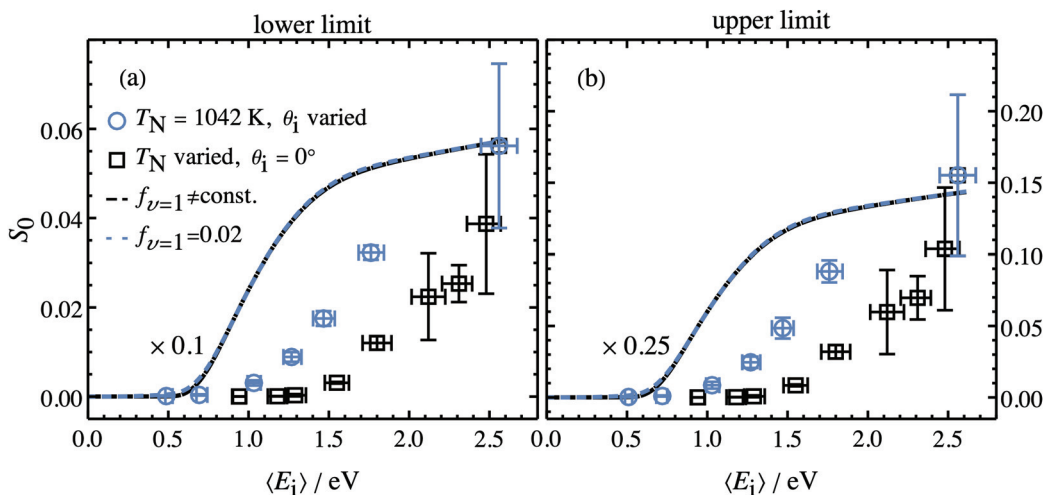


Figure 5.11 Comparison of the experimentally determined S_0 with theoretical predictions of Liu *et al.* [58, 60] averaged over the experimental conditions. Panel (a): While DS1 and DS2 in the lower limit are depicted by open black and blue symbols, dashed black and blue lines depict the theoretical curves averaged over the experimental incident vibrational state and translational energy distributions of DS1 and DS2. For better comparability, the latter ones are scaled by a factor of 0.1. Panel (b): The same as in (a), but DS1 and DS2 are shown in the upper limit and the theoretical curves are scaled by a factor of 0.25.

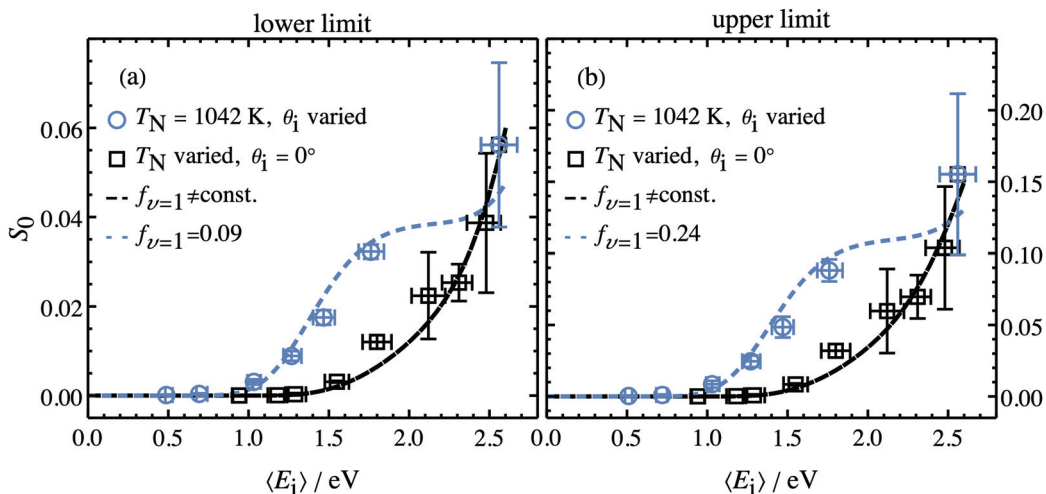


Figure 5.12 Comparison of the experimentally determined S_0 with theoretical curves fitted to the data. Panel (a): While DS1 and DS2 in the lower limit are depicted by open black and blue symbols, dashed black and blue lines depict the theoretical curves where for both curves individual shifts on the energy axis $\Delta E_{0,0}$ and $\Delta E_{0,1}$ and a correction factor c_{vib} to the relative vibrational population in $v = 1$, f_{vib} , were fitted to the data. The fitting procedure (see text) resulted in $f_{\text{max}}(v = 1) = 0.09$, $\Delta E_{0,0} = 2.5 \text{ eV}$, and $\Delta E_{0,1} = 0.9 \text{ eV}$. Panel (b): The same as in (a), but DS1 and DS2 are shown in the upper limit. Here, the fitting resulted in $f_{\text{max}}(v = 1) = 0.24$, $\Delta E_{0,0} = 2.3 \text{ eV}$, and $\Delta E_{0,1} = 0.9 \text{ eV}$.

vibrational population in $v = 1$, c_{vib} , and energy differences $\Delta E_{0,i}$ that can independently shift $S_{0,\text{theo}}^{v=0}(E)$ and $S_{0,\text{theo}}^{v=1}(E)$ on the energy axis. Eq. 5.13 then becomes:

$$S_{0,\text{theo}}(E) = \sum_{i=0}^1 c_{\text{vib}} \times f(v=i) \int_0^\infty S_{0,\text{theo}}^{v=i}(E' - \Delta E_{0,i}) g[E', E_0(E), \alpha(E)] dE' \quad (5.14)$$

Indeed, a fit including these additional three parameters is able to nicely reproduce the experimental data as seen in Fig. 5.12 for the lower as well as the upper limit (including only c_{vib} or $\Delta E_{0,i}$ in Eq. 5.13 did not result in a reasonable fit). From the fitting parameters provided in Tab. 5.1 it can be concluded that the shifts to higher energy $\Delta E_{0,0}$ and $\Delta E_{0,1}$ are relatively consistent for both S_0 limits. That is, independent of the absolute S_0 values the dissociation barriers as well as the vibrational efficacy seem to have been underestimated by theory. On the other hand, c_{vib} , which is already high at 4 for the lower limit, increases to 12 in the upper limit case. That is, to be able to represent the data, the vibrational population in $v = 1$ would have been approximately 12 times higher than experimentally observed, which corresponds to

a maximal population in $v = 1$ of $f_{\text{max}}(v=1) = 0.24$ ($f_{\text{max}}(v=1) = 0.09$ in the lower limit). At this point it is worth mentioning that I doubt that I have underestimated the experimental vibrational population so significantly. However, there is one further parameter in the analysis of the data and the fitting procedures that I have not mentioned so far. The main problem in the experimental data apart from the absolute shift

on the energy axis is the large relative shift between the two data sets. So far I have assumed the difference in vibrational population to be the reason behind this different. However, in the process of the analysis and data preparation, I presupposed that for DS2 measured at tilted angles the effective translational energy leading to dissociation can be calculated assuming normal energy scaling. While this might be a valid assumption in many cases, it is not necessarily true. Studying HCl scattering from Au(111) deposited on atomically flat mica with velocity-map imaging, Roscioli and co-workers found that at least under near-grazing incidence angles (75°) the in-plane $\langle E_{\parallel} \rangle$ was anti-correlated with the final rotational energy [122]. That is, the parallel momentum of the molecules must have interacted with the surface. At this point I simply cannot exclude that with increasing incidence angle (as for DS2) deviations from the commonly accepted concept of normal energy scaling might occur, nor can I predict in which exact way the "parallel component" of the incidence energy would help HCl molecules surmounting the barrier to dissociation or even hinder them from doing so.

Table 5.1 Derived fit parameters to bring the theoretical curves in accordance with the data for the lower and upper limit. $\Delta E_{0,0}$ and $\Delta E_{0,1}$ are given in units of eV.

limit	c_{vib}	$\Delta E_{0,0}$	$\Delta E_{0,1}$
lower	4	2.5	0.9
upper	12	2.3	0.9

5.3.2 Further Theoretical Work

After the results presented in my thesis had been published [123], we engaged in vivid discussions with several groups specialized in theoretical descriptions of surface scattering processes that have resulted in multiple subsequent publications on this reaction [95, 96, 100, 109, 124]. Considering the initial work of Liu *et al.* [58, 60], to which I compared the experimental result in the previous section, our concerns were mainly threefold:

First, while employing potentially very accurate quantum dynamics, only molecular DOF were included in the calculations. That is, the surface was treated as being static and thus could neither transfer to nor accept translational energy from the molecules. This approach contradicts the findings on the translational inelasticity discussed above where in general more than 50 % of $\langle E_i \rangle$ were lost to the surface. Even though trajectories leading to dissociation might not necessarily include as much translational energy transfer as directly scattered ones, neglecting surface DOF in the first place could lead to wrongly predicted $\langle E_i \rangle$ dependencies of S_0 . In fact, one argument for the enhanced VEP of $\text{HCl}(v = 1 \rightarrow 2)$ on Au(111) was that molecules retained vibrational excitation from the stretched bond while approaching the transition state (TS) towards dissociation. This is also in accordance with the further enhanced loss of translational energy observed for vibrationally excited molecules (see Fig. 5.7).

Second, the DFT functional used in Refs. [58, 60] was PW91 which predicted a barrier height of 0.64 eV. However, when this barrier height was compared with the outcome of further functionals like PBE, revPBE, and RPBE [100], where a range of TS energies of 0.64 - 1.05 eV was obtained, it became clear that the barrier highly depends on the computational details. Although the barrier height is not the only parameter governing the reaction (e. g., the TS geometry and thus position on the PES also play a role), it most notably varied the calculated reactivities which complicates comparison to experiments. Third, as I have seen in the case of vibrational excitation, HCl molecules do seem to interact with surface EHPs giving rise to electronic nonadiabaticity, which is probably even enhanced at the TS. However, the calculations in Refs. [58, 60] were carried out under the BOA which means that interactions between nuclear and electronic DOF were not taken into account. As seen for H atoms scattered from Au(111), there are situations in which molecular energy can be efficiently dissipated by EHPs which would most probably lower the dissociation probabilities [18, 120, 121]. All of the concerns raised above were addressed in the theoretical works that have been published in the meantime. The main differences to Refs. [58, 60], the consequences of which will be discussed in the following paragraphs, can be summarized as follows:

1. Use of different functionals to review their effect on the TS (see Ref. [124]).
2. Employing AIMD including motion of surface atoms to check the effect of finite surface temperature and translational energy transfer (see Refs. [95, 96]).

3. Including electronic nonadiabatic effects in the form of electronic friction (see Refs. [95, 100]).

Effect of the DFT functional

In a follow-up publication, Liu *et al.* extended their quantum dynamics studies with calculations on a new RPBE based PES fitted with neural networks [124]. Since the further computational details were largely the same as in the previous study (e. g., four-layer slab, 2×2 surface unit cell), this comparison is probably most suitable to show the effect of the DFT functional.

First, with RPBE the barrier energy E_b increased by 0.42 eV from 0.64 eV to 1.08 eV. Moreover, the potential energy of the dissociation products H and Cl is increased approximately by the same amount (from 0.27 eV to 0.74 eV) so that the reverse reaction barrier to associative desorption remained very similar (0.34 eV *vs.* 0.39 eV). While the general shape of the curve for S_0 depending on $\langle E_i \rangle$ was indistinguishable at first glance, it was shifted by ~ 0.4 eV to higher $\langle E_i \rangle$ which exactly corresponds to the difference in E_b . Interestingly, the TS geometry, that is the molecule's bond elongation and its height above the surface, were very similar for both functionals. Thus, it seems like the position on the translational energy axis directly scales with the barrier height which was recently also reported for the dissociation of HCl on Ag(111) by the same group [107]. This supports the shift of the PW91 derived $S_0^{\nu=0}(\langle E_i \rangle)$ on the energy axis to fit the experimental data in Fig. 5.12. A very comparable TS energy ($E_b = 1.05$ eV) and geometry was also observed by Füchsel *et al.* [95] employing the same functional. In contrast, also using RPBE for DCl/Au(111) a barrier energy of only 0.91 eV was obtained by Kolb and Guo when the first two surface layers were not set to be frozen but allowed to move ([96]). Although DCl was used instead of HCl, the difference should be minor since Liu *et al.* also calculated E_b for DCl/Au(111) to be 0.65 eV (compared to 0.64 eV for HCl) and the reactivities, also probably wrong on an absolute scale, were almost the same for both molecules.

Surface Motion

In their study of DCl/Au(111) Kolb and Guo used the top two free-to-move surface layers to examine the translational energy transfer and dissociation probabilities *via* AIMD simulations [96]. Compared to the experimental results, the resulting dissociation probabilities ($S_0^{\text{AIMD}}(2.0\text{ eV}) \approx 0.16$) & $S_0^{\text{AIMD}}(2.5\text{ eV}) \approx 0.29$) were still higher than the lower and upper limit by a factor of ~ 8 and $\sim 3 - 4$, respectively. De-activating the surface motion but leaving other computational details the same as before, S_0 increased by $\sim 23\%$. It needs to be noted, though, that the DCl molecules were assumed to exhibit out-of-plane translational as well as vibrational and rotational energies corresponding to 300 K. That is, at increased vibrational energies as in the experiment the difference between theoretical and experimental S_0

might be even larger. Further, the translational energy loss calculated at $\langle E_i \rangle = 1.25$ eV was only 33 % which is substantially less than the approximately 55 % experimentally observed. While Füchsel *et al.* also found 30 – 36 % in their PBE AIMD simulations [95], molecular dynamics calculations on the PBE derived PES with a rigid surface showed only 2 – 4 % energy loss. That is, even though the theoretical energy loss to the surface atoms was less than in the experiments, the energetical effect of surface motion could clearly be seen. Comparing AIMD calculations for different surface conditions, the authors found a decrease of ~ 12 % in S_0 going from a rigid surface to $T_s = 0$ K for $\langle E_i \rangle = 1.4$ eV. With increasing $\langle E_i \rangle$ the differences between rigid and surfaces in motion diminished. Increasing T_s to 298 K, the dissociation probability was even higher than for the rigid surface at $\langle E_i \rangle = 2$ eV. In their latest study, where both groups collaborated, they again carried out AIMD simulations comparing different functionals [100]. This time, SRP32-vdW was used since the included VAN DER WAALS interactions best resembled the physisorption well of 0.23 eV estimated from experimental work [43]. With this functional, translational energy losses of 47 – 51 % at $\langle E_i \rangle \approx 1$ eV were calculated which is much closer to the experimental values. Despite this substantially increased energy transfer to the surface, the dissociation probability only decreased by approximately 5 % for $\langle E_i \rangle = 2.56$ eV from 0.402 to 0.382.

Electronical Nonadiabaticity

In their computational studies, Füchsel *et al.* also included electronical nonadiabaticity *via* EF in the local density friction approximation in the independent atom approximation (LDFA-IAA) for MDEF [95] and AIMDEF [100]; a method which successfully modeled the large translational energy loss of H atoms scattered from Au(111) [18]. Even though for short atom-surface distances the friction coefficients were larger for Cl atoms, at the TS the H atom position was much closer to the surface so that the dissipation rate was dominated by friction of the H atom. Yet, in neither study the inclusion of EF in addition to an otherwise identical computational framework led to a substantial decrease in the dissociation probability. For MDEF, the reduction was only 7 – 1 % (for $\langle E_i \rangle = 1.29 - 2.56$ eV at the rigid surface approximation) while for AIMDEF it was 16 – 4 % for the same translational energies [100]. Interestingly, the relative reduction in reactivity due to EF decreased with increasing $\langle E_i \rangle$. Actually, the energy dissipation rate is supposed to increase with the shorter atom-surface distances which are reached at higher incidence velocities. However, two details must be noted here: First, owing to the high computational cost of AIMD simulations, in the case of $\langle E_i \rangle = 2.56$ eV the difference between AIMD and AIMDEF was based on an absolute number difference of *seven* trajectories leading to dissociation out of 500. Second, an increase of the surface unit cell from (2×2) to (3×3) further decreased S_0 under these conditions by another 4 %. Thus, statistical as well as methodological uncertainties might still be relatively large and blur the actual effects (the authors estimated the uncertainty in S_0 to be ~ 6 % based on an absolute uncertainty of *ten* trajectories).

Summary

Referring to the enumeration above this detailed examination, the results of the theoretical studies on the dissociation of HCl on Au(111) can be summarized as follows:

1. With the choice of the DFT functional the barrier height to dissociation E_b varied by ~ 0.4 eV. With increasing E_b the dissociation probability decreased considerably.
2. Even though AIMD simulations with the SRP32-vdW functional resulted in $\sim 50\%$ translational energy loss, allowing surface atoms to move did not substantially influence S_0 .
3. Implementation of electronic nonadiabaticity *via* EF on the LDFA level did not significantly reduce S_0 .

Of course, in their publications on computational simulations the authors also addressed potential errors in our experimental work. At this point, it needs to be pointed out that the previously published experimental values for S_0 were approximately 3 – 4 times smaller than the lower limit reported in this thesis (and thus $\sim 7 - 10$ times smaller than the upper limit). These differences mainly arise from optimized coverage and flux calculations with which some of the critique is already addressed in the case of the upper limit (like the absolute pressure calibration and the T_s dependence of the chlorine coverage, see Sec. 3.3). The main issue discussed extensively in Ref. [95] is the possibility that the conversion from APPH determined from Auger spectra to the Cl coverage was wrongly calibrated. Füchsel *et al.* mainly base their arguments on the works of Spencer and Lambert [92] and Kastanas and Koel [91] which suggested a saturation coverage of $\Theta_{\text{Cl}} \approx 3$ ML instead of the 1 ML that I used. While in the former publication the APPH calibration curve is provided that I also used to calibrate my APPH values, no specific estimate on the actual saturation coverage is given. Yet, the authors postulated the formation of AuCl₃ on the surface which would most probably lead to a saturation coverage higher than 1 ML. A more precise value for $\Theta_{\text{Cl,sat.}}$ is presented only in Ref. [91] where the authors calibrate the Cl/Au ratio based on previously determined O/Au ratios from the adsorption of ozone on Au(111) [125]. However, in the very same publication they provided XPS data that suggested a value of $\Theta_{\text{Cl,sat.}} = 0.8$ ML while the determined binding energies contradicted the formation of gold chlorides. This was further backed by UPS and LEED studies so that towards the end of their publication, Kastanas and Koel stated that "[most of] our data can be used to argue against the formation of bulk gold chlorides" [91].

In the most recent work on Cl adsorption on Au(111), Gao *et al.* studied Cl₂ adsorption with AES, LEED, STM, XPS and theoretical methods (DFT) [126]. On the one hand the authors concluded that the formation of gold chlorides *cannot* be excluded, but should only start to play a role at coverages larger than ~ 0.33 ML. On the other hand, relying on a precisely known sulfur standard the saturation coverage was determined to be $\Theta_{\text{Cl,sat.}} = 1$ ML. Thus,

while the complex state of Cl on Au(111) remains to be fully deciphered, I would argue that the use of $\Theta_{\text{Cl,sat.}} = 1 \text{ ML}$ is justified.

In Fig. 5.13, a summary of all currently available theoretically determined dissociation probabilities is shown. Here, the lower and upper limit of DS1 and DS2 are indicated by the lightly colored areas in gray and blue, respectively, for improved optical readability. While the dashed lines denote the quantum dynamics results of Liu *et al.* [58, 60, 124] calculated with PW91 in green and RPBE in yellow (both averaged over the experimental conditions as discussed above and lowered by a factor of 0.1), symbols depict the AIMD results from Kolb and Guo (open red symbols, RPBE, lowered by 0.2) [96], MD/EF results from Füchsel *et al.* (open and filled blue symbols, PBE, lowered by 0.2) [95], and AIMD/EF results from the collaboration of both groups (open and filled black symbols, SRP32-vdW, lowered by 0.2) [100]. Although molecules were equipped with vibrational and rotational energy according to a MBD at 300 K and not according to the measured distributions, the best correspondence between theory and experiment was achieved by the AIMD simulations of Kolb and Guo, the S_0 values of which were placed directly between the lower and upper limit by the multiplication with 0.2. However, I have to point out again that the simulations were actually carried out for DCl and not HCl. The next best fit was achieved with the AIMDEF simulations using the SRP32-vdW functional. Two things here are noteworthy: First, as discussed above the implementation of electronic friction barely improved the differences between theory and experiment which can be seen from the small deviations of the filled from the open symbols. Second, the shape of all computationally determined curves rather seemed to follow the shape of DS2 (that is, $\Delta S_0/\Delta \langle E_i \rangle$ decreases with increasing $\langle E_i \rangle$), where the vibrational population was kept constant, even though the simulations included the vibrational populations at the corresponding experimental nozzle temperatures.

In summary, even though computational studies of the HCl/Au(111) dissociation subsequent to the first publications continuously refined system parameters (such as surface motion/temperature, vibrational and rotational energy of the molecule, VAN DER WAALS interactions) to more realistically model the experimental data, the resulting theoretical dissociation probabilities remained approximately 3 – 5 times larger than the experimental ones.

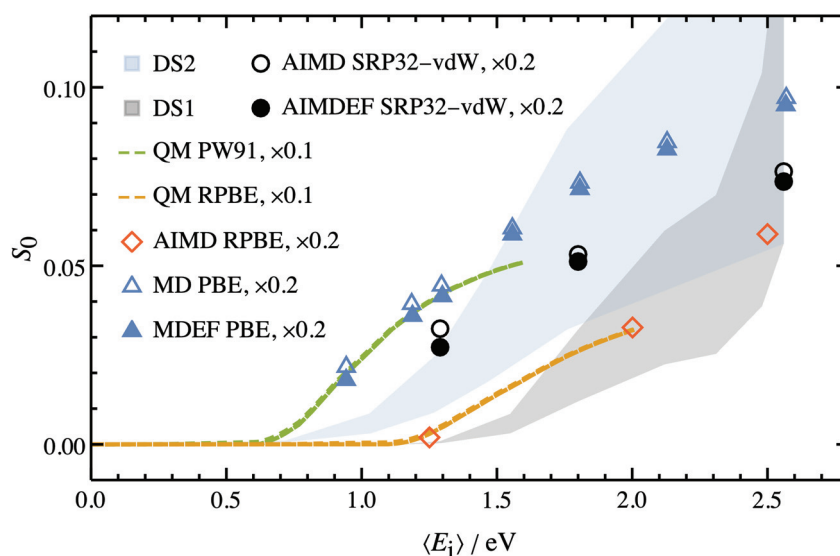


Figure 5.13 Comparison of the experimentally determined S_0 with the gathered theoretical predictions recently published. For improved optical readability the lower and upper limit of DS1 and DS2 are indicated by the lightly colored areas in gray and blue, respectively. While the dashed lines denote the quantum dynamics results of Liu *et al.* [58, 60, 124] calculated with PW91 in green and RPBE in yellow (both averaged over the experimental conditions as discussed above and lowered by a factor of 0.1), symbols depict the AIMD results from Kolb and Guo (open red symbols, RPBE, lowered by 0.2) [96], MD/EF results from Füchsel *et al.* (open and filled blue symbols, PBE, lowered by 0.2) [95], and AIMD/EF results from the same group (open and filled black symbols, SRP32-vdW, lowered by 0.2) [100].

5.3.3 Associative Desorption

The results from analyzing the REMPI-TPD spectra can be summarized as follows:

1. Applying a dose of HCl with the cold or hot nozzle to the cold surface ($T_s \approx 77$ K) and subsequently heating the surface led to desorption of HCl molecules in $v = 0, J = 0$. While in the former case the desorption seemed to follow first order kinetics with $E_a = 0.24(1)$ eV, in the latter case a combination of first order and second order desorption ($E_a = 0.20(2)$ eV) could be observed.
2. Dosing the surface at higher temperatures (tested for $T_s \approx 170$ K, 273 K and 423 K) did not result in an HCl peak around 85 K in the TPD afterwards (as expected). Instead, a Cl *atom* peak emerged at ~ 800 K, clearly exhibiting first order kinetics (shape, coverage dependence). Its activation energy of $E_a = 2.06(2)$ eV matches previously published values.
3. Due to its very low desorption temperature and thus limited number of data points in the TPD spectra, the desorption of H₂ could not be analyzed.
4. With the REMPI laser tuned to the Cl ground state transition, a presumably second order peak was observed that could not be conclusively assigned to a certain species.

Especially the second point deserves closer attention. One of the most critical points in the evaluation of the dissociation probability of HCl on Au(111) was the assumption that the desorption of H₂ from the surface was much faster than that of HCl. This would result in accumulation of Cl atoms that remain on the surface since the pool of H atoms got depleted by the H₂ recombination and Cl/Cl₂ should only desorb at much higher temperatures than those used in the dissociation experiments.⁶ At low temperature dosing ($T_s \approx 77$ K), this was based on the desorption of H₂ occurring at lower temperatures than that of HCl during the REMPI-TPD measurements. However, as seen in Fig. 3.43 the actual binding state of HCl on the surface prior to desorption was not easily determined. Here, the TPD spectra of Cl atoms can help to at least validate the above assumption. It could be that at $T_s \approx 77$ K the surface was quickly covered by HCl in some physisorption-like state and only few molecules could actually dissociate leading to the H₂ peak and parts of the HCl peaks in the TPD spectra. In this case, no Cl atoms would have been left on the surface to desorb at ~ 800 K. If the surface was dosed at higher T_s , however, HCl molecules could readily dissociate and H₂ could quickly desorb from the surface leaving behind the Cl atoms that were observed in the TPD spectra in these cases.

In addition to the "static" TPD experiments, where species (which were relatively stable

⁶ I want to shortly mentioned that Füchsel *et al.* also looked for recombinative desorption in their AIMDEF simulations. Out of 177 trajectories involving dissociation on a (3 × 3) unit cell, only a single one led to recombination [100].

at the dosing T_s) left the surface upon heating (which lowered their residence time into the regime of seconds), the "dynamic" fingerprints in form of the Cl_2 arrival time distributions provided further validation of the kinetic assumptions. Cl atoms could only leave the surface in the form of atomic Cl (spectroscopically not monitored in this case) or Cl_2 molecules (as detected) in substantial amounts if the co-adsorbed H atoms had left the surface as H_2 . I need to point out that in order to reduce the residence time⁷ of the Cl_2 molecules to several hundred microseconds, T_s had to be increased close to the melting temperatures of Au(111) and Ag(111). This drastic difference to the surface temperature during the dosing experiments (170 K) could generally have resulted in altered kinetics since the desorption rate is not only influenced by the pure desorption process but also by diffusion on the surface, of course.

Neglecting other processes than desorption, it should in principle be possible to simulate not only the TPD spectra but also the kinetic traces of Cl_2 molecules leaving the surface during one dosing pulse of HCl at high surface temperatures. While the procedure is very similar to the simulation of TPD spectra described in Sec. 3.3.6, care has to be taken with the units of time: For the dynamic measurements, the time scale of interest is in the microsecond to millisecond regime. In addition, there is one further difference to the TPD simulation in general that prevented me from successfully simulating the kinetic traces. In TPD experiments, the temperature can be varied over several hundred K within seconds to minutes (depending on the heating rate). Over this temperature range, the desorption rate constants can change over several orders of magnitude depending on the activation energies (approaching the pre-exponential factor in the high temperature limit). That is, as long as the E_a for individual desorption reactions are separated enough, the species can be treated individually and different desorption processes will not interfere too much (even though certain reaction channels can be missing in the TPD because lower temperature processes have depleted the species' reservoir). This is different at high temperatures as the 1070 K at which the kinetic traces of Cl_2 were observed. Here, small differences in the pre-exponential factor can have large effects in the competition between different reaction channels which consume the same adsorbed species as in the case of HCl, Cl and Cl_2 which all draw from adsorbed Cl. While there are several ways in which E_a can be determined *via* the temperature dependence of reaction rates, the determination of ν requires accurate knowledge of the involved coverage and/or amount of desorbing species, which itself is considerably more difficult to determine.

In conclusion, while the REMPI-TPD spectra as well as the kinetic traces of Cl_2 provided additional validation of the kinetic assumptions concerning the determination of dissociation probabilities and were in general compatible with previously reported values of activation energies, further dedicated experiments are necessary to resolve the full kinetic picture.

⁷ "Residence time" might be slightly misleading here since in this case the Cl_2 molecules are supposed to be nascent only in the desorption process

6 Conclusions

In my thesis, I have presented the experimental results of my work on scattering HCl molecules from Au(111) and Ag(111) surfaces. In particular, I studied vibrational excitation, translational inelasticity and the dissociative adsorption in combination with associative desorption. All of these phenomena occurring at the surface are subject to energy transfer between molecular and surface DOFs and are thus entangled to a certain degree.

While I found vibrational excitation probabilities from the vibrational ground to the first excited state that were relatively low on both surfaces compared to other molecule/surface systems, VEPs for the excitation from the first excited to the second excited vibrational state were substantially higher on Au(111). In contrast to other systems like NO/Au(111), the vibrational excitation probabilities of HCl could be divided into electronically adiabatic and nonadiabatic contributions, where only the latter depended on the surface temperature due to the associated availability of excited electron-hole pairs. Comparison with TOF measurements on translational inelasticity suggested that the adiabatic component was also reflected in the final translational energy of molecules that had undergone vibrational excitation - they were considerably slower than those scattered in vibrationally elastic channels. While the translational inelasticity of the latter was well represented by a rather simple hard cube model on Au(111), on Ag(111) values for the mean final translational energy $\langle E_f \rangle$ stayed well above that limit.

On this surface, stronger nonadiabatic interactions presumably manifested in slightly enhanced VEPs compared to Au(111) as well as higher translational energy losses for molecules incident in vibrationally excited states. While their effect on dissociation probabilities could not be settled, the height of the associated energetic barrier, which was calculated to be lower on Ag(111), probably prevented the $\nu = 1 \rightarrow 2$ excitation from being observed here. Even though the dissociation probabilities on Ag(111) were also predicted to be higher than on Au(111), I could not determine them within the current technical limitations. On Au(111), the values for S_0 that I presented were significantly lower than those of several computational studies. Although increasingly complex simulations and re-evaluation of my data led to improved convergence of theoretical and experimental

values, the latter remained lower by a factor of 3 – 5. Complementary to the AUGER electron spectroscopy (AES) measurements, which proved the existence of chlorine species on the surface, and REMPI-TPD spectra, which revealed desorbing HCl molecules and Cl atoms, scattering experiments at high surface temperatures offered dynamic fingerprints of the dissociation. For both surfaces, kinetic traces of desorbing Cl₂ were obtained which responded to incident beam as well as surface conditions.

All observed phenomena are parts of a holistic picture of the dynamics at play when HCl molecules encounter Au(111) and Ag(111) surfaces. As long as certain DOF are not completely decoupled from the rest of the system, vibrational and translational inelasticity as well as dissociative adsorption and associative desorption are all manifestations of the same forces acting on the atoms. That is the reason why, ideally, accurate PES for MD or AIMD calculations should be able to correctly simulate all of these processes simultaneously (as pursued by Füchsel *et al.* [100], for example). Only then we as a scientific community will be able to approach the "world's greatest microscope" (Alec Wodtke, Ref. [9]). However, I also agree with Füchsel *et al.* who "advocate that future experiments on HCl + Au(111) eliminate as much of the uncertainties [...] to allow the best possible comparison to future calculations" [95]. Thus I will give an outlook on future experiments that in my opinion would help to complete the picture of HCl scattering dynamics and to improve the comparability of experiment and theory.

First, as discussed before, to the best of my knowledge there are no other reports on vibrational excitation probabilities starting from vibrational states higher than $v = 0$. Therefore, systematically studying vibrational transitions like $v = 1 \rightarrow 2, 3$ for NO/Au(111) and comparing the VEPs with published values for the $v = 0 \rightarrow 1, 2$ excitation would be interesting with regard to the role of the TS to dissociation. In this respect, studies of other molecule/surface systems, where the barrier is energetically more easily accessible, might be even more important.

Concerning the analysis of the dissociation, one issue in comparison with the computational studies was the effect of vibrational excitation on the dissociation probabilities (see Sec. 5.3). The uncertainties arose from the problem that the nozzle needed to be heated to increase the incidence energy. At the same time, applying heat to the molecular beam also increased the population in higher vibrational states. In comparison, leaving the nozzle temperature constant and increasing the incidence angle θ_i to decrease $\langle E_i \rangle$ relied on the validity of normal energy scaling. Thus, the effect of vibrational excitation on S_0 was either entangled with the effect of the incidence energy or angle. However, using pulsed nanosecond lasers only ~0.5% of the molecules in the molecular beam pulse could be vibrationally excited which supposedly was not enough to observe a purely vibrational effect on the dissociation probabilities without changing $\langle E_i \rangle$ or θ_i . One solution to this problem could be the implementation of a cw IR laser source to achieve a theoretically complete population inversion *via rapid adiabatic passage*. This technique was employed by Beck and co-workers to study vibrational effects on the sticking of D₂O on Ni(111) [86]

and ice [93] as well as dissociation of methane on various Ni surfaces and Pt(111) [127–129], for example. Vibrational population in HCl($v = 1$) far beyond the $\sim 0.5\%$ achieved in this work would facilitate the distinction between the aforementioned effects on S_0 .

Three more fundamental issues with the presented results on dissociative adsorption are concerned with the applicability of AUGER electron spectroscopy for the determination of dissociation probabilities. First, my analysis relies on calibrating the observed AUGER peak-to-peak height ratios with some kind of saturation value that is related to a certain coverage on the surface. As discussed above, the coverage at saturation and thus the actual binding state and stoichiometry for Cl on Au(111) are under dispute. Second, the analysis further implicitly relies on desorption kinetics that favor Cl to remain on the surface at the experimental temperatures which could not be conclusively proven. Finally, since simulations for both metals have been carried out, an experimental comparison between Au(111) and Ag(111) would be beneficial.

Recently, ion imaging has been used in our group to study velocity-resolved kinetics of the CO desorption and oxidation on different platinum surfaces [130, 131]. It has proven to be a powerful tool to accurately determine activation energies and pre-exponential factors. Further, compared to the sometimes tedious IR-UV double-resonance TOF methods and UV laser position dependent angle determinations, it delivers velocity and potentially also angular distributions in no time on a shot-to-shot basis. With this technology at hand, one should be able to disentangle the desorption processes occurring at the surface and determine their kinetic parameters. As I have shown, Cl₂ desorption could be observed in dynamic scattering experiments on both surfaces. Additionally, hints for HCl desorption were also seen at least on Ag(111)¹, which in combination leaves me confident that opposed to AES, kinetics measurements should in principle be successful on Au(111) as well as Ag(111). Exploiting either REMPI or non-resonant multiphoton ionization using a high-intensity femtosecond laser, a variety of species like HCl, Cl₂, H₂, and Cl should be detectable in a state-selective and/or mass-selective way (by specific time delays between voltage pulses of a repeller and MCPs). By carefully choosing the incident and potentially pre-adsorbed species as well as the surface temperature range, it should be possible to determine activation energies and pre-exponential factors for the desorption of the individual molecules as well as of inevitable mixtures of species emerging when HCl dissociates. With these kinetic parameters it should be possible to simulate the processes happening at the surface while dosing it with HCl at $T_s = 170$ K and thus to validate the assumptions made about the competing desorption of HCl and H₂. Ideally, these experiments would be accompanied by more sophisticated TPD studies in attempts to clarify the state of HCl molecules and their dissociation products on the surface. Those studies might include mass-selective detection of desorbing species as well as state-selection *via* REMPI. For example, monitoring the population ratios of desorbing v states (and thus vibration depen-

¹ On Au(111), there were also certain conditions under which slow components in the TOF could be seen. However, the suspected TD components behaved somewhat irregularly and often, the TOF spectra could barely be reproduced. Further dedicated studies would be necessary.

dent desorption probabilities) could also shed light onto the question of vibrational effects on dissociation probabilities. Furthermore, if it was possible to differentiate between directly scattered HCl molecules, simple trapping/desorption and associative desorption, e.g. based on detection angles relative to the surface or different velocities, one could potentially determine the incidence energy and angle dependent dissociation probability by invoking *detailed balance*. This was previously done for H₂ on Cu(111) [37, 38] and H₂/D₂ on Au(111) [132], for example. I would thus finally suggest to revisit parts of the phenomena reported here with the help of velocity resolved kinetics experiments, in particular the dissociative adsorption and associative desorption, to settle the remaining open questions.

APPENDIX

A Appendix

The following sections contain information which I considered important but which would have hampered the flow of reading in the main text. Additionally, examples of obstacles associated with correct measurements of certain quantities, e. g. due to specific geometrical constraints and/or non-ideal conditions, are explored. In our group, the issue of measuring velocity and angular distributions with our machine as accurately as possible has extensively been discussed. I will thus try to capture as much aspects of these discussions as I can fit in here in order to motivate following (doctoral) students, post-docs, and anyone else working with this or a similar machine to think about these considerations, apply them to their work and further refine them if necessary.

A.1 Theoretical Methods

A.1.1 Density Functional Theory

In their seminal papers, Hohenberg, Kohn, and Sham introduced *density functional theory* (DFT) in 1964 and 1965 [48, 49].¹ In short, as other quantum chemical calculations it is based on the BOA approximation for solving the many-body time-independent SCHRÖDINGER equation

$$\hat{H}\Psi(\vec{r}_i, \vec{R}_i) = E\Psi(\vec{r}_i, \vec{R}_i)$$

which is split up into one for the nuclei and one for the electrons, respectively,

$$\hat{H}_n\psi(\vec{R}_i) = E\psi(\vec{R}_i) \quad \text{and} \quad \hat{H}_e\psi(\vec{r}_i) = E\psi(\vec{r}_i)$$

¹ Which earned one of them, Walter Kohn, the NOBEL Prize in Chemistry in 1998.

Appendix A. Appendix

where \vec{r}_i and \vec{R}_i are the coordinates of the electrons and nuclei, respectively. The electronic Hamiltonian is the sum of the kinetic energy of the electrons and the electron-electron, electron-nuclei, and nuclei-nuclei interactions:

$$\hat{H}_e = \hat{T}_e + \hat{V}_{ee} + \hat{V}_{eN} + \hat{V}_{NN}$$

It was shown by the authors that the relation between the electronic wavefunction $\psi(\vec{r}_i)$ obtained from solutions of the SCHRÖDINGER equation and the electronic density $\rho(\vec{r})$ can be inverted such that ψ becomes a functional of $\rho(\vec{r})$

$$\rho(\vec{r}) = \rho[\psi(\vec{r}_i)] \longrightarrow \psi(\vec{r}_i) = \psi[\rho(\vec{r})]$$

which also transforms the ground-state energy E_0 into a functional of $\rho(\vec{r})$. Thus, the calculational advantage of DFT is based on the dependence of $E_0[\rho(\vec{r})]$ (and in the end the total ground-state PES) on only the 3 coordinates needed to describe the electronic density instead of $3N$ variables (where N is the number of electrons) for other quantum chemical methods. For a fixed nuclear geometry R the electronic energy is

$$E_R[\rho(\vec{r})] = T_0[\rho(\vec{r})] + \int v_{\text{ext}}(\vec{r})\rho(\vec{r}) + E_c[\rho(\vec{r})] + E_{\text{XC}}[\rho(\vec{r})]$$

where T_0 is the kinetic energy of *independent, non-interacting* electrons, v_{ext} is the external nuclear potential, E_c is the Coulomb self energy, and E_{XC} finally is the *exchange-correlation* energy. Variational minimization of E_R yields the KOHN-SHAM equation:

$$\left[-\frac{1}{2}\nabla^2 + v_{\text{eff}} \right] \phi_i = \epsilon_i \phi_i.$$

where the effective potential v_{eff} is the sum of v_{ext} and the derivatives with respect to $\rho(\vec{r})$ of E_c and E_{XC} . The electron density $\rho(\vec{r})$ can be iteratively optimized by self-consistent field methods to finally obtain the total energy and further output quantities.

With the comparison of experimental and theoretical results in mind, it needs to be emphasized here that in principle DFT gives exact results within the BOA. The exchange-correlation functional E_{XC} is introduced to correct for the errors in the theory resulting from approximating the many-electron operators \hat{T}_e and \hat{V}_{ee} with the auxiliary non-interacting $T_0[\rho(\vec{r})]$ and E_c . However, in practice the general expression for $E_{\text{XC}}[\rho(\vec{r})]$ is unknown, making the search for it (or its best approximation) "*the quest for the holy grail of electronic structure theory*" [133].

Since the introduction of KOHN-SHAM DFT a manifold of XC functionals has been proposed on different levels of complexity: from the local density approximation (LDA) to the generalized gradient approximation (GGA), which includes not only the local electron density but also its gradient, on to meta-GGAs, hybrid functionals etc. Many of these might have astonishing accuracy even comparable to high order wave function theory (e. g. see

Refs. [134, 135]). Yet, in the field of dynamical simulations of molecule-surface scattering rather basic GGA functionals like PW91, PBE, and RPBE are widely used. Since electronic density calculations are often the first step towards complex trajectory simulations, the choice of the functional can have a big impact on the finally calculated properties.

In its basic form DFT can only be used to describe adiabatic interactions on a single PES since the dynamics of nuclei and electrons are assumed to be decoupled. However, as has been shown in the preceding sections, nonadiabaticity does play an important role in various scattering dynamics from metal surfaces. Therefore, further DFT-based theories have been developed that are capable of including or at least approximating nonadiabatic interactions.

A.2 Velocity and Kinetic Energy Distributions

Certain desired quantities could not be measured directly, i. e. velocity and kinetic energy distributions. Instead, I used time-of-flight (TOF) techniques to obtain temporal distributions that can be converted into velocity distributions knowing the traveling distance of the molecules. The conversion process has been described several times before [82, 136] but I will still mention it here for the sake of completeness.

A.2.1 Density-to-Flux and Domain Conversion

TOF spectra represent the detection probability per differential time element that needs to be converted to the velocity domain in order to obtain correct velocity distributions $P(v)$. Further, being a density-sensitive method REMPI signals S are proportional to the number density of the detected molecules.² Thus, the recorded density distributions need to be converted into flux distributions. Since a number density is given in units of m^{-3} and a flux, as the number of molecules that pass a certain area in a certain time, is given in units of $\text{m}^{-2}\text{s}^{-1}$, this conversion is achieved by multiplication with the molecules' time dependent velocity $v(t)$.³ In fact, since our TOF method includes two nanosecond laser pulses⁴, the density-to-flux conversion needs to be applied twice:

$$S(t)v^2(t)dt = P(v)dv \tag{A.1}$$

² With a duration of a few nanoseconds, the laser pulse can only interact with molecules for a time span that is approximately 10^2 shorter than the time it takes the molecules to travel across the pulse volume. Thus, the latter can be treated as being at rest compared to the laser pulse.

³ For a given flux, the density of molecules with velocity v_1 is twice the density of molecules with velocity $v_2 = 2v_1$ which in return pass an area twice as often in the same time.

⁴ During the IR laser pulse the more molecules are tagged the lower their velocity is. Thus, in principle one could say that the velocity distribution of the flux is transformed into one of density in this step.

Appendix A. Appendix

Solving for the time-dependent intensity leads to

$$S(t) = P(v) \left| \frac{dv}{dt} \right| v^{-2}. \quad (\text{A.2})$$

Here, the appropriate JACOBIAN (cf. Ref. [82]) is

$$\left| \frac{dv}{dt} \right| = \frac{l}{t^2}, \quad (\text{A.3})$$

with the flight length l and the flight time t . Inserting into Eq. A.2 leads to:

$$\begin{aligned} S(t) &= P(v) \left| \frac{dv}{dt} \right| v^{-2} \\ &= P(v) \frac{l}{t^2} \left(\frac{t}{l} \right)^2 = P(v) \frac{1}{l} \end{aligned} \quad (\text{A.4})$$

In general, velocity distributions were fitted with a flowing three-dimensional MAXWELL-BOLTZMANN distribution $P(v)$

$$P(v) = A v^3 \exp \left[- \left(\frac{v - v_0}{\alpha} \right)^2 \right] \quad (\text{2.4})$$

with the amplitude A , the center velocity v_0 and the width parameter α . Inserting Eq. 2.4 in Eq. A.4 and replacing v generated the function that was fitted to the raw TOF spectra to obtain v_0 and α :

$$S(t) = A \left(\frac{l}{t} \right)^3 \exp \left[- \left(\frac{\left(\frac{l}{t} \right) - v_0}{\alpha} \right)^2 \right] \frac{1}{l} \quad (\text{2.3})$$

Finally, the thus generated velocity distributions were converted into the kinetic energy domain:

$$\begin{aligned} P(E) dE &= P(v) dv \\ P(E) &= P(v) \left| \frac{dv}{dE} \right| \end{aligned} \quad (\text{A.5})$$

with

$$\left| \frac{dv}{dE} \right| = \frac{1}{mv} = \frac{1}{m \sqrt{\frac{2E}{m}}}, \quad (\text{A.6})$$

where m is the mass of HCl and $v = \sqrt{2E/m}$. Insertion into Eq. A.5 and combination with Eq. 2.4 leads to:

$$\begin{aligned}
 P(E) &= A \sqrt{\frac{2E}{m}}^3 \exp \left[- \left(\frac{\left(\sqrt{\frac{2E}{m}} \right) - v_0}{\alpha} \right)^2 \right] \frac{1}{m \sqrt{\frac{2E}{m}}} \\
 &= A \frac{2E}{m^2} \exp \left[- \left(\frac{\left(\sqrt{\frac{2E}{m}} \right) - v_0}{\alpha} \right)^2 \right]
 \end{aligned} \tag{2.5}$$

Following this procedure I was able to calculate velocity as well as kinetic energy distributions from the measured TOF spectra. It needs to be mentioned, though, that the actual geometrical situation is slightly more complicated than molecules traveling from one infinitely small point in space (the IR laser pulse) to another (the REMPI laser pulse).

A.2.2 Detection Geometry

The general detection geometry was similar in all TOF experiments (cf. Sec. 2.3.3). In general, molecules were first tagged with an IR laser pulse and then detected with a REMPI laser pulse after they had traveled a defined distance. Here, the potential problem is the extent of the tagging and detection volume especially along the x -axis (the horizontal axis that is perpendicular to the molecular beam). This is illustrated in Fig. A.1 for the case of measuring velocity distributions of scattered molecules.

Those molecules that are tagged in the darker red area travel with a certain velocity (depicted are three exemplary velocities \vec{v}_1 , \vec{v}_2 , and \vec{v}_3) and a certain angular distribution (depicted by the gray cone) until they are detected in the darker blue area at a time t . Although their velocity component along the y -axis (the molecules' traveling direction) is the same, $v_{1,y} = v_{2,y} = v_{3,y}$, their velocity value (their speed) is different: $|\vec{v}_1| = |\vec{v}_3| > |\vec{v}_2|$. That also means that molecules at the edges of the angular distribution with the same speed as those in the middle, $|\vec{v}_1| = |\vec{v}_2| = |\vec{v}_3|$, arrive at the detection volume at a time $t + dt$. Thus, the overall TOF spectrum is shifted towards later times which in the end results in a velocity distribution that is shifted to lower velocities. To which extent this negatively affects the real TOF measurements depends on the actual tagging and detection volume, the width of the velocity distribution, and the angular distribution, i. e. the divergence of the molecular beam.

In order to get an idea of these effects I carried out simulations of TOF spectra. In principle, an ensemble of particles was generated starting from a randomly chosen point inside the excitation area⁵ with a velocity vector randomly chosen from given velocity and angular distributions. This ensemble was evolved in time and the particles that were located inside

⁵ The simulations were carried out in 2D for the sake of simplicity. Adding the third dimension should not make a big difference due to the negligible extent of the tagging and detection volumes in z direction.

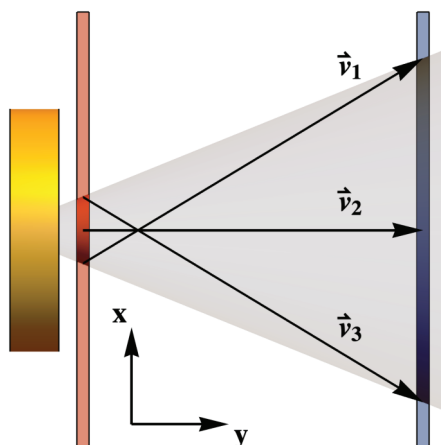


Figure A.1 This sketch illustrates a typical geometry for measuring TOF spectra of scattered molecules (top view). The gray cone depicts the scattered molecular beam after hitting the gold crystal. At a distance of 1 mm from the surface molecules are tagged by the IR laser pulse and then detected by the REMPI laser pulse another 14 mm downstream, depicted by the red and blue areas, respectively. The actual interaction area is marked by the corresponding darker color. Additionally shown are velocity vectors of molecules leaving the tagging area that are detected at the same time (see text; \vec{v}_1 and \vec{v}_3 indicate the longest possible vectors/distances).

the detection area at a certain time step were counted. Finally, the resulting TOF spectrum was fitted and converted into a velocity distribution that could be compared to the input distribution. By varying the size of the tagging and detection areas (i. e. especially along the x -axis) and the input angular and velocity distributions their individual effects could be evaluated.

Fig. A.2 shows exemplary results of these simulations where the input parameters were $v_0 = 800 \text{ m s}^{-1}$ and $\alpha = 600 \text{ m s}^{-1}$ or $v_0 = 2000 \text{ m s}^{-1}$ and $\alpha = 100 \text{ m s}^{-1}$ for a broad (e. g. scattered) or narrow (e. g. incident) velocity distribution, respectively. The tagging area had a length of 2 mm along the x -axis and the detection area was either chosen to be 10 mm or infinitely long while the width (i. e. the laser beam diameter) was 0.5 mm. In panel (a), the relative⁶ center velocity v_0^{rel} is plotted against the exponent n of the input angular distribution of the form $\cos^n[\alpha]$. As can be seen for the broad (depicted by filled symbols) as well as for the narrow (depicted by open symbols) velocity distribution, v_0^{rel} approaches unity with increasing n . That makes sense: For narrower angular distributions, molecules move closer to the center line and thus cause less distortion to the TOF spectra. A similar effect can be observed if the different detection lengths are compared. For the (probably more reasonable) case of detecting 10 mm along the x -axis the increase in v_0^{rel} is rather moderate and approaches a plateau of 0.98 - 0.99 even for broad angular distributions.

⁶ That is the ratio of v_0 obtained from the fit according to Eq. 2.4 and the input value of v_0 . In this case, the 3D MAXWELL-BOLTZMANN distribution in Eq. 2.4 was converted from flux to density for the input as well as the fitting velocity distribution since the IR laser pulse has already filtered out a factor of v .

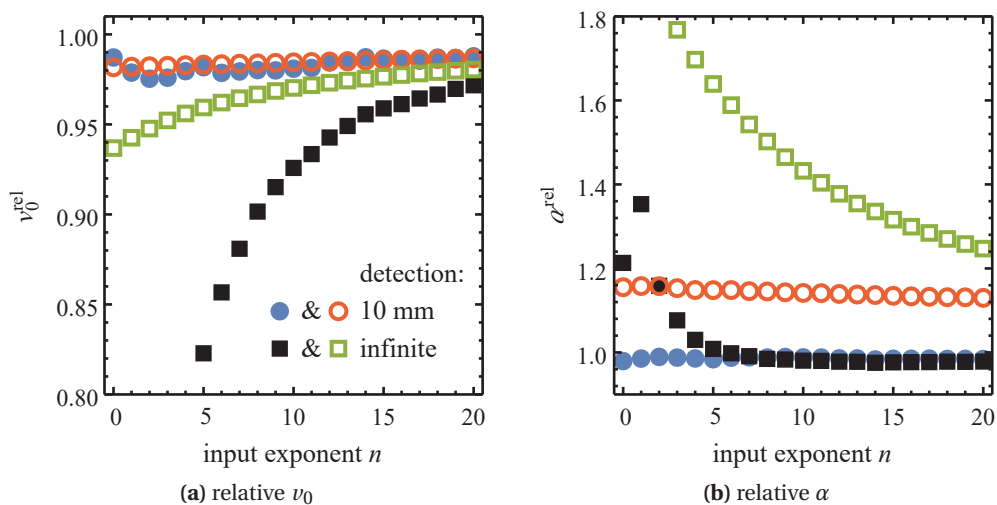


Figure A.2 Results of TOF spectra simulations. In panel (a) the relative center velocity v_0^{rel} is plotted against the exponent n of the input angular distribution over a typically encountered range. Shown are values for a broad and narrow velocity distributions depicted by filled and open symbols, respectively, and for detection areas of 10 mm and infinite length. Panel (b) shows the corresponding relative width α^{rel} of the velocity distributions. See text for explanation.

If detection along the complete REMPI laser beam is assumed, there is a much steeper increase in v_0^{rel} which even for $n = 20$ remains below 0.97.

In panel (b) of Fig. A.2 the corresponding relative width α^{rel} is shown. Here, the width decreases with increasing exponent and the deviations from the input parameter are much higher for the narrow velocity distribution (open symbols). This again seems plausible since broader angular distributions result in broader TOF spectra and the narrower velocity distribution is more easily distorted by this broadening.

It turns out that the effective detection length along the x -axis is probably the most crucial parameter for an accurate measurement of the velocity distribution. In previous works the whole problem was addressed by a convolution of the TOF fitting function with the angular distribution and integration along the detection volume [136]. However, even then these properties need to be known - and it is still difficult to determine them. Thus I would like to assess the error in the calculated velocity distributions if the detection volume was not accounted for. According to the simulations the resulting systematic error in v_0 is approximately 1 – 8% for angular distributions with exponents from 10 – 20 which are typical for direct scattering processes. That is, even for the rather unrealistic case of an infinitely long detection volume, the error remains below 10%. If a more reasonable extent along the x -axis is assumed, the error should only be 1 – 3%. The actual detection volume depends on effective focusing, the absorption cross section, the REMPI scheme⁷, and the

⁷ Opposed to NO detection with a (1 + 1) scheme, the (2 + 1) scheme in HCl detection requires one more photon and thus results in a detection volume more confined around the focus.

Appendix A. Appendix

photon flux.

Compared to an statistical error of approximately $\pm 5 - 10\%$ that stems from uncertainties in aligning the laser beams correctly and thus erroneous flight lengths, I assume that the error described above can safely be neglected. In any case, its direction is known and it can therefore be kept in mind that the center velocities ν_0 obtained from TOF data can be a few percent to small.

A.3 Angular Distributions

Measuring angular distributions of molecules coming from a surface in general seems like a rather simple task. Traditionally, a detector (e. g. a mass spectrometer) is mounted on a goniometer so that it can be moved around the surface on a sphere always facing the crystal surface. With a correctly positioned aperture the angular distribution can be recorded keeping in mind that the detector is probably sensitive to particle density and not the flux of scattered and/or desorbing particles [137].

Instead of having a detector on a goniometer, in our machine the scattered/desorbing molecules (to be precise, their density) are detected by moving the REMPI laser beam on a line perpendicular to the incident beam which is illustrated by the blue cuboids⁸ in Fig. A.3. Knowing the distance of the laser beam from the surface the angles corresponding to the z positions can be calculated. There are, however, several issues associated with this way of measuring angular distributions that need to be considered.

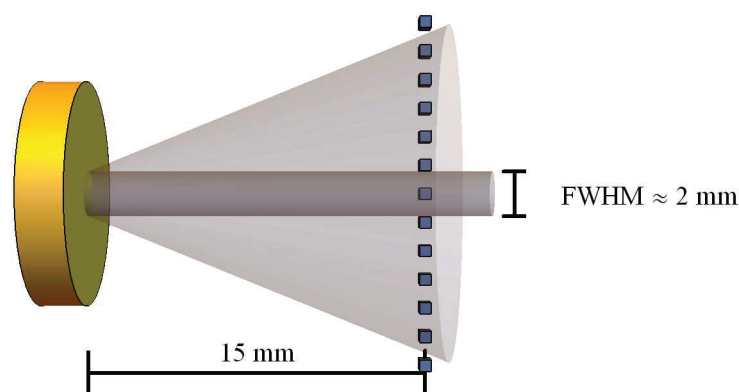


Figure A.3 This sketch illustrates the geometry for a typical measurement of angular distributions. The gray tube depicts the incident beam with a FWHM of ~ 2 mm which expands into the gray cone after hitting the gold crystal. At a distance of 15 mm from the surface molecules are detected by scanning the REMPI laser, depicted by the blue cuboids, perpendicular to the incident beam.

A.3.1 Incident Beam Width and Density

Molecules scattered from the surface obviously do not stem from a point source. Instead, they are "emitted" from an area on the surface determined by the cross-section and density of the incident molecular beam. If each spot on the surface, i. e. each scattering/binding site, is considered a point source that emits molecules with a certain angular distribution, these individual distributions add up resulting in a broadened, *blurred* distribution whose

⁸ Cuboids are used instead of tubes or intersecting cones for illustration of the REMPI beam because this shape simplifies following simulations.

shape depends on the parameters of the incident beam. Fig. A.4 (a) illustrates this phenomenon by superimposed semi-transparent cones. Whether or not this blurring effect is strong enough to affect the measured angular distributions depends on the ratio of the distance between the surface and the detection spot d and the extent of the incident beam spot defined by its radius r . Fig. A.4 (b) shows a typical incident beam width that was obtained by moving the REMPI laser beam on a vertical line through the incident beam as described above. Depicted by a solid blue line is a GAUSSIAN fit to the peak-normalized raw data that exhibits a FWHM of 2.1 mm. To check whether this beam width would influence the angular distribution measurements, 2D simulations were carried out.

First, the origin on the surface was modeled as a line with a length of $2r$ consisting of evenly-spaced point sources⁹ that emit molecules according to the following angular distribution:

$$f(z, a, n) = \begin{cases} \cos^n[\alpha(z-a)] & \text{if } -\frac{\pi}{2} \leq \alpha(z-a) \leq \frac{\pi}{2} \\ 0 & \text{if } \alpha(z-a) < -\frac{\pi}{2} \quad \text{or} \quad \alpha(z-a) > \frac{\pi}{2} \end{cases} \quad (\text{A.7})$$

$$\alpha(z-a) = \arctan\left[\frac{z-a}{d}\right] \quad (\text{A.8})$$

where

- z z position of the laser beam in mm
- a z position of the point source in mm
- d distance from the surface to the laser beam in mm
- n exponent determining the width of the angular distribution

In the simulation, r ranged from 0 to 15 mm (which would make the incident beam cross-section three times as large as the surface). For each chosen value of r , angular distributions from the point sources on the surfaces (depicted by the red spots in Fig. A.4 (a)) were summed up at the laser detection spots. The result was fitted by the distribution in Eq. A.7 where a was set to 0. This procedure was repeated for exponents n ranging from 0 to 20. Then, a critical incident beam radius $r_{\text{crit.}}$ was determined by scanning the fitted exponents *vs.* the beam radius in ascending order for the first pair of values where $n_{\text{input}} - n_{\text{fitted}} \geq 0.5$. That is, at radii greater than $r_{\text{crit.}}$ the fitted exponent of an angular distribution in the form of Eq. A.7 would be interpreted as deviating from the true value. Fig. A.4 (c) shows this critical incident beam radius in dependence on the input exponent. As can be seen from the dashed black line that indicates a radius equal to half the FWHM in Fig. A.4 (b), in our

⁹ That is, in this simulation the incident beam is treated as a tube with uniform particle density instead of having a GAUSSIAN density distribution.

usual setup the *blurring* effect should only influence angular distribution measurements at rather high values for the exponent ($n \gtrsim 19$).

Mathematically, the same result as described above can be obtained by a convolution of the angular distribution in Eq. A.7 with unit box functions¹⁰ of different widths. If the convolved function is evaluated and re-fitted by Eq. A.7, the result exactly matches Fig. A.4 (c). To test the effect of the actual density distribution of the incident beam, overlapping angular distributions originating from point sources now weighted by the actual incident beam profile with a FWHM of 2.1 mm were simulated. As expected, the fitted exponents only start to deviate slightly at high values for n (see Fig. A.4 (d)).

¹⁰This function is the simplest model for the incident beam but in MATHEMATICA's built-in convolution code it works much better than a GAUSSIAN distribution, for example.

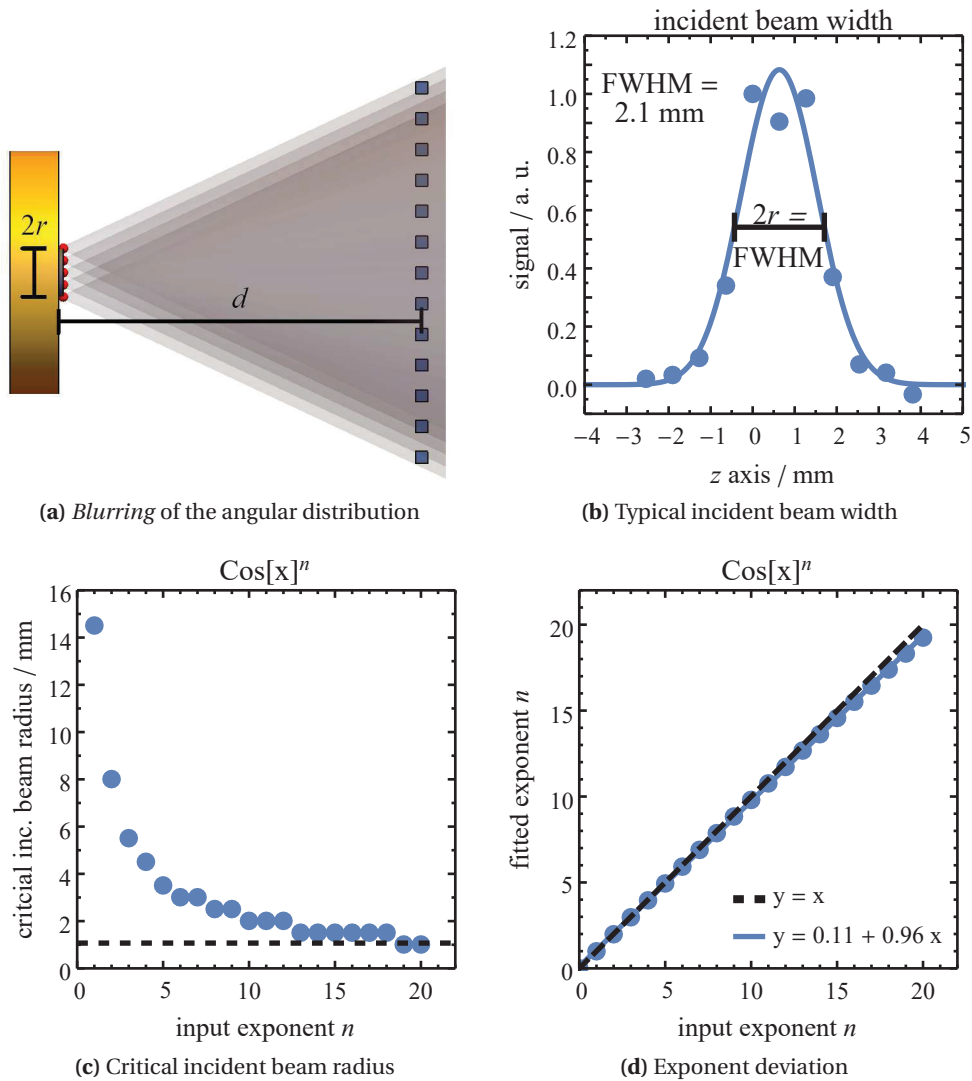


Figure A.4 Testing the influence of the incident beam width on the measured angular distribution in 2D. In (a), the effect of several point sources of angular distributions on the surface is visualized by overlapping semi-transparent cones that result in a *blurring* of the actual angular distribution. Its intensity depends on the ratio of the distance d and the incident beam cross-section which is determined in panel (b). A calculated critical beam radius above which the *blurring* would actually affect the measurement is shown in (c) depending on the input parameter for n . The value for r that is determined in (b) is depicted by a dashed black line. According to panel (c), only angular distributions with exponents greater than approximately $n = 18$ will be affected by the actual extent of the molecular beam. This is confirmed in panel (d) where overlapping angular distributions were simulated and the resulting fitted exponents are plotted against the corresponding input exponents.

A.3.2 Line Detection

Density Dilution due to Beam Divergence

Instead of moving on a circular orbit around the surface the detection laser beam is moved on a vertical line parallel to the front of the crystal. Thus, the distance between the surface and the detection volume is not constant but increases with increasing scattering angle α by $\cos^{-1}[\alpha]$. Imagine a point source on the surface from which a molecular beam pulse is scattered with a certain particle flux/density distribution determined by its angular distribution. If the detection spot is moved away from the surface along the propagation path of the molecular pulse, the detected density of molecules decreases with increasing distance to the surface due to the spatial divergence of the pulse. For the case of an isotropic angular distribution (i. e. $\cos[\alpha]^0$) this is illustrated in Fig. A.5 (a) where the blue circles depict the line scan that is actually carried out in the experiments and the red circles depict the ideal situation of an orbital measurement with constant distance to the surface. In the former case, the distance to the surface is greater especially at larger angles leading to a reduced density that can be seen from the gray particles exhibiting less overlap compared to the red orbital detection.

Correcting for the spatial dilution is straightforward given the distance r from the surface is known. Fig. A.5 (b) shows the result of a simulation where the detection spot is moved along the surface normal and the particles inside this spot are counted. As can be seen from the solid black line the detected particle density is inversely proportional to r . Thus, in 2D angular distributions have to be corrected by multiplying the measured density with the (relative) surface-detection spot distance r . In 3D, the molecular pulse not only diverges along the z - but also along the x -axis and thus the density decreases with r^{-2} . However, since the detection laser beam propagates along the x -axis, the actual r -dependence decreases from r^{-2} to r^{-1} with increasing elongation of the detection volume depending on how much of the azimuthal distribution it covers. That also means, that this correction factor depends on the angular distribution itself.

Temporal Dilution and Shift

Performing a line scan instead of an orbital one introduces problems not only with spatial dilution but also in the time domain. First, the molecular pulse exhibits a velocity distribution and not a single velocity. Thus, the pulse drifts further apart the longer the traveled distance is resulting in a temporal dilution (see Fig. A.6). That is, the same part of the molecular pulse has a lower particle density when it has traveled a longer distance even if there was no spatial dilution (see above).

Second, the experiments are conducted in a way that the z position is scanned while the timing delay between the nozzle opening and the laser pulse is kept constant. That means that at the outer measuring points not the previously determined peak of the molecular

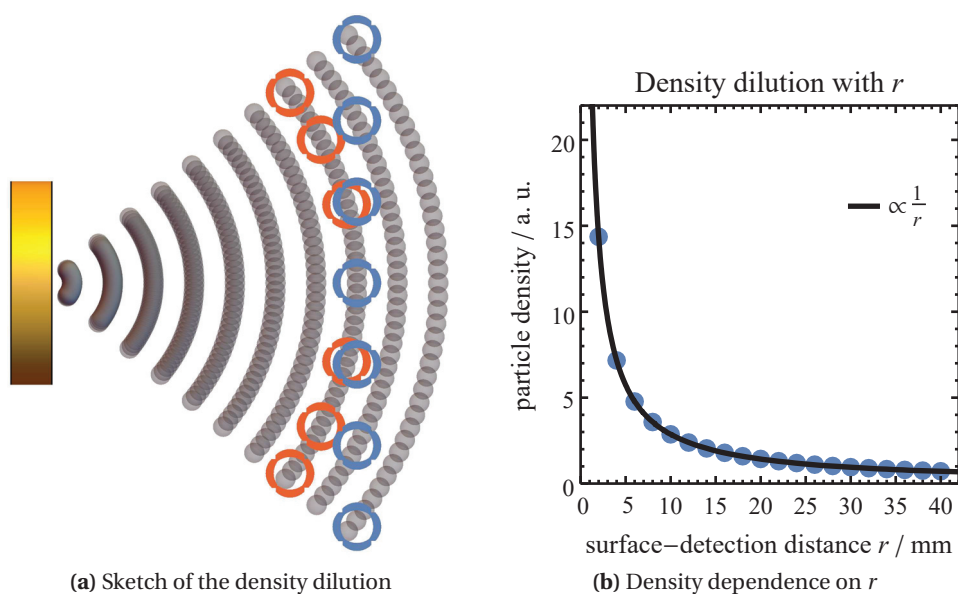


Figure A.5 Diluted density due to the beam divergence. In (a) particles (gray spheres) that are scattered from the surface with an isotropic angular distribution are shown. Two detection schemes are depicted by blue and red circles: the actual line detection and an ideal orbital detection, respectively. In the former case, the detected density of particles deviates from the ideal value that would be detected by the red circles. Panel (b) shows the inverse proportionality between the particle density and the surface-detection spot distance r .

pulse but a slightly earlier part is detected. Assuming an outermost detection spot at $z = 10$ mm which would correspond to a scattering angle of $\sim 50^\circ$ and a reasonable velocity of 1000 m s^{-1} gives a temporal shift of $\sim 3 \mu\text{s}$. Whether or not this small shift noticeably distorts the angular distribution depends on the actual temporal shape and width of the scattered molecular pulse. Thus, to account for these uncertainties the temporal distributions of the scattered molecular pulse need to be measured at the same points where the angular distributions are recorded. Knowing the different widths and peak heights in comparison to the timing of the angular distribution measurements these can be corrected. There is one further aspect that ideally needs to be considered. The velocity distribution that determines the density-to-flux conversion usually depends on the scattering angle for reasons of normal energy transfer, possible physisorption barriers *etc.* That is, ideally not only the temporal distributions but also the velocity distributions are measured along the z -axis. Depending on the scattering process to be examined this can cause issues with detection sensitivity especially at the outer measuring positions. This was the case, for example, for the angular distribution measurements of vibrationally excited molecules.

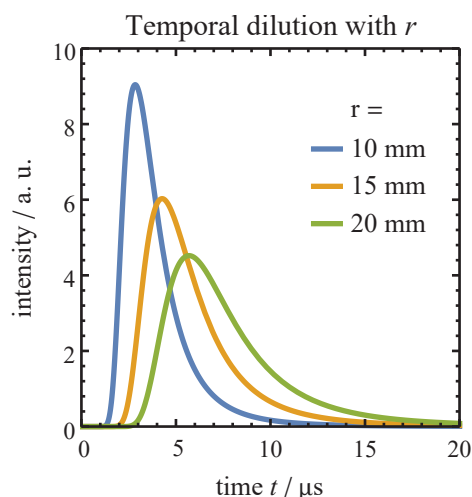


Figure A.6 Diluted density due to the spread in the velocity distribution. Shown is the temporal distribution of a molecular pulse of H_2 molecules initially without any temporal spread and a velocity distribution according to a flowing MAXWELL-BOLTZMANN distribution at room temperature for three different values of r . With increasing distance, the temporal spread increases and thus the peak intensity decreases.

A.3.3 Ion Collection Efficiency

All previous issues have dealt with the detection geometry that is based on the z position of the REMPI laser spot relative to the surface position. However, there is another geometrical relation that introduces z dependent distortion of measured angular distributions. What was called "detection" above effectively only referred to the step of ionization *via* the REMPI laser. The actual detector are the MCPs plus anode located above the ionization point. The fraction of generated ions that is collected by the MCPs depends on the (x, y, z) position of the ionization spot. For a given y position the z dependence of the obtained signal can be measured by filling the surface chamber with the gas of interest at low pressures ($\sim 10^{-8}$ Torr) and recording an "angular distribution" of the background gas with isotropic density (cf. Fig. A.3).

Fig. A.7 shows this ion collection efficiency at $y = 0$ (i. e., centered below the MCPs) as the measured intensity plotted against the z position, where $z = 0$ was the center of the molecular beam line and positive values for z mean that the detection spot was moved closer to the detector.¹¹ Shown as open symbols is the ion signal obtained at a constant background pressure of CO recorded at two different days under otherwise constant experimental conditions. Solid lines depict polynomial fits to the data. The signals' remarkable dependence on the z position illustrates the importance of correcting for this efficiency.

¹¹These specific measurements were carried out with CO instead of HCl which repeatedly caused trouble when it was filled into the surface chamber *via* the leak valve. However, the results for HCl should be similar since the masses of both molecules are comparable.

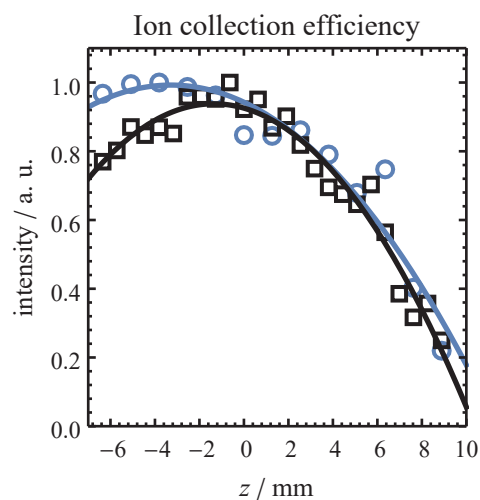


Figure A.7 Ion collection efficiency at $y = 0$ (i. e., centered below the MCPs) as the measured intensity plotted against the z position, where $z = 0$ was the center of the molecular beam line and positive values for z mean that the detection spot was moved closer to the detector. Shown as open symbols is the ion signal obtained at a constant background pressure of CO recorded at two different days under otherwise constant experimental conditions whereas solid lines depict polynomial fits to the data.

Bibliography

- [1] Nobel Media AB. *The Nobel Prize in Chemistry 1918*. 2014. URL: http://www.nobelprize.org/nobel_prizes/chemistry/laureates/1918/ (visited on 03/30/2017).
- [2] Nobel Media AB. *The Nobel Prize in Chemistry 1931*. 2014. URL: http://www.nobelprize.org/nobel_prizes/chemistry/laureates/1931/ (visited on 03/30/2017).
- [3] Nobel Media AB. *The Nobel Prize in Chemistry 2007*. 2014. URL: http://www.nobelprize.org/nobel_prizes/chemistry/laureates/2007/ (visited on 03/30/2017).
- [4] U.S. Geological Survey. *Mineral Commodities Summaries 2017*. Tech. rep. Reston, Virginia: U.S. Geological Survey, 2017, p. 202. DOI: 10.3133/70180197.
- [5] Max Appl. “Ammonia, 2. Production Processes”. In: *Ullmann's Encyclopedia of Industrial Chemistry*. Weinheim, Germany: Wiley-VCH Verlag GmbH & Co. KGaA, 2011, pp. 139–225. ISBN: 9783527306732. DOI: 10.1002/14356007.o02_o11. URL: http://doi.wiley.com/10.1002/14356007.o02_o11.
- [6] Geert-Jan Kroes. “Towards chemically accurate simulation of molecule–surface reactions”. In: *Physical Chemistry Chemical Physics* 14.43 (2012), p. 14966. ISSN: 1463-9076. DOI: 10.1039/c2cp42471a.
- [7] Ke Yang et al. “Tests of the RPBE, revPBE, τ -HCTHhyb, ω B97X-D, and MOHLYP density functional approximations and 29 others against representative databases for diverse bond energies and barrier heights in catalysis”. In: *The Journal of Chemical Physics* 132.16 (2010), p. 164117. ISSN: 0021-9606. DOI: 10.1063/1.3382342. URL: <http://aip.scitation.org/doi/10.1063/1.3382342>.
- [8] Jörg Behler. “Constructing high-dimensional neural network potentials: A tutorial review”. In: *International Journal of Quantum Chemistry* 115.16 (2015), pp. 1032–1050. ISSN: 00207608. DOI: 10.1002/qua.24890. URL: <http://doi.wiley.com/10.1002/qua.24890>.
- [9] Kai Golibrzuch et al. “The Dynamics of Molecular Interactions and Chemical Reactions at Metal Surfaces: Testing the Foundations of Theory”. In: *Annual Review of Physical Chemistry* 66.1 (2015), pp. 399–425. ISSN: 0066-426X. DOI: 10.1146/annurev-physchem-040214-121958. URL: <http://www.annualreviews.org/doi/abs/10.1146/annurev-physchem-040214-121958>.

Bibliography

- [10] M. Born and R. Oppenheimer. “Zur Quantentheorie der Molekeln”. In: *Annalen der Physik* 20.84 (1927), pp. 457–484. ISSN: 00033804. DOI: 10.1002/andp.19273892002. arXiv: 1206.4239. URL: <http://onlinelibrary.wiley.com/doi/10.1002/andp.19273892002/abstract>.
- [11] C. T. Rettner et al. “Observation of direct vibrational excitation in gas-surface collisions: NO on Ag (111)”. In: *Physical Review Letters* 55.18 (1985), pp. 1904–1907. ISSN: 0031-9007. DOI: 10.1103/PhysRevLett.55.1904. URL: <https://link.aps.org/doi/10.1103/PhysRevLett.55.1904>.
- [12] C. T. Rettner et al. “Direct vibrational excitation in gas-surface collisions of NO with Ag(111)”. In: *Surface Science* 192.1 (1987), pp. 107–130. ISSN: 00396028. DOI: 10.1016/S0039-6028(87)81165-2. URL: <http://linkinghub.elsevier.com/retrieve/pii/S0039602887811652>.
- [13] Bruce D. Kay, T. D. Raymond, and Michael E. Coltrin. “Observation of Direct Multiquantum Vibrational Excitation in Gas-Surface Scattering: NH₃ on Au(111)”. In: *Physical Review Letters* 59.24 (1987), pp. 2792–2794.
- [14] D. M. Newns. “Electron-hole pair mechanism for excitation of intramolecular vibrations in molecule-surface scattering”. In: *Surface Science* 171.3 (1986), pp. 600–614.
- [15] J. W. Gadzuk and S. Holloway. “Vibrational excitation in gas-surface collisions”. In: *Physical Review B* 33.6 (1986), pp. 4298–4300. DOI: 10.1103/PhysRevB.33.4298.
- [16] H. Nienhaus et al. “Electron-Hole Pair Creation at Ag and Cu Surfaces by Adsorption of Atomic Hydrogen and Deuterium”. In: *Physical Review Letters* 82.2 (1999), pp. 446–449. ISSN: 0031-9007. DOI: 10.1103/PhysRevLett.82.446. URL: <https://link.aps.org/doi/10.1103/PhysRevLett.82.446>.
- [17] Beate Mildner, Eckart Hasselbrink, and Detlef Diesing. “Electronic excitations induced by surface reactions of H and D on gold”. In: *Chemical Physics Letters* 432.1-3 (2006), pp. 133–138. ISSN: 00092614. DOI: 10.1016/j.cplett.2006.10.048. URL: <http://linkinghub.elsevier.com/retrieve/pii/S0009261406015508>.
- [18] Oliver Bünermann et al. “Electron-hole pair excitation determines the mechanism of hydrogen atom adsorption”. In: *Science* 350.6266 (2015), pp. 1346–1349. ISSN: 0036-8075. DOI: 10.1126/science.aad4972. URL: <http://science.sciencemag.org/content/350/6266/1346.abstract>.
- [19] Yuhui Huang et al. “Vibrational Promotion of Electron Transfer”. In: *Science* 290.5489 (2000), pp. 111–114. ISSN: 00368075. DOI: 10.1126/science.290.5489.111. URL: <http://www.sciencemag.org/cgi/doi/10.1126/science.290.5489.111>.

- [20] Jason D. White et al. "Vibrationally promoted electron emission from low work-function metal surfaces". In: *The Journal of Chemical Physics* 124.6 (2006), p. 064702. ISSN: 0021-9606. DOI: 10.1063/1.2166360. URL: <http://aip.scitation.org/doi/10.1063/1.2166360>.
- [21] Jerry L. LaRue et al. "Electron kinetic energies from vibrationally promoted surface exoemission: Evidence for a vibrational autodetachment mechanism". In: *Journal of Physical Chemistry A* 115.50 (2011), pp. 14306–14314. ISSN: 10895639. DOI: 10.1021/jp205868g.
- [22] Nils Bartels et al. "Dynamical steering in an electron transfer surface reaction: Oriented NO($v = 3$, $0.08 < E_i < 0.89$ eV) relaxation in collisions with a Au(111) surface". In: *The Journal of Chemical Physics* 140.5 (2014), p. 054710. ISSN: 0021-9606. DOI: 10.1063/1.4863862. URL: <http://aip.scitation.org/doi/10.1063/1.4863862>.
- [23] Nils Bartels et al. "Controlling an Electron-Transfer Reaction at a Metal Surface by Manipulating Reactant Motion and Orientation". In: *Angewandte Chemie International Edition* 53.50 (2014), pp. 13690–13694. ISSN: 14337851. DOI: 10.1002/anie.201407051. URL: <http://doi.wiley.com/10.1002/anie.201407051>.
- [24] Russell Cooper et al. "Vibrational overtone excitation in electron mediated energy transfer at metal surfaces". In: *Chemical Science* 1.1 (2010), p. 55. ISSN: 2041-6520. DOI: 10.1039/c0sc00141d. URL: <http://xlink.rsc.org/?DOI=c0sc00141d>.
- [25] Russell Cooper et al. "On the determination of absolute vibrational excitation probabilities in molecule-surface scattering: Case study of NO on Au(111)". In: *The Journal of Chemical Physics* 137.6 (2012), p. 064705. DOI: 10.1063/1.4738596.
- [26] Y. Huang et al. "Observation of Vibrational Excitation and Deexcitation for NO ($v = 2$) Scattering from Au (111): Evidence for Electron-Hole-Pair Mediated Energy Transfer". In: *Physical Review Letters* 84.13 (2000), pp. 2985–2988.
- [27] Kai Golibrzuch et al. "The importance of accurate adiabatic interaction potentials for the correct description of electronically nonadiabatic vibrational energy transfer: A combined experimental and theoretical study of NO($v = 3$) collisions with a Au(111) surface". In: *The Journal of Chemical Physics* 140.4 (2014), p. 044701. ISSN: 0021-9606. DOI: 10.1063/1.4861660. URL: <http://aip.scitation.org/doi/10.1063/1.4861660>.
- [28] Pranav R. Shirhatti et al. "Electron hole pair mediated vibrational excitation in CO scattering from Au(111): Incidence energy and surface temperature dependence". In: *Journal of Chemical Physics* 141.12 (2014), p. 124704. DOI: 10.1063/1.4894814.
- [29] Jörn Werdecker et al. "Electronically Nonadiabatic Vibrational Excitation of N₂ Scattered from Pt(111)". In: *The Journal of Physical Chemistry C* 119.26 (2015), p. 14722. ISSN: 1932-7447. DOI: 10.1021/acs.jpcc.5b00202. URL: <http://pubs.acs.org/doi/abs/10.1021/acs.jpcc.5b00202>.

Bibliography

- [30] Qin Ran et al. "Observation of a Change of Vibrational Excitation Mechanism with Surface Temperature: HCl Collisions with Au(111)". In: *Physical Review Letters* 98.23 (2007), p. 237601. ISSN: 0031-9007. DOI: 10.1103/PhysRevLett.98.237601. URL: <http://link.aps.org/doi/10.1103/PhysRevLett.98.237601>.
- [31] Kai Golibrzuch et al. "Experimental and Theoretical Study of Multi-Quantum Vibrational Excitation: NO($v = 0 \rightarrow 1, 2, 3$) in Collisions with Au(111)". In: *The Journal of Physical Chemistry A* 117.32 (2013), pp. 7091–7101. ISSN: 1089-5639. DOI: 10.1021/jp400313b. URL: <http://pubs.acs.org/doi/abs/10.1021/jp400313b>.
- [32] Alec M. Wodtke, Yuhui Huang, and Daniel J. Auerbach. "Non-Arrhenius surface temperature dependence in vibrational excitation of NO on Au(111): possible evidence for the importance of surface electronic states". In: *Chemical Physics Letters* 364.3-4 (2002), pp. 231–236. ISSN: 00092614. DOI: 10.1016/S0009-2614(02)01313-1. URL: <http://linkinghub.elsevier.com/retrieve/pii/S0009261402013131>.
- [33] Elizabeth K. Watts, Jennifer L.W. Siders, and Greg O. Sitz. "Vibrational excitation of NO scattered from Cu(110)". In: *Surface Science* 374.1-3 (1997), pp. 191–196. ISSN: 00396028. DOI: 10.1016/S0039-6028(96)01194-6. URL: <http://linkinghub.elsevier.com/retrieve/pii/S0039602896011946>.
- [34] Bastian C. Krüger et al. "Vibrational Inelasticity of Highly Vibrationally Excited NO on Ag(111)". In: *The Journal of Physical Chemistry Letters* 7.3 (2016), pp. 441–446. ISSN: 1948-7185. DOI: 10.1021/acs.jpcllett.5b02448. URL: <http://pubs.acs.org/doi/abs/10.1021/acs.jpcllett.5b02448>.
- [35] Roman J. V. Wagner et al. "Vibrational Relaxation of Highly Vibrationally Excited CO Scattered from Au(111): Evidence for CO⁻ Formation". In: *The Journal of Physical Chemistry Letters* 111 (2017), pp. 4887–4892. ISSN: 1948-7185. DOI: 10.1021/acs.jpcllett.7b02207. URL: <http://pubs.acs.org/doi/abs/10.1021/acs.jpcllett.7b02207>.
- [36] C. T. Rettner, D. J. Auerbach, and H. A. Michelsen. "Observation of direct vibrational excitation in collisions of H₂ and D₂ with a Cu(111) surface". In: *Physical Review Letters* 68.16 (1992), pp. 2547–2550. ISSN: 1079-7114. DOI: 10.1103/PhysRevLett.68.2547. URL: http://prl.aps.org/abstract/PRL/v68/i16/p2547_1.
- [37] D. J. Auerbach, C. T. Rettner, and H. A. Michelsen. "Interaction dynamics of hydrogen at a Cu(111) surface". In: *Surface Science* 283.1-3 (1993), pp. 1–8. ISSN: 00396028. DOI: 10.1016/0039-6028(93)90951-F.
- [38] C. T. Rettner, H. A. Michelsen, and D. J. Auerbach. "Quantum-state-specific dynamics of the dissociative adsorption and associative desorption of H₂ at a Cu(111) surface". In: *The Journal of Chemical Physics* 102.11 (1995), pp. 4625–4641. ISSN: 0021-9606. DOI: 10.1063/1.469511. URL: <http://aip.scitation.org/doi/10.1063/1.469511>.

- [39] Jian Wang and Shao-Qing Wang. “Surface energy and work function of fcc and bcc crystals: Density functional study”. In: *Surface Science* 630 (2014), pp. 216–224. ISSN: 00396028. DOI: 10.1016/j.susc.2014.08.017. URL: <http://linkinghub.elsevier.com/retrieve/pii/S0039602814002441>.
- [40] Nicholas E. Singh-Miller and Nicola Marzari. “Surface energies, work functions, and surface relaxations of low-index metallic surfaces from first principles”. In: *Physical Review B* 80.23 (2009), p. 235407. ISSN: 1098-0121. DOI: 10.1103/PhysRevB.80.235407. arXiv: 0801.1077. URL: <https://link.aps.org/doi/10.1103/PhysRevB.80.235407>.
- [41] H. L. Skriver and N. M. Rosengaard. “Surface energy and work function of elemental metals”. In: *Physical Review B* 46.11 (1992), pp. 7157–7168. ISSN: 0163-1829. DOI: 10.1103/PhysRevB.46.7157. URL: <https://link.aps.org/doi/10.1103/PhysRevB.46.7157>.
- [42] Russell D. Johnson III. *NIST Computational Chemistry Comparison and Benchmark Database*. 2016. URL: <http://cccbdb.nist.gov/> (visited on 01/01/2017).
- [43] Keith R. Lykke and Bruce D. Kay. “Rotationally inelastic gas-surface scattering: HCl from Au (111)”. In: *J. Chem. Phys.* 92.111 (1990), p. 2614. ISSN: 00219606. DOI: 10.1063/1.457955. URL: <http://link.aip.org/link/?JCPSA6/92/2614/1>.
- [44] Qin Ran et al. “Direct translation-to-vibrational energy transfer of HCl on gold: Measurement of absolute vibrational excitation probabilities”. In: *Nuclear Instruments and Methods in Physics Research, Section B: Beam Interactions with Materials and Atoms* 258.1 (2007), pp. 1–6. ISSN: 0168583X. DOI: 10.1016/j.nimb.2006.12.077.
- [45] Qin Ran et al. “An advanced molecule-surface scattering instrument for study of vibrational energy transfer in gas-solid collisions.” In: *The Review of Scientific Instruments* 78.10 (2007), p. 104104. ISSN: 0034-6748. DOI: 10.1063/1.2796149. URL: <http://www.ncbi.nlm.nih.gov/pubmed/17979439>.
- [46] J. W. Gadzuk. “Vibrational excitation in molecule–surface collisions due to temporary negative molecular ion formation”. In: *The Journal of Chemical Physics* 79.12 (1983), pp. 6341–6348. ISSN: 0021-9606. DOI: 10.1063/1.445742. URL: <http://aip.scitation.org/doi/10.1063/1.445742>.
- [47] Daniel Matsiev et al. “On the temperature dependence of electronically non-adiabatic vibrational energy transfer in molecule–surface collisions”. In: *Phys. Chem. Chem. Phys.* 13.18 (2011), pp. 8153–8162. ISSN: 1463-9076. DOI: 10.1039/C0CP01418D. URL: <http://xlink.rsc.org/?DOI=C0CP01418D>.
- [48] Walter Kohn and L. J. Sham. “Self-Consistent Equations Including Exchange and Correlation Effects”. In: *Physical Review* 140.4A (1965), A1133–A1138.
- [49] P. Hohenberg and Walter Kohn. “Inhomogeneous Electron Gas”. In: *Physical Review* 136.3B (1964), B864–B871. ISSN: 01631829. DOI: 10.1103/PhysRevB.7.1912. arXiv: 1108.5632.

Bibliography

- [50] Neil Shenvi, Sharani Roy, and John C. Tully. “Nonadiabatic dynamics at metal surfaces: Independent-electron surface hopping”. In: *The Journal of Chemical Physics* 130.17 (2009), p. 174107. ISSN: 0021-9606. DOI: 10.1063/1.3125436. URL: <http://aip.scitation.org/doi/10.1063/1.3125436>.
- [51] Neil Shenvi, Sharani Roy, and John C. Tully. “Dynamical steering and electronic excitation in NO scattering from a gold surface”. In: *Science* 326.5954 (2009), pp. 829–832. ISSN: 1095-9203. DOI: 10.1126/science.1179240. URL: <http://www.ncbi.nlm.nih.gov/pubmed/19892977>.
- [52] Sharani Roy, Neil A. Shenvi, and John C. Tully. “Model Hamiltonian for the interaction of NO with the Au(111) surface”. In: *The Journal of Chemical Physics* 130.17 (2009), p. 174716. ISSN: 0021-9606. DOI: 10.1063/1.3122989. URL: <http://aip.scitation.org/doi/10.1063/1.3122989>.
- [53] Bastian C. Krüger et al. “NO Vibrational Energy Transfer on a Metal Surface: Still a Challenge to First-Principles Theory”. In: *The Journal of Physical Chemistry C* 119.6 (2015), pp. 3268–3272. ISSN: 1932-7447. DOI: 10.1021/acs.jpcc.5b00388. URL: <http://pubs.acs.org/doi/abs/10.1021/acs.jpcc.5b00388>.
- [54] Wenjie Dou and Joseph E. Subotnik. “Perspective: How to understand electronic friction”. In: *Journal of Chemical Physics* 148.23 (2018). ISSN: 00219606. DOI: 10.1063/1.5035412.
- [55] Martin Head-Gordon and John C. Tully. “Molecular dynamics with electronic frictions”. In: *The Journal of Chemical Physics* 103.23 (1995), pp. 10137–10145. ISSN: 0021-9606. DOI: 10.1063/1.469915. URL: <http://aip.scitation.org/doi/10.1063/1.469915>.
- [56] Reinhard J. Maurer et al. “Ab initio tensorial electronic friction for molecules on metal surfaces: Nonadiabatic vibrational relaxation”. In: *Physical Review B* 94.11 (2016), p. 115432. ISSN: 2469-9950. DOI: 10.1103/PhysRevB.94.115432. URL: <https://link.aps.org/doi/10.1103/PhysRevB.94.115432>.
- [57] Christof Bartels et al. “Energy transfer at metal surfaces: the need to go beyond the electronic friction picture”. In: *Chemical Science* 2.9 (2011), p. 1647. ISSN: 2041-6520. DOI: 10.1039/c1sc00181g.
- [58] Tianhui Liu, Bina Fu, and Dong H. Zhang. “Six-dimensional quantum dynamics study for the dissociative adsorption of HCl on Au(111) surface”. In: *The Journal of Chemical Physics* 139.18 (2013), p. 184705. ISSN: 00219606. DOI: 10.1063/1.4829508. URL: <http://www.ncbi.nlm.nih.gov/pubmed/24320289>.
- [59] Tianhui Liu, Bina Fu, and Dong H. Zhang. “Six-dimensional quantum dynamics study for the dissociative adsorption of DCl on Au(111) surface”. In: *Journal of Chemical Physics* 140.14 (2014), p. 144701. ISSN: 00219606. DOI: 10.1063/1.4870594.

- [60] Tianhui Liu, Bina Fu, and Dong H. Zhang. “Six-dimensional potential energy surface of the dissociative chemisorption of HCl on Au(111) using neural networks”. In: *Science China Chemistry* 57.1 (2014), pp. 147–155. ISSN: 16747291. DOI: 10.1007/s11426-013-5005-7.
- [61] J. C. Polanyi and W. H. Wong. “Location of Energy Barriers. I. Effect on the Dynamics of Reactions A + BC”. In: *The Journal of Chemical Physics* 51.1969 (1969), p. 1439. ISSN: 00219606. DOI: 10.1063/1.1672194.
- [62] John C. Polanyi. “Some Concepts in Reaction Dynamics”. In: *Accounts of Chemical Research* 5.5 (1972), pp. 161–168. ISSN: 0001-4842. DOI: 10.1021/ar50079a001.
- [63] Jan Geweke et al. “Vibrational energy transfer near a dissociative adsorption transition state: State-to-state study of HCl collisions at Au(111)”. In: *The Journal of Chemical Physics* 145.5 (2016), p. 054709. ISSN: 0021-9606. DOI: 10.1063/1.4959968. URL: <http://scitation.aip.org/content/aip/journal/jcp/145/5/10.1063/1.4959968>.
- [64] John H. Moore et al. *Building Scientific Apparatus*. 4th. Cambridge: Cambridge University Press, 2009, p. 629. ISBN: 978-0-521-87858-6. URL: www.cambridge.org/9780521878586.
- [65] Daniel W. Kohn, Horst Clauberg, and Peter Chen. “Flash pyrolysis nozzle for generation of radicals in a supersonic jet expansion”. In: *Review of Scientific Instruments* 63.8 (1992), pp. 4003–4005. ISSN: 0034-6748. DOI: 10.1063/1.1143254. URL: <http://aip.scitation.org/doi/10.1063/1.1143254>.
- [66] Giacinto Scoles. *Atomic and Molecular Beam Methods*. Ed. by Giacinto Scoles et al. New York: Oxford University Press, 1988, p. 721. ISBN: 0-19-504280-8.
- [67] Hans Pauly. *Atom, Molecule, and Cluster Beams I: Basic Theory, Production and Detection of Thermal Energy Beams*. Vol. 28. Springer Series on Atomic, Optical, and Plasma Physics. Berlin, Heidelberg: Springer Berlin Heidelberg, 2000, p. 344. ISBN: 978-3-642-08623-6. DOI: 10.1007/978-3-662-04213-7. URL: <http://link.springer.com/10.1007/978-3-662-04213-7>.
- [68] David R. Lide et al. *CRC Handbook of Chemistry and Physics, Internet Version 2005*. Boca Raton, FL: CRC Press, 2005.
- [69] Catherine Ouannes and Thérèse Wilson. “Quenching of singlet oxygen by tertiary aliphatic amines. Effect of DABCO (1,4-diazabicyclo[2.2.2]octane)”. In: *Journal of the American Chemical Society* 90.23 (1968), pp. 6527–6528. ISSN: 0002-7863. DOI: 10.1021/ja01025a059. URL: <http://pubs.acs.org/doi/abs/10.1021/ja01025a059>.
- [70] J.V. V. Barth et al. “Scanning tunneling microscopy observations on the reconstructed Au(111) surface: Atomic structure, long-range superstructure, rotational domains, and surface defects”. In: *Physical Review B* 42.15 (1990), pp. 9307–9318. ISSN: 0163-1829. DOI: 10.1103/PhysRevB.42.9307. URL: <http://link.aps.org/doi/10.1103/PhysRevB.42.9307>.

Bibliography

- [71] H. Bulou and C. Goyhenex. "Local strain analysis of the herringbone reconstruction of Au(111) through atomistic simulations". In: *Physical Review B* 65.4 (2002), p. 045407. ISSN: 0163-1829. DOI: 10.1103/PhysRevB.65.045407. URL: <http://link.aps.org/doi/10.1103/PhysRevB.65.045407>.
- [72] Sivaram Arepalli et al. "Detection of Cl atoms and HCl molecules by resonantly enhanced multiphoton ionization". In: *Chemical Physics Letters* 118.1 (1985), pp. 88–92. ISSN: 00092614. DOI: 10.1016/0009-2614(85)85272-6.
- [73] Thomas A. Spiglanin, David W. Chandler, and David H. Parker. "Mass-resolved laser ionization spectroscopy of HCl". In: *Chemical Physics Letters* 137.5 (1987), pp. 414–420. ISSN: 00092614. DOI: 10.1016/0009-2614(87)80225-7.
- [74] Eric A. Rohlfing, David W. Chandler, and David H. Parker. "Direct measurement of rotational energy transfer rate constants for H³⁵Cl ($v = 1$)". In: *The Journal of Chemical Physics* 87.9 (1987), p. 5229. ISSN: 00219606. DOI: 10.1063/1.453691. URL: <http://scitation.aip.org/content/aip/journal/jcp/87/9/10.1063/1.453691>.
- [75] David S. Green, Grant A. Bickel, and Stephen C. Wallace. "(2 + 1) Resonance enhanced multiphoton ionization of hydrogen chloride in a pulsed supersonic jet: Vacuum wavenumbers of rotational lines with detailed band analysis for excited electronic states of H₃₅Cl¹". In: *Journal of Molecular Spectroscopy* 150 (1991), pp. 354–387. ISSN: 00222852. DOI: 10.1016/0022-2852(91)90240-B.
- [76] Peter Senn. "The computation of RKR potential energy curves of diatomic molecules using Mathematica". In: *Computers & Chemistry* 19.4 (1995), pp. 437–439. ISSN: 00978485. DOI: 10.1016/0097-8485(95)00016-L. URL: <http://linkinghub.elsevier.com/retrieve/pii/009784859500016L>.
- [77] William R. Simpson et al. "Reaction of Cl with vibrationally excited CH₄ and CHD₃: State-to-state differential cross sections and steric effects for the HCl product". In: *Journal of Chemical Physics* 103.17 (1995), pp. 7313–7335.
- [78] National Institute of Standards and Technology. *NIST Standard Reference Database*. 2017. URL: <http://webbook.nist.gov/cgi/cbook.cgi?ID=C630080&Units=SI&Mask=1000#Diatomic> (visited on 03/22/2017).
- [79] Siegfried Hofmann. *Auger- and X-Ray Photoelectron Spectroscopy in Materials Science*. Vol. 49. Springer Series in Surface Sciences. Berlin, Heidelberg: Springer Berlin Heidelberg, 2013. ISBN: 978-3-642-27380-3. DOI: 10.1007/978-3-642-27381-0. URL: <http://link.springer.com/10.1007/978-3-642-27381-0>.
- [80] Lawrence E. Davis et al. *Handbook of Auger Electron Spectroscopy*. 2nd. Physical Electronics Industries, Inc., 1976.
- [81] Daniel Matsiev. "Molecular Beams Scattering from Metal Surfaces: Observation of Vibrational Excitation in HCl Collisions with Au(111)". PhD thesis. University of California, Santa Barbara, 2007.

- [82] Igor Rahinov et al. "Efficient vibrational and translational excitations of a solid metal surface: State-to-state time-of-flight measurements of HCl($v=2, J=1$) scattering from Au(111)". In: *The Journal of Chemical Physics* 129.21 (2008), p. 214708. ISSN: 1089-7690. DOI: 10.1063/1.3028542. URL: <http://www.ncbi.nlm.nih.gov/pubmed/19063576>.
- [83] L. Landau and E. Teller. "Zur Theorie der Schalldispersion". In: *Physikalische Zeitschrift der Sowjetunion* 10 (1936), pp. 34–43.
- [84] E. E. Nikitin and J. Troe. "70 years of Landau–Teller theory for collisional energy transfer. Semiclassical three-dimensional generalizations of the classical collinear model". In: *Phys. Chem. Chem. Phys.* 10.11 (2008), pp. 1483–1501. ISSN: 1463-9076. DOI: 10.1039/B715095D. URL: <http://xlink.rsc.org/?DOI=B715095D>.
- [85] David A. King and Michael G. Wells. "Molecular beam investigation of adsorption kinetics on bulk metal targets: Nitrogen on tungsten". In: *Surface Science* 29.2 (1972), pp. 454–482. ISSN: 00396028. DOI: 10.1016/0039-6028(72)90232-4.
- [86] P. Morten Hundt et al. "Vibrationally Promoted Dissociation of Water on Ni(111)". In: *Science* 344.6183 (2014), pp. 504–507. ISSN: 0036-8075. DOI: 10.1126/science.1251277. URL: <http://www.ncbi.nlm.nih.gov/pubmed/24786076><http://www.sciencemag.org/cgi/doi/10.1126/science.1251277>.
- [87] Mathieu P. Schmid et al. "Molecular-beam/surface-science apparatus for state-resolved chemisorption studies using pulsed-laser preparation". In: *Review of Scientific Instruments* 74.9 (2003), pp. 4110–4120. ISSN: 0034-6748. DOI: 10.1063/1.1599064. URL: <http://aip.scitation.org/doi/10.1063/1.1599064>.
- [88] Daniel P. Engelhart et al. "Temperature programmed desorption of weakly bound adsorbates on Au(111)". In: *Surface Science* 650 (2016), pp. 11–16. ISSN: 00396028. DOI: 10.1016/j.susc.2015.06.010. URL: <http://dx.doi.org/10.1016/j.susc.2015.06.010><https://linkinghub.elsevier.com/retrieve/pii/S0039602815001685>.
- [89] Klaus P. Huber and Gerhard H. Herzberg. "Constants of Diatomic Molecules". In: *NIST Chemistry WebBook, NIST Standard Reference Database Number 69*. Ed. by P. J. Linstrom and W. G. Mallard. Gaithersburg MD: National Institute of Standards and Technology. DOI: 10.18434/T4D303. URL: <https://doi.org/10.18434/T4D303>.
- [90] Paul M. Mayer and Tomas Baer. "A photoionization study of vibrational cooling in molecular beams". In: *International Journal of Mass Spectrometry and Ion Processes* 156.3 (1996), pp. 133–139. ISSN: 01681176. DOI: 10.1016/S0168-1176(96)04422-9. URL: <https://linkinghub.elsevier.com/retrieve/pii/S0168117696044229>.
- [91] George N. Kastanas and Bruce E. Koel. "Interaction of Cl₂ with the Au(111) surface in the temperature range of 120 to 1000 K". In: *Applied Surface Science* 64 (1993), pp. 235–249. ISSN: 01694332. DOI: 10.1016/0169-4332(93)90030-F.

Bibliography

- [92] N.D. Spencer and R.M. Lambert. "Chlorine chemisorption and surface chloride formation on Au(111)". In: *Surface Science Letters* 107 (1981), A223. ISSN: 01672584. DOI: 10.1016/0167-2584(81)90556-9.
- [93] P. Morten Hundt, Regis Bisson, and Rainer D. Beck. "The sticking probability of D₂O-water on ice: Isotope effects and the influence of vibrational excitation." In: *J. Chem. Phys.* 137.7 (2012), p. 074701. ISSN: 1089-7690. DOI: 10.1063/1.4742914. URL: <http://www.ncbi.nlm.nih.gov/pubmed/22920131>.
- [94] Helen Chadwick and Rainer D. Beck. "Quantum state resolved gas-surface reaction dynamics experiments: a tutorial review". In: *Chemical Society Reviews* 45.13 (2016), pp. 3576–3594. ISSN: 0306-0012. DOI: 10.1039/C5CS00476D. URL: <https://dx.doi.org/10.1039/C5CS00476D>.
- [95] Gernot Fuchs et al. "Enigmatic HCl + Au(111) Reaction: A Puzzle for Theory and Experiment". In: *The Journal of Physical Chemistry C* 120.45 (2016), pp. 25760–25779. ISSN: 1932-7447. DOI: 10.1021/acs.jpcc.6b07453. URL: <http://pubs.acs.org/doi/abs/10.1021/acs.jpcc.6b07453>.
- [96] Brian Kolb and Hua Guo. "Communication: Energy transfer and reaction dynamics for DCl scattering on Au(111): An ab initio molecular dynamics study". In: *The Journal of Chemical Physics* 145.1 (2016), p. 011102. ISSN: 0021-9606. DOI: 10.1063/1.4956453. URL: <http://scitation.aip.org/content/aip/journal/jcp/145/1/10.1063/1.4956453>.
- [97] Ming Pan, David W. Flaherty, and C. Buddie Mullins. "Low-temperature hydrogenation of acetaldehyde to ethanol on H-precovered Au(111)". In: *Journal of Physical Chemistry Letters* 2.12 (2011), pp. 1363–1367. ISSN: 19487185. DOI: 10.1021/jz200577n.
- [98] David A King. "Thermal desorption from metal surfaces: A review". In: *Surface Science* 47.1 (1975), pp. 384–402. ISSN: 00396028. DOI: 10.1016/0039-6028(75)90302-7. URL: <https://linkinghub.elsevier.com/retrieve/pii/0039602875903027>.
- [99] Deborah Holmes Parker, Mark E. Jones, and Bruce E. Koel. "Determination of the reaction order and activation energy for desorption kinetics using TPD spectra: Application to D₂ desorption from Ag(111)". In: *Surface Science* 233.1-2 (1990), pp. 65–73. ISSN: 00396028. DOI: 10.1016/0039-6028(90)90176-9. URL: <http://linkinghub.elsevier.com/retrieve/pii/0039602890901769>.
- [100] Gernot Fuchs et al. "Reactive and Nonreactive Scattering of HCl from Au(111): An Ab Initio Molecular Dynamics Study". In: *The Journal of Physical Chemistry C* 123.4 (2019), pp. 2287–2299. ISSN: 1932-7447. DOI: 10.1021/acs.jpcc.8b10686. URL: <http://pubs.acs.org/doi/10.1021/acs.jpcc.8b10686>.

- [101] Mohamed S.N. Al-Kahali et al. "Mass-resolved multiphoton ionization spectroscopy of jet-cooled Cl_2 . II. The (2+1) REMPI spectrum between 76 000 and 90 000 cm^{-1} ". In: *Journal of Chemical Physics* 104.5 (1996), pp. 1833–1838. ISSN: 00219606. DOI: 10.1063/1.470980.
- [102] Christoph Steinsiek et al. "Work Function Dependence of Vibrational Relaxation Probabilities: $\text{NO}(v = 2)$ Scattering from Ultrathin Metallic Films of $\text{Ag}/\text{Au}(111)$ ". In: *The Journal of Physical Chemistry C* 122.18 (2018), pp. 10027–10033. ISSN: 1932-7447. DOI: 10.1021/acs.jpcc.8b01950. URL: <http://pubs.acs.org/doi/10.1021/acs.jpcc.8b01950>.
- [103] Christoph Steinsiek et al. "Translational Inelasticity of NO and CO in Scattering from Ultrathin Metallic Films of $\text{Ag}/\text{Au}(111)$ ". In: *The Journal of Physical Chemistry C* 122.33 (2018), pp. 18942–18948. ISSN: 1932-7447. DOI: 10.1021/acs.jpcc.8b04158. URL: <http://pubs.acs.org/doi/10.1021/acs.jpcc.8b04158>.
- [104] Charles T. Rettner. "Reaction of an H-atom beam with $\text{Cl}/\text{Au}(111)$: Dynamics of concurrent Eley–Rideal and Langmuir–Hinshelwood mechanisms". In: *The Journal of Chemical Physics* 101.111 (1994), pp. 1529–1546. ISSN: 00219606. DOI: 10.1063/1.467776. URL: <http://scitation.aip.org/content/aip/journal/jcp/101/2/10.1063/1.467776>.
- [105] Joseph G. Quattrucci and Bret Jackson. "Quasiclassical study of Eley–Rideal and hot atom reactions of H atoms with Cl adsorbed on a $\text{Au}(111)$ surface". In: *The Journal of Chemical Physics* 122.7 (2005), p. 074705. ISSN: 00219606. DOI: 10.1063/1.1851498.
- [106] Tianhui Liu, Bina Fu, and Dong H. Zhang. "Six-dimensional potential energy surfaces of the dissociative chemisorption of HCl on $\text{Ag}(111)$ with three density functionals". In: *The Journal of Chemical Physics* 149.5 (2018), p. 054702. ISSN: 0021-9606. DOI: 10.1063/1.5036805. URL: <http://aip.scitation.org/doi/10.1063/1.5036805>.
- [107] Tianhui Liu, Bina Fu, and Dong H. Zhang. "Six-dimensional quantum dynamics for the dissociative chemisorption of HCl on rigid $\text{Ag}(111)$ on three potential energy surfaces with different density functionals". In: *The Journal of Chemical Physics* 149.17 (2018), p. 174702. ISSN: 0021-9606. DOI: 10.1063/1.5053827. URL: <http://aip.scitation.org/doi/10.1063/1.5053827>.
- [108] M. Bowker and K. C. Waugh. "The adsorption of chlorine and chlorination of $\text{Ag}(111)$ ". In: *Surface Science* 134.3 (1983), pp. 639–664. ISSN: 00396028. DOI: 10.1016/0039-6028(83)90063-8.
- [109] Brian Kolb et al. "High-Dimensional Atomistic Neural Network Potentials for Molecule-Surface Interactions: HCl Scattering from $\text{Au}(111)$ ". In: *The Journal of Physical Chemistry Letters* 111 (2017), pp. 666–672. ISSN: 1948-7185. DOI: 10.1021/acs.jpcclett.6b02994. URL: <http://pubs.acs.org/doi/abs/10.1021/acs.jpcclett.6b02994>.

Bibliography

- [110] C. Díaz and R. A. Olsen. “A note on the vibrational efficacy in molecule-surface reactions.” In: *The Journal of Chemical Physics* 130.9 (2009), p. 094706. ISSN: 1089-7690. DOI: 10.1063/1.3080613. URL: <http://www.ncbi.nlm.nih.gov/pubmed/19275417>.
- [111] Michael Grotemeyer and Eckhard Pehlke. “Electronic Energy Dissipation During Scattering of Vibrationally Excited Molecules at Metal Surfaces: Ab initio Simulations for HCl/Au(111)”. In: *Physical Review Letters* 112.4 (2014), p. 043201. ISSN: 0031-9007. DOI: 10.1103/PhysRevLett.112.043201. URL: <http://link.aps.org/doi/10.1103/PhysRevLett.112.043201>.
- [112] Yingying Wang et al. “Mechanism of N₂O Formation During NO Reduction on the Au(111) Surface”. In: *The Journal of Physical Chemistry C* 114.6 (2010), pp. 2711–2716. ISSN: 1932-7447. DOI: 10.1021/jp9103596. URL: <https://pubs.acs.org/doi/10.1021/ef9500898https://pubs.acs.org/doi/10.1021/jp9103596>.
- [113] Roman J. V. Wagner et al. “Electron transfer mediates vibrational relaxation of CO in collisions with Ag(111)”. In: *Physical Chemistry Chemical Physics* (2019). ISSN: 1463-9076. DOI: 10.1039/C8CP06041J. URL: <http://xlink.rsc.org/?DOI=C8CP06041J>.
- [114] B. Baule. “Theoretische Behandlung der Erscheinungen in verdünnten Gasen”. In: *Annalen der Physik* 349.9 (1914), pp. 145–176.
- [115] Russell Cooper et al. “Efficient translational excitation of a solid metal surface: State-to-state translational energy distributions of vibrational ground state HCl scattering from Au(111)”. In: *Journal of Vacuum Science & Technology A: Vacuum, Surfaces, and Films* 27.4 (2009), p. 907. ISSN: 07342101. DOI: 10.1116/1.3071971. URL: <http://scitation.aip.org/content/avs/journal/jvsta/27/4/10.1116/1.3071971>.
- [116] Kai Golibrzuch et al. “Incidence energy dependent state-to-state time-of-flight measurements of NO($v = 3$) collisions with Au(111): the fate of incidence vibrational and translational energy.” In: *Physical Chemistry Chemical Physics* 16.16 (2014), pp. 7602–10. ISSN: 1463-9084. DOI: 10.1039/c3cp55224a. URL: <http://www.ncbi.nlm.nih.gov/pubmed/24637916>.
- [117] Dmitriy Borodin. “Molecular Beam Studies of HCl Adsorption on Au (111) Surface”. Bachelor’s Thesis. Georg-August-Universität Göttingen, 2015.
- [118] Kai Golibrzuch et al. “State-to-state time-of-flight measurements of NO scattering from Au(111): Direct observation of translation-to-vibration coupling in electronically nonadiabatic energy transfer”. In: *Journal of Physical Chemistry A* 117.36 (2013), pp. 8750–8760. ISSN: 1520-5215. DOI: 10.1021/jp403382b.
- [119] A. Amirav and Mark J. Cardillo. “Electron-hole pair creation by atomic scattering at surfaces”. In: *Physical Review Letters* 57.18 (1986), pp. 2299–2302. ISSN: 00319007. DOI: 10.1103/PhysRevLett.57.2299.

- [120] Hongyan Jiang et al. “Inelastic H and D atom scattering from Au(111) as benchmark for theory”. In: *The Journal of Chemical Physics* 150.18 (2019), p. 184704. ISSN: 0021-9606. DOI: 10.1063/1.5094693. URL: <http://aip.scitation.org/doi/10.1063/1.5094693>.
- [121] Yvonne Dorenkamp et al. “Hydrogen collisions with transition metal surfaces: Universal electronically nonadiabatic adsorption”. In: *The Journal of Chemical Physics* 148.3 (2018), p. 034706. ISSN: 0021-9606. DOI: 10.1063/1.5008982. URL: <http://aip.scitation.org/doi/10.1063/1.5008982>.
- [122] J. R. Roscioli et al. “State-resolved velocity map imaging of surface-scattered molecular flux”. In: *Phys. Chem. Chem. Phys.* 14.12 (2012), pp. 4070–4080. ISSN: 1463-9076. DOI: 10.1039/C1CP22938A. URL: <http://www.ncbi.nlm.nih.gov/pubmed/22159155><http://xlink.rsc.org/?DOI=C1CP22938A>.
- [123] Pranav R. Shirhatti et al. “Activated Dissociation of HCl on Au(111)”. In: *The Journal of Physical Chemistry Letters* 7.7 (2016), pp. 1346–1350. ISSN: 1948-7185. DOI: 10.1021/acs.jpcllett.6b00289. URL: <http://pubs.acs.org/doi/abs/10.1021/acs.jpcllett.6b00289>.
- [124] Tianhui Liu, Bina Fu, and Dong H. Zhang. “HCl dissociating on a rigid Au(111) surface: A six-dimensional quantum mechanical study on a new potential energy surface based on the RPBE functional”. In: *The Journal of Chemical Physics* 146.16 (2017), p. 164706. ISSN: 0021-9606. DOI: 10.1063/1.4982051. URL: <http://aip.scitation.org/doi/10.1063/1.4982051>.
- [125] N. Saliba, D. H. Parker, and B. E. Koel. “Adsorption of oxygen on Au(111) by exposure to ozone”. In: *Surface Science* 410.2-3 (1998), pp. 270–282. ISSN: 00396028. DOI: 10.1016/S0039-6028(98)00309-4. URL: <https://linkinghub.elsevier.com/retrieve/pii/S0039602898003094>.
- [126] Weiwei Gao et al. “Chlorine Adsorption on Au(111): Chlorine Overlay or Surface Chloride?” In: *Journal of the American Chemical Society* 130.11 (2008), pp. 3560–3565. ISSN: 0002-7863. DOI: 10.1021/ja077989a. URL: <https://pubs.acs.org/doi/10.1021/ja077989a>.
- [127] P. Morten Hundt et al. “Vibrational Activation of Methane Chemisorption: The Role of Symmetry”. In: *The Journal of Physical Chemistry Letters* 5.11 (2014), pp. 1963–1967. ISSN: 1948-7185. DOI: 10.1021/jz500728d. URL: <http://pubs.acs.org/doi/10.1021/jz500728d>.
- [128] P. Morten Hundt et al. “Bond-Selective and Mode-Specific Dissociation of CH₃D and CH₂D₂ on Pt(111)”. In: *The Journal of Physical Chemistry A* 119.50 (2015), pp. 12442–12448. ISSN: 1089-5639. DOI: 10.1021/acs.jpca.5b07949. URL: <http://pubs.acs.org/doi/10.1021/acs.jpca.5b07949>.

Bibliography

- [129] Bruce L. Yoder et al. "Alignment dependent chemisorption of vibrationally excited CH_4 ($v = 3$) on Ni(100), Ni(110), and Ni(111)". In: *The Journal of Chemical Physics* 135.22 (2011), p. 224703. ISSN: 0021-9606. DOI: 10.1063/1.3665136. URL: <http://aip.scitation.org/doi/10.1063/1.3665136>.
- [130] Dan J. Harding et al. "Ion and velocity map imaging for surface dynamics and kinetics". In: *The Journal of Chemical Physics* 147.1 (2017), p. 013939. ISSN: 0021-9606. DOI: 10.1063/1.4983307. URL: <http://aip.scitation.org/doi/10.1063/1.4983307>.
- [131] Jannis Neugebahren et al. "Velocity-resolved kinetics of site-specific carbon monoxide oxidation on platinum surfaces". In: *Nature* 558.7709 (2018), pp. 280–283. ISSN: 0028-0836. DOI: 10.1038/s41586-018-0188-x. URL: <http://www.nature.com/articles/s41586-018-0188-x>.
- [132] Quan Shuai et al. "Evidence for Electron–Hole Pair Excitation in the Associative Desorption of H_2 and D_2 from Au(111)". In: *The Journal of Physical Chemistry Letters* 8.111 (2017), pp. 1657–1663. ISSN: 1948-7185. DOI: 10.1021/acs.jpcclett.7b00265. URL: <http://pubs.acs.org/doi/abs/10.1021/acs.jpcclett.7b00265>.
- [133] Axel D. Becke. "Perspective: Fifty years of density-functional theory in chemical physics". In: *The Journal of Chemical Physics* 140.2014 (2014), 18A301. ISSN: 0021-9606. DOI: 10.1063/1.4869598. URL: <http://aip.scitation.org/doi/10.1063/1.4869598>.
- [134] Alexandre Tkatchenko et al. "Accurate and Efficient Method for Many-Body van der Waals Interactions". In: *Physical Review Letters* 108.23 (2012), p. 236402. ISSN: 0031-9007. DOI: 10.1103/PhysRevLett.108.236402. URL: <https://link.aps.org/doi/10.1103/PhysRevLett.108.236402>.
- [135] Haoyu S. Yu, Shaohong L. Li, and Donald G. Truhlar. "Perspective: Kohn-Sham density functional theory descending a staircase". In: *The Journal of Chemical Physics* 145.13 (2016), p. 130901. ISSN: 0021-9606. DOI: 10.1063/1.4963168. URL: <http://aip.scitation.org/doi/10.1063/1.4963168>.
- [136] Kai Golibrzuch. "Quantum-state specific scattering of molecules from surfaces". PhD thesis. 2014, p. 169.
- [137] George Comsa and Rudolf David. "Dynamical parameters of desorbing molecules". In: *Surface Science Reports* 5.4 (1985), pp. 145–198. ISSN: 01675729. DOI: 10.1016/0167-5729(85)90009-3. URL: <http://linkinghub.elsevier.com/retrieve/pii/0167572985900093>.

CURRICULUM VITAE

Jan Geweke

current email: jan.geweke@mpibpc.mpg.de

permanent email: j.geweke@gmx.de

Education

- 2015–2019** **PhD** École Polytechnique Fédérale de Lausanne, Switzerland
Title: Scattering HCl Molecules from Au(111) and Ag(111) Surfaces
Supervisors: Prof. Alec Wodtke (Max Planck Institute for Biophysical Chemistry & University of Göttingen, Göttingen, Germany)
Prof. Rainer Beck (EPFL, Lausanne, Switzerland)
- 2011–2013** **MSc** University of Göttingen, Germany
Title: Graphene on Chemically Modified Surfaces
Supervisor: Prof. Alec Wodtke (Max Planck Institute for Biophysical Chemistry & University of Göttingen, Göttingen, Germany)
- 2008–2011** **BSc** University of Hamburg, Germany
Title: Synthesis of pyramidal CdSe nanoparticles and the influence of chlorine containing additives on their shape
Supervisor: Prof. Christian Klinke (University of Hamburg, Germany)
- 2007** **Abitur** Herzog-Ernst-Gymnasium Uelzen, Germany

Publications

P. R. Shirhatti, I. Rahinov, K. Golibrzuch, J. Werdecker, J. Geweke, J. Altschäffel, S. Kumar, D. J. Auerbach, C. Bartels and A. M. Wodtke, "Observation of the adsorption and desorption of vibrationally excited molecules on a metal surface", *Nat. Chem.*, **2018**, 10, 592–598. DOI: 10.1038/s41557-018-0003-1.

C. Steinsiek, P. R. Shirhatti, J. Geweke, J. A. Lau, J. Altschäffel, A. Kandratsenka, C. Bartels and A. M. Wodtke, "Translational Inelasticity of NO and CO in Scattering from Ultrathin Metallic Films of Ag/Au(111)", *J. Phys. Chem. C*, **2018**, 122, 18942–18948. DOI: 10.1021/acs.jpcc.8b04158.

C. Steinsiek, P. R. Shirhatti, J. Geweke, C. Bartels and A. M. Wodtke, "Work Function Dependence of Vibrational Relaxation Probabilities: NO($v = 2$) Scattering from Ultrathin Metallic Films of Ag/Au(111)", *J. Phys. Chem. C*, **2018**, 122, 10027–10033. DOI: 10.1021/acs.jpcc.8b01950.

J. Geweke, P. R. Shirhatti, I. Rahinov, C. Bartels and A. M. Wodtke, "Vibrational energy transfer near a dissociative adsorption transition state: State-to-state study of HCl collisions at Au(111)", *J. Chem. Phys.*, **2016**, 145, 054709. DOI: 10.1063/1.4959968.

P. R. Shirhatti, J. Geweke, C. Steinsiek, C. Bartels, I. Rahinov, D. J. Auerbach and A. M. Wodtke, "Activated Dissociation of HCl on Au(111)", *J. Phys. Chem. Lett.*, **2016**, 7, 1346–1350. DOI: 10.1021/acs.jpcclett.6b00289.

K. Golibrzuch, P. R. Shirhatti, J. Geweke, J. Werdecker, A. Kandratsenka, D. J. Auerbach, A. M. Wodtke and C. Bartels, "CO Desorption from a Catalytic Surface: Elucidation of the Role of Steps by Velocity-Selected Residence Time Measurements", *J. Am. Chem. Soc.*, **2015**, 137, 1465–1475. DOI: 10.1021/ja509530k.

M. Meyns, F. Iacono, C. Palencia, J. Geweke, M. D. Coderch, U. E. A. Fittschen, J. M. Gallego, R. Otero, B. H. Juárez and C. Klinke, "Shape Evolution of CdSe Nanoparticles Controlled by Halogen Compounds", *Chem. Mater.*, **2014**, 26, 1813–1821. DOI: 10.1021/cm4037082.

